

First Principles Theory of Organic Molecules on Metal surfaces: Formate, 3-Thiophene-carboxylate and Glycinate on Cu(110)

Von der Fakultät für Mathematik, Informatik und Naturwissenschaften der
Rheinisch-Westfälischen Technischen Hochschule Aachen
zur Erlangung des akademischen Grades eines Doktors der Naturwissenschaften
genehmigte Dissertation

vorgelegt von

Master of Science

Nicolae Atodiresei

aus Paşcani (Romania)

Berichter:

Herr apl. Prof. Dr. rer. nat. Kurt Schroeder
Herr Univ.-Prof. Dr. rer. nat. Stefan Blügel

Tag der mündlichen Prüfung: 12. Oktober 2004

Diese Dissertation ist auf den Internetseiten der Hochschulbibliothek online verfügbar.

Contents

Introduction	7
Chapter 1	
Density Functional Theory	
1.1. Density Functional Theory	11
1.2. The Kohn-Sham Formulation	16
1.3. Exchange-Correlation Terms in Density Functional Theory	19
1.3.1. Local Density Approximation (LDA)	20
1.3.2. Generalized Gradient Approximation (GGA)	22
Chapter 2	
Density Functional Theory in a Plane Wave implementation	
2.1. Supercell Approach	24
2.2. Bloch's Theorem and the Plane-Wave Basis Set	25
2.3. Kohn-Sham Equations in Plane-Wave Form	26
2.4. \vec{k} -point Sampling	27
Chapter 3	
Pseudopotentials	
3.1. Pseudopotentials	28
3.2. Generation of Norm-Conserving Pseudopotentials	30
3.3. Semi-local Pseudopotential and Kleinman-Bylander Form of the Pseudopotential	32
3.4. The PAW Pseudopotential	33
3.5. Partial Core-Correction	35
3.6. General Scheme for Pseudopotential Generation	36
3.7. Comments on the Generation of the Pseudopotentials	38

Chapter 4

The EStCoMPP-Program

4.1. The Energy Minimization	40
4.2. Explicit Form of the Equations in the EStCoMPP-program	
The Kinetic Energy	43
The local Energy	43
The Non-local Part of the Energy	45
The Ewald-Energy	47
The Hellman-Feynman Forces	47
The Loop-Structure and the Algorithms	49
4.3. Iterative Eigenvalue Determination	50
4.4. The Electronic Self-consistency and Molecular Relaxation Loops	51

Chapter 5

Cadmium Complexes in Si and Ge	53
---------------------------------------	----

Chapter 6

Formate on Cu(110) surface

6.1 Introduction	58
6.2 Formate Free Radical	61
6.3 Formate-Cu(110) Surface Systems	64
6.4 “Low Formate Coverage”	70
6.5 “High Formate Coverage”	73
6.6 Oxygen Precovered Cu(110), “High Formate Coverage”	76

Chapter 7

3-Thiophene carboxylate on Cu(110) surface

7.1 Introduction	81
7.2 3-Thiophene Carboxylate Free Radical	83
7.3 3-Thiophene Carboxylate-Cu(110) System	87

Chapter 8

Glycinate on Cu(110)-Surface

8.1 Generalities	99
8.2 Chirality and the Biological Importance	100
8.3 Experimental Structure Determination	100
8.4 Glycinate Free Radical	103

8.5 Glycinate-Cu(110) System	106
Energetics and Bond Strength	113
Atomic and Electronic Structure	116
Summary	122
Appendixes	
Appendix A.1.	
Functional (variational) derivative	127
Appendix A.2.	
Exchange-correlation terms in DFT	129
Appendix A.3.	
Explicit formula of the terms used in calculation of exchange-correlation energy and potential	131
Appendix A.4.	
Formulae	133
Appendix A.5.	
Details about the GGA implementation in the subroutines of EStCoMPP-Program	140
Appendix B	
Partial core-correction in real space	143
Appendix C	
Parameters and tests of the PAW-pseudopotentials	144
Appendix D	
PLDOS for clean Cu(110) surface	178
Bibliography	180

Introduction

New ways have to be explored if the miniaturization of the electronic devices is to continue at the same pace as in the last decades. Besides incurring in exponentially increasing fabrication costs, the down-scaling of (optical) lithographic processes in the “top-down” approach for silicon chip manufacturing will soon lead to fundamental physical limits [IO00]. An alternative possibility is to explore the so-called “bottom-up” approach, which is based on the formation of functional devices out of prefabricated molecular building blocks with intrinsic electronic properties - an area generally referred to as molecular electronics and nanodevices. Molecules can be viewed as the ultimate limit of electronic devices, since their size is about 1nm. By using appropriately designed organic molecules, the density of transistors per chip might potentially be increased by up to a factor of 10^5 compared to present standards [IGA00, RT00].

The possibility of tailoring organic molecules with particular properties, the tunability of their characteristics, and the efficiency and flexibility of deposition methods, are reasons for a strong effort to show their applicability as competitive materials with respect to inorganic semiconductors. The idea of being able to control and explore ways to incorporate organic functions into existing technologies and to build molecule-based nanoscale electronic circuits with rectifying, logic and switching functions has stimulated experimental attempts to build such molecular electronics, and theoretical efforts to describe and predict their properties.

Organic functionalisation of the metallic surfaces has important applications, e.g. in catalysis, sensors, adhesion, corrosion inhibition, molecular recognition, optoelectronics and lithography [Rav03]. Electronic transport involving molecules is attracting increasing interest because single molecules might be able to control electron transport. The inclusion of biological active molecules and the concept of bioelectronic devices add further weight to this idea. Within such a technological complex, it is clear that the development of future organic/inorganic interfaces is critically dependent on establishing a fundamental understanding of the various bonding and lateral interactions that govern the ultimate orientation, conformation and two dimensional organization of these molecules at the surface.

As a consequence, in all cases, molecule-surface interaction plays a vital role, since the binding and ordering of molecules on surfaces is in general controlled by a delicate balance between competing molecule-substrate and intermolecular interactions. Another consequence of the complex interactions involved, certain

molecular behavior, although valid for molecules in the gas phase, cannot be transferred *a priori* to a situation, in which the molecules are adsorbed on the substrate. For example, the exact adsorption conformation may play an important role when measuring the conductance through a single molecule.

During recent years a whole range of highly sophisticated experimental techniques have been developed for testing the properties of the molecules on surfaces [IFF03]: AES (Auger electron spectroscopy), AFM (atomic force spectroscopy), EELS or HREELS (high resolution electron energy loss spectroscopy), LEED (low energy electron diffraction), STM (scanning tunneling microscopy), STS (scanning tunneling spectroscopy), XPD (X-ray photoelectron diffraction), XPS (X-ray photoelectron spectroscopy). All these techniques offer valuable insights into the ordering of molecules on the surfaces and into molecule-surface interactions. In general, the information obtained with some of the experimental techniques (as AES, LEED, HREELS, XPD, XPS) is averaged over large areas of the sample substrate compared to the characteristic molecular distances on the surface. Although high-resolution STM/STS can manipulate matter with atomic scale precision the information obtained in most of the molecule-substrate cases is not free of ambiguities. This clearly limits the ability to yield information on local properties, which is essential in the present context.

A fundamental new insight into the very detailed binding geometries and ordering of the molecules on surfaces and specificity of the interaction that occur between anchored molecules can be obtained by performing *ab initio* calculations. Among many fascinating questions connected with the problem of adsorption, two basic ones can be answered using *ab initio* methods: the first refers to the structure and energies of the adsorbed molecules and the second, perhaps more subtle question, is concerned with the way in which the electronic properties of the substrate material and the molecules are modified by the adsorption.

The basis of *ab initio* calculations is the density functional theory (**DFT**), which states that the ground state properties of a many-electron system are exclusively determined by the electron density. It has been shown that the quantum mechanical many-particle problem can be mapped onto a system of non-interacting electrons moving in an effective potential. Using the generalized gradient approximation (**GGA**) for the exchange-correlation functional, the pseudopotential method in a supercell approach, i.e. reciprocal space formulation [IZC79], and iterative numerical methods for solving the single-particle equations [Fle87], the *ab initio* method can be applied to large and complex molecular-surface systems.

For this purpose we have developed in our group the program package **EStCoMPP**, an “Electronic Structure Code for Materials Properties and Processes”, which has been used throughout this thesis. It is an *ab initio* molecular dynamics program in the spirit of Car and Parrinello based on a plane-wave basis set. The physical system is represented as a periodical supercell. The **EStCoMPP** program contains the projector-augmented-wave method (**PAW**) in a formulation similar to the one proposed by Blöchl [Blö94], but also includes elements of a pseudocharge method proposed by M. Weinert [Wei81] for the full potential linearized augmented plane wave method. It is optimally suited for calculating forces exerted on the atoms and to determine the equilibrium structures of complex systems of surfaces and

molecule-surface systems. The program package contains the **EStCoMPP-Visualization Tool (EStCoMPP-VT)** [AA02] that is used to visualize the position of the atoms in the unit cell and electron densities calculated with **EStCoMPP**-program.

We shortly describe the basics of the DFT in Chapter 1 including the generalized gradient approximation to the exchange-correlation functional, which is used to describe molecules and molecule-surface systems accurately. Chapter 2 contains the description of the plane-wave representation of the density functional theory, and Chapter 3 is devoted to the pseudopotential concept and generation of the pseudopotentials in the Kleinman-Bylander and the PAW formalism. As the final chapter of the theoretical background Chapter 4 contains the flow diagram of the **EStCoMPP**-code and the implementation of all theoretical ideas.

In order to verify the accuracy of the results obtained with our program we have calculated the geometrical structure of Cd impurities with vacancies and interstitials in Si/Ge bulk. Our results, which are presented in Chapter 5, have been used by a collaborating group (using a KKR all-electron method) and the specific geometry has been properly assigned to the measured electric field gradient (EFG) in Si/Ge.

In order to understand the interface organic molecules-metallic substrate it is important to study model systems in detail. In this thesis the structure (bonding geometry and electronic structure) and local order of several molecular layers on Cu(110) surface have been investigated. Formate, 3-thiophene carboxylate or glycinate molecules form such molecular layers. All these molecules contain the carboxylate group but their geometrical structures differ: while formate and 3-thiophene carboxylate are planar molecules the glycinate has a 3-dimensional geometry. All investigated molecules chemically bind to Cu(110) via the carboxylate group. A lot of very complex organic and biological molecules, which are interesting from the surface science point of view, use the carboxyl group as an anchoring group to bind to metal surfaces. For recent reviews on molecular adsorption see [Rav03], [BR03].

Formic acid is the simplest molecule that contains a carboxyl group. The adsorption of formic acid on copper single crystal surfaces, in particular Cu(110), has attracted considerable attention due to the identification of formate as a key stable intermediate in methanol synthesis which is carried out commercially using copper-based catalysts. Formic acid adsorbs at the Cu(110) surface the result being a perpendicular formate-molecular layer on the metallic surface. Chapter 6 of the thesis is concerned with the bonding geometry and electronic structure of formate molecules for different coverages on clean and oxygen-precovered Cu(110) surfaces.

The family of five-membered heterocycles, which includes 3-thiophene carboxylic acid, is the main constituent of the polymeric organic conductors. There is an increasing interest in the adhesion and growth of oriented polymeric materials on surfaces. Many investigations are performed in order to understand the properties of the polymer-precursor-substrate interfaces. With such information it should be possible to fabricate a specific polymer-surface structure, of which chemistry and physics can be controlled and optimized to achieve specifically desired properties. The chemical adsorption of 3-thiophene carboxylic on the Cu(110) surface produces

an ordered 3-thiophene carboxylate molecular layer in which the molecules are perpendicular on the surface. Chapter 7 of this thesis investigates the bonding to the surface, the lateral interactions, the orientation and alignment of adsorbed 3-thiophene carboxylate molecules on Cu(110) surface.

The study of bonding geometries of model species such as simple aminoacids can assist the interpretation of more complex systems including aspects of biochemically and chirally active films. For example, the structures, conformations and local ordering in the self-assembled monolayers determine the possible interaction with other incoming species in the process of molecular recognition. The functional groups involved in the bonding of the molecule to the surface will not be available for coupling to other species from the surrounding medium. Glycine is the simplest aminoacid, it has an important function in the neurotransmitter system. Glycine adsorption on the Cu(110) surface produces a flat layer of glycinate molecules, binding to the surface via both functional groups (carboxylate and amino). Some experiments suggested the formation of heterochiral domains (two molecules where both enantiomers are present in the unit cell) as well as homochiral domains (two molecules of one enantiomer type are in the unit cell), other experiments report the existence of only heterochiral domains. Chapter 8 of this thesis is concerned with the study of the bonding properties of the glycinate molecules and the stability of possible different domains that can be formed at the Cu(110) surface. The results obtained allow a unique assignment of the registry of glycinate molecules at the Cu(110) surface.

Chapter 1

1.1. Density Functional Theory

First principles or ‘*ab initio*’ methods are based on the quantum mechanical equations governing the behavior of the system studied. The aim of these methods is not to solve the many-body Schrödinger equation exactly, but to select a method to find adequate approximations to the full solution, in order to predict the properties one wants to study. *Ab initio* calculations can be considered a bridge between classical theory and experiment, which is why they are sometimes referred to as “computer experiments”. They provide insight into phenomena that are too complex to be treated analytically, and allow the determination of material properties if experiments are not feasible. Thus first principles calculations are valuable tools that can aid the explanation and deepen the understanding of conventional experiments.

The ground-state properties of any non-relativistic time-independent quantum system can in principle be determined by solving the stationary Schrödinger equation:

$$\hat{H}\Psi(\vec{r}_1, \vec{r}_2, \vec{r}_3, \dots, \vec{r}_N, \vec{R}_1, \vec{R}_2, \vec{R}_3, \dots, \vec{R}_M) = E\Psi(\vec{r}_1, \vec{r}_2, \vec{r}_3, \dots, \vec{r}_N, \vec{R}_1, \vec{R}_2, \vec{R}_3, \dots, \vec{R}_M) \quad (1.1-1)$$

where $\hat{H}, \Psi(\vec{r}_1, \vec{r}_2, \vec{r}_3, \dots, \vec{r}_N, \vec{R}_1, \vec{R}_2, \vec{R}_3, \dots, \vec{R}_M), E$ are the Hamiltonian, the many body wave function and the total energy of the system. Here we distinguish between the coordinates of the nuclei \vec{R}_i and of the electrons \vec{r}_i constituting the system considered. They interact via the Coulomb law, and the total Hamiltonian for such a system is given by:

$$\begin{aligned} \hat{H} = & -\sum_{i=1}^M \frac{\hbar^2}{2m_{Z_i}} \nabla_{\vec{R}_i}^2 - \sum_{i=1}^N \frac{\hbar^2}{2m_e} \nabla_{\vec{r}_i}^2 + \frac{1}{4\pi\epsilon_0} \sum_{i=1}^M \sum_{j=1}^M \frac{Z_i Z_j}{|\vec{R}_i - \vec{R}_j|} \\ & - \frac{1}{4\pi\epsilon_0} \sum_{i=1}^N \sum_{j=1}^M \frac{Z_j e}{|\vec{R}_j - \vec{r}_i|} + \frac{1}{4\pi\epsilon_0} \sum_{i=1}^N \sum_{j=1}^N \frac{e^2}{|\vec{r}_j - \vec{r}_i|} \end{aligned} \quad (1.1-2)$$

where \mathbf{M} and \mathbf{N} are the total number of nuclei and electrons, respectively; $\{\mathbf{m}_{Z_i}, \mathbf{Z}_i, \bar{\mathbf{R}}_i\}$ are the mass, charge and position of nuclei, $\{\mathbf{m}_e, \bar{\mathbf{r}}_i, \mathbf{e}\}$ represent the mass, position and charge of the electrons.

The first two terms of equation (1.1-2) represent the kinetic energies of nuclei and electrons; the following terms are the Coulomb energies due to ion-ion repulsion, ion-electron attraction, and electron-electron repulsion. The Schrödinger equation above can only be solved exactly for the hydrogen atom. Only a few other model systems also yield differential equations with exact solutions, depending on the functional form of potential energy and number of particles, like particles in a box, rigid rotors, and harmonic oscillators. In practice, for a real solid, a number of physically reasonable approximations are required which will be discussed in the following:

In most instances the “adiabatic” or Born-Oppenheimer approximation [BH54] can be made, separating the degrees of freedom of electrons and nuclei. Due to the large difference in mass, $\mathbf{m}_e / \mathbf{m}_{Z_i} \ll 1$, the electrons will respond instantaneously to the movement of the much heavier nuclei, (sic) the nuclear coordinates can be considered as external parameters for the electronic part of the system. In this approximation the electronic ground state energy, which depends on the nuclear coordinates, enters the separated nuclear problem as part of the potential energy. In this thesis the nuclear motion will be treated classically by Newtonian dynamics.

Using this Born-Oppenheimer approximation, the electrons move in a fixed external potential due to the nuclei, and the electronic part of the Hamiltonian can be written as:

$$\hat{H} = -\sum_{i=1}^N \frac{\hbar^2}{2\mathbf{m}_e} \nabla_{\bar{\mathbf{r}}_i}^2 - \frac{1}{4\pi\epsilon_0} \sum_{i=1}^N \sum_{j=1}^M \frac{\mathbf{Z}_j \mathbf{e}}{|\bar{\mathbf{R}}_j - \bar{\mathbf{r}}_i|} + \frac{1}{4\pi\epsilon_0} \sum_{i=1}^N \sum_{\substack{j=1 \\ j>i}}^N \frac{\mathbf{e}^2}{|\bar{\mathbf{r}}_j - \bar{\mathbf{r}}_i|} \quad (1.1-3)$$

However, solving the electronic Schrödinger equation with its many degrees of freedom is still impossible for most realistic systems.

Hartee ([Har28]) suggested the “independent electron approximation”, in which the many-electron wave function $\Psi(\bar{\mathbf{r}}_1, \bar{\mathbf{r}}_2, \bar{\mathbf{r}}_3, \dots, \bar{\mathbf{r}}_N)$ is a product of single particle functions $\Psi_i(\bar{\mathbf{r}}_i)$. Electrons are spin-1/2 particles and have to obey the Pauli principle, which states that the many-electron wave function has to be anti-symmetric with respect to the permutation of any two-electron coordinates. Including the spin degrees of freedom $\bar{\mathbf{s}}_i$ for the electrons this condition leads to:

$$\Psi(\dots, \bar{\mathbf{r}}_i \bar{\mathbf{s}}_i, \dots, \bar{\mathbf{r}}_j \bar{\mathbf{s}}_j, \dots) = -\Psi(\dots, \bar{\mathbf{r}}_i \bar{\mathbf{s}}_j, \dots, \bar{\mathbf{r}}_j \bar{\mathbf{s}}_i, \dots) \quad (1.1-4)$$

The Hartree Ansatz has been expanded to include this symmetry restriction by Hartree and Fock ([SO82], [HRS86]). The N-electron wave function is approximated by a Slater determinant, i.e. an anti-symmetrised product of N-orthonormal single electron

wave functions $\Psi_i(\vec{r}_i, s_i)$, each consisting of a spatial orbital $\phi_i(\vec{r})$ and a spin function $\sigma(s_i)$ ¹:

$$\Psi_{HF}(\vec{r}_1 s_1, \vec{r}_2 s_2, \vec{r}_3 s_3, \dots, \vec{r}_N s_N) = \frac{1}{\sqrt{N!}} \begin{vmatrix} \Psi_1(\vec{r}_1 s_1) & \Psi_2(\vec{r}_1 s_1) & \dots & \Psi_N(\vec{r}_1 s_1) \\ \Psi_1(\vec{r}_2 s_2) & \Psi_2(\vec{r}_2 s_2) & \dots & \Psi_N(\vec{r}_2 s_2) \\ \vdots & \vdots & \ddots & \vdots \\ \Psi_1(\vec{r}_N s_N) & \Psi_2(\vec{r}_N s_N) & \dots & \Psi_N(\vec{r}_N s_N) \end{vmatrix} \quad (1.1-5)$$

The single particle orbitals fulfill the orthonormality conditions:

$$\int \int_{s_z} \Psi_i^*(\vec{r} \vec{s}) \Psi_j(\vec{r} \vec{s}) d\vec{r} = \langle \Psi_i | \Psi_j \rangle = \int d\vec{r} \phi_i(\vec{r}) \phi_j(\vec{r}) \sum_{s_z} \sigma_i(s) \sigma_j(s) = \delta_{ij} \quad (1.1-6)$$

Generalizations of this approach in order to take into account correlations between electrons beyond the anti-symmetrization use linear combinations of Slater determinants. This method is known as “configuration interaction” ([SO82], [Ful95]).

Most numerical approaches to treat the interacting many-electron problem are based on the electron density-functional formalism. Hohenberg and Kohn have established two remarkable theorems applying to any system consisting of electrons moving under the influence of an external potential $v_{ext}(\vec{r})$ (e.g. Ions)².

● **Theorem 1:** The external potential and the total energy of an interacting many-electron system are unique functionals of the electron density $n(\vec{r})$.

Following Hohenberg and Kohn, the ground state energy can be written as:

$$E[n(\vec{r})] = \int n(\vec{r}) v_{ext}(\vec{r}) d\vec{r} + F[n(\vec{r})] \quad (1.1-7)$$

where $F[n(\vec{r})]$ is an unknown but universal (i.e. not explicitly depended on the external potential) functional of the electron density $n(\vec{r})$.

The proof of Theorem 1 proceeds by reductio ad absurdum: First, one observes that the Hamiltonian \hat{H} for the system, and thus the ground-state energy E , are uniquely determined by the external potential. They are related by:

$$\hat{H} = \hat{F} + \hat{V}_{ext}, \quad E[n(\vec{r})] = \langle \Psi | \hat{H} | \Psi \rangle \quad (1.1-8)$$

¹ $\sigma(s_z = +1/2) = \alpha$; $\sigma(s_z = -1/2) = \beta$ represent spin-up and spin-down functions

² The following formulae refer to a system where $\hbar = 1$, $m_e = \frac{1}{2}$, $e^2 = 2$, $c = \frac{2}{\alpha} = 274.074$ as used in the

Electronic Structure Code for Material Properties and Processes (**EstCoMPP**). The energy is expressed in Rydberg and the length scale is the Bohr radius: $1\text{Ry} \equiv 13.6058\text{eV}$, $a_B = 0.529177 \text{ \AA}$. These units are called “atomic units”.

Comparing to Eq.(1-3), where the external potential is the Coulomb potential of the nuclei, one sees that the operator \hat{F} ³ consists of a kinetic energy operator \hat{T} and the electron-electron interaction operator \hat{V}_{ee} :

$$\hat{F} = \hat{T} + \hat{V}_{ee} \quad (1.1-9)$$

and the functional $F[n(\vec{r})]$ is its ground-state expectation value of this operator.

Hohenberg and Kohn have shown that it is not possible to obtain the same ground-state electron density by two different potentials, and in turn that two different electron densities have to derive from two different potentials. In other words, the electron density uniquely determines the external potential, and thus all ground state properties, in particular the ground-state energy, its derivatives, and the positions of the nuclei.

The second Hohenberg-Kohn theorem represents in essence a minimum principle for the density:

● **Theorem 2:** The exact ground-state density $n_0(\vec{r})$ for a given external potential minimizes the energy functional $E[n(\vec{r})]$, and the minimum value is the exact ground state density.

$$E[n_0(\vec{r})] = E_0 \quad (1.1-10)$$

While Hohenberg and Kohn proved their theorems indirectly with the assumption that the density $n(\vec{r})$ is uniquely determined by the external potential (**V**-representation of the density), Levy ([Lev79]) derived the minimum properties of the energy functional directly via the Ritz variational principle.

He defined the energy-functional as:

$$E[n(\vec{r})] := \min \langle \Psi | H | \Psi \rangle \quad (1.1-11)$$

The expectation value of the Hamiltonian operator has to be minimized with respect to the norm conserving, anti-symmetric many-particle wave function Ψ , which reproduces a given electron-density $n(\vec{r})$ (Ψ representation of $n(\vec{r})$). The ground-state density $n_0(\vec{r})$ and the ground-state energy $E[n_0(\vec{r})]$ are determined by minimizing the energy-functional:

$$\delta E[n(\vec{r})] = 0 \quad (1.1-12)$$

The subsidiary condition of particle conservation

$$\int d\vec{r}^3 n(\vec{r}) = N \quad (1.1-13)$$

is taken into account using a Lagrangian-parameter μ . This leads to the minimization of a modified energy-functional

³ The electron operator \hat{F} is the same for all N-electron systems.

DENSITY FUNCTIONAL THEORY

$$\delta \left[E[n(\vec{r})] - \mu \left(\int d^3\vec{r} - N \right) \right] = 0 \quad (1.1-14)$$

which yields the following Euler-Lagrange equation:

$$\left. \frac{\delta E[n(\vec{r})]}{\delta n(\vec{r})} \right|_{n_0(\vec{r})} = \mu \quad (1.1-15)$$

An explicit form of the energy-functional could not be derived from the approach of Hohenberg and Kohn, or from Levy's formulation. Thus additional approximations have to be made.

1.2. The Kohn-Sham Formulation

Density Functional Theory provides the theoretical ground for reformulating the ground-state many-electron system as a variational problem on the charge density. The constrained minimization on the density functional, with the subsidiary condition of particle conservation, can be written as:

$$\delta \left[F[n(\vec{r})] + \int v_{ext}(\vec{r}) n(\vec{r}) d\vec{r} - \mu \left(\int n(\vec{r}) d\vec{r} - N \right) \right] = 0 \quad (1.2-1)$$

where μ is a Lagrange multiplier. This leads to the Euler-Lagrange equation for the charge density:

$$\mu = \frac{\delta F[n(\vec{r})]}{\delta n(\vec{r})} + v_{ext}(\vec{r}) \quad (1.2-2)$$

To be able to treat an inhomogeneous system of interacting electrons, Hohenberg and Kohn have formally divided the universal unknown functional $F[n(\vec{r})]$ into three terms:

$$F[n(\vec{r})] = T_0[n(\vec{r})] + E_H[n(\vec{r})] + E_{xc}[n(\vec{r})] \quad (1.2-3)$$

$T_0[n(\vec{r})]$ is the kinetic energy functional of N non-interacting electrons of density $n(\vec{r})$, and $E_H[n(\vec{r})]$ represent the classical electrostatic (Hartree repulsion) energy of the electrons:

$$E_H[n(\vec{r})] = \frac{1}{2} \iint \frac{n(\vec{r}) n(\vec{r}')}{|\vec{r} - \vec{r}'|} d\vec{r} d\vec{r}' \quad (1.2-4)$$

All unknown many-electron effects are shifted into the third functional. The decomposition above entails an implicit definition for this exchange-correlation functional $E_{xc}[n(\vec{r})]$, which consists of non-classical contributions to the electron-electron interaction, and the difference between the true kinetic energy and the non-interacting one.

The fact that $E_{xc}[n(\vec{r})]$ is only a small fraction of the total energy, and that it can be approximated surprisingly well for most systems, is mostly responsible for the success of the Kohn-Sham formulation. The approximations for the exchange-correlation energy will be discussed later.

The Euler-Lagrange equation can now be rewritten as:

$$\mu = \frac{\delta T_0[n(\vec{r})]}{\delta n(\vec{r})} + v_{KS}(\vec{r}) \quad (1.2-5)$$

where the $v_{KS}(\vec{r})$ is given by

$$v_{KS}(\vec{r}) = v_{ext}(\vec{r}) + v_H(\vec{r}) + v_{xc}(\vec{r}) \quad (1.2-6)$$

THE KOHN-SHAM FORMULATION

with the Hartree potential $v_H(\vec{r})$

$$v_H(\vec{r}) = \frac{\delta E_H[n(\vec{r})]}{\delta n(\vec{r})} = \int \frac{n(\vec{r}')}{|\vec{r} - \vec{r}'|} d\vec{r}' \quad (1.2-7)$$

and the exchange-correlation potential:

$$v_{xc}(\vec{r}) = \frac{\delta E_{xc}[n(\vec{r})]}{\delta n(\vec{r})} \quad (1.2-8)$$

Equation (1.2-5) shows that the many-body electron problem with N interacting electrons has now been reformulated as a problem of N non-interacting electrons which move in an effective potential $v_{KS}(\vec{r})$.

The effective potential is a functional of the charge density itself, and the problem has to be solved self-consistently.

The solution for the N -electron, non-interacting reference system can be written as a Slater determinant introduced earlier (1.1-5):

$$\Psi_{KS} = \frac{1}{\sqrt{N!}} \det |\Psi_1(\vec{r}_1) \Psi_2(\vec{r}_2) \Psi_3(\vec{r}_3) \dots \Psi_N(\vec{r}_N)| \quad (1.2-9)$$

The kinetic energy functional $T_0[n(\vec{r})]$ can be expressed in terms of N orthonormal orbitals $\Psi_i(\vec{r})$:

$$T[n(\vec{r})] = -\frac{1}{2} \sum_{i=1}^N \int \Psi_i^*(\vec{r}) \nabla^2 \Psi_i(\vec{r}) d\vec{r} \quad (1.2-10)$$

and the electron density can also be parameterized in terms of these one-electron wave functions:

$$n(\vec{r}) = \sum_{i=1}^N |\Psi_i(\vec{r})|^2 \quad (1.2-11)$$

where the sum is over the occupied orbitals (belonging to the N lowest eigenvalues).

We now can formulate the variation principle for the ground state by varying the density through the variation of a single electron wave function.

$$dn(\vec{r}) = \sum_i \left[\frac{\delta n(\vec{r})}{\delta \Psi_i^*(\vec{r})} d\Psi_i^*(\vec{r}) + \frac{\delta n(\vec{r})}{\delta \Psi_i(\vec{r})} d\Psi_i(\vec{r}) \right] \quad (1.2-12)$$

The variation can be done independently for each Ψ_i^* and Ψ_i . Taking into account the orthonormalization condition of the single particle wave functions by Lagrange parameters, the variational principle reads:

$$\frac{\delta}{\delta \Psi_i^*} \left\{ T_0[n(\vec{r})] + \int v_{ext}[n(\vec{r})] n(\vec{r}) d\vec{r} + E_H[n(\vec{r})] + E_{xc}[n(\vec{r})] - \sum_{j=1}^N \varepsilon_j \left(\int d\vec{r} \Psi_j^*(\vec{r}) \Psi_j(\vec{r}) - 1 \right) \right\} = 0 \quad (1.2-13)$$

with $i = 1 - N$; this yields the Kohn-Sham equations for the wave functions:

$$\left(-\frac{1}{2} \nabla^2 + v_{KS}(\vec{r}) \right) \Psi_i(\vec{r}) = \varepsilon_i \Psi_i(\vec{r}) \quad (1.2-14)$$

THE KOHN-SHAM FORMULATION

They have to be solved self-consistently using equations (1.2-11), (1.2-6) to (1.2-8).

This Kohn-Sham approach represents a mapping of the interacting many-electron system onto a system of non-interacting electrons moving in an effective potential due to all the other electrons. The self-consistent solution of the Kohn-Sham equation gives the set of the wave function Ψ_i that minimizes the Kohn-Sham energy-functional. If the exchange-correlation energy functional were known exactly, the functional derivative with respect to the density would produce an exchange correlation potential that includes the effects of exchange and correlation exactly. The eigenvalues of the Kohn-Sham equations are formally one-particle energies. However, since they are only Lagrangian parameters in the density functional theory they have strictly speaking no physical meaning. The same argument holds for the one-particle wave functions, which have no physical meaning as well. Nevertheless, following Koopmans-theorem, an interpretation of the ε_i and $\Psi_i(\vec{r})$ as eigenvalues and one-particle wave functions is generally possible ([JG89]). For delocalized states, where the correlation can be neglected compared to exchange, the spectroscopically measured ionization energies and the energies calculated with the density functional theory are indeed in good agreement. This is not necessarily true for the strongly localized states (e.g. atomic states). However, the surface states and molecular states, which are calculated in this thesis, are sufficiently delocalized and can be approximately interpreted as physical states.

1.3. Exchange-Correlation Terms in Density Functional Theory

The exchange-correlation energy is the only part of the total electronic energy that cannot be calculated numerically exactly. It contains the correlations between the electrons due to the quantum mechanical symmetry requirements (Pauli principle), which yield exchange energy. Beyond that it contains the electron-electron interaction that yields the correlation energy.

An exact expression can be written for the exchange-correlation energy in terms of the exchange-correlation-pair density $n_{xc}(\vec{r}, \vec{r}')$ [JG89].

$$E_{xc}[n(\vec{r})] = \frac{1}{2} \int n(\vec{r}) d\vec{r} \int \frac{n_{xc}(\vec{r}, \vec{r}')}{|\vec{r} - \vec{r}'|} d\vec{r}' \quad (1.3-1)$$

$n_{xc}(\vec{r}, \vec{r}')$ describes the deviation of the conditional density to find an electron at $(\vec{r}, d\vec{r}')$ when it is known that there is an electron at $(\vec{r}, d\vec{r})$. For $\vec{r} \rightarrow \vec{r}'$, $n_{xc}(\vec{r}, \vec{r}')$ is reduced from its value of non-interacting electrons due to the electron-electron correlation described above, i.e. it describes an exchange-correlation hole.

The exchange correlation energy can be viewed as the energy resulting from the interaction between an electron and its exchange-correlation hole.

Using the normalization of the pair correlation function a sum rule can be formulated for the exchange-correlation hole:

$$\int n_{xc}(\vec{r}, \vec{r}') d\vec{r}' = -1 \quad (1.3-2)$$

With the substitution $\vec{R} = \vec{r} - \vec{r}'$ one can write the exchange-correlation hole as

$$E_{xc} = \frac{1}{2} \int d\vec{r} n(\vec{r}) \int_0^\infty d\vec{R} R^2 \frac{1}{R} \int d\Omega n(\vec{r}, \vec{R}) = -\frac{1}{2} \int d\vec{r} n(\vec{r}) \left\langle \frac{1}{R} \right\rangle_{\vec{r}} \quad (1.3-3)$$

The minus sign guarantees that with (1.3-2) the average $\left\langle \frac{1}{R} \right\rangle_{\vec{r}}$ is a positive number. This expression shows that, when the provided sum rule (1.3-2) is satisfied, the exchange-correlation energy enters only via the average $\left\langle \frac{1}{R} \right\rangle_{\vec{r}}$, i.e. via the first moment of the function $n_{xc}(\vec{r}, \vec{r}')$. In particular, the angular dependency is averaged out.

Since the exchange correlation function $n_{xc}(\vec{r}, \vec{r}')$ is not known exactly, approximations have to be constructed which fulfill the sum rule (1.3-2) and approximate the average $\left\langle \frac{1}{R} \right\rangle_{\vec{r}}$ for each \vec{r} as good as possible.

Exchange-Correlation Approximations in Density Functional Theory

The exchange-correlation functionals have the general form

$$E_{xc}[n(\vec{r})] = \int n(\vec{r}) \varepsilon_{xc}[n(\vec{r})] d\vec{r} \quad (1.3-4)$$

In order to model the exchange-correlation hole via exchange-correlation functionals we need to find a way in which the density surrounding each electron is approximated in a form of exchange-correlation energy per particle $\varepsilon_{xc}[n(\vec{r})]$.

1.3.1. Local density approximation (LDA)

LDA is a reasonable and simple approximation of the exchange-correlation that makes the Kohn-Sham **DFT** method a very practical one. In this approach it is assumed that the true exchange-correlation energy of a many-electron system can locally be approximated by the exchange-correlation energy associated with a homogeneous electron gas of the same density ([Wig34], [MJW80], [VWN80]). For the homogeneous electron gas the form of exchange correlation energy can be calculated exactly [CA80]. It is the only system where the exchange correlation energy density is precisely known.

In LDA, the exchange-correlation electron density $\varepsilon_{xc}[n(\vec{r})]$ at the point \vec{r} is equal to the exchange-correlation electron density, $\varepsilon_{xc}^{\text{hom}}[n(\vec{r})]$, of the homogeneous electron gas of density $n(\vec{r})$. This is a function $\varepsilon_{xc}^{\text{hom}}(n(\vec{r}))$ and not anymore a functional of electron density $n(\vec{r})$. The total exchange-correlation energy, dependent on the local density, can be obtained by a spatial integration

$$E_{xc}^{\text{LDA}}[n(\vec{r})] = \int n(\vec{r}) \varepsilon_{xc}^{\text{hom}}(n(\vec{r})) d\vec{r} \quad (1.3-5)$$

The total exchange-correlation energy can be decomposed in exchange $E_x^{\text{LDA}}[n(\vec{r})]$ and correlation $E_c^{\text{LDA}}[n(\vec{r})]$ contributions⁴.

⁴ Correspondingly, the electron density will be decomposed in exchange $\varepsilon_x^{\text{hom}}(n(\vec{r}))$ and correlation $\varepsilon_c^{\text{hom}}(n(\vec{r}))$ parts.

In LDA, the exchange-correlation potential is written as:

$$V_{xc}^{LDA}[n(\vec{r})] = \frac{\delta E_{xc}^{LDA}[n(\vec{r})]}{\delta n(\vec{r})} = \frac{\partial [n(\vec{r}) \varepsilon_{xc}^{\text{hom}}(n(\vec{r}))]}{\delta n(\vec{r})} = \varepsilon_{xc}^{\text{hom}}(n(\vec{r})) + n(\vec{r}) \left(\frac{d \varepsilon_{xc}^{\text{hom}}(n(\vec{r}))}{d n(\vec{r})} \right) \quad (1.3-6)$$

The exchange energy density $\varepsilon_x^{\text{hom}}(n(\vec{r}))$ can be calculated exactly solving the Hartree-Fock equations for a homogeneous electron gas, and the correlation $\varepsilon_c^{\text{hom}}(n(\vec{r}))$ electron density is obtained using Quantum Monte-Carlo simulation for both low and high density limits to fix the coefficients in an interpolation formula [CA80]. Earlier approximations due to the Wigner [Wig34] or generalization to the relativistic case [VWN80] are also implemented in our code.

The **DFT** can be generalized for spin-polarized electron systems by taking into account the spin-electron densities $n^\uparrow(\vec{r})$ and $n^\downarrow(\vec{r})$ for the spin-up and spin-down electrons, respectively, as independent functions. The electron density and the magnetization density are defined by:

$$\begin{aligned} n(\vec{r}) &= n^\uparrow(\vec{r}) + n^\downarrow(\vec{r}) \\ m(\vec{r}) &= n^\uparrow(\vec{r}) - n^\downarrow(\vec{r}) \end{aligned} \quad (1.3-7)$$

Then the total energy functional has to be considered a functional of two densities:

$$E[n(\vec{r})] \Rightarrow E[n^\uparrow(\vec{r}), n^\downarrow(\vec{r})] \quad (1.3-8)$$

which is minimized with respect to both spin-up $n_0^\uparrow(\vec{r})$ and spin-down $n_0^\downarrow(\vec{r})$ ground-state densities.

Also the **LDA** can be generalized to the local-spin density approximation (**LSDA**) where the exchange-correlation electron density of the homogeneous spin-polarized electron gas $\varepsilon_{xc}^{\text{hom}}(n^\uparrow(\vec{r}), n^\downarrow(\vec{r}))$ is dependent on spin-up and spin-down densities.

Despite its simplicity, the local density approximation works well and is very successful in solid systems with extended slowly varying wave functions [JG89]. However, because the **LDA** ignores the correction to the exchange correlation energy at a point \vec{r} due to the surrounding inhomogeneities of the electron density, its success is not guaranteed in systems with strong spatial variations of the charge density as e.g. in a molecule. Thus, for chemistry applications more general exchange-correlation functionals have been invented ([Bec93], [PW92], [PBE96-98]).

1.3.2. Generalized gradient approximation (GGA)

A better approximation of the exchange-correlation functional is known as the generalized gradient approximation (**GGA**) in which the exchange-correlation energy is not only a function of the electron density but also depends on the electron density gradients.

The total exchange-correlation energy in the **GGA** can be conveniently written in terms of an analytic function $F_{XC}[n(\vec{r}), \nabla n(\vec{r})]$ known as the enhancement factor that directly modifies the **LDA** exchange-correlation energy density:

$$E_{XC}^{GGA}[n(\vec{r})] = \int n(\vec{r}) \varepsilon_{XC}^{\text{hom}}(n(\vec{r})) F_{XC}[n(\vec{r}), \nabla n(\vec{r})] d\vec{r} \quad (1.3-9)$$

The enhancement factor $F_{XC}[n(\vec{r}), \nabla n(\vec{r})]$ has two separate parts due to the exchange and correlation contributions. It is conveniently written in terms of the Seitz radius r_s , which characterizes the electron density (see equation 1.3-12), and the dimensionless reduced density gradient $s(\vec{r})$:

$$s(\vec{r}) = \frac{|\nabla n(\vec{r})|}{2k_F(\vec{r})n(\vec{r})}, \text{ with the Fermi-wave-vector } k_F = \{3\pi^2 n(\vec{r})\}^{\frac{1}{3}} \quad (1.3-10)$$

The generalized gradient approximation implemented in the code is the one proposed by Perdew, Burke and Ernzerhof (**PBE**) [PW92, PBE96-98] in which all parameters other than those due to the correlation contributions are fundamental constants.

For **GGA** the expansion of **DFT** for the spin-polarized electron systems is done by generalization of the non-polarized electron systems considering the two spin-electron densities $n^\uparrow(\vec{r})$ and $n^\downarrow(\vec{r})$ for the spin-up and spin-down electrons, respectively.

The **PBE** correlation-energy functional is given by:

$$E_C^{PBE}[n^\uparrow(\vec{r}), n^\downarrow(\vec{r})] = \int n(\vec{r}) \{e_c(r_s, \zeta) + H(r_s, \zeta, t)\} d^3\vec{r} \quad (1.3-11)$$

where r_s , the density parameter, characterizes the electron density

$$n(\vec{r}) = n^\uparrow(\vec{r}) + n^\downarrow(\vec{r}) = \frac{3}{4\pi(r_s a_B)^3} \text{ with the Bohr radius } a_B = \frac{\hbar^2}{me^2} \quad (1.3-12)$$

ζ is the relative spin polarization of the electrons, and t is a measure of the density gradient:

$$\zeta = \frac{n^\uparrow(\vec{r}) - n^\downarrow(\vec{r})}{n^\uparrow(\vec{r}) + n^\downarrow(\vec{r})} \quad t = \left(\frac{\pi}{4}\right)^{\frac{1}{2}} \left(\frac{9\pi}{4}\right)^{\frac{1}{6}} \frac{s}{\Phi r_s^{\frac{1}{2}}} \quad (1.3-13)$$

The parametrized electron correlation energy, $e_c(\mathbf{r}_s, \zeta)$, is given by the spin-interpolation formula ([PW92], [VWN80], [BH72]):

$$e_c(\mathbf{r}_s, \zeta) = e_c(\mathbf{r}_s, 0) + \alpha_c(\mathbf{r}_s) \frac{f(\zeta)}{f''(0)} (1 - \zeta^4) + [e_c(\mathbf{r}_s, 1) - e_c(\mathbf{r}_s, 0)] f(\zeta) \zeta^4 \quad (1.3-14)$$

$$\text{with } f(0)=1, \quad f(1)=1, \quad f''(0)=1.709921, \quad \alpha_c(\mathbf{r}_s) = f''(0)[e_c(\mathbf{r}_s, 1) - e_c(\mathbf{r}_s, 0)] \quad (1.3-15)$$

The function $H(\mathbf{r}_s, \zeta, t)$ is written as [PBE96-98]

$$H(\mathbf{r}_s, \zeta, t) = \gamma \Phi^3 \ln \left\{ 1 + \frac{\beta}{\gamma} t^2 \left(\frac{1 + A t^2}{1 + A t^2 + A^2 t^4} \right) \right\} \quad (1.3-16)$$

$$\text{where} \quad \Phi(\zeta) = \frac{1}{2} \left\{ (1 + \zeta)^{\frac{2}{3}} + (1 - \zeta)^{\frac{2}{3}} \right\} \quad (1.3-17)$$

$$\text{and} \quad A = \left(\frac{\beta}{\gamma} \right) \frac{1}{\exp \left(-\frac{e_c(\mathbf{r}_s, \zeta)}{\gamma \Phi^3} \right) - 1} \quad (1.3-18)$$

The constants are $\beta = 0.066725$ and $\gamma = 0.031091$, each in Hartree units. The expressions have formal validity conditions: $s \ll 1$ and $t \ll 1$. Then, important sum rules on the exchange-correlation hole will be preserved.

The **PBE** exchange-energy functional for the non-spin polarized system has the form:

$$E_X^{PBE} [n(\vec{r})] = \int n(\vec{r}) F_X(s) d^3 \vec{r} \quad (1.3-19)$$

with

$$F_X(s) = 1 + \kappa - \frac{\kappa}{1 + \frac{\mu s^2}{\kappa}}; \quad \kappa = 0.804 \quad \text{and} \quad \mu = 0.21951 \quad (1.3-20)$$

The corresponding spin density functional for the exchange energy is given by:

$$E_X^{PBE} [n^\uparrow(\vec{r}), n^\downarrow(\vec{r})] = \frac{1}{2} E_X^{PBE} [2n^\uparrow(\vec{r})] + \frac{1}{2} E_X^{PBE} [2n^\downarrow(\vec{r})] \quad (1.3-21)$$

An important property of **PBE-GGA** is that it reduces to **LSDA** for uniform electron densities (density gradient $|s| \rightarrow 0$).

For the details about formulas and implementation of **GGA** in the **EStCoMPP**-program see the appendixes A.1.-A.5.

Chapter 2

Density Functional Theory in a Plane Wave implementation

This section will briefly describe the plane-wave pseudopotential implementation of the Kohn-Sham formulation that is used throughout this thesis. The method is suited to describe systems with periodic boundary conditions, as is natural for infinite bulk crystals, or systems which are sufficiently localized and can be embedded in a large enough supercell which is periodically repeated.

2.1. Supercell approach

In a perfect crystal the elementary unit cell is defined as the smallest structure whose periodical continuation describes the entire crystal. The unit cell can be completely characterized by three basis-vectors: \vec{a}_1 , \vec{a}_2 , \vec{a}_3 . Using these, one can construct lattice-vector \vec{R}^n , which points to positions of different elementary unit cells. The periodicity condition is by definition imposed on all properties $f(\vec{r})$ of the lattice.

$$\vec{R}^n = n_1 \vec{a}_1 + n_2 \vec{a}_2 + n_3 \vec{a}_3, \quad f(\vec{r} + \vec{R}^n) = f(\vec{r}) \quad (2.1-1)$$

with n_1, n_2, n_3 integers. E.g. the potential $V(\vec{r})$ and the charge density $n(\vec{r})$ will also be periodic. Thus one has to calculate only the properties of a single unit cell (with few degrees of freedom) to describe the properties of the entire periodic crystal.

The volume of the unit cell is defined by the basis vectors as:

$$\Omega = \vec{a}_1 \cdot (\vec{a}_2 \times \vec{a}_3) \quad (2.1-2)$$

Using the conventional definition of reciprocal space basis-vectors:

$$\vec{b}_i = 2\pi \frac{\vec{a}_j \times \vec{a}_k}{\Omega}, \quad (2.1-3)$$

we can write the reciprocal lattice-vector as:

$$\vec{G}^m = g_1 \vec{b}_1 + g_2 \vec{b}_2 + g_3 \vec{b}_3. \quad (2.1-4)$$

The real-space lattice-vectors \vec{R}^n , and their reciprocal space counterparts \vec{G}^m are related by

$$e^{i\vec{G}\cdot\vec{R}} = 1 \quad (2.1-5)$$

Inhomogeneities like point defects or surfaces destroy the periodicity of the solid. But the advantages of periodicity can be kept by introducing a “supercell”. In this “supercell” approach a unit cell larger than the elementary unit cell of the bulk is constructed, which contains the non-periodic defect. Due to the periodic repetition of the supercell one calculates the properties of a crystal with a periodic arrangement of the defects rather than those of an extended crystal with a single defect. This supercell has to be chosen sufficiently large, so that the defect-defect interactions in neighboring supercells are negligible. Extending this method to interfaces is done straightforward by treating the interface itself as a two-dimensional defect, and extending the supercell in the direction perpendicular to the interface. Special care has to be taken when the supercell method is applied to surfaces. The vacuum region has to be chosen large enough to avoid overlap of charge densities of opposing surfaces due to surface states that decay only slowly in vacuum.

2.2. Bloch's theorem and the plane-wave basis set

The induced periodicity in the external potential implies that the Hamiltonian commutes with the translational operator defined by the periodic boundary conditions. Bloch's theorem states that the set of eigenstates $\Psi_{\nu,\vec{k}}(\vec{r})$ for these operators can be conveniently expressed as the product of a plane-wave part $e^{i\vec{k}\cdot\vec{r}}$ and a lattice periodic part $u_{\nu,\vec{k}}(\vec{r})$

$$\Psi_{\nu,\vec{k}}(\vec{r}) = e^{i\vec{k}\cdot\vec{r}} u_{\nu,\vec{k}}(\vec{r}) \quad (2.2-6)$$

where the ν indicates the band index, and \vec{k} is a continuous wave-vector.

The periodicity of $u_{\nu,\vec{k}}(\vec{r})$ is exploited when representing the wave function in terms of a discrete basis of orthogonal plane-waves:

$$u_{\nu,\vec{k}}(\vec{r}) = \sum_{\vec{G}} c_{\nu,\vec{k}}(\vec{G}) e^{i\vec{G}\cdot\vec{r}} \quad (2.2-7)$$

with the plane-wave coefficients $c_{\nu,\vec{k}}(\vec{G})$.

Thus the electron wave functions can be expanded in terms of linear combinations of plane-waves as well:

$$\Psi_{\nu,\vec{k}}(\vec{r}) = \sum_{\vec{G}} c_{\nu,\vec{k}}(\vec{G}) e^{i(\vec{k}+\vec{G})\cdot\vec{r}} \quad (2.2-8)$$

Using the fact that the wave function does not change if an arbitrary reciprocal lattice vector \vec{G} is added to the wave-vector \vec{k} , the wave-vector \vec{k} can be confined within a minimum region bounded by the planes bisecting perpendicularly the lines from the origin to the neighboring reciprocal lattice points. This region is called the first Brillouin zone (1st BZ).

While in principle an infinite basis set is needed to represent the electron wave functions, only a finite set of plane waves is sufficient to describe the rather smooth valence electron wave functions which are mostly responsible for the bonding of the solid, and thus the chemical behaviour of the system, e.g. ionization, electrical and thermal conduction etc. Expanding only the valence electrons in plane waves, the basis set can thus be truncated to include only plane-waves with a kinetic energy smaller than a particular cutoff energy:

$$E_{cut} = |\vec{G}_{cut}|^2 \quad (2.2-9)$$

While an advantage of using plane-wave basis sets for the valence electrons is that the accuracy of the calculation can be systematically improved by increasing the energy cutoff E_{cut} , i.e. increasing the number of plane waves in the basis set, one should mention that the main disadvantage of plane-waves is that they are not efficient for describing wave functions with large curvature as is found in the core regions of atoms. This means that treating such regions of space would require an immense number of plane waves in order to be sufficiently accurate. A convenient way to avoid this disadvantage is using pseudopotentials, which will be described in the next chapters.

2.3. Kohn-Sham Equations in Plane-Wave Form

Using a plane-wave basis set to represent the electronic wave functions in periodic systems leads to a rather simple form of the Kohn-Sham equations. In reciprocal space the Kohn-Sham potential can be written as:

$$v_{KS}(\mathbf{r}) = \sum_{\vec{G}} v_{KS}(\vec{G}) \cdot e^{i\vec{G}\cdot\mathbf{r}} \quad (2.2-10)$$

in which $v_{KS}(\vec{G})$ represents the Fourier transform of the corresponding real-space quantity.

Substituting $v_{KS}(\mathbf{r})$, and the plane-wave representation for $\Psi_{v,\vec{k}}(\vec{r})$ in Eq. (1.2-14) leads to a reciprocal-space representation of the Kohn-Sham equation:

$$\sum_{\vec{G}'} \left[\frac{1}{2} |\vec{k} + \vec{G}|^2 \delta_{\vec{G},\vec{G}'} + v_{ext}(\vec{G} - \vec{G}') + v_H(\vec{G} - \vec{G}') + v_{xc}(\vec{G} - \vec{G}') \right] c_{v,\vec{k}}(\vec{G}) = \epsilon_v(\vec{k}) c_{v,\vec{k}}(\vec{G}) \quad (2.2-11)$$

It can easily be seen that the kinetic energy is diagonal in reciprocal space, and that the remaining three terms on the left-hand-side are the Fourier components of the external, Hartree and exchange-correlation potentials, respectively. Since there are efficient algorithms available (Fast Fourier Transform), for switching back and forth from real-space to reciprocal-space representation, it is computationally most efficient to calculate the expectation values in the representation (reciprocal space or real space) for which the operator is diagonal or for which there is a simple expression. While the $\vec{G} = 0$ component of the Hartree and external potentials diverge due to the long-range nature of the Coulomb interaction, they cancel each other to give a constant value that can be set arbitrarily, and does not affect the physical properties of the system.

2.4 \vec{k} -point sampling

Imposing periodic boundary conditions on the wave functions, one can show that the electronic eigenstates are only allowed for a discrete set of real wave vectors \vec{k} , where the number of \vec{k} 's in the set is equal to the number of cells in the crystal.

Applying Bloch's theorem, one can show that any real-space integral over an infinite, periodic system can be replaced by an integral in reciprocal-space over the first Brillouin zone. The reciprocal-space integral can be numerically evaluated as a sum over an infinite number of \vec{k} -points. In practice one can exploit the fact that electronic wave functions do not change appreciably over small distances in \vec{k} -space, so that all the integrations can be performed as summations over a finite, but sufficiently dense mesh of \vec{k} -points. Thus, any integrated real-space function $f(\vec{r})$ with the corresponding Fourier transform $F(\vec{k})$, e.g. the density, or the total energy, can be computed as a discrete sum:

$$\int_{BZ} F(\vec{k}) d\vec{k} = \frac{1}{\Omega} \sum_i \omega_i F(\vec{k}_i) \quad (2.2-12)$$

where Ω is the volume of the unit cell and ω_i are weighting factors of the sampling points \vec{k}_i .

The accuracy of the calculation with respect to the \vec{k} -point density can be easily verified by calculating the total energy of the system as a function of the density of the \vec{k} -point mesh. Not only the density, but also the positions of the \vec{k} -points within the Brillouin zone must be chosen carefully. The calculations performed in this thesis employ the Monkhorst-Pack ([PM77]) method where \vec{k} -points are distributed homogeneously in the Brillouin zone:

$$\vec{k}_i = x_{1i}\vec{b}_1 + x_{2i}\vec{b}_2 + x_{3i}\vec{b}_3, \quad x_{ji} = \frac{i}{2n_j}, \quad i=1,\dots,n_j \quad (2.2-11)$$

where $\vec{b}_1, \vec{b}_2, \vec{b}_3$ are the reciprocal lattice vectors, and the n_j ($j=1, 2, 3$) characterize the number of special points in the set along the direction \vec{b}_j . Additional shifting of the grid may also improve the convergence with respect to \vec{k} -point density ([CC73], [JC73], [PM77]).

The symmetry of the system is used to produce a smaller “special \vec{k} -point” subset of the full mesh, which contains only points located in the irreducible part of the first Brillouin zone. The number of \vec{k} -points that is represented by one of the special \vec{k} -points then defines the weighting factors ω_i . All Brillouin zone integrals can thus be transformed into a sum over special \vec{k} -points, thereby reducing the computational cost significantly.

In summary, the cutoff energy of the plane-wave basis set and the choice of the \vec{k} -point set determine the accuracy of the electronic wave function representation, and thus the accuracy of the charge density, the electronic potential and the total energy. The computational cost scales linearly with the number of \vec{k} -points and with the cube of the plane-wave cutoff: $|\mathbf{G}_{cut}|^3$.

Chapter 3

3.1. Pseudopotentials

In solids we can distinguish two types of electrons with different properties: core-electrons, which occupy the strongly localized orbitals of the closed inner atomic shells, and valence-electrons occupying the outer shell wave functions which extend much farther in space. It is well known that the electronic structure of the core-electrons remains almost unchanged in different chemical environments and that the binding energies in condensed matter are almost exclusively determined by the overlapping of valence electrons of the atoms. A plane wave basis set is not suitable for describing the exact core and valence electron wave functions since an immense number of plane waves would be required to accurately describe the wave functions oscillations in the core regions in order to maintain orthogonality between valence and core electrons. As a result, all-electron plane wave calculations will require a huge computational effort that is simply not practical.

The first approximation that we can make is to assume that the core charge densities of neighboring atoms do not overlap, and that these densities are not affected by the slight redistribution of the valence electrons due to the binding effect.

In the pseudopotential approximation the strong ionic potential $v_{ion}(\vec{r})$ in the core region is replaced by a weaker pseudopotential $v_{ion}^{PS}(\vec{r})$ for the valence electrons that should remove the rapid oscillations of valence wave functions in the core region. Outside of the core region defined by a cutoff radius r_{cut} , the true all-electron potential and the pseudopotential are identical. Correspondingly the set of pseudo-wave functions $\Psi^{PS}(\vec{r})$ and the all-electron wave functions $\Psi^{AE}(\vec{r})$ for the valence electrons are identical outside the chosen cutoff radius r_{cut} . The construction of the pseudopotential should guarantee that $\Psi^{PS}(\vec{r})$ does not possess the nodal structure that causes the oscillations inside r_{cut} , which means that the pseudo-wave functions can be described with a reasonable number of plane waves.

Two basic, but conflicting, criteria determine the usefulness of a pseudopotential:

- (1) It is preferable to use a “soft” pseudopotential. This means that a small number of plane waves would be necessary to describe the electronic pseudo-wave function, which translates into a small computational effort.
- (2) The pseudopotential should be “transferable” in different chemical environments. This means that the pseudopotential should give the correct ground-state energy of valence electrons for many different systems.

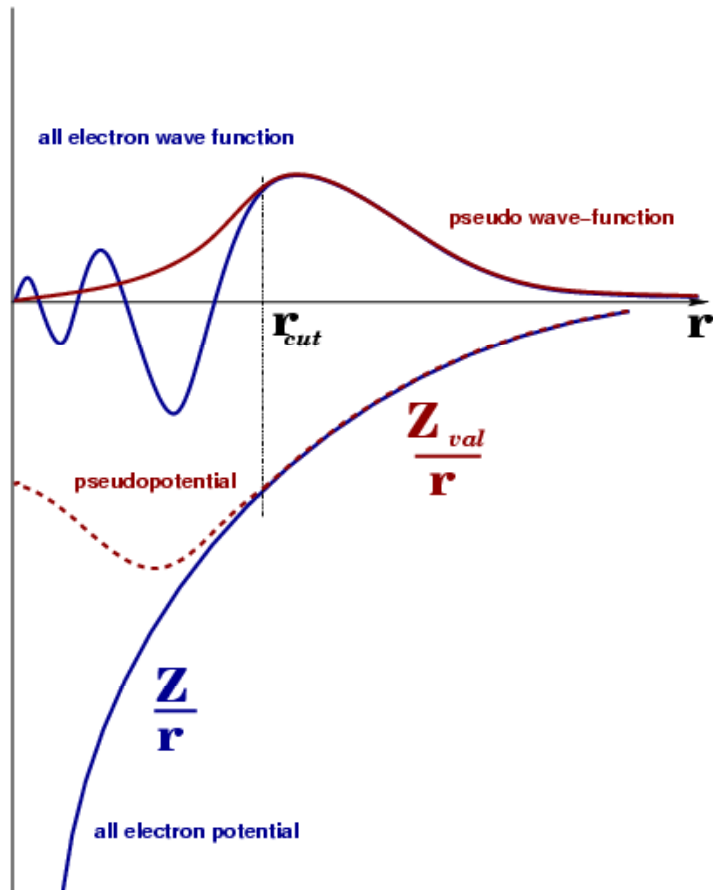
PSEUDOPOTENTIAL CONCEPT

Condition (1) can easily be met by using a large cutoff radius while condition (2) requires a small cutoff radius. In the actual construction a compromise has to be found in each case, and the number of plane wave necessary to obtain good results is very atom specific.

Density functional theory requires a good representation of the electron density of the system in order to accurately calculate the total energy. This requires that the density described by the pseudo-wave function must be close to the true electron density in most space and in particular, that the norm of the wave functions should be equal.

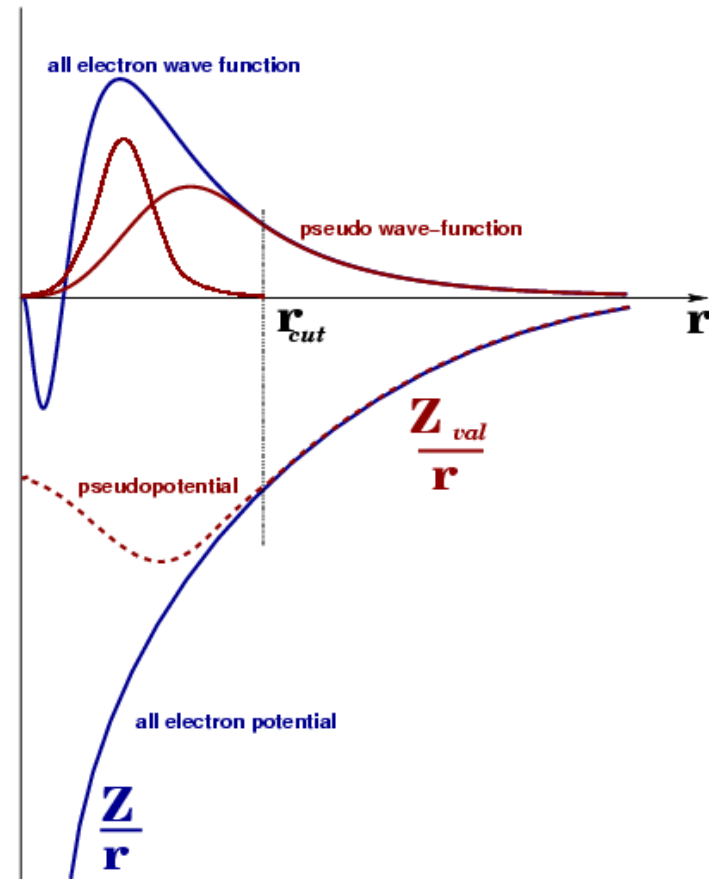
If one uses a one to one correspondence between all-electron wave functions, i.e. for each true valence wave function of the atom one pseudo-wave function is constructed (which is an eigenfunction of the pseudopotential) , this leads to the concept of “norm-conserving” pseudopotentials. Such a scheme works well for atoms where the outer shell valence electrons occupy states that are orthogonal to inner shell states of the same angular momentum and are thus pushed outside of the core (e.g. Al, Si, P(3s3p), Ga, Ge, As(4s4p), In, Sn, Sb(5s5p)). These valence functions have a large maximum rather far outside the core region. If, however, the valence wave functions to be described are the first of the respective l -channel {e.g. B,C,N,O (2p) or transition metals (3d)} the functions are rather localized and have a maximum close to the core region. In this case in general more than one function per l -channel is necessary to describe the pseudovalence functions properly. The l -dependent pseudopotentials are constructed to have more than one eigenfunction which are not necessarily orthogonal to each other. For these “projector-augmented pseudopotentials” the norm-conservation condition cannot be guaranteed for each eigenfunction separately in the construction of the pseudopotentials, but has to be introduced during the application.

PSEUDOPOTENTIAL CONCEPT



KB: norm-conserving pseudopotentials

- one projector per each l -channel
- the norm of the pseudo-wave function is equal to the norm of the all electron wave function



PAW: non norm-conserving pseudopotentials

- two projectors per each l -channel
- the norm of each pseudo-wave function is NOT equal to the norm of the all electron wave function

Figure Pseudopotential 1: An illustration of the pseudopotential concept: the all-electron wave function is identical with the pseudo-wave function beyond a cutoff radius r_{cut} . The pseudopotential and the all electron potential have the same scattering behavior outside of a sphere of radius r_{cut} .

3.2. Generation of Norm-conserving Pseudopotentials

The pseudopotentials used in DFT calculations are generated from all-electron atomic calculations by self-consistently solving the radial Schrödinger equation¹ for an isolated atom for the ground-state and a few excited-states ([BHS82], [Y82], [Eng92b], [Eng95a]):

$$\left[-\frac{1}{2} \frac{d^2}{d\vec{r}^2} + \frac{l(l+1)}{2\vec{r}^2} - \frac{Z}{\vec{r}} + v_H(\vec{r}) + v_{xc}(\vec{r}) \right] \Psi_{n,l}^{AE}(\vec{r}) = \varepsilon_{n,l} \Psi_{n,l}^{AE}(\vec{r}) \quad (3.2-1)$$

where $v_H(\vec{r})$ and $v_{xc}(\vec{r})$ are the Hartree and exchange-correlation potentials; $\Psi_{n,l}^{AE}(\vec{r})$ and $\varepsilon_{n,l}$ are the all-electron (AE) atomic wave function and eigenvalue for each angular momentum component l . Then one chooses a cutoff radius $r_{cut,l}$ for each l -channel of the valence electrons and constructs the pseudo atomic wave function $\Psi^{PS}(\vec{r})$ and a pseudopotential $V_{ps,l}(\vec{r})$, which deviate from the all-electron corresponding terms only inside of the cutoff radius.

The pseudopotentials and the pseudo (PS) wave functions $\Psi_l^{PS}(\vec{r})$ have to satisfy three important criteria:

- the valence pseudo-wave functions have to be nodeless, be continuously differentiable, and identical to the all-electron wave functions outside of the given cutoff radius $r_{cut,l}$;
- the pseudo-eigenvalues of the valence electrons must be equal to the corresponding all-electron eigenvalues $\varepsilon_l^{PS} = \varepsilon_l^{AE}$;
- the logarithmic derivatives of the all-electron wave functions and the corresponding pseudo wave functions have to be identical at any radius outside $r_{cut,l}$ so that the scattering properties are very accurately described [GKS90]

$$\left. \frac{\partial (\ln(\Psi_l^{PS}(\vec{r}, \varepsilon)))}{\partial \vec{r}} = \frac{\partial (\ln(\Psi_{valence,l}^{AE}(\vec{r}, \varepsilon)))}{\partial \vec{r}} \right|_{R \geq r_{cut,l}} \quad (3.2-2)$$

The pseudopotential construction is not unique; indeed the above conditions allow a considerable amount of freedom for generating pseudo-wave functions. Many different ways have been developed for constructing pseudopotentials ([BHS82], [Van85, Van90], [TM90-91], [Blö94]). Once a particular pseudo-wave function is created, the ionic pseudopotential is then obtained by inverting the radial Schrödinger equation:

$$v_{ion,l}^{PS}(\vec{r}) = \varepsilon_l - v_H^{PS}(\vec{r}) - v_{xc}^{PS}(\vec{r}) - \frac{l(l+1)}{2\vec{r}^2} + \frac{1}{2\Psi_l^{PS}(\vec{r})} \frac{d^2}{d\vec{r}^2} \Psi_l^{PS}(\vec{r}) \quad (3.2-3)$$

¹ Exactly speaking, we solve Kohn-Sham equations, since we use the density functional description also for the atoms.

where $v_H^{PS}(\vec{r})$ and $v_{XC}^{PS}(\vec{r})$ are calculated from the pseudo-wave functions. In this way a specific pseudopotential is generated for each angular momentum component l .

3.3. Semi-local Pseudopotential and Kleinman-Bylander Form of the Pseudopotential

The l -dependent pseudopotentials are obtained in a “semi-local form” (projectors in angular-momentum space but functions of $|\vec{r}|$) and, since all l -dependent potentials have the same long-range Coulomb-behavior it is easy to separate a l -independent common local potential and l -dependent semi-local parts that are limited only to the core region:

$$v_{ion}^{PS}(\vec{r}) = \sum_l v_l^{PS}(|\vec{r}|) \hat{P}_l = \sum_l v_{loc}(|\vec{r}|) \hat{P}_l + \sum_l (v_l^{SL}(|\vec{r}|) - v_{loc}(|\vec{r}|)) \hat{P}_l = v_{loc}(|\vec{r}|) + \sum_l \Delta v_l^{SL}(|\vec{r}|) \hat{P}_l \quad (3.3-1)$$

The matrix elements of such semi-local pseudopotential in a plane wave basis set have the form:

$$\begin{aligned} \Delta v_l^{SL}(\vec{k} + \vec{G}, \vec{k} + \vec{G}') &= \frac{1}{\Omega} \langle e^{i(\vec{k} + \vec{G})\vec{r}} | \Delta v_l^{SL}(\vec{r}) \hat{P}_l | e^{i(\vec{k} + \vec{G}')\vec{r}} \rangle_l \\ &= \frac{4\pi}{\Omega} (2l+1) P_l(\cos \gamma_{\vec{k} + \vec{G}, \vec{k} + \vec{G}'}) \times \int \vec{r}^2 j_l(|\vec{k} + \vec{G}||\vec{r}|) \Delta v_l^{SL}(\vec{r}) j_l(|\vec{k} + \vec{G}'||\vec{r}|) d\vec{r} \end{aligned} \quad (3.3-2)$$

where Ω is the volume of the unit cell, j_l a spherical Bessel-function, P_l a Legendre-polynomial and $\gamma_{\vec{k} + \vec{G}, \vec{k} + \vec{G}'}$ the angle between $(\vec{k} + \vec{G})$ and $(\vec{k} + \vec{G}')$. Thus one can see that the pseudopotential contribution to the Hamiltonian is a matrix with the dimension $(N \times N)$, N being the number of plane waves. The computational effort for diagonalization of such a matrix scales with N^3 . Since N scales with the number of the atoms in the system, it becomes clear that the sizes of the systems that can be handled are limited.

As a further generalization of the pseudopotential approach, Kleinman and Bylander (KB) [KB82] observed that greater efficiency could be attained if the non-locality will be not restricted to the angular momentum part, but if the radial component will also be converted into a separable non-local form. Therefore in the KB-approach, the semi-local form is converted into the fully non-local form:

$$\Delta v_l(\vec{r}) \hat{P}_l \approx \Delta \hat{v}_l^{KB}(\vec{r}) = \sum_{m=-l}^{+l} \frac{|\Delta v_l(\vec{r}) \Psi_{lm}\rangle \langle \Psi_{lm} \Delta v_l(\vec{r})|}{\langle \Psi_{lm} | \Delta v_l(\vec{r}) | \Psi_{lm} \rangle} \quad (3.3-3)$$

where Ψ_{lm} are the pseudo-wave functions which were used for the construction of the semi-local pseudopotential $\Delta v_l(\vec{r})$.

Using the lm -representation of the wave functions:

$$\Psi_{lm}(\vec{r}) = \frac{g_l(r)}{r} Y_{lm}(\theta, \varphi) \quad (3.3-4)$$

the plane wave matrix –element of $\Delta v_l(r)$ can be rewritten as:

$$\Delta v_l^{KB}(\vec{k} + \vec{G}, \vec{k} + \vec{G}') = \frac{(4\pi)^2}{\Omega} \sum_m Y_{lm}^*(\Omega_{\vec{k}+\vec{G}}) Y_{lm}(\Omega_{\vec{k}+\vec{G}'}) \times \frac{T_l^*(|\vec{k} + \vec{G}|) T_l(|\vec{k} + \vec{G}'|)}{W_l} \quad (3.3-5)$$

where $Y_{lm}(\Omega_{\vec{k}+\vec{G}'})$ are spherical harmonics and

$$\begin{aligned} T_l(|\vec{k} + \vec{G}|) &= \int \vec{r} \cdot \vec{g}_l(r) \Delta v_l(r) \cdot \vec{j}_l(|\vec{k} + \vec{G}| \vec{r}) d\vec{r} \\ W_l &= \int g_l(r) \Delta v_l(r) g_l(r) d\vec{r} \end{aligned} \quad (3.3-6)$$

The Kleinman-Bylander form drastically reduces the computational requirements in a pseudopotential calculation, the computation of non-local part scales like $N \cdot \log(N)$ when the iterative diagonalization schemes are used. However, one has to consider that, in the construction of the pseudopotential, unphysical low energy eigenstates (so called “ghost-states”) have to be avoided ([GKS90], [GSS91]).

3.4. The PAW Pseudopotential

The projector augmented wave method combines in an original way the concept of the pseudopotential (PS) and linear augmented plane wave method (LAPW) in a manner that one can reconstruct all-electron valence wave functions. Here we follow the idea put forward by Blöchl [Blö94] and implemented by W. Kromen [Kro01].

The basic idea in the PAW method is that one can access the all-electron wave function (AE) $|\Psi\rangle$ from the smooth pseudo wave function (PS) $|\tilde{\Psi}\rangle$, not necessary norm-conserving, via a linear transformation T . So the expectation value of any operator \hat{H} can be calculated accordingly to the formula:

$$\langle \hat{H} \rangle = \langle \Psi | \hat{H} | \Psi \rangle = \langle \tilde{\Psi} | T^\dagger \hat{H} T | \tilde{\Psi} \rangle = \langle \tilde{\Psi} | \hat{\tilde{H}} | \tilde{\Psi} \rangle \quad (3.4-1)$$

with $|\Psi\rangle = T |\tilde{\Psi}\rangle$ and $\hat{\tilde{H}} = T^\dagger \hat{H} T$.

The linear transformation is designed to smooth the all electron wave function in the vicinity of the nuclei and one constructs the linear transformation from a sum of local-atom-centered transformations:

$$T = 1 + \sum_{atom} T_{atom} \quad (3.4-2)$$

where each local contribution T_{atom} acts only within the so called augmentation region defined by Ω_{atom} around each atom. Outside of the augmentation region the AE wave functions and PS wave functions are identical because the all-electron potential and the pseudopotential have the same scattering properties.

PSEUDOPOTENTIAL CONCEPT

The form of the local-atom-centered transformation can be obtained via the AE partial wave function $|\varphi_i\rangle$ and the smoothed PS partial wave function $|\tilde{\varphi}_i\rangle$ of the isolated atom as defined by the relation²:

$$|\varphi_i\rangle = (1 + T_{atom}) |\tilde{\varphi}_i\rangle \quad (3.4-3)$$

The AE wave function and PS wave function are assumed to be linear combinations of the partial waves inside of the augmentation spheres Ω_{atom} :

$$|\tilde{\Psi}\rangle = \sum_i c_i |\tilde{\varphi}_i\rangle; \quad |\Psi\rangle = \sum_i c_i |\varphi_i\rangle = T |\tilde{\Psi}\rangle \quad (3.4-4)$$

with the c_i being so called expansion coefficients defined as the product of the projector wave function and PS wave function:

$$c_i = \langle \tilde{p}_i | \tilde{\Psi} \rangle \quad (3.4-5)$$

under the orthogonality and completeness condition within Ω_{atom} ³:

$$\langle \tilde{p}_i | \tilde{\varphi}_j \rangle = \delta_{i,j}; \quad \sum_i |\tilde{\varphi}_i\rangle \langle \tilde{p}_i| = 1 \quad (3.4-6)$$

Finally the AE wave function is written as a sum of PS wave function and a partial-wave dependent part:

$$|\Psi\rangle = |\tilde{\Psi}\rangle + \sum_i (|\varphi_i\rangle - |\tilde{\varphi}_i\rangle) \langle \tilde{p}_i | \tilde{\Psi} \rangle \quad (3.4-7)$$

$$T = 1 + \sum_i (|\varphi_i\rangle - |\tilde{\varphi}_i\rangle) \langle \tilde{p}_i | \quad (3.4-8)$$

where the AE partial wave function $|\varphi_i\rangle$ and the PS partial wave function $|\tilde{\varphi}_i\rangle$ are canceling each other outside of the augmentation region Ω_{atom} , the projector \tilde{p}_i being zero outside of Ω_{atom} .

Due to equation (3.4-7) in the PAW formalism, the true valence charge $n(\vec{r})$ is decomposed into three contributions:

$$n(\vec{r}) = \tilde{n}(\vec{r}) + n^\Omega(\vec{r}) - \tilde{n}^\Omega(\vec{r}), \quad (3.4-9)$$

where $\tilde{n}(\vec{r})$ represents the charge over the entire space due to the extended pseudo wave functions (it is the charge due to the plane wave expansion of the smooth pseudo wave functions), $\tilde{n}^\Omega(\vec{r})$ is the “smooth” charge due to the pseudo wave functions inside of the augmentation sphere Ω_{atom} and $n^\Omega(\vec{r})$ represents the “true” charge within the augmentation sphere (it is the charge due to the all electron wave functions inside of Ω_{atom}). An important observation here is that the subtraction of the “smooth” charge and addition of the “true” charge inside of the augmentation region is allowed only because both charges can be

² Normally, the AE-partial wave functions are solutions of the radial Schrödinger equations for the isolated atom, which are orthogonalized on the core states.

³ The one center expansion $\sum_i |\tilde{\varphi}_i\rangle \langle \tilde{p}_i | \tilde{\Psi} \rangle$ of a PS wave function is identical to the PS wave function $|\tilde{\Psi}\rangle$ itself.

constructed so that they have the same multipole expansion and thus yield the same electrostatic potential outside Ω_{atom} .

3.5. Partial Core-Correction

In the pseudopotential formalism it is assumed that the charge densities are divided into core and valence contribution. The part of the energy due to the core contribution is assumed constant and subtracted. More often this contribution is completely neglected, because the total electronic energy is evaluated only from valence charge densities and their interaction with the local and non-local parts of the pseudopotentials. All these approximations assume that the interaction between the core and valence electrons are contained in the pseudopotential. This means that the exchange-correlation energy can be linearized into two separated contributions ([LFC82], [Eng92b], [Eng95a]).

$$v_{XC} [n_{core}^{AE}(\vec{r}) + n^{ps}(\vec{r})] \approx v_{XC} [n_{core}^{AE}(\vec{r})] + v_{XC} [n^{ps}(\vec{r})] \quad (3.5-1)$$

The experience shows that if the core and valence charge densities are spatially well separated the linearization does not introduce big errors, but if there exists a significant overlap between the two densities the linearization will introduce errors in the calculation of total energies and forces.

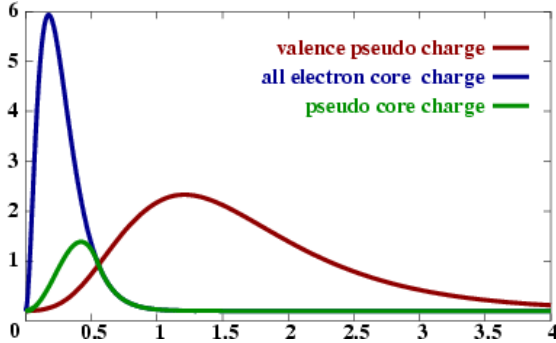


Figure Partial core-correction: The constructed pseudo core charge (green line) coincides with the all electron core charge beyond a cutoff radius r_{PCC} . In the figure the radius is fitted at the intersection point of valence pseudo charge (red line) with the all electron core charge (blue line).

In order to eliminate the errors due to this linearization in the non-linear exchange-correlation functional, the core charge and the valence charge need to be added whenever the exchange-correlation potential and energy are calculated.

The core charge has a significant effect only where the core charge and the valence charge have similar magnitudes and it is without importance close to the nucleus. So one can replace the true core charge density with a partial core charge density, which is equal to the true core charge outside of some radius r_{PCC} and arbitrary inside. The relations used in the construction of the partial core charge are:

$$n_{PCC}(\mathbf{r}) = \begin{cases} A \cdot r \sin(B \cdot r), & r \leq r_{PCC} \\ n_{core}^{AE}(\mathbf{r}), & r \geq r_{PCC} \end{cases} \quad (3.5-1)$$

where the parameters A, B are determined by fitting the value and the gradient of the core charge density and its radial gradient at r_{PCC} .

Finally the exchange and correlation potential are calculated using the sum of the two charges $n_{PCC}(\vec{r}) + n^{ps}(\vec{r})$:

$$\begin{aligned} v_{XC}[n^{ps}(\vec{r})] &\rightarrow v_{XC}[n_{PCC}(\vec{r}) + n^{ps}(\vec{r})] \\ E_{XC}[n^{ps}(\vec{r})] &\rightarrow E_{XC}[n_{PCC}(\vec{r}) + n^{ps}(\vec{r})] \end{aligned} \quad (3.5-2)$$

In the case of a pseudopotential in which a “soft” or “small” core is taken into account (corresponding to a large radius), a very easy way to include the partial core correction charges is via Fourier transform. To our experience it turns out that it is very important to take into account the tail of the core charge in the region where it is comparable to the valence charge. This means that a small radius of the partial core correction needs to be used and a “hard” partial core correction is constructed. The problem that arises now is that the Fourier components necessary to describe the valence charge are not sufficient to describe the partial core charge and the back Fourier transform to the real space with a finite number of plane waves, will introduce oscillations (negative values of the real space charge) when the true core charge density approaches zero.

Since the exchange-correlation energy and potential are calculated in real space, it is better to include the partial core-correction directly in real space. This was implemented into the EStCoMPP-code.

By Fourier transformation to real space, the valence charge is calculated on the points of a regular three-dimensional real space grid defined in the unit cell. Since the positions of all atoms are known, in the new scheme for each atom one calculates the partial core charge density at the points of this three-dimensional real space grid, which are inside of a sphere of radius r_{sphere} . Details on the implementation can be found in the Appendix Partial Core-Correction.

3.6. General Scheme for Pseudopotential Generation

This section will briefly describe the steps required to generate a pseudopotential.

A. Kleinman-Bylander (KB) pseudopotential: This type of pseudopotential uses one projector for each l -channel and the norm-conservation is enforced. This means that the spatial integral of the square of each pseudo-wave function is equal with the integral of the square of the corresponding all-electron valence wave function. (for details see [Eng92]). One more atom with different occupancy of the l -channels can be used in the generation of the KB-pseudopotential. For the KB-pseudopotential following parameters have to be chosen:

- a specific form of the **exchange-correlation functional**, that is the same for all configurations (and is used in the application of the generated pseudopotential);
- **atomic configuration**: one needs to specify the occupancy of the l -channels. For each l -channel of each atom a projector will be constructed. The final pseudopotential can be built from different l -channels of different atoms;

PSEUDOPOTENTIAL CONCEPT

- if the *partial core-correction* (PCC) is taken into account, one has to specify the radius at which the PCC is fitted;
- *cutoff radii* for each l -channel of each atom;
- *cutoff function* for extrapolating the pseudowave function to zero (see [BHS82], [Van85], [Van90], [RRKJ90], [Eng92]);
- the l -channel that is used as *local potential*.

Although different radii for each l -channel can be used in the construction of the pseudopotential, the pseudopotential sphere is defined as the largest cutoff radius of all l -channels. In any application of the pseudopotential the bond length of the neighboring atoms should be larger than the sum of radii of the pseudopotential spheres of the respective atoms.

B. PAW-pseudopotential: This type of pseudopotential uses two projectors for each l -channel. The norm-conservation for the valence wave functions is not enforced anymore. In principle the KB- pseudopotential can be constructed from a single configuration. The PAW-pseudopotential requires at least two configurations because one constructs two projectors per l -channel. One configuration usually is the ground-state with a given occupancy of the l -channels. For this the characteristic ground state eigenvalues yield the bound states projectors. The second configuration has the same occupancy of the l -channels as the first configuration, but in addition it contains the $l+1$ -channel with zero occupancy. For the second configuration one has the freedom to choose different reference energies. Usually, but not necessarily, they are positioned in the range of valence eigenvalues of a given compound. In general, these energies are not eigenvalues and yield as solutions non-bound states. For a PAW-pseudopotential following parameters have to be chosen:

- an *exchange-correlation functional* that is the same for all configurations;
- *atomic configuration*: one has the freedom to specify the occupancies of the l -channels. These are not necessarily corresponding to the ground states of the atom. For each l -channel of each atom a projector will be constructed. The final pseudopotential is built from the two projectors of each l -channel (the projectors correspond to a bound and unbound state);
- if the *partial core-correction* (PCC) is taken into account, one has to specify the radius at which the PCC is fitted. Normally, for the PAW- pseudopotentials of transitional metals a large PCC needs to be taken into account;
- *cutoff radii* for each l -channel of each atom. Although the occupancy of the l -channels with the same l is equal, the cutoff radii can be different. The **augmentation radius** of the pseudopotential is defined as the largest cutoff radius of the l -channels;
- *cutoff function* for extrapolating the pseudo-wave function to zero (see [BHS82], [Van85], [Van90], [RRKJ90], [Eng92], [Kro01]);
- the *local potential* is always the $l+1$ -channel of the second configuration with zero occupancy;
- the *energy-cutoff* (G_{\max} -plane wave energy-cutoff given in $\text{Ry}^{1/2}$) used in the multipole expansion of the “true” and “smooth” charges inside of the pseudopotential sphere (see [Kro01] page 58, [Wei81]).

In order to clarify if the constructed pseudopotentials are good approximations, i.e. if they can reproduce the scattering properties of the atoms in the energy range of the valence electrons, for both types of pseudopotentials KB- and PAW-, a series of tests needs to be done in the atomic program. First, all-electron and pseudo calculations are performed for some test atomic configurations: excited and/or ionic states. The corresponding valence all-electron and

pseudo eigenstates and exited energies should be practically identical. The second test is the calculation of the logarithmic derivatives of the valence all-electron and pseudo wave functions ([GKS90], [GSS91]). The pseudo-wave functions are by definition node-less. The analyses of the logarithmic derivatives help us to identify if unphysical lower energies states (“ghost states” that are introducing nodes in the pseudo wave functions) appear or not. If this is the case, different parameters (atomic configurations, cutoff radii, reference energies) have to be chosen until the “ghost states” disappear. This may be a very cumbersome procedure (see below). The “Rappe-criterion” is the third test done in the generation program ([RRKJ90]). With this one can estimate the plane wave basis set (cutoff energy) necessary to obtain convergent results for the total energy.

The final tests are done by calculations of the properties of the real electronic systems with the generated pseudopotentials (the lattice constants of solids, bond lengths and angles of molecules).

The Appendix „Parameters and tests of the PAW-pseudopotentials“ describes applicable PAW-pseudopotentials for different elements. The generation parameters as well as tests and results for the LDA ([VWN80]) and GGA-PBE ([PBE96-98]) with and without partial core-correction are given.

3.7. Comments on the Generation of the Pseudopotentials

Since there are no strict rules how one can choose the correct parameters for generating a good transferable pseudopotential, it remains still an art to find the proper cutoff radii and reference energies for each l -channel rather than a simple application of a mathematical algorithm. A good transferable pseudopotential is obtained when it can be used in different chemical environments and can describe the physical properties well. This means that the pseudopotential should have a small cutoff radius, smaller than half the nearest-neighbor distance of the given compound.

For someone trying to generate pseudopotentials one of the biggest “problem” is the appearance of a so-called “ghost-state”: an unphysical lower energy state that introduces nodes in the pseudo-wave function. In the case of the norm-conserving pseudopotentials (Kleinman-Bylander type), which are using just one projector and one reference eigenvalue (corresponding to the valence bound state) per l -channel, the only solution to avoid the “ghost-state” is to increase the cutoff radius for the specific channel for which the “ghost-state” appears. In some instances one needs to change the radius as well or even the l -channel considered as local potential.

In the case of the PAW-scheme of generating the pseudopotentials one has more freedom because this method is using two projectors for each l -channel at two different reference energies: one is eigenvalue for each l -channel in the ground state configuration and the other one is arbitrarily chosen, but in general it should be in the range of the valence energies in the solid. The “ghost-state” problem appears in this case also, but one has more parameters that can be changed in order to avoid their appearance. When the unphysical lower energy “ghost-state” appears first one should try to change the reference energy for the second

PSEUDOPOTENTIAL CONCEPT

projector to higher or lower values. Experience shows that there are specific energy intervals for which no “ghost-states” appear. The next step is that for different energies in this interval a series of calculations of a single atom in a big box and different compounds need to be performed to see what energy is the proper one for the given pseudopotential. In the case that any change in energy cannot eliminate the “ghost-state” one should change the cutoff radius of the specific l -channel for one of the two projectors or for both. There is no direct connection between the radii of the two projectors of the same l -channel so that one has the freedom to choose different radii. If the “ghost-states” still persist, the next change could be using different reference energies of the local potential, and then different radii. To my experience one has to generate 15-20 pseudopotentials before getting one that can be tested in different chemical environments (bulks or/and molecules). Again up to 20 pseudopotentials which apparently give reliable results for the atom have to be tested till one arrives at the conclusion that a specific pseudopotential with specific parameters (cutoff radii and reference energies) gives good results in solid state calculations.

To increase variability, the atomic generation program has been modified in such a way that one can generate a pseudopotential using the ionic states as reference configuration. In this case three atoms are required to generate the pseudopotential: the first is the ionic configuration with the eigenvalues as bound states, the second atom has the same ionic configuration but has one more l -channel used as local potential and the third atom has to be the atomic neutral ground-state configuration. In the PAW-code, which uses the pseudopotentials as input to perform calculation for real systems, one needs to provide the pseudo-charge of the neutral atoms as input charge. If an ionic configuration is used for generating the pseudopotential, the charge has to be taken from the neutral atom configuration, e.g. from the third atom configuration.

Also, the atomic generation program was generalized for the use of different l -channels as local potential (and not only the highest l). But all efforts to use other than the highest l -channel as local potential have failed to produce applicable, reliable pseudopotentials.

Chapter 4

The EStCoMPP-Program

The Electronic Structure Code for Materials Properties and Processes , EStCoMPP, was created by S. Blügel and K. Schroeder and developed by B. Engels, P. Richard, R. Berger and W. Kromen in the framework of their PhD-Theses ([Eng25a], [Ric96], [Ber02], [Kro01]). The following chapter is a brief introduction into the methods and algorithms used in the EStCoMPP program for calculating total energy and forces.

4.1. The Energy Minimization

In order to calculate the physical properties of a system for a given atomic configuration, the electronic states that minimize the Kohn-Sham energy have to be determined. To achieve this, an iterative scheme is used, where starting from a trial electron-density the eigenvalue equations are solved (also by iterative methods), and a new electron-density is generated successively until self-consistency is reached.

The energy-functional consists of several separable contributions: the kinetic energy of non-interacting electrons $E_{kin}^0[n(\vec{r})]$, the energy $E_{ext}[n(\vec{r})]$ of the electrons with density $n(\vec{r})$ in the external potential $v(\vec{r})$, the Hartree energy $E_H[n(\vec{r})]$ due to the electron-electron Coulomb interactions, the exchange-correlation energy-functional $E_{xc}[n(\vec{r})]$ where the remaining many-particle effects are included, and the Coulomb interactions of the ions, i.e. the Ewald-energy $E_{Ew}[n(\vec{r})]$. When we describe the electron-ion interaction by pseudopotentials (local and non-local contributions) the Hartree, the local pseudopotential, and the Ewald energies diverge separately. They can be combined to non-diverging expressions by adding and subtracting appropriate compensating charges. Fixing the energy scale by setting the average electronic potential to zero, an additional constant contribution $E_{loc}[n(\vec{r})]$ to the total energy has to be taken into account.

$$E_{tot}[n(\vec{r})] = E_{kin}^0[n(\vec{r})] + E_{ext}[n(\vec{r})] + E_H[n(\vec{r})] + E_{xc}[n(\vec{r})] + E_{Ew}[n(\vec{r})] + E_{loc}[n(\vec{r})] \quad (4.1-1)$$

The matrix-vectors products $H|\Psi\rangle$ are evaluated in real-space or in reciprocal-space, depending on the functional form of the operators in the Hamiltonian. To avoid bad convergency of the self-consistency iterations due to oscillations of states close to the Fermi-level (i.e. states that are occupied in one iteration step and unoccupied in the next one) the sharp Fermi-distribution for $T = 0$ is smeared out at the Fermi-energy by introducing a finite

temperature T . The occupation numbers of the states with eigenenergies $\varepsilon_{\nu,\bar{k}}$ are then defined as:

$$f_{\nu,\bar{k}} = \frac{1}{e^{(\varepsilon_{\nu,\bar{k}} - \varepsilon_F)/k_B T} + 1} \quad (4.1-2)$$

This leads to a smooth variation of the occupation numbers around the Fermi-energy, but at the same time introduces a temperature dependence of the total energy, which can be interpreted as the free-energy of the electron system:

$$F = E - TS \quad (4.1-3)$$

The entropy of the independent electrons can be expressed by:

$$S = -2 \cdot k_B \sum_{\nu,\bar{k}} \omega_{\bar{k}} \left(f_{\nu,\bar{k}} \cdot \ln(f_{\nu,\bar{k}}) + (1 - f_{\nu,\bar{k}}) \cdot \ln(1 - f_{\nu,\bar{k}}) \right) \quad (4.1-4)$$

The factor 2 arises from spin-degeneracy. Normally the free energy of the system converges faster than the total energy. For a small temperature $T \neq 0$ the total energy and the free energy of the system can be written as small deviations from the true ground state energy E_0 :

$$\begin{aligned} E &= E_0 + \gamma T^2 \\ F &= E_0 - \gamma T^2 \end{aligned} \quad (4.2-5)$$

The ground state energy at $T=0$ can thus be approximated as:

$$E_0 = \frac{1}{2}(E + F) \quad (4.2-5)$$

At the beginning of the iteration cycle, one can choose a larger temperature to assure that the density, and implicitly the free energy, converges smoothly. The temperature can then be decreased to assure that the extrapolation to the ground state energy is correct. The iteration cycle to reach the ground state electron density (and ground state energy) is demonstrated in the following flow chart.

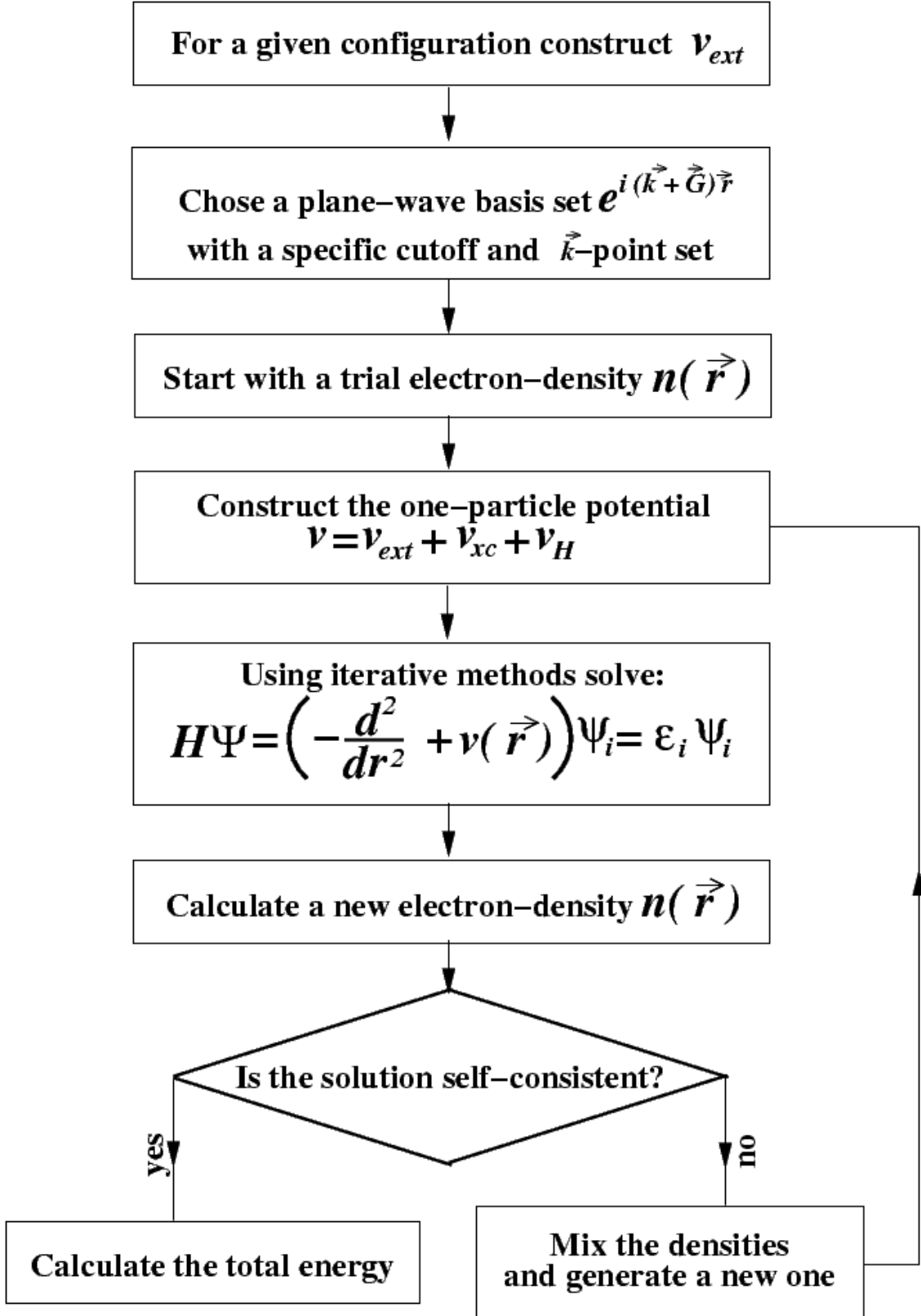


Figure 1: Flowchart of the iterative procedure used in the calculation of the electronic ground-state density.

4.2. Explicit Form of the Equations in the EStCoMPP-Program

A brief presentation of the equations used in the EStCoMPP code is given on the next pages. The detailed description of the pseudopotential generation code and the program used for solid state calculations can be found in the PhD-Theses of B. Engels, P. Richard, R. Berger and W. Kromen ([Eng25a], [Ric96], [Ber02], [Kro01]).

The Kinetic Energy

The kinetic-energy functional is diagonal in \vec{k} -space, and thus evaluated there:

$$E_{kin}[n(\vec{r})] = \langle \Psi | -\frac{\partial^2}{\partial \mathbf{r}^2} | \Psi \rangle_{\Omega} = \sum_{\nu, \vec{k}} \omega_{\vec{k}} f_{\nu, \vec{k}} \langle \Psi_{\nu, \vec{k}} | -\frac{\partial^2}{\partial \mathbf{r}^2} | \Psi_{\nu, \vec{k}} \rangle$$

$$E_{kin}[n(\vec{r})] = \sum_{\nu, \vec{k}} \sum_{\vec{G}} \omega_{\vec{k}} f_{\nu, \vec{k}} |\vec{k} + \vec{G}|^2 u_{\nu, \vec{k}}^*(\vec{G}) u_{\nu, \vec{k}}(\vec{G}) \quad (4.2-1)$$

The matrix-vector product can be written as:

$$\langle \vec{r} | E_{kin}^0 | \Psi_{\nu, \vec{k}} \rangle_{\Omega} = \frac{1}{\sqrt{\Omega}} \sum_{\vec{G}} |\vec{k} + \vec{G}|^2 u_{\nu, \vec{k}}(\vec{G}) e^{-i(\vec{k} + \vec{G})\vec{r}} \quad (4.2-2)$$

with the matrix elements:

$$\langle \vec{k} + \vec{G} | E_{kin}^0 | \Psi_{\nu, \vec{k}} \rangle_{\Omega} = |\vec{k} + \vec{G}|^2 u_{\nu, \vec{k}}(\vec{G}) \quad (4.2-3)$$

$$\langle \vec{k} + \vec{G} | E_{kin}^0 | \vec{k}' + \vec{G}' \rangle_{\Omega} = |\vec{k} + \vec{G}|^2 \delta_{\vec{k}, \vec{k}'} \delta_{\vec{G}, \vec{G}'} \quad (4.2-4)$$

The Local Energy

The local energy consists of three contributions: the exchange-correlation energy, the local part of the pseudopotential, and the Hartree energy. In order to avoid the calculation of the convolution-integrals in \vec{k} -space, the local potentials are always applied to the wave functions in real space. Therefore, the real-space representations have to be obtained from the simpler reciprocal-space form via fast-Fourier transformations (FFT's). The Hartree-potential is determined by Poissons' equation (4.2-5), for which the Fourier transformations yields (4.2-6):

$$\frac{\partial^2 v_H(\mathbf{r})}{\partial \mathbf{r}^2} = -8 \cdot \pi \cdot n(\vec{r}) \quad (4.2-5)$$

$$v_H(\vec{G}) = \frac{1}{\Omega} \int_{\Omega} v_H(\vec{r}) e^{i\vec{G}\vec{r}} d^3\vec{r} = \frac{1}{\Omega} \frac{8\pi}{G^2} n(\vec{G}) \quad (4.2-6):$$

The Hartree-potential is calculated in reciprocal space since the Laplacian operator is diagonal there. The matrix-vector products (4.2-7), and the matrix-elements (4.2-8) have the form:

$$\langle \vec{r} | v_H(\vec{G}) | \Psi_{v,\vec{k}} \rangle = \frac{1}{\sqrt{\Omega}} \sum_{\vec{G}} \left(\sum_{\vec{G}'} v_H(\vec{G}') u_{v,\vec{k}}(\vec{G} - \vec{G}') \right) e^{-i(\vec{k} + \vec{G})\vec{r}} \quad (4.2-7)$$

$$\langle \vec{k}' + \vec{G}' | v_H(\vec{G}) | \vec{k} + \vec{G} \rangle = \sum_{\vec{G}'} v_H(\vec{G}') \quad (4.2-8)$$

The calculation of the exchange-correlation energy in the local density approximation (LDA) is done in real-space, while for the generalized gradient approximation (GGA) the derivatives of the charge density are calculated analytically in reciprocal space, and then Fourier transformed to real space, where the gradients are calculated numerically from these derivatives (A detailed explanation of the GGA concept and implementation in the EStCoMPP code can be found in Appendixes A.1.-A.5.

The local part of the pseudopotential consists of spherical-symmetric contributions of atoms at positions $\vec{R} + \vec{\tau}_{\mu}$, (sic) the local pseudopotential is given by:

$$v_{loc}(\vec{r}) = \sum_{\mu} v_{loc}^{\alpha(\mu)} \left| \vec{r} - \vec{R} - \vec{\tau}_{\mu} \right| \quad (4.2-9)$$

where $\alpha(\mu)$ indicates that chemically identical atoms μ are contributing with the same pseudopotential located at different positions $\vec{\tau}_{\mu}$ in the supercell. The corresponding Fourier-transform:

$$v_{loc}(\vec{r}) = \sum_{\mu, \vec{G}} S_{\vec{\tau}_{\mu}}(\vec{G}) v_{loc}^{\alpha(\mu)}(\vec{G}) e^{-i\vec{G}\vec{r}} \quad (4.2-10)$$

leads to the reciprocal-space representation:

$$v_{loc}(\vec{G}) = \sum_{\mu} S_{\vec{\tau}_{\mu}}(\vec{G}) v_{loc}^{\alpha(\mu)}(\vec{G}) \quad (4.2-11)$$

where

$$v_{loc}^{\alpha(\mu)}(\vec{G}) = \frac{1}{\Omega} \int_{\Omega} v_{loc}^{\alpha(\mu)}(\vec{r}) e^{i\vec{G}\vec{r}} d^3\vec{r} \quad (4.2-12)$$

with the structure-factors:

$$S_{\vec{\tau}_{\mu}}(\vec{G}) = e^{-i\vec{G}\vec{\tau}_{\mu}} \quad (4.2-13)$$

Finally the expressions for matrix-vectors products are:

$$\langle \vec{r} | v_{loc} | \Psi_{v,\vec{k}} \rangle_{\Omega} = \sum_{\vec{G}, \vec{G}'} \sum_{\mu} \frac{1}{\Omega} S_{\vec{\tau}_{\mu}}(\vec{G}') v_{loc}^{\alpha(\mu)}(\vec{G}) \times u_{v,\vec{k}}(\vec{G} - \vec{G}') e^{-i(\vec{k} + \vec{G})\vec{r}} \quad (4.2-14)$$

$$\langle \vec{k} + \vec{G} | v_{loc}^{\alpha(\mu)} | \Psi_{v,\vec{k}} \rangle_{\Omega} = \sum_{\vec{G}} \sum_{\mu} S_{\vec{\tau}_{\mu}}(\vec{G}) v_{loc}^{\alpha(\mu)}(\vec{G}) \cdot u_{v,\vec{k}}(\vec{G} - \vec{G}') \quad (4.2-15)$$

The electron-ion Coulomb interaction leads to a long-range term $\approx \frac{-2Z}{r}$ for each of the local pseudopotential.

To allow the numerical integration of $v_{loc}^{\alpha(\mu)}(\vec{G})$ in \vec{k} -space, the long-range part has to be separated and solved analytically.

The Non-local Part of the Energy

The l -dependent contribution to the total energy of the atoms μ of kind α is contained in the non-local part of the pseudopotentials. The expressions used to evaluate this energy are different for the norm- and non-norm-conserving (**PAW**) pseudopotentials.

In the case of the norm-conserving **Kleinman-Bylander pseudopotentials** the non-local part $\sum_l \Delta v_{loc}^{\alpha(\mu)}(\vec{r}) \hat{P}_l$ is given by ([Eng95a], [Ric96]):

$$\tilde{v}_{KB} = \sum_{\mu} \sum_{l=0}^{l_{\max}} \sum_{m=-l}^{+l} E_{KB}^{l,\alpha(\mu)} S_{\vec{\tau}_{\mu}} |t_{l,m,\alpha(\mu)}\rangle \langle t_{l,m,\alpha(\mu)}| \quad (4.2-16)$$

in which $S_{\vec{\tau}_{\mu}}$ represents the translation-operator used to move the non-local part of the pseudopotential to the positions $\vec{\tau}_{\mu}$ of the atoms. The matrix-vector products are given by:

$$\langle \vec{r} | v_{KB} | \Psi_{\vec{k}\nu} \rangle_{\Omega} = \sum_{\mu} \sum_{l=0}^{l_{\max}} \sum_{m=-l}^{+l} \left(\sum_{\vec{G}} T_{l,m,\mu}^* (\vec{k}, \vec{G}') u_{\vec{k},\nu}(\vec{G}) \right) E_{KB}^{l,\alpha(\mu)} \times \frac{1}{\Omega} \sum_{\vec{G}} T_{l,m,\mu}^* (\vec{k}, \vec{G}) e^{-i(\vec{k}+\vec{G})\vec{r}} \quad (4.2-17)$$

$$\langle \vec{k} + \vec{G} | v_{KB} | \Psi_{\vec{k}\nu} \rangle_{\Omega} = \sum_{\mu} \sum_{l=0}^{l_{\max}} \sum_{m=-l}^{+l} T_{l,m,\mu} (\vec{k}, \vec{G}) E_{KB}^{l,\alpha(\mu)} \times \frac{1}{\Omega} \sum_{\vec{G}'} T_{l,m,\mu}^* (\vec{k}, \vec{G}') u_{\vec{k},\nu}(\vec{G}')$$

where

$$T_{l,m,\mu} (\vec{k}, \vec{G}) = S_{\vec{\tau}_{\mu}} (\vec{G}) \cdot Y_{lm}(\theta_{\vec{k}+\vec{G}}, \varphi_{\vec{k}+\vec{G}}) \cdot t_{l,\alpha(\mu)}(|\vec{k} + \vec{G}|) \quad (4.2-18)$$

and

$$t_{l,\alpha(\mu)}(|\vec{k} + \vec{G}|) = \frac{4}{\sqrt{\Omega}} \int d\vec{r} t_{l,\alpha(\mu)}(\vec{r}) j_l(|\vec{k} + \vec{G}|\vec{r}) \quad (4.2-19)$$

For the norm-conserving pseudopotentials the non-local part is easily calculated in reciprocal space due to the dyadic structure of the **KB**-potentials.

The non-local part of the **non-norm-conserving pseudopotentials (PAW)** is expressed in \vec{k} -space as ([Kro01]):

$$\langle \vec{k} + \vec{G} | v_{NL} | \vec{k} + \vec{G}' \rangle = \sum_{\mu;\gamma,\gamma'} \langle \vec{k} + \vec{G} | \tilde{p}_{\gamma}^{\mu} \rangle D_{\gamma,\gamma'}^{\mu} \langle \tilde{p}_{\gamma'}^{\mu} | \vec{k} + \vec{G}' \rangle \quad (4.2-20)$$

$$\langle \vec{k} + \vec{G} | v_{NL} | \tilde{\Psi}_{\vec{k}\nu} \rangle = \sum_{\mu;\gamma} \langle \vec{k} + \vec{G} | \tilde{p}_{\gamma}^{\mu} \rangle \sum_{\gamma'} D_{\gamma,\gamma'}^{\mu} \langle \tilde{p}_{\gamma'}^{\mu} | \tilde{\Psi}_{\vec{k}\nu} \rangle \quad (4.2-21)$$

for which the $\langle \vec{k} + \vec{G} | \tilde{p}_\gamma^\mu \rangle$ and $\langle \tilde{p}_\gamma^\mu | \tilde{\Psi}_{\vec{k}\nu} \rangle$ are evaluated in reciprocal space:

$$\langle \vec{k} + \vec{G} | \tilde{p}_\gamma^\mu \rangle = i^l e^{i\vec{k} \cdot \vec{\tau}_\mu} S^\mu(\vec{G}) \tilde{p}_{l,i}^{\alpha(\mu)}(|\vec{k} + \vec{G}|) \sqrt{4\pi} \cdot Y(\vec{k} + \vec{G}) \quad (4.2-22)$$

$$\langle \tilde{\Psi}_{\vec{k}\nu} | \tilde{p}_\gamma^\mu \rangle = \sum_{\vec{G}} \langle \tilde{\Psi}_{\vec{k}\nu} | \vec{k} + \vec{G} \rangle \langle \vec{k} + \vec{G} | \tilde{p}_\gamma^\mu \rangle \quad (4.2-23)$$

with:

$$\tilde{p}_\gamma^{\alpha(\mu)}(\vec{r}) = \frac{1}{r} Y_L(\hat{r}) \tilde{p}_{l,i}^{\alpha(\mu)}(\vec{r}) \quad (4.2-24)$$

$$\tilde{p}_{l,i}^{\alpha(\mu)}(\vec{k} + \vec{G}) = \sqrt{\frac{4\pi}{\Omega}} \int_0^{R_\mu} r \cdot j_l(|\vec{k} + \vec{G}| r) \tilde{p}_{l,i}^{\alpha(\mu)}(\vec{r}) d\vec{r} \quad (4.2-25)$$

$S^\mu(\vec{G})$ represents the structure factors, $\alpha(\mu)$ is the type of atom μ , \tilde{p}_γ^μ ; $\gamma = (l, i)$ are the projector functions localized in the augmentation sphere of the type of atom μ ; Y_L are the spherical harmonics, j_l the spherical Bessel-functions, L represent the (l, m) -channels and i represent the index of the projectors belonging to the same atom and l -channel, but generated at different energies.

The Ewald-Energy

The Coulomb interaction between ions in the supercell is taken into account by the Ewald-energy:

$$E_{Ew} = \frac{1}{2} \sum_{\vec{R}^n} \sum_{\mu, \mu'} \frac{Z_\mu Z_{\mu'}}{|\vec{\tau}_\mu - (\vec{R}^n + \vec{\tau}_{\mu'})|} \left(1 - \delta_{\vec{\tau}_\mu, \vec{R}^n + \vec{\tau}_{\mu'}} \right) = \frac{1}{2} \sum_{\vec{G} \neq 0} \sum_{\mu, \mu'} Z_\mu Z_{\mu'} \frac{1}{\Omega} \frac{4\pi}{G^2} e^{-i\vec{G} \cdot (\vec{\tau}_\mu - \vec{\tau}_{\mu'})} \quad (4.2-26)$$

$$E_{Ew} = \ddot{E}_{Ew} + \frac{1}{2} \frac{4\pi e^2}{\Omega} \frac{Z_v}{G^2} \Big|_{\vec{G}=0} \quad (4.2-27)$$

which contains a divergent term for $|\vec{G}| = 0$. A practical way to evaluate the Ewald-energy is to split equation (4.2-27) into contributions that are calculated separately in real and reciprocal space. The divergent terms at $|\vec{G}| = 0$, for the Hartree energy and the local pseudopotential, can be written like:

$$E_H + E_{loc} = \ddot{E}_H + \ddot{E}_{loc} + \Omega \cdot \left(-\frac{1}{2} \frac{4\pi e^2}{\Omega^2} \frac{Z_v}{G^2} - \alpha \frac{Z_v}{\Omega} \right) \quad (4.2-28)$$

$$\text{with } \alpha = \sum_{\mu} \int_{\infty} \left(\mathbf{v}_{loc}^{\alpha(\mu)}(\vec{r}) + \frac{2Z_v^{\alpha(\mu)}(\vec{r})}{r} \right) d\vec{r} \quad (4.2-29),$$

All the divergent terms $|\vec{G}| = 0$ of the Hartree energy, local pseudopotential energy, and Ewald-energy compensate each other. The term $\alpha \frac{Z_v}{\Omega}$ is the remaining contribution to the total energy, when we set the sum of the average Hartree potential and local pseudopotentials equal to zero in the eigenvalue problem.

The Hellman-Feynman Forces

The total energy of a system in the Born-Oppenheimer approximation is the sum of the total electronic-energy of the supercell $E_{tot}[\mathbf{n}(\vec{r}), \{\tau_\mu\}]$ (which depends parametrically on the coordinates of the ions), and the energy due to the Coulomb-interaction of the ions:

$$E_{tot}[\mathbf{n}(\vec{r}), \{\tau_\mu\}] = E_{el}[\mathbf{n}(\vec{r}), \{\tau_\mu\}] + E_{Ew}[\tau_\mu] \quad (4.2-30)$$

The forces exerted on the ions are derivatives of the total energy-functional $E_{tot}[\mathbf{n}(\vec{r}), \{\tau_\mu\}]$ with respect to the coordinates of the ions τ_μ with μ being the numbers of atoms:

$$\mathbf{F}_{tot} = -\frac{\partial}{\partial \tau_\mu} E_{el}[\mathbf{n}(\vec{r}), \tau_\mu] - \frac{\partial}{\partial \tau_\mu} E_{Ew}[\tau_\mu] \quad (4.2-31)$$

The forces on the ions due to the direct Coulomb-interaction E_{Ew} are easily calculated by:

$$\mathbf{F}_{ion}(\tau_\mu) = -\frac{1}{2} \frac{\partial}{\partial \tau_\mu} \sum_{\mu'} \frac{Z_\mu Z_{\mu'}}{|\tau_\mu - \tau_{\mu'}|} \quad (4.2-32)$$

while the forces due to the electronic energy are given by the relation:

$$\mathbf{F}_{el}(\tau_\mu) = -\frac{\partial}{\partial \tau_\mu} \langle \Psi(\tau_\mu) | \hat{H} | \Psi(\tau_\mu) \rangle \quad (4.2-33)$$

where \hat{H} is the Hamilton operator of the electronic system. The evaluation of equation (39) is difficult since the wave functions depend implicitly on the atom coordinates. In the Born-Oppenheimer approximation this equation can be reduced to the Hellman-Feynman forces:

$$\begin{aligned} \mathbf{F}_{HF}(\tau_\mu) &= -\frac{\partial}{\partial \tau_\mu} \langle \Psi(\tau_\mu) | \hat{H} | \Psi(\tau_\mu) \rangle = \left\langle \Psi(\tau_\mu) \left| -\frac{\partial}{\partial \tau_\mu} \hat{H} \right| \Psi(\tau_\mu) \right\rangle - E_0 \frac{\partial}{\partial \tau_\mu} \langle \Psi(\tau_\mu) | \Psi(\tau_\mu) \rangle \\ &= \left\langle \Psi(\tau_\mu) \left| -\frac{\partial \hat{H}}{\partial \tau_\mu} \right| \Psi(\tau_\mu) \right\rangle \end{aligned} \quad (4.2-34)$$

where we have exploited the fact that we use normalized N -particle wave functions for which $\hat{H} | \Psi \rangle = E_0 | \Psi \rangle$ and $\langle \Psi | \Psi \rangle = 1$.

Taking into account that the charge is conserved and its energy-functional is minimal for the ground-state charge density $n_0(\vec{r})$, the functional derivative of the total electronic-energy functional with respect to the charge density $n(\vec{r})$ is the chemical potential μ :

$$\mu = \frac{\partial E[n(\vec{r}), \tau_\mu]}{n(\vec{r})} \quad (4.2-35)$$

The final expression for the electronic contribution to the forces is:

$$\begin{aligned} \mathbf{F}_{el}(\tau_\mu) &= -\frac{\partial}{\partial \tau_\mu} E_{el}[n(\vec{r}), \tau_\mu] - \int \left(\frac{\partial E_{tot}[n(\vec{r}), \tau_\mu]}{\partial n(\vec{r})} \right) \frac{\partial n(\vec{r}, \tau_\mu)}{\partial \tau_\mu} d\vec{r}^3 \\ \mathbf{F}_{el}(\tau_\mu) &= -\frac{\partial}{\partial \tau_\mu} E_{el}[n(\vec{r}), \tau_\mu] - \mu_l \cdot \int \frac{\partial n(\vec{r}, \tau_\mu)}{\partial \tau_\mu} d\vec{r}^3 = -\frac{\partial}{\partial \tau_\mu} E_{el}[n(\vec{r}), \tau_\mu] - \underbrace{\mu}_{=0} \cdot \frac{\partial N}{\partial \tau_\mu} \end{aligned} \quad (4.2-36)$$

The last term is zero because the total charge does not vary with the positions of the atoms. In conclusion, the force on atom μ due to the electronic-energy is just the partial derivative of the electronic-energy functional with respect to the coordinates τ_μ of the atoms.

The Loop-Structure and the Algorithms

In the previous pages the concepts of density functional theory, and of the pseudopotential method have been discussed. In order to determine the atomic and electronic structure of a system one needs to proceed with the following steps:

- calculate the electronic structure
- calculate the forces on the atoms
- relax the atoms towards the equilibrium positions.

In the EStCoMPP code all this steps are done using iterative procedures in nested loops:

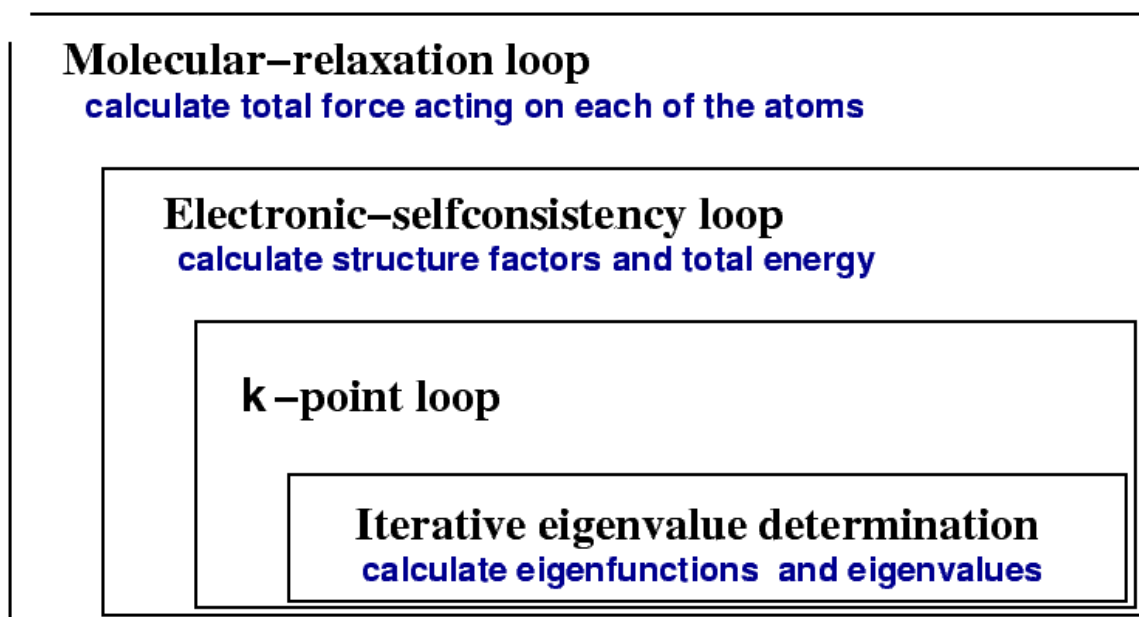


Figure 2: Loop-structure schemes in the EStCoMPP -program

In the following we will discuss this loops, starting with the innermost one.

4.3. Iterative Eigenvalue Determination

For a given ionic configuration, the electronic states that minimize the Kohn-Sham energy have to be determined. As a typical example we want to treat supercells containing about 200 atoms for which a high-energy cutoff may be required (about 150 plane waves per atom). Due to the large dimensions of the Hamiltonian matrix (30000×30000), the preferred method is to iteratively improve upon initial trial functions. Then, to determine the electron density of the system, typically only the lowest 2-10% of the eigenvalues and eigenvectors have to be determined.

Many different methods are available to carry out the iterative eigenvalue determination. The method implemented in the ESTCOMPP code is the Davidson-Kosugi algorithm ([Dav75], [Kos84]), which is an extended version of the Block-Davidson algorithm with a fixed dimension of the sub-space to avoid memory problems. In the original Davidson algorithm one correction vector is successively added in each iteration, and the matrix is then diagonalized in the subspace spanned by the starting- and correction-vectors. In the improved Block-Davidson algorithm ([Liu78]), correction-vectors for each of the starting-vectors are calculated in each iteration, and added to the subspace. In the Davidson-Kosugi scheme the subspace in each iteration is rotated by the choice of new starting-vectors.

A scheme of the iterative procedure can be written as ([Ric96]):

- guess the starting vectors $|\Psi_i\rangle^{(0)}$
- solve the matrix products $|\mathbf{H}\Psi_i\rangle^{(j)} = \mathbf{H}|\Psi_i\rangle^{(j)}$
- determine the correction-vectors $|\Psi_i^{corr}\rangle^{(i)}$
- calculate the new starting vectors $|\Psi_i\rangle^{(j+1)}$
- iterate until the norm of the correction-vectors is smaller than a given quality criterion

The Kohn-Sham Hamiltonian is not well conditioned because of the broad spectrum of eigenvalues that result from the wide range of energies associated with the basis states. Thus plane-waves with high kinetic energy always tend to dominate the search directions for the minimization algorithms, even though the corresponding wave-function coefficients are small. The solution is to use a preconditioning, which essentially divides the coefficients of the high kinetic energy waves by their kinetic energy while leaving the low kinetic energy waves untouched. Effectively this procedure compresses the range of eigenvalue energies, leading to a faster convergence.

4.4. The Electronic Self-consistency and Molecular Relaxation Loops

Within the Born-Oppenheimer approximation the degrees of freedom of the system can be separated into electronic and ionic degree of freedoms, so that the energy functional can be divided into two parts:

- electronic degrees of freedom \Rightarrow the charge density $n(\vec{r})$ and the effective potential $v_{eff}[n(\vec{r})]$.
- the atomic-positions degrees of freedom: τ_μ .

In the electronic self-consistency we solve the Kohn-Sham equations iteratively. In the n -th step a trial function $n^{(n)}(\vec{r})$ for electron density is used, and from the solutions, we construct a new electron density $n^{(n+1)}(\vec{r})$. In general, this can be considered as a functional of the trial density:

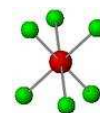
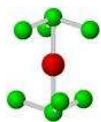
$$n^{(n+1)}(\vec{r}) = F[n^{(n)}(\vec{r})] \quad (4.4-1)$$

Self-consistency is reached, i.e. the fixed position of the functional is found, when

$$F[n^{(n)}(\vec{r})] - n^{(n+1)}(\vec{r}) = 0, \quad n \rightarrow \infty \quad (4.4-2)$$

A similar fix point scheme can be formulated for the ionic degrees of freedom using the coordinates $\{\tau^n\}$ and forces $\vec{F}\{\tau^n\}$. Both fix point problems are solved in our **EStCoMPP-code** by Quasi-Newton schemes¹ [Fle87].

¹ There are several possibilities to implement the iteration schemes. Those implemented in **EStCoMPP-code** are discussed in [Blü88].



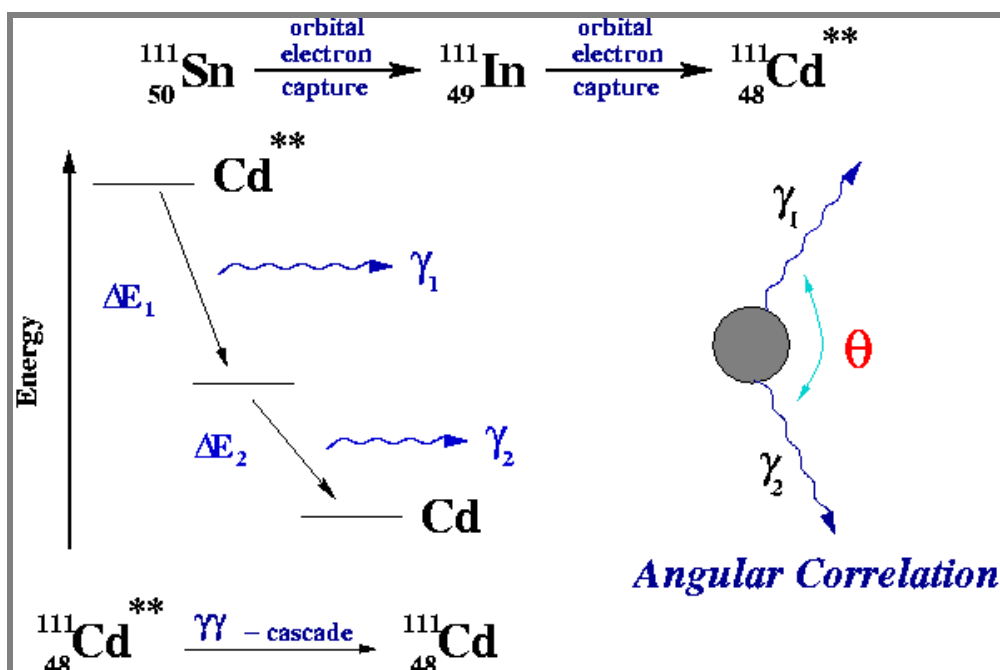
Chapter 5

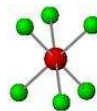
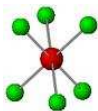
Cadmium Complexes in Si and Ge

As a first application of the PAW-program we calculated complexes of Cd in Si and Ge. Perturbed angular correlation (PAC) experiments are performed in order to measure the electrical field gradient (EFG) that provides useful information about the interaction of the Cd probe atom with other defects. The electric field gradient describes the interaction of the electrons with the electric quadrupole moment of the nuclei. It is given by the second derivative of the coulomb potential at the nuclear site. The EFG vanishes for cubic or tetrahedral symmetry; it is different from zero only when the local symmetry is lowered by other defects. This means that the EFG gives detailed information about the symmetry of the complexes that are formed ([AW93], [WS89], [WKG89]).

The PAC technique is based on a radioactive decay. The method requires a radioactive isotope in an excited nuclear state that decays via a γ - γ cascade. There is an angular correlation between the directions of emission of these two γ rays. For a nucleus isolated in vacuum the angle θ between the two directions is 180° . When the nucleus is placed in an environment of lower symmetry (solid or protein) the angular correlation is perturbed. The probability of detecting γ_2 in the direction given by θ is influenced by the electric field gradient (EFG) caused by the charges surrounding the nucleus.

Figure Perturbed Angular Correlation: The emission of γ_2 is not random with respect to the emission of γ_1 , on the contrary an Angular Correlation between the direction of emission of the two γ -rays exist.





^{111}In isotopes are implanted in Si and Ge host crystals. They decay by electron capture to an excited state of ^{111}Cd , which by a $\gamma-\gamma$ cascade decays to its ground-state. This makes the determination of the EFG possible via the Perturbed Angular Correlation (see Figure “Perturbed Angular Correlation”). From the experimental results the size and the symmetry of the electric field gradient felt by the decaying nucleus can be extracted. Details of the electronic and atomic structure of the defect causing the EFG cannot be determined directly.

This information can be obtained by *ab initio* calculations. We have used two complementary *ab initio* methods: the PAW-method is used to determine the correct local geometry and the all-electron Korriga-Kohn-Rostoker (KKR) Green-function method is used to calculate the electric field gradient (EFG) ([KR54], [HH03]).

The PAW-method is well suited for the calculation of the atomic and electronic structure of complexes in semiconductors. First, one can describe the localized d-levels of such a metal with a reasonable number of plane waves using the PAW method. Secondly, in the calculation a sufficiently large supercell can be constructed so that the interactions of the defects with those in the neighboring supercells are avoided so that isolated defects are simulated. The plane wave basis allows treating arbitrarily large displacements of the atoms from their ideal lattice positions.

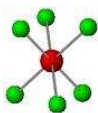
Cd-vacancy complexes

Two different configurations for possible Cd-vacancy complexes have been considered in the calculation: one is the Cd-substitutional-vacancy-complex and the other the Cd-split-vacancy-complex along to [111] direction. They have previously been suggested by the experimental groups ([HRS98], [FVP90], [FMW87], [DGR87], [Sie98], [ZSH97]). In our calculation to optimize the structure we use for the Si and Ge norm-conserving (KB-type) pseudopotentials and for Cd a PAW-pseudopotential. The detailed parameters of the pseudopotentials are presented in the Appendix „Parameters and Tests of the PAW-pseudopotentials“. The cutoff energy used in the calculations is 20.25 Ry ($G_{\text{max}} = 4.5 \text{ Ry}^{1/2}$). All the calculations are done using LDA for the exchange-correlation functional in a supercell containing 107 atoms with C_{3v}^1 symmetry (see Figure “Cd-vacancy complex 1”).

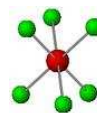
Decay of Cd-substitutional complex: A series of calculations have been performed where all the 7 atoms (Cd and its six nearest-neighbors) are allowed to relax. When the Cd atom is allowed to relax it moves towards the vacancy. The energy is continuously going down without any energy barrier until the final configuration is reached, where the Cd is sitting in the so-called “split”-vacancy configuration: the Cd is in a bond center position between two empty sites as shown in the Figure “Cd- vacancy complex 2”.

To obtain the energy difference of the Cd-split-vacancy and substitutional Cd-vacancy complexes we have optimized two configurations:

- (a) **Cd-split-vacancy complex:** In this starting configuration the Cd atom is placed in the bond center between two half vacancies and all 7 atoms (Cd and its 6 nearest-neighbors) are allowed to relax. The final configuration found is the same as obtained when starting from the Cd-substitutional complex and the Cd is relaxing to the bond center.
- (b) **Substitutional-Cd-vacancy complex:** In this configuration the Cd is fixed and only the 6 NN-atoms are allowed to relax.



Cd-VACANCY COMPLEX



The split-vacancy configuration is more stable by approximately 1.0eV for both hosts, Si and Ge. The instability of the substitutional-Cd-vacancy complex can be explained by the large size of the Cd atom. It is pushed by the three Si or Ge nearest-neighbors towards the vacancy (see Table “Cd-vacancy complex 1”). In the meantime we have found a similar behavior for the other oversized impurities (Sn, Sb, Bi) in Si and Ge [Ref. to be published].

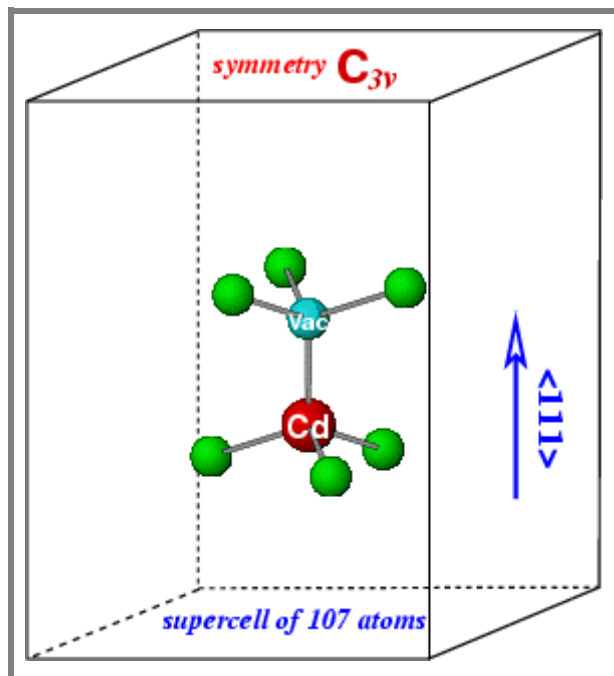
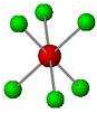


Figure Cd-vacancy complex 1:
Schematic picture of the supercell containing substitutional-Cd vacancy complex.

Table Cd-vacancy complex 1: The relaxations of Cd atom and nearest-neighbor atoms (the indices 1 or 2 represent the NN to the Cd and vacancy sites, respectively, and the relaxations are given in percentage of NN-distance of the host crystal).

bulk	Cd-vacancy 7 atoms relaxed	Cd-split vacancy 7 atoms relaxed	Cd-vacancy 6 atoms relaxed
Si	Cd-atom 50.00% NN-atoms 3.12%	Cd-atom 0.00% NN-atoms 3.12%	¹ NN-atoms outwards 4.30% ² NN-atoms inwards 5.73%
Ge	Cd-atom 50.00% NN-atoms 6.02%	Cd-atom 0.00% NN-atoms 6.03%	¹ NN-atoms outwards 4.89% ² NN-atoms inwards 8.34%

Our calculated relaxations for the Cd-split vacancy configurations are in good agreement with those of KKR-method, which gives relaxations of the NN-atoms of 4.2% in Si and 6.6% in Ge. The small differences between pseudopotential calculations and all-electron are due to the different description of the electron-ion interaction. They are of the same order of magnitude as in other instances (see Appendix “Parameters and Tests of the PAW-pseudopotentials”, Table “Cu(110) surface 1”).



Cd-VACANCY COMPLEX

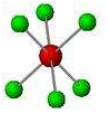
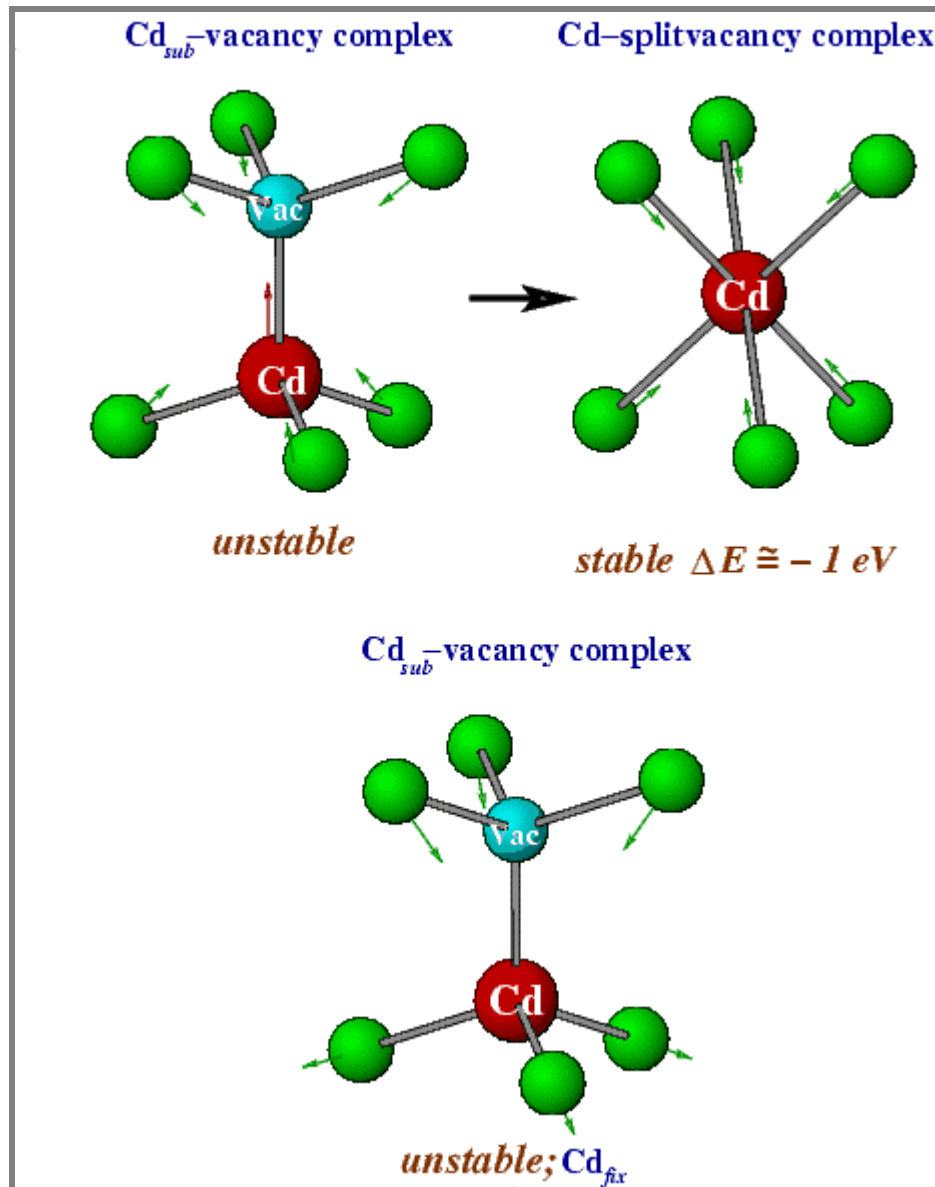


Figure Cd-vacancy complex 2: two schemes to relax the Cd- vacancy complex:

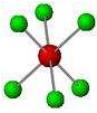
- upper panel the Cd is allowed to move (and the 6 NN-atoms).
- lower panel Cd is fixed in the (unstable) substitutional position.

The final stable configuration is the split-vacancy complex with the Cd in a bond center site.

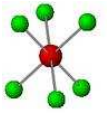


In the Figure “Cd-vacancy complex 3” we present the partial local density of states (PLDOS) at the Cd site for the relaxed configurations: (a) Cd-split vacancy and (b) Cd-fixed at the substitutional site in Ge bulk. According to a symmetry-adapted analysis the electronic structure of the Cd-split-vacancy-complex can be considered to derive from the divacancy [HH03]. Due to the presence of the Cd-atom dangling bond electrons at the Si (Ge) neighbors feel an attractive potential, and thus their energy is reduced. On the Cd atom one can see three effects:

- (1) For the split-vacancy configuration the large peak around -9.5eV is shifted by $\sim 0.2\text{eV}$ to higher energies compared to the substitutional-Cd complex. This shifting is due to the



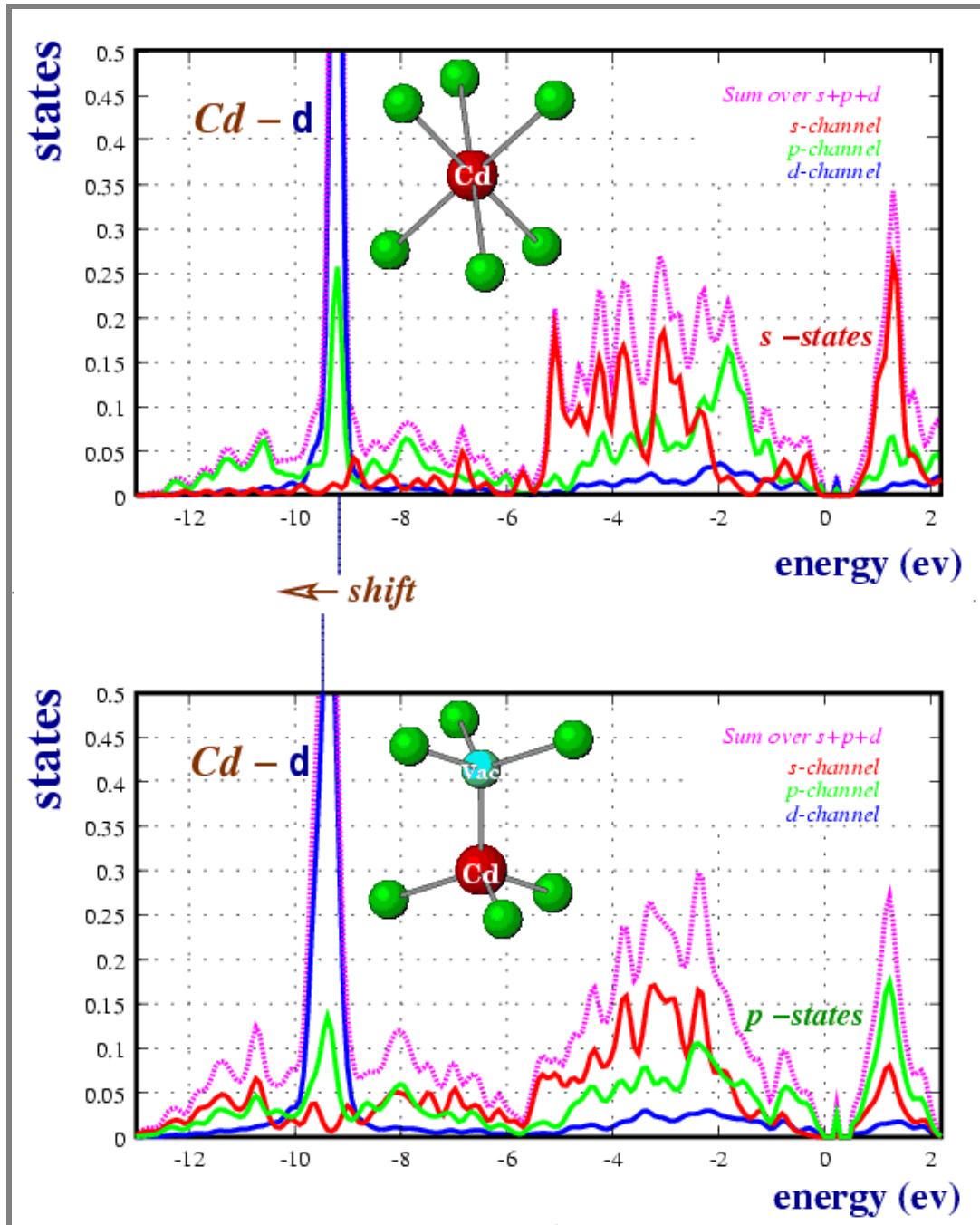
Cd-VACANCY COMPLEX



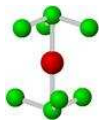
higher hybridization of **p** and **d** electrons for substitutional-Cd with the **s** and **p** electrons of Si/Ge nearest-neighbor atoms.

- (2) Reduction of the splitting of higher lying **p**-state.
- (3) Splitting of the **s**-level with an overall shift of the occupied **s**-states to lower energies.

Figure Cd-vacancy complex 3: The PLDOS at Cd site in Ge.



The split vacancy configuration has a higher symmetry D_{3d} . This explains also the small EFG measured for these Cd-vacancy complexes in Si and Ge. The calculated EFGs with the KKR formalism (27.99 MHz for Si and 55.69 MHz for Ge) is in very good agreement with the experiment allowing a unique assignment to the small measured EFG of 28 MHz in Si and 54 MHz in Ge. ([HH03], [HAS04])



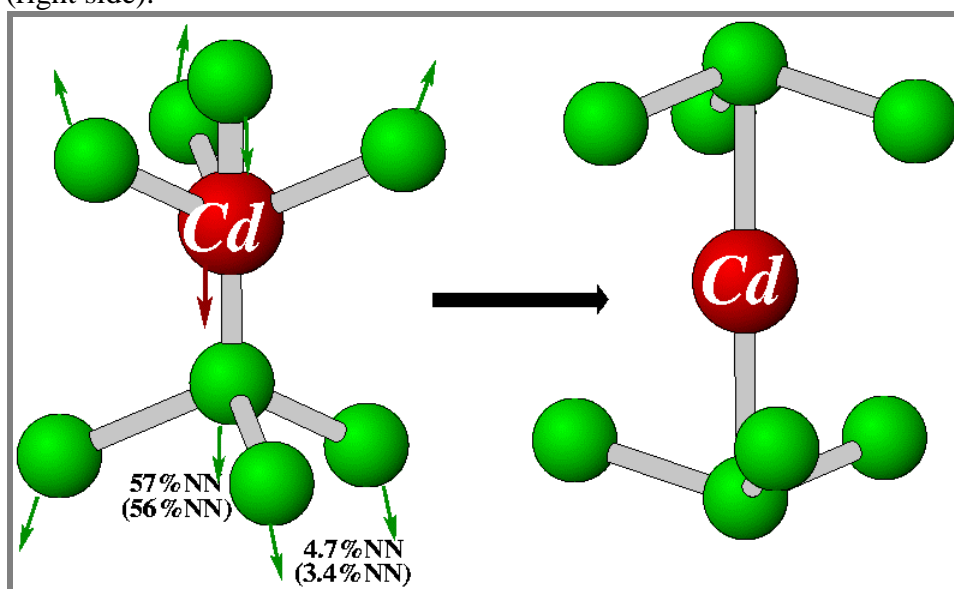
Cd-interstitial complexes

The Cd-interstitial complex is a possible candidate for the large EFG of 415 MHz measured by two groups in Ge ([HSZ98], [FVP90]). We have first studied the substitutional-Cd interstitial-complex: a self-interstitial on a tetrahedral site adjacent to a substitutional-Cd impurity.

In our calculation to optimize the structure we used the same pseudopotentials and basis set as before for the vacancy complexes. All the calculations are done using LDA for the exchange-correlation functional in the same supercell as for the vacancy complexes with C_{3v}^1 symmetry but this time containing 109 atoms.

To our surprise we found that this configuration is very unstable exhibiting a large force on the Cd atom. By relaxing this configuration the three adjacent atoms in the [111] direction, i.e. the self-interstitial, the Cd atom and the NN host atom in the [111] direction move more or less uniformly, until the Cd atom settles in the bond-center position and the two host atoms about halfway between the interstitial and the substitutional positions. In the final configuration (see Figure “Cd-interstitial complex 1”) the relaxations of the first NN-atoms are of 4.7 %NN, and for the NN-atoms along to [111] direction 57%NN from the ideal substitutional site. (the KKR relaxations are of 3.4%NN and 56%NN).

Figure Cd-interstitial complex complex 1: The Cd-interstitial complex with the Cd on the substitutional site (left side) leads after relaxation to the symmetrical complex with Cd on the bond center and two host atoms shifted halfway between the substitutional and interstitial positions (right side).



For Ge the calculated EFG of -415 MHz [HH03] for the symmetrical Cd-split-interstitial-complex agrees well with the experimental value of ± 395 MHz assigned by Haesslein et. al. to a Cd-interstitial complex ([HSZ98]).



Chapter 6

Formate on Cu(110) surface

6.1 Introduction

Most of the important chemical reactions in nature and technology take place at surfaces and interfaces. There are a vast number of economically important processes, which rely on these reactions, such as catalysis in chemical production, corrosion, the fabrication of computer chips, magnetic storage on computer disks and the behavior of biomaterials. A large effort is made to obtain an atomic based picture of chemical interactions and reactions at the surface. The first question refers to the identification of the molecular species and the atomic positions. The next step is the understanding of the reasons why the atoms are located the way they are and why certain atom groups are more reactive than others. The answers are directly related to the electronic structure and how the bonds are formed.

The adsorption of formic acid on copper single crystal surfaces, in particular Cu(110), has attracted considerable attention due to the identification of formate as a key stable intermediate in methanol synthesis which is carried out commercially using copper based catalysts [Wau92].

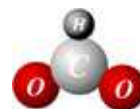
Recent developments have enabled the field of surface science to progress from the study of simple adsorbates to the investigation of bigger and more complicated molecules, e.g. organic acids and aminoacids. The carboxyl group is known to be an anchoring group used by molecules to chemically bind on the surfaces [Rav03, BR03]. From the theoretical point of view, in a first step one should understand the binding to the surface of the simplest molecule that contains the carboxyl group, which is the formic acid, and then proceed to more complex molecular structures.

Experiments have studied formic acid adsorption on both clean and oxygen precovered surfaces of copper. At elevated temperatures (300-450°C) formate molecules are chemically adsorbed at the Cu surface by dehydrogenation (clean surface; see Figure “Formate on Cu(110) 1”) or release of water (oxygen precovered surface) [Lei94]. To determine the formate adsorption structures, several experimental methods have been used: near-edge X-ray-absorption fine spectroscopy (NEXAFS), surface extended X-ray-absorption fine structure (SEXAFS), low-energy electron diffraction (LEED), Auger electron spectroscopy, temperature programmed desorption (TPD), scanning tunneling microscopy (STM), reflection-absorption infrared spectroscopy (RAIRS) and in-situ infra-red reflection-absorption spectroscopy (IRAS) ([PHC85], [LEI94], [PBJ97], [SPB98], [SPP99]).

With some of the experimental methods it was difficult to determine how the formate molecules are chemisorbed on the copper surface, in an upright or tilted geometry, or if they are bound in a bidentate or monodentate geometry (for the monodentate case the oxygen forms a single bond with a copper atom, for the bidentate geometry the oxygen atoms are bound to the copper atoms). Only NEXAFS and SEXAFS have suggested specific geometries: the molecules are adsorbed with their molecular plane perpendicular to the metal

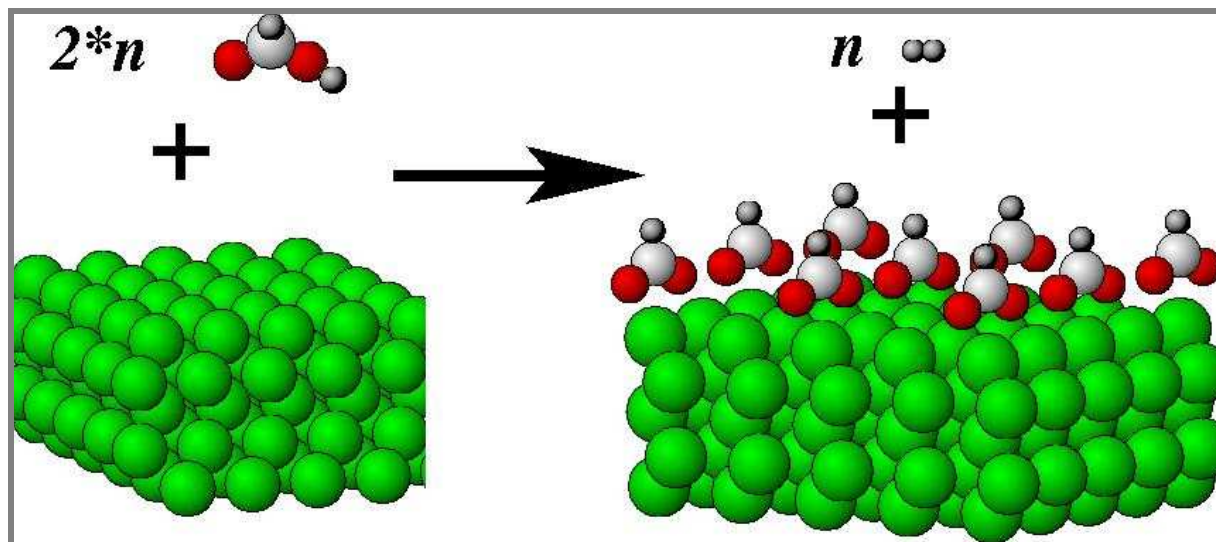


FORMATE ON Cu(110) SURFACE



surface. The molecules are arranged in rows with the plane formed by the carboxylic group along the $[1\bar{1}0]$ direction [PHC85].

Figure Formate on Cu(110) 1: On the clean copper surfaces only dehydrogenation of formic acid is observed (Cu-green, O-red, C-gray, H-dark grey).



Experiments suggested that the formate molecules are forming a (2x2) structure on the Cu(110) surface. At low coverage there is just one molecule in the unit cell whereas at high coverage the unit cell contains two molecules. On the clean surface, at high coverage, the formate molecules are forming short domains and to some extent they are randomly distributed. It is assumed that there are repulsive intermolecular interactions between the molecules in the $[100]$ direction that increases their mobility at the surface. This prevents the observation of an ordered LEED pattern or clearly interpretable STM image [PBJ97].

Some experiments suggested that the single oxygen atoms are sitting on top of the copper surface atoms, but SEXAFS analysis suggested that the oxygen atoms are on bridge positions binding two Cu atoms [PHC85, PBJ97].

According to the experiments the clean surface formate structure has similarities to the (2x2) formate structure that has been reported for the formic acid adsorption on the 0.5ML oxygen precovered copper surface (this means that before formic acid adsorption there are two oxygen atoms in the (2x2) unit cell). In the last case the (2x2) formate structure can be imaged with STM with good resolution indicating that the formate molecules are much more localized than on the clean surface. It seems that the repulsive interaction between the molecules can be overcome in the case of the oxygen-precovered surface. The higher formate coverage is enforced through the energetically favorable reaction of formic acid deprotonation by the preadsorbed oxygen [PBJ97, PJB97]. In this case the carboxylic hydrogen leaves the surface not as H_2 but rather as H_2O (one additional O atom per (2x2) unit cell remains, i.e. 0.25ML).

For the adsorption geometry of formate on Cu(110) a series of theoretical calculations using ab initio density functional theory as well as semiempirical methods have been reported in the literature. All of them are based on the cluster approach: a cluster of 8 up to 10 copper atoms is used to model the metal surface where the copper atoms are kept at their ideal bulk positions. These methods take into account just one formate molecule on the surface, and they describe well only the local structure of the molecule-metal surface system at very low



FORMATE ON Cu(110) SURFACE



coverage. With these methods no information concerning the intermolecular interactions can be obtained.

In the present work several geometries, corresponding to different coverages, for the adsorption of the formate on Cu(110) are optimized using the supercell approach. The results obtained with this method can be compared with the cluster approach at low coverage. The supercell approach has the advantage of a better simulation of the real system because it can take into account a real infinite surface and also includes the steric interactions between the molecules when the coverage increases.

A series of additional calculations have been performed to check our method. First, we have optimized the structure of the formate (free radical) molecule and the structure of the (1x1) copper Cu(110) surface. The obtained results are comparable with the other theoretical data reported in the literature and with the experimental results [GG99, PLH04, RYB95]. Then we have used these relaxed coordinates of the molecule and copper surface as starting positions in the molecule-surface calculations. The obtained results are discussed on the next pages.

We first discuss the structure (bond length and bond angles) of the free formate radical, as well as its electronic structure. Then, we discuss the adsorption geometry of formate on Cu(110)-surface with low coverage (1 formate molecule per (2x2) unit cell), and with high coverage (2 formate molecules per (2x2) unit cell), with and without additional oxygen.

We found that in the most stable structures the formate is always sitting perpendicular to the Cu(110)-surface, and it is adsorbed in a bridge position (the O-C-O group forms a bridge between two Cu atoms). Other tested configurations are less stable by at least 0.9 eV per formate molecule.



6.2 Formate free radical

The electronic and geometrical structure of the formate radical has been optimized using the PBE-GGA functional for the exchange-correlation. The molecule has been placed in a cubic box with $a = 8.5$ Å. The exact parameters of the pseudopotentials (for C, O) used are given in the Appendix “Parameters and Tests of the PAW-pseudopotentials”. Several calculations have been done using gamma point and different k-point sets (up to $3 \times 3 \times 3$) with or without C_{2v} symmetry. Taking into account the symmetry, the results are the same for all the k-point sets. The bond lengths and O-C-O-angle are given in the Table “Formate 1”. They agree well with the other theoretical data for the formate radical that have been reported in the literature [GG99, PLH04].

Table Formate 1: the bond length and O-C-O angle for free formate radical.

bond length/angle	this work	Ref-[GG99]	Ref-[PLH04]
CH	1.140	1.095	1.100
CO	1.247	1.261	1.257
OCO	110.87 ⁰	111.6 ⁰	111.2 ⁰

Electronic Structure

In order to understand the bindings in the formate molecule in a simple picture one can view the carbon atom as sp^2 hybridized. It has three simple σ bonds with the hydrogen and the two oxygen atoms, and a p_z orbital perpendicular on the O-C-O plane. Each of the oxygen atoms has a p_z orbital perpendicular to the plane formed by the simple σ bond to the carbon and the two lone electron pairs. Each p_z orbital of the carbon and oxygen atoms is occupied with one electron. The p_z orbital of the C is formally forming two half π -type bonds with the oxygen atoms (each having a p_z orbital occupied with one electron). Since the two half π -type bonds need two electrons (one will be taken from the carbon and the other from the oxygen atoms), the two oxygen atoms will share an extra p_z electron. As a result each oxygen atom is rich in valence electrons. Formally, the redistribution of the oxygen valence electrons is as follows: one part of them are forming a simple σ bond and a half π -bond with the C, and another part represents the two lone electron pairs and one half of the shared p_z electron. These last ones are involved in the bonding to the Cu(110) surface.

The Partial Local Density of States (PLDOS) (see Anhang D in [Kro01]) on a sphere (with the radius half of nearest-neighboring distance) around each atom has been calculated in order to understand and explain the electronic structure of isolated formate radical (see Figure “Formate 2”). Our calculated electronic levels reproduce those reported in the literature for the free formate radical ([FHB83], [RC87], [BD87], [BD88], [KFL65]). The electronic distribution and decomposition of the molecular orbitals as analyzed in the mentioned papers ([FHB83], [RC87], [BD87], [BD88]) is shown in Figure “Formate 3”. The lower level at -23.5 eV corresponds to the $3a_1$ level and the highest one to the $4b_2$ level (0.0 eV). There are two nearly degenerate levels: $3b_2$ and $1b_1(\pi)$ (-5.0 eV). The PLDOS project the molecular wave function into s- and p-type contributions at the site of the each atom. We will start our discussion with the highest occupied levels.

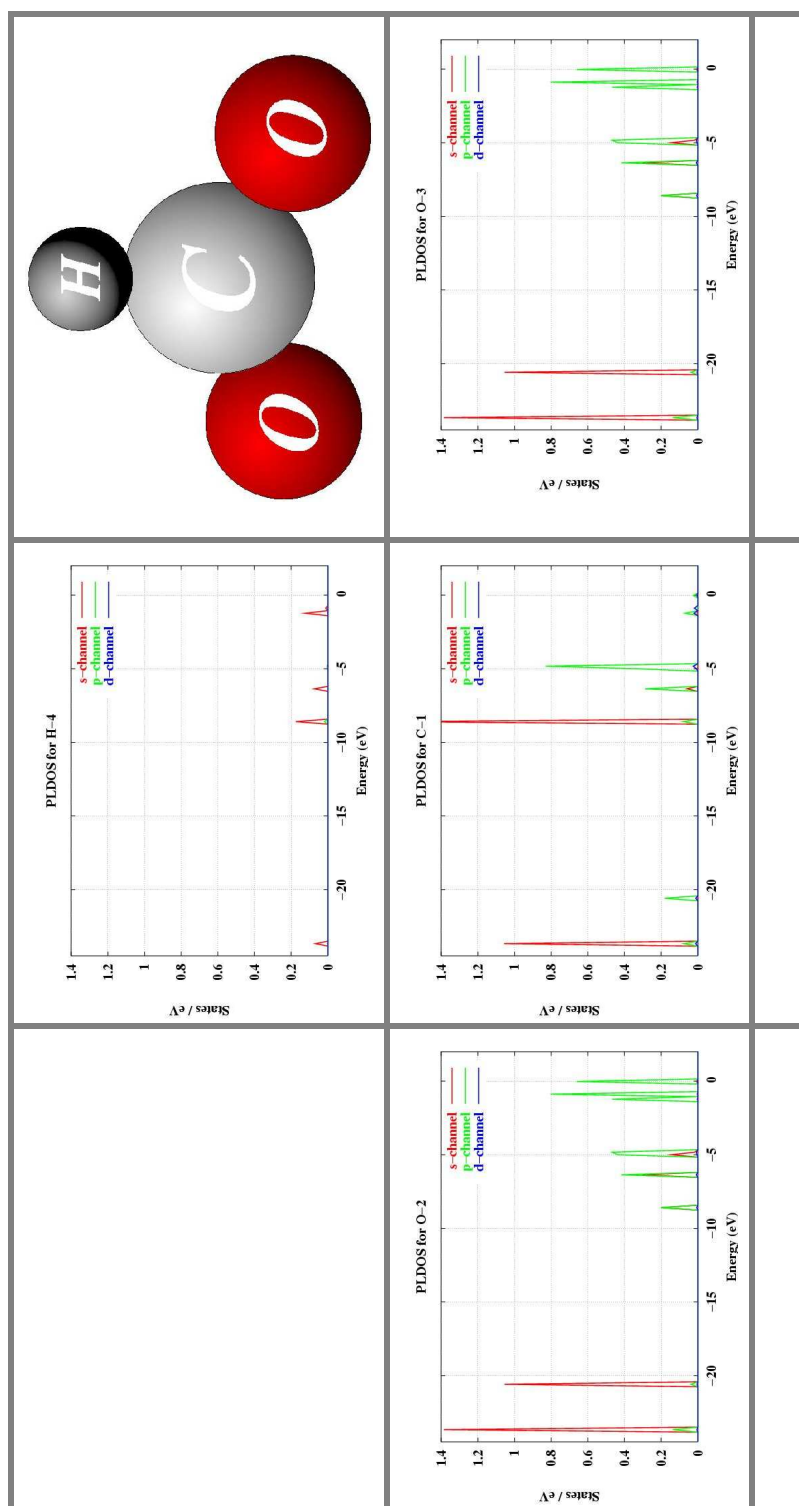


FORMATE FREE RADICAL



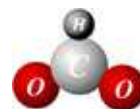
The weakly bounded p-type electrons with the characteristic energy levels at -1.0eV, -0.5eV, 0.0eV and corresponding to the $4b_2$, $6a_1$, $1a_2$ levels in molecular orbital picture are mostly located at the oxygen atoms. The electrons that correspond to these states will participate in the binding to the copper surface. The PLDOS of C, O atoms show 4 peaks, at -5.0 (two nearly degenerate ones), -7.5 and -8.5 eV energy levels, with the corresponding molecular orbitals $3b_2$, $1b_1(\pi)$, $5a_1$ and $4a_1$. The electrons corresponding to these peaks have intensities at all atoms. They represent the binding electrons between the molecules' atoms.

Figure Formate 2: Partial local density of states of the formate molecule (free radical)





FORMATE FREE RADICAL



The oxygen atoms have characteristic localized s-type states at -23.5 and -21.0 eV corresponding in a molecular orbital picture to the $3a_1$ and $2b_2$ states. In our PLDOS for the C atom we find some intensity for the $3a_1$ level. Since we integrate over a sphere whose radius is half of the bond length around the C atom we cut through electron distribution corresponding to the $3a_1$ level (see Figure “Formate 3”).

	(i)	(ii) (only the p-orbitals are shown)
$4b_2$		
$6a_1$		
$1a_2(\pi)$	-	
$3b_2$		
$1b_1(\pi)$	-	
$5a_1$		-
$4a_1$		-
$2b_2$		-
$3a_1$		-

Figure Formate 3: Electron distribution and schematic representation of the valence molecular orbitals in the isolated formate radical. The $3a_1$ level is the lowest in energy and the $4b_2$ is the highest one. The $3b_2$ and $1b_1(\pi)$ are degenerate.

(i) Orbital contours enclose 90, 70, 50, 30 and 10% of the probability density as shown in ref. [FHB83] (C-H define the z-axis, the oxygen atoms the y-axis and perpendicular to this plane is the x-axis).

(ii) Rough picture of the atomic orbitals and their sign some at C and O site (only the p-orbitals are shown). With respect to the molecular (y-z) plane, the $1b_1$ and $1a_2$ are the π -orbitals. They are formed by linear combinations of the $2p_x$ orbitals of carbon and oxygen. The $3b_2$, $4b_2$ and $6a_1$ are the σ -orbitals. They are the product of linear combinations of the 1s orbital of the hydrogen ($6a_1$) and the 2s, $2p_y$, and $2p_z$ orbitals of carbon and oxygen ($3b_2$, $4b_2$, $6a_1$) [RC87], [BD87], [BD88].



6.3 Formate-Cu(110) surface systems

All GGA calculations of formate molecules adsorbed on Cu(110) surface have been performed using an inversion symmetric slab containing five copper layers. The unit cell has the dimensions $4 \cdot a \cdot \sqrt{2}$ (perpendicular to the surface), and $2 \cdot a$, $a \cdot \sqrt{2}$ (parallel), with $a = 3.641 \text{ \AA}$ being the bulk lattice constant of the copper-fcc. An energy cutoff of 25 Ry ($G_{\text{max}} = 5.0$) and a 1x3x4 k-point set have been used.

In the case of low coverage, one molecule in (2x2) unit cell, two of the most probable configurations have been optimized. In one configuration the oxygen atoms are sitting on top of the copper surface atoms. This is the so-called bridge position (the C atom is a bridge between two Cu atoms) where each of the oxygen atoms is forming one single bond with a copper atom. In the second configuration the molecule is bound in a so-called top position (C on top of a Cu atom) where each of the oxygen atoms is sitting on the surface between two copper nearest-neighbor atoms (see Figure “Formate-Cu(110) system 1”).

For high coverage on the clean surface, where two molecules are present in a (2x2) unit cell, three different configurations can exist: one with both molecules in bridge position, another one with both molecules in top position, and a third configuration with one molecule in the bridge position and the other one in top position (see Figure “Formate-Cu(110) system 2a and 2b”).

In the case of the oxygen precovered Cu(110) surface with two formate molecules in the (2x2) unit cell, the oxygen atom of the 0.25 monolayer (ML) has been placed in a hollow site (between four copper atoms of the first layer and on top of a copper atom of the second layer). In this case four configurations are possible at the metal surface. One contains both molecules in bridge position and another one has both molecules in top position. For these configurations all hollow sites of the copper surface in the unit cell are equivalent (see Figure “Formate-Cu(110) system 3a”). In the case when one molecule is in bridge position and the other one in top position there are two non-equivalent positions of the oxygen atom relative to the copper surface and formate molecules (see Figure “Formate-Cu(110) system 3a”).

In all calculated structures the molecules and the first two layers have been allowed to relax without any constraint. In the starting configurations the positions of the copper atoms are corresponding to those of the optimized (1x1) unit cell of the copper (110) surface. For the molecules the relaxed atom positions of the formate free radical have been used as starting positions.



FORMATE-Cu(110) SURFACE SYSTEMS

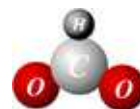
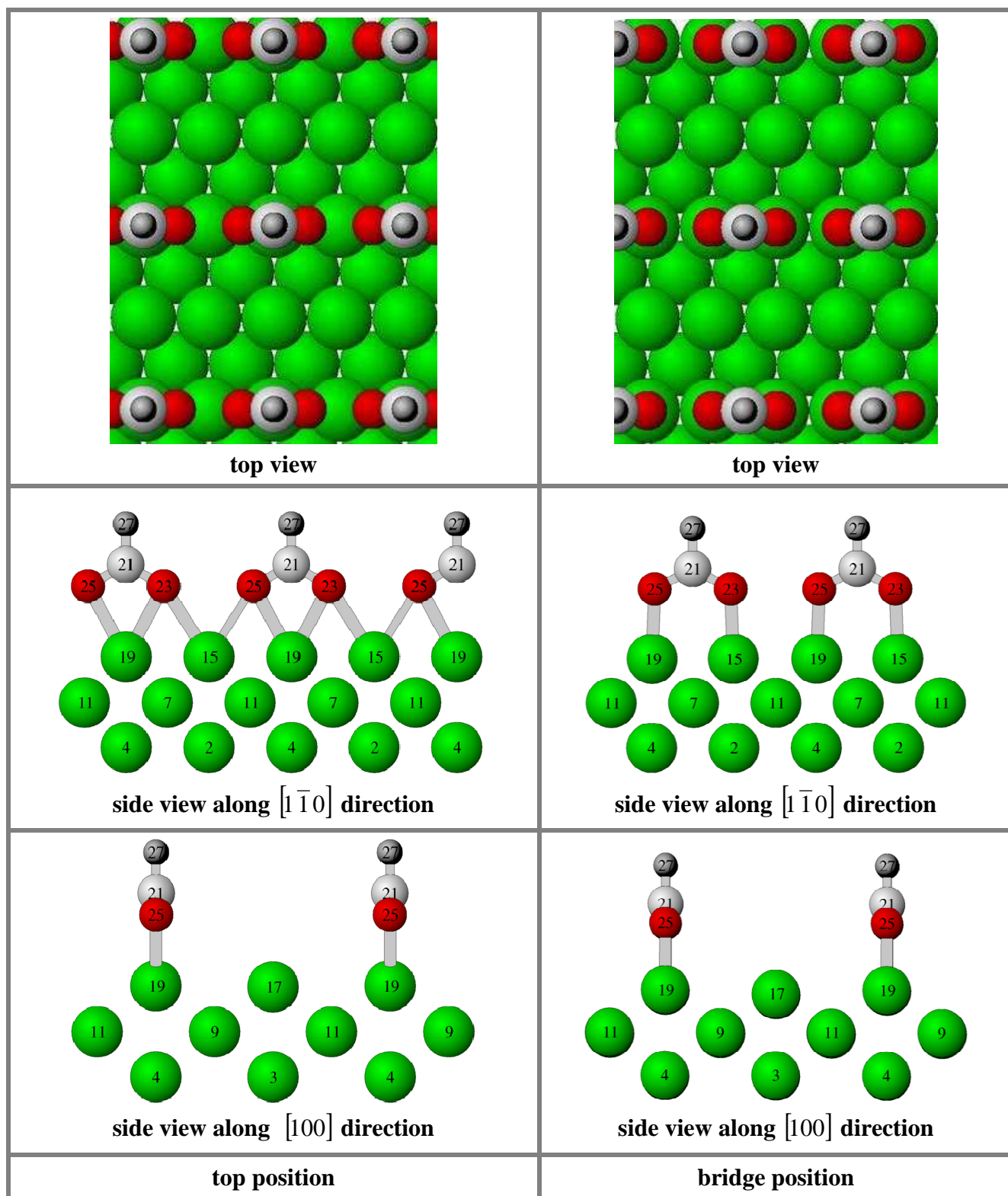


Figure Formate-Cu(110) system 1: Adsorption geometry of one formate molecule in (2x2) unit cell on a clean Cu(110) surface: left-side the top position (C on top of Cu) and right-side the bridge position (C on bridge) (Cu-green, O-red, C-gray, H-dark grey).





FORMATE-Cu(110) SURFACE SYSTEMS

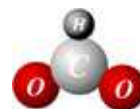
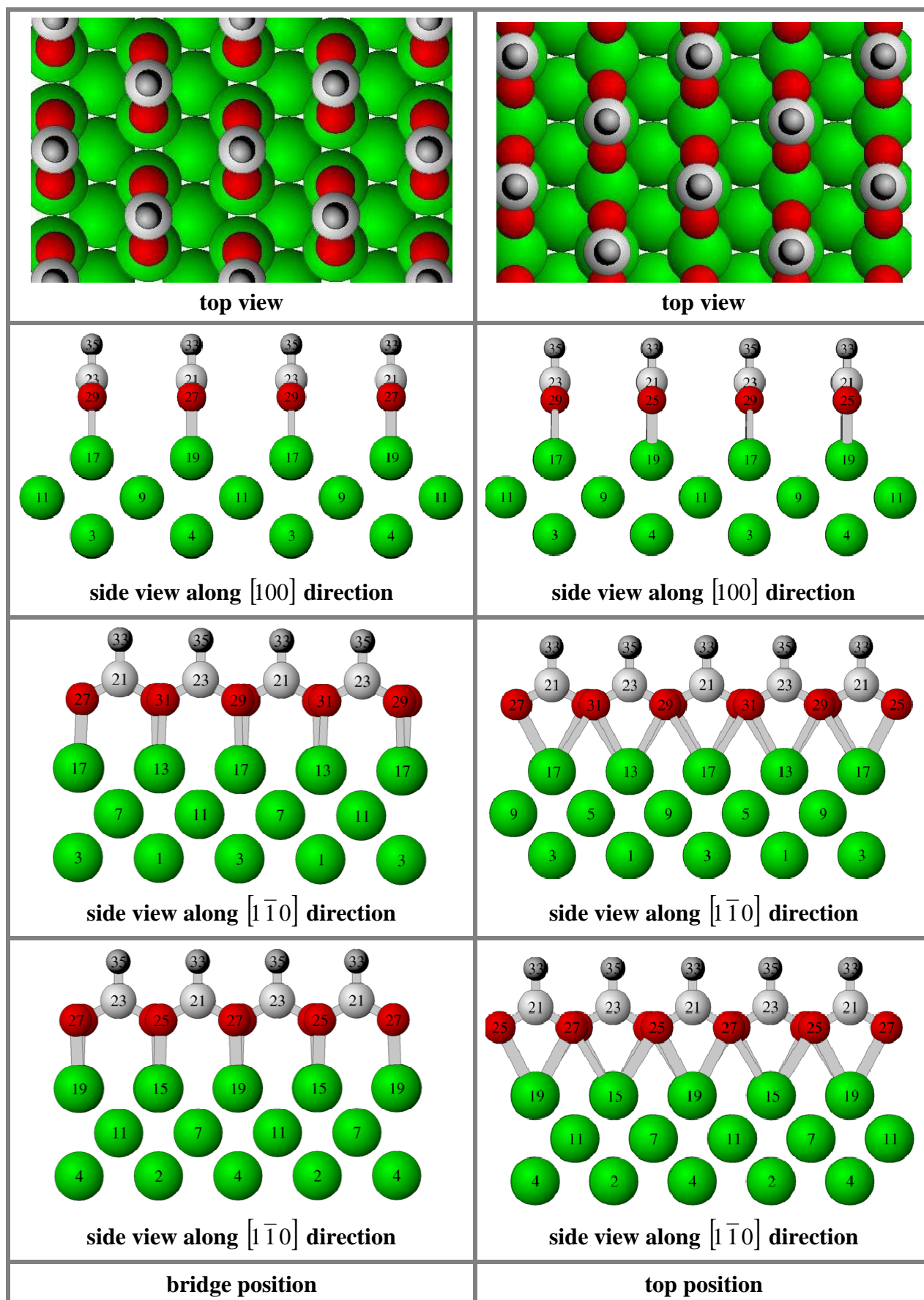


Figure Formate-Cu(110) system 2a: Adsorption geometry of two formate molecules in a (2x2) unit cell on the clean surface (both molecules are either in bridge or in top positions).





FORMATE-Cu(110) SURFACE SYSTEMS

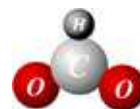
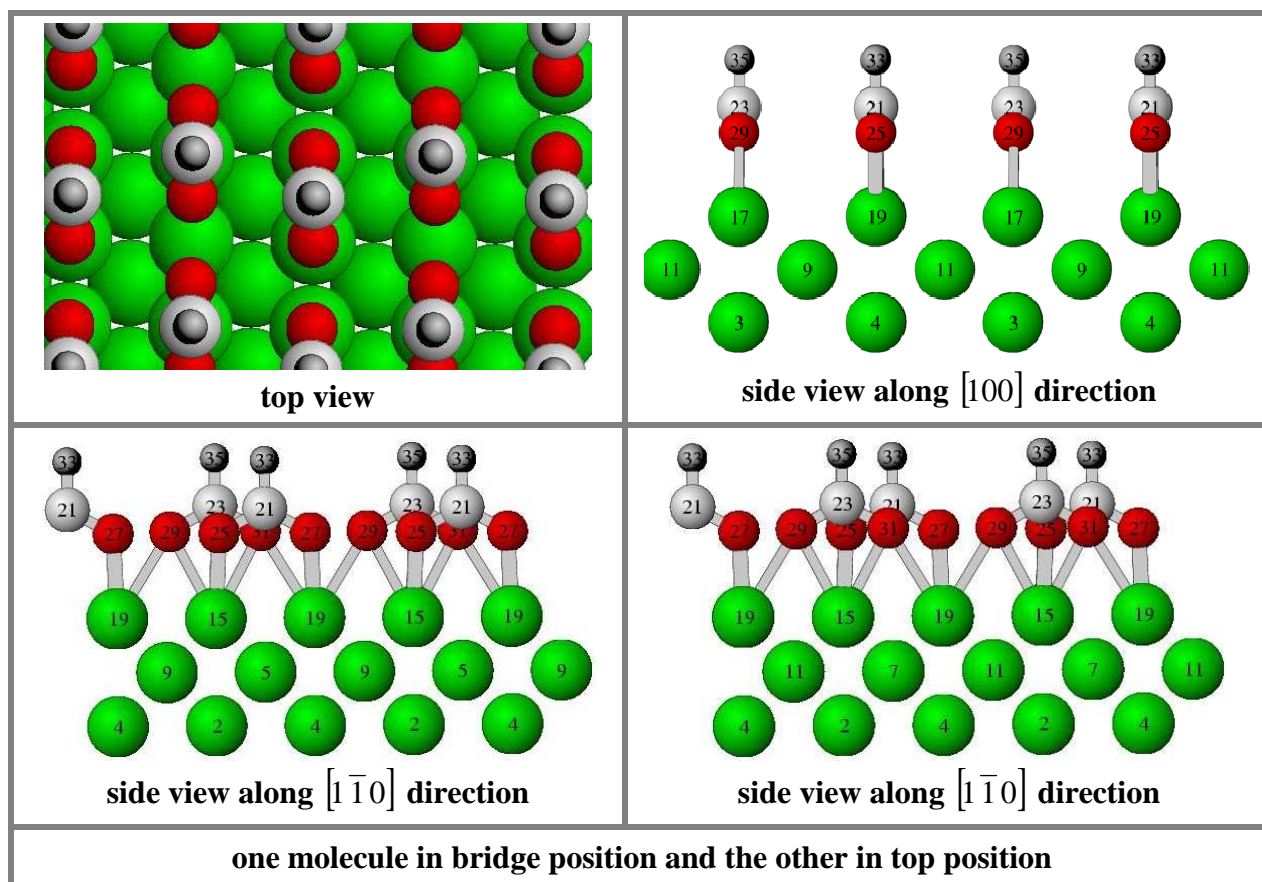


Figure Formate-Cu(110) system 2b: Adsorption geometry of two formate molecules in a (2x2) unit cell on the clean Cu(110) surface, one molecule in bridge and the other one in top positions (Cu-green, O-red, C-gray, H-dark grey).





FORMATE-Cu(110) SURFACE SYSTEMS

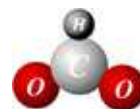
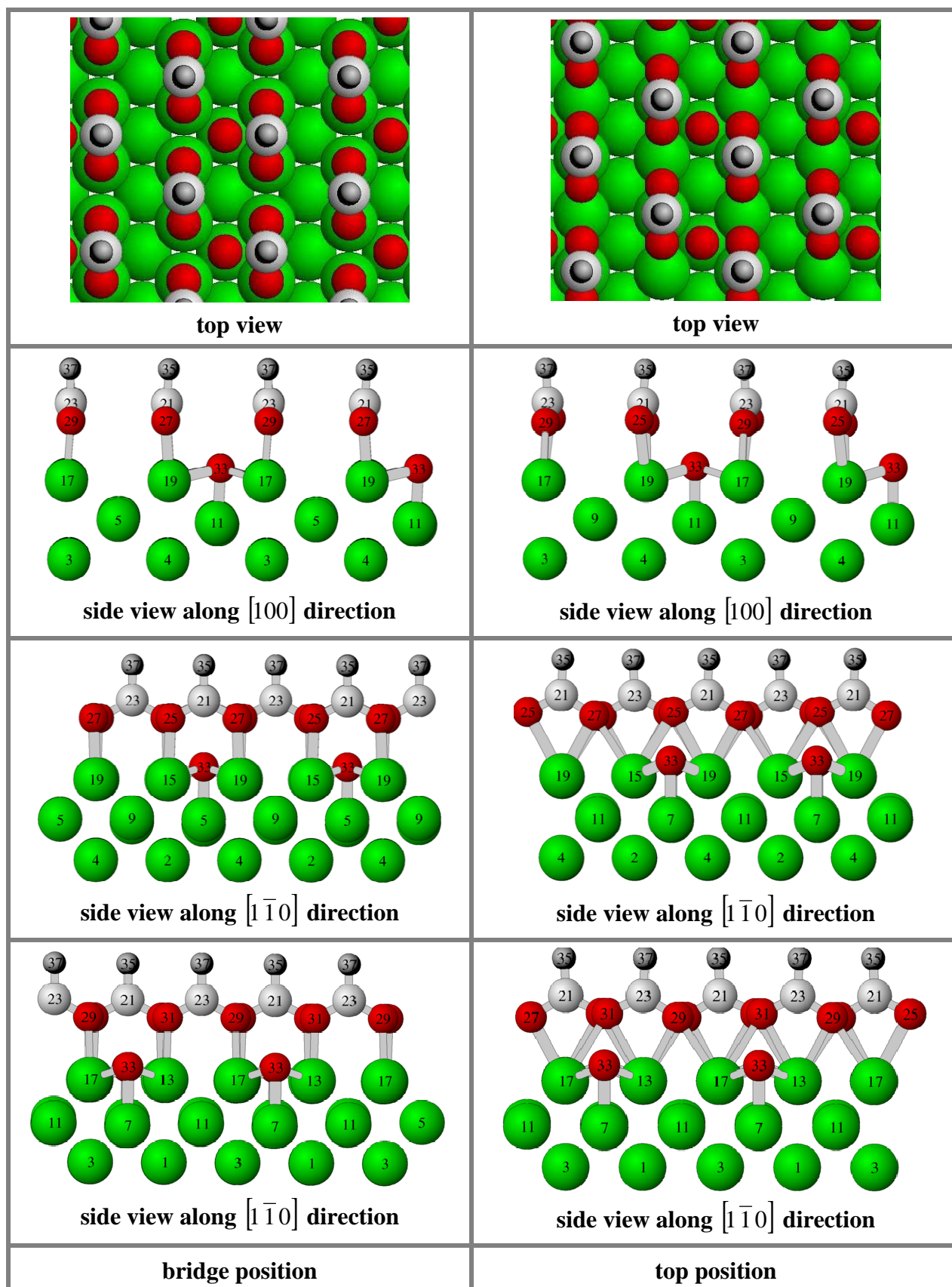


Figure Formate-Cu(110) system 3a: Adsorption geometry of two formate molecules and an oxygen atom in a (2x2) unit cell (0.25ML oxygen precovered surface). Both formate molecules are in equivalent positions (bridge or top) (Cu-green, O-red, C-gray, H-dark grey).





FORMATE-Cu(110) SURFACE SYSTEMS

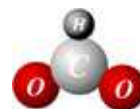
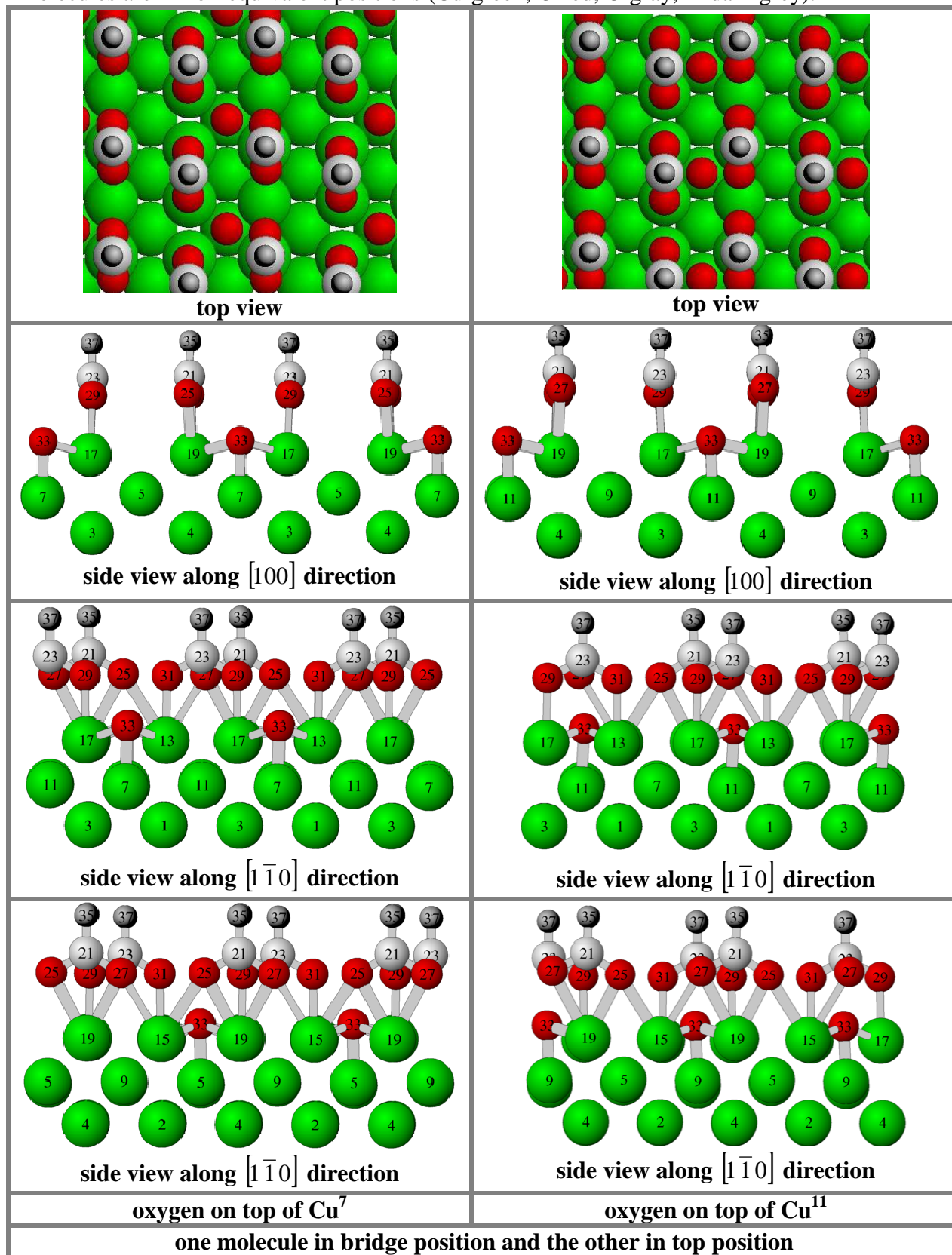


Figure Formate-Cu(110) system 3b: Adsorption geometry of two formate molecules and an oxygen atom in a (2x2) unit cell (0.25ML oxygen precovered surface). The two formate molecules are in non-equivalent positions (Cu-green, O-red, C-gray, H-dark grey).



The relative energies of all configurations and the bond lengths in the calculated configurations are presented in the next tables. The Cu-O distances larger than 3Å are not



listed. A general observation is that in all calculated configurations (for different coverages of the formate molecules) the most stable ones contain the molecules only in bridge position with each oxygen binding to one Cu atom.

6.4 “Low formate coverage”

Atomic structure and energetics

At low coverage (one molecule per unit cell) the bridge position is with 0.92 eV more stable than the top position. This is explained by the stronger interaction of the oxygen and copper atoms since in the bridge position the distances O-Cu are much smaller. The oxygen atoms are bound to the surface in a monodentate geometry (each oxygen of the carboxylic group binds to a single copper atom). Due to the copper-oxygen interaction for both configurations the O-C-O angle is larger than for the single formate free radical (128.4° for bridge, 125.3° for top, 110.8° for free radical).

Table Formate-Cu(110) system 1: Bond lengths and relative energies for one formate molecule in (2x2) unit cell (For the numbering of the atoms we refer to Figure “Formate-Cu(110) system 1”).

bond length (Å)	bridge	top	Interlayer relaxations (% relative to the ideal)	bridge	top
C ²¹ -H ²⁷	1.141	1.146	Cu ¹³ -Cu ¹¹	-10.06	-2.02
C ²¹ -O ²³	1.321	1.324	Cu ¹⁵ -Cu ¹¹	-0.85	0.37
C ²¹ -O ²⁵	1.321	1.324	Cu ¹⁷ -Cu ¹¹	-10.06	-1.95
O ²³ -Cu ¹⁵	1.994	2.441	Cu ¹⁹ -Cu ¹¹	-0.84	0.32
O ²³ -Cu ¹⁹	-	2.434	Clean Cu(110) surface	-11.00	
O ²⁵ -Cu ¹⁹	1.994	2.320			
O ²⁵ -Cu ¹⁵	-	2.314	Relative total energies (eV)	0.00	0.92
O ²³ C ²¹ O ²⁵ angle	128.41 ⁰	125.32 ⁰			

The relaxations of the copper atoms of the first layer are quite different depending if Cu-O interactions exist or not. For the bridge position of the molecule the copper atoms that are not binding directly to the oxygen atoms show similar inward relaxations as on the clean Cu(110) surface. In contrast, the relaxation of the copper atoms that are forming the bonds with the oxygen atoms is very small, the positions of these atoms are close to unrelaxed ideal surface positions. In the top position each oxygen atom of the molecule forms bonds with two nearest-neighbor copper atoms, the relaxations of the copper atoms are quite small, the positions of the copper surface atoms are close to the ideal unrelaxed (110) surface.

Electronic structure

The electronic structure of the configuration with the molecule in bridge position is analyzed with the help of the Partial Local Density of States, PLDOS (see Figure “Formate-Cu(110) system 4a and 4b”). The inner Cu-atoms (Cu¹, Cu², Cu³, Cu⁴) have the bulk characteristics with the d-band (and some p-states) in the energy interval of -5.0...-2.0 eV. Most s-type states appear at a lower energy interval -8.5...-4.5 eV.



FORMATE-Cu(110) SURFACE SYSTEMS

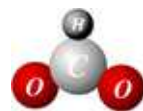
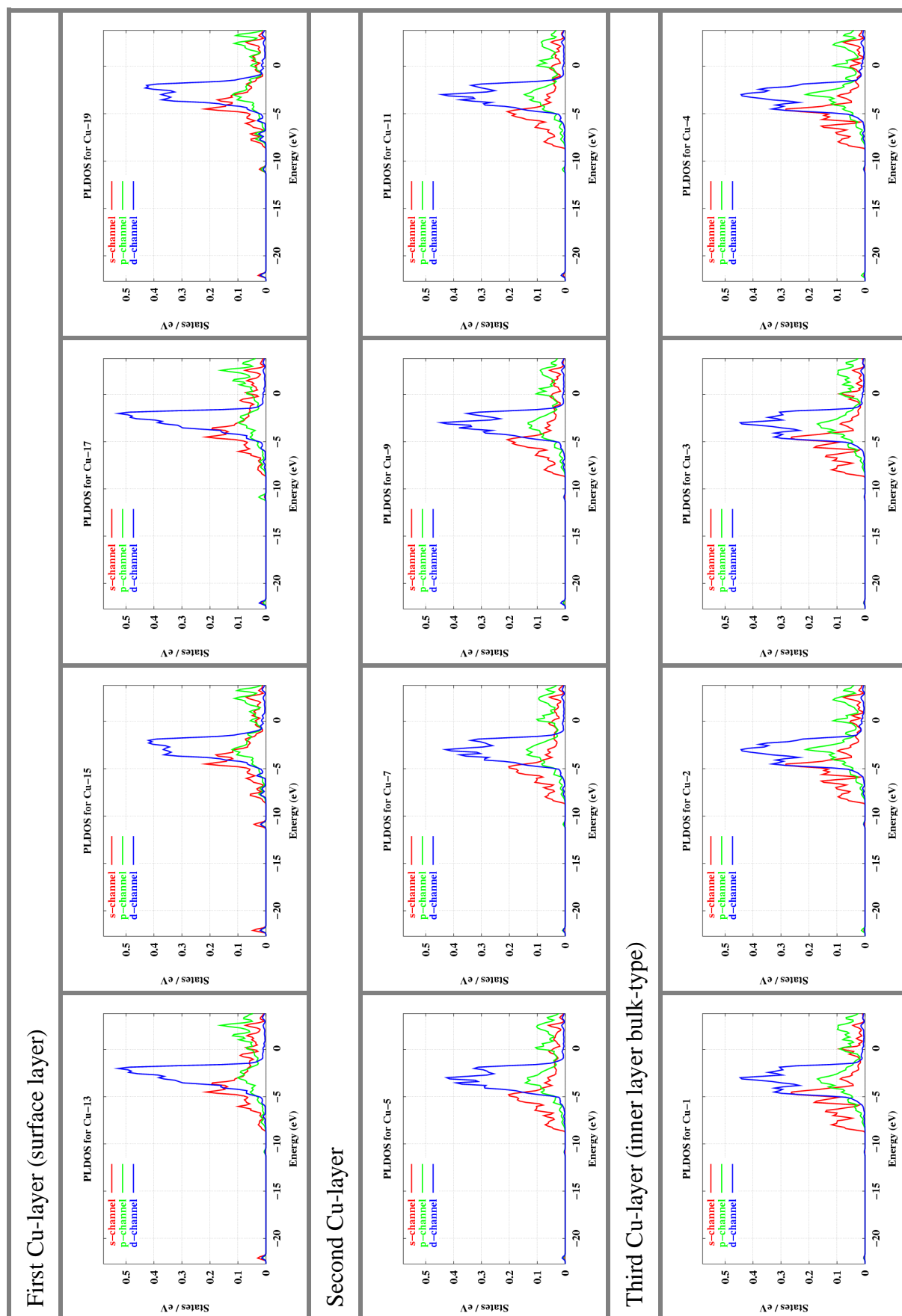


Figure Formate-Cu(110) system 4a: The PLDOS of the Cu-slab atoms for the supercell containing one formate molecule in (2x2) unit cell on a clean Cu(110) surface

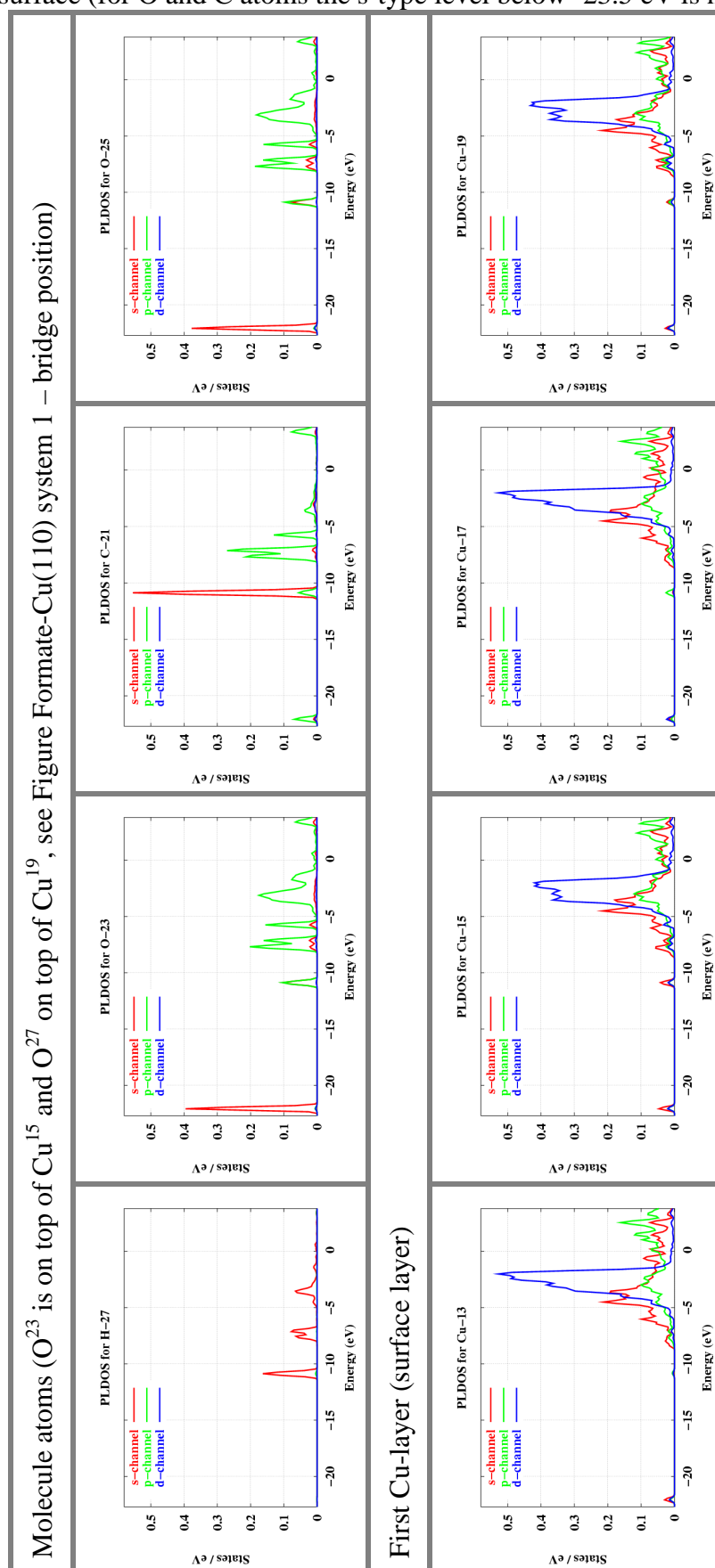




FORMATE-Cu(110) SURFACE SYSTEMS



Figure Formate-Cu(110) system 4b: The PLDOS of the Cu outermost surface atoms and formate molecule atoms the system containing one formate molecule in (2x2) unit cell on a clean Cu(110) surface (for O and C atoms the s-type level below -23.5 eV is not shown).





For the next surface layer, the atoms Cu⁵, Cu⁷, Cu⁹, Cu¹¹, the d-band is narrowing (energy range from -4.5... -2.0 eV). This behavior is due to the smaller coordination number of these atoms. The Cu-surface atoms show distinct characteristics: copper atoms, Cu¹³ and Cu¹⁷, that are not forming direct bonds with the oxygen atoms of the formate molecule have the same characteristics as copper surface atoms on the clean surface: a high but narrow d-band in the energy range of -4.0...-1.8 eV (see Appendix “PLDOS for clean Cu(110) surface”). The shape of the d-band of the Cu¹⁵ and Cu¹⁹ (that are binding the O²³ and O²⁵) is different. The analysis of the PLDOS for the molecule atoms show that the binding levels in the molecule are located in the energy range from -11.0 to -5.0 eV. The oxygen atoms show as in the isolated molecule the s-type localized states below -22.5 eV. The Cu-O bindings, via p-type states of oxygen atoms and the d-type states of the copper atoms, are in the energy range -4.0...-1.8 eV. In this interval the oxygen atom shows a specific high p-type peak at -3.0 eV.

Comparison to literature

The molecular geometries and the Cu-O bonds calculated in this work agree well with the theoretical results reported in the literature [GG99, PLH04, Bec93] and the experimental data [LCK98]. The theoretical results in the literature are for the bridge position of a simple formate molecule using the cluster approach and Density Functional Theory (DFT), Restricted Hartree-Fock (RHF) and semiempirical theoretical approaches [GG99, PLH04,]. In the reported DFT calculation a localized basis set has been used and B3LYP hybrid functional for the exchange correlation [Bec93].

In the literature, there are experimental data and theoretical calculations for other organo-metallic complexes of Cu⁺ with formic acid and diformate molecules. In these complexes the oxygen atoms bind in monodentate geometry to the copper atoms. It is shown that the Cu⁺-O attractive interaction is very strong with the Cu-O bond length being 1.910 Å for the diformate molecule and 1.958 Å for the formic acid [JD01, HO97]. The reported Cu-O bond length is close to our calculated Cu-O bond length (1.994 Å) for the bridge position of formate molecules on the Cu(110) surface. It is generally accepted that Cu-O distances of 1.91 up to 2.0 Å correspond to strong Cu-O interaction. In our system, the binding of the oxygen atoms to the Cu surface atoms leads to an outward relaxation of the copper atoms from their relaxed positions of the clean surface.

6.5 “High formate coverage”

We present the details of the formate arrangements for high coverage in two tables.

- (a) intramolecular bond lengths and bond angles and atomic distances in the Cu surface
- (b) Cu-O bond lengths and relative energies.

For the numbering of the atoms we refer to Figures “Formate-Cu(110) system 2a and 2b”.

Atomic structure and energetics

The geometries of the formate molecules are quite similar in all configurations with two molecules per unit cell. The differences appear in the Cu-O bond lengths and the relaxations of the copper surface atoms. We have seen that for low coverage (with one molecule per unit cell) in the most stable configuration (bridge position) the oxygen-bound



FORMATE-Cu(110) SURFACE SYSTEMS



copper atoms relax outward relative to the clean surface. Increasing the coverage, with two molecules per unit cell in bridge positions, the outward relaxations of the copper surface atoms are larger than for the low coverage (see Tables “Formate-Cu(110) system 2a and 1”).

Table Formate-Cu(110) system 2a: Two formate molecules in (2x2) unit cell on the clean surface. (bond lengths of the molecule atoms are in angstroms and relaxations of the copper atoms of the first layer are expressed in percentage relative to the ideal interlayer distance where the copper atom have the bulk terminated positions).

bond length (Å)	bridge	top	bridge top
$C^{21}-H^{33}$	1.142	1.143	1.141
$C^{23}-H^{35}$	1.142	1.143	1.145
$C^{21}-O^{25}$	1.320	1.323	1.322
$C^{21}-O^{27}$	1.320	1.323	1.321
$C^{23}-O^{29}$	1.320	1.323	1.323
$C^{23}-O^{31}$	1.320	1.323	1.326
angles $O^{25}C^{21}O^{27}$ $O^{29}C^{23}O^{31}$	129.10^0 128.69^0	126.35 126.35	128.51^0 126.12^0
Interlayer relaxations (% relative to the ideal)			
$Cu^{13}-Cu^{11}$	+1.17	-0.54	-0.04
$Cu^{15}-Cu^{11}$	+1.17	-1.34	-0.72
$Cu^{17}-Cu^{11}$	+1.17	-1.34	-1.56
$Cu^{19}-Cu^{11}$	+1.17	-0.54	-0.70
Clean Cu(110) surface	-11.00		

Table Formate-Cu(110) system 2b: Cu-O bond lengths and relative energies for two formate molecules in (2x2) unit cell on the clean surface (oxygen-copper bond lengths are given in Å).

Molecule positions		Cu^{13}	Cu^{15}	Cu^{17}	Cu^{19}	Energy (eV)
bridge	O^{25}	-	1.998	-	-	0.0000
	O^{27}	-	-	-	1.998	
	O^{29}	-	-	1.998	-	
	O^{31}	1.998	-	-	-	
one bridge and one top	O^{25}	-	1.993	-	-	1.0694
	O^{27}	-	-	-	1.989	
	O^{29}	2.334	-	2.461	-	
	O^{31}	2.340	-	2.475	-	
top	O^{25}	-	2.456	-	2.327	2.0520
	O^{27}	-	2.450	-	2.334	
	O^{29}	2.334	-	2.448	-	
	O^{31}	2.326	-	2.456	-	

The most stable configuration for high coverage (two formate molecules in (2x2) unit cell) is the one with both molecules in the bridge position. In the table above the difference in



the energies for the other configurations are given, the energy of the bridge configuration is taken as reference. A positive energy indicates that the specific structure is less stable. The small Cu-O bond length when both molecules are in bridge position is indicative of a strong attractive Cu-O interaction [JD01, HO97]. In the most stable structure the Cu-O bonds are all equal. Also the outward relaxations of all copper atoms of the first layer are the same. Due to the C-O bonds the inward relaxation of the clean Cu(110) surface is over-compensated.

When one of the molecules is placed in top position, (mixed configuration) the energy increases by 1.07 eV, a little more than the 0.92084 eV found for low coverage. The increase of the energy is mostly due to the different Cu-O bonds. A small contribution comes from different relaxations of the copper surface atoms. The same is true when both molecules are in top position. The increase of the energy (2.0520 eV) is larger than the 2×0.92084 eV.

Observation 1: The contribution to the total energy due to repulsion or attraction between the formate molecules can be estimated by comparing a given area of the Cu-surface with two different arrangements of the formate molecules: (i) the formate is spread out on the copper surface with low coverage, i.e one molecule per (2x2) unit cell, and (ii) the formate molecules are present on only half of the surface with double (high) coverage, i.e. two molecules per (2x2) unit cell, and half of Cu-surface is free of formate. The two situations yield the following energy difference:

$$\frac{1}{2} \{ 2 \cdot E_{Cu(110)}^{1-Formate} - (E_{Cu(110)} + E_{Cu(110)}^{2-Formate}) \} = \Delta E$$

where $E_{Cu(110)}^{1-Formate}$, $E_{Cu(110)}^{2-Formate}$ are the energies of the (2x2) unit cell with one or two molecules, respectively, on Cu(110) (with the molecules in bridge positions), and $E_{Cu(110)}$ represents the energy of the clean surface. If $\Delta E > 0$ the interaction between the molecules is attractive and it is repulsive if $\Delta E < 0$.

Our results for the total energies of the different Cu-surfaces (with and without formate) yield a small positive energy difference, $\Delta E = +0.1294$ eV per molecule. This would mean an attractive interaction of the formate molecules, in contradiction with the earlier interpretation of the experimental observations [PBJ97], which postulate a repulsive interaction between formate molecules on Cu(110) surface from the fact that the high coverage configuration is not achievable by long exposure of the Cu(110) surface with formic acid in the gas phase.

However, while our calculations test the equilibrium configurations of formate molecules on the surface at $T = 0$, the experiments draw the conclusions from the kinetics of the adsorption reaction. The ultimate test will be to calculate the barrier for adsorption of a second formate molecule in the c(2x2) unit cell. This is a very demanding calculation and has to be left to future calculations.



6.6 Oxygen precovered Cu(110), ‘High formate coverage’

We give the details of the arrangement of the formate molecules on oxygen precovered Cu(110) surface in three different tables.

- (a) the intramolecular bond lengths and bond angles and the interlayer relaxations of the Cu(110) surface,
- (b) the bond lengths of the oxygen atoms of the formate molecules with the copper surface atoms and the energies of the different formate adsorption geometries.
- (c) the bond lengths of the extra oxygen atoms to the Cu surface atoms.

For the numbering of the atoms we refer to Figures “Formate-Cu(110) system 3a and 3b”.

Atomic structure and energetics

In the case of the oxygen precovered Cu(110) surface the most stable configuration also turns out to be the one with both molecules occupying bridge positions. It is characteristic for all configurations that due to the Cu-O bonds the first copper layer relaxes outward above the ideal bulk terminated positions and the first interlayer distance increases. Again the inward relaxation for the clean Cu(110) surface is over-compensated.

The extra oxygen atom (the remaining 0.25 ML after water release) is slightly displaced from its fourfold hollow site starting position. For all configurations the Cu-O³³ bond length (Cu⁷-O³³, Cu¹¹-O³³) relative to the second layer atom are practically the same. The bond length of the lone oxygen atom to copper atoms of the second layer is shorter than the one formed by the oxygen of the molecules with the copper atoms of the first layer (see Table “Formate-Cu(110) system 3b and 3c”).

In the Table “Formate-Cu(110) system 3b” the energy of the most stable configuration (both formate molecules in bridge positions) is taken as reference. The positive energy indicates the reduced stability of the other configurations.

The calculated Cu^{7/11}-O³³ bond lengths are in good agreement with experimental results and theoretical calculations of the oxygen precovered Cu(110) surface [LKC98, HO97, DFS91, BPO86, FGJ90, ST93, UMU01]. The O³³ position is slightly above the first layer of copper atoms (see Figure “Formate-Cu(110) system 3a and 3b”).

Liem et al. [LKC98] have reported that at low coverage of oxygen on the Cu(110) surface the most favorable adsorption site of the additional oxygen atom is not the hollow site (high symmetry fourfold coordination). The equilibrium position corresponds to a pseudo threefold coordinated adsorption site. The oxygen is in a midpoint between a hollow site and two copper nearest-neighbor atoms along to $[1\bar{1}0]$ direction. This is explained by the closer coordination (shorter bond lengths) of the oxygen to the copper atoms for the pseudo threefold coordinated adsorption site.



FORMATE-Cu(110) SURFACE SYSTEMS



Table Formate-Cu(110) system 3a: Intramolecular and Cu-surface bond lengths for two formate molecules in (2x2) unit cell on the oxygen precovered Cu(110) surface (bond lengths of the molecule atoms are in angstroms and relaxations of the copper atoms of the first layer are expressed in percentage relative to the ideal interlayer distance where the copper atom have the bulk terminated positions).

bond length (Å)	bridge	bridge top (O ³³ -Cu ⁷)	bridge top (O ³³ -Cu ¹¹)	top
C ²¹ -H ³⁵	1.139	1.153	1.150	1.142
C ²³ -H ³⁷	1.142	1.147	1.145	1.140
C ²¹ -O ²⁵	1.321	1.332	1.313	1.314
C ²¹ -O ²⁷	1.321	1.315	1.328	1.331
C ²³ -O ²⁹	1.318	1.323	1.319	1.331
C ²³ -O ³¹	1.317	1.320	1.313	1.333
angles O ²⁵ C ²¹ O ²⁷	129.75 ⁰	125.30 ⁰	125.58 ⁰	126.38
O ²⁹ C ²³ O ³¹	128.24 ⁰	128.68 ⁰	127.44 ⁰	126.39
Interlayer relaxations (% relative to the ideal)				
Cu ¹³ -Cu ¹¹	+8.28	+11.27	+5.66	+8.16
Cu ¹⁵ -Cu ¹¹	+8.27	+11.69	+5.63	+7.22
Cu ¹⁷ -Cu ¹¹	+8.28	+11.62	+5.81	+7.22
Cu ¹⁹ -Cu ¹¹	+8.27	+13.81	+6.85	+8.13
Clean Cu(110) surface	-11.00			

Table Formate-Cu(110) system 3b: Cu-O bond lengths (Å) and relaxation energies (in eV) for two formate molecules in (2x2) unit cell on the oxygen precovered surface

Molecules positions		Cu ¹³	Cu ¹⁵	Cu ¹⁷	Cu ¹⁹	Energy (eV)
bridge	O ²⁵	-	1.993	-	-	0.0000
	O ²⁷	-	-	-	1.993	
	O ²⁹	-	-	1.989	-	
	O ³¹	1.988	-	-	-	
one bridge and one top Cu ⁷ -O ³³	O ²⁵	-	2.493	-	2.347	1.1576
	O ²⁷	-	2.428	-	2.301	
	O ²⁹	-	-	1.987	-	
	O ³¹	1.986	-	-	-	
one bridge and one top Cu ¹¹ -O ³³	O ²⁵	-	2.449	-	2.281	1.6247
	O ²⁷	-	2.566	-	-	
	O ²⁹	-	-	2.003	-	
	O ³¹	1.998	-	-	-	
top	O ²⁵	-	2.494	-	2.377	1.8527
	O ²⁷	-	2.381	-	2.235	
	O ²⁹	2.235	-	2.382	-	
	O ³¹	2.377	-	2.494	-	

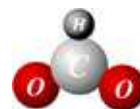


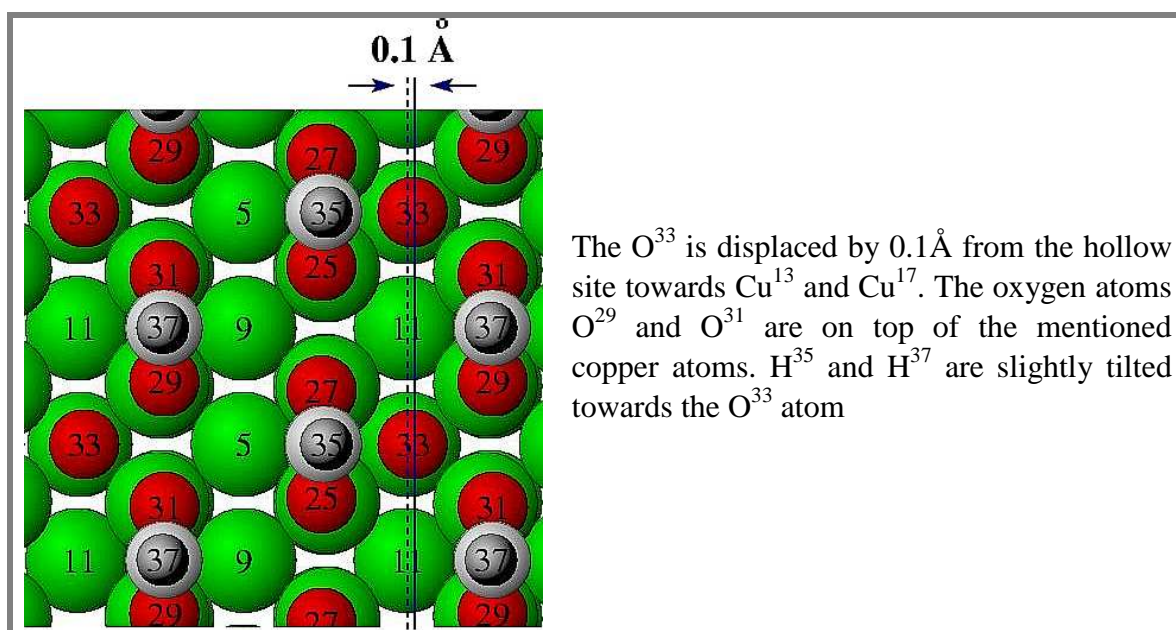
Table Formate-Cu(110) system 3c: Bond lengths (\AA) of the additional oxygen (O^{33}) for two formate molecules in (2x2) unit cell on the oxygen precovered surface.

$\text{O}^{33}\text{-Cu}$	Cu^7	Cu^{11}	Cu^{13}	Cu^{15}	Cu^{17}	Cu^{19}
bridge	1.869	-	2.135	2.305	2.135	2.305
one bridge and one top $\text{Cu}^7\text{-O}^{33}$	1.865	-	2.211	2.243	2.280	2.294
one bridge and one top $\text{Cu}^{11}\text{-O}^{33}$	-	1.875	2.100	2.200	2.227	2.321
top	1.879		1.239	2.239	2.239	2.238

We found that for the most stable configuration of the formate molecule adsorption on 0.25 ML oxygen precovered Cu(110) surface (both molecules in the bridge position) the additional oxygen atom follows the same trend: it likes to coordinate closer to the three Cu-surface atoms (see in Table “Formate-Cu(110) system 3b”). The O^{33} forms slightly shorter bonds to Cu^{13} and Cu^{17} and longer ones with Cu^{15} and Cu^{19} . The direction of relaxation is the same as the one suggested in the Ref. [LKC98], towards to Cu nearest-neighbors on the $[1\bar{1}0]$ direction (see Figure “Formate-Cu(110) system 3a” and Figure “Formate-Cu(110) system 5”).

For the oxygen precovered Cu(110) surface the energy difference between the most stable configuration (both molecules in bridge position) and the less stable one (both molecules in top position) is 1.8527eV. This value is only 11.02 meV larger than 2×0.92084 eV (where 0.92084eV is the energy difference between top and bridge configurations with one molecule in a (2x2) unit cell). In the case of two formate molecules in a (2x2) unit cell on clean Cu(110) surface this energy difference is 210.32 meV.

Figure Formate-Cu(110) system 5: Displacement of additional oxygen for two formate molecules in bridge positions and an oxygen atom in a (2x2) unit cell (0.25ML oxygen precovered surface) (Cu-green, O-red, C-gray, H-dark grey).





The presence of additional oxygen apparently influences the energy difference between different formate adsorptions geometries. This is not surprising since the Cu atoms participating in the formate binding are also involved in the binding of the extra oxygen.

Observation 2: For a characterization of the effect of the preadsorbed oxygen on the formate-formate interaction we compare the adsorption energies of the formate-Cu(110) system “high coverage” with and without additional oxygen (considering both molecules in bridge positions) in a similar manner as in “Observation 1” in the previous chapter.

$$\frac{1}{2} \left\{ E_{\text{Cu(110) oxygen}}^{2\text{-Formate}} - \left(E_{\text{Cu(110) oxygen}} + 2 \cdot E_{\text{Formate}} \right) \right\} - \frac{1}{2} \left\{ E_{\text{Cu(110)}}^{2\text{-Formate}} - \left(E_{\text{Cu(110)}} + 2 \cdot E_{\text{Formate}} \right) \right\} = \Delta E_{\text{bind}}$$

where the term with the first curly brackets represents the negative binding energy per formate on precovered-oxygen Cu(110) and the second one is the negative binding energy per formate without oxygen. $E_{\text{Cu(110) oxygen}}^{2\text{-Formate}}$ is the energy of the 2 formate-oxygen precovered Cu(110)

system, $E_{\text{Cu(110)}}^{2\text{-Formate}}$ is the energy of the 2 formate-Cu(110) system, $E_{\text{Cu(110) oxygen}}$ the energy of the

oxygen precovered (0.25ML) Cu(110) system, $E_{\text{Cu(110)}}$ the energy of the clean Cu(110)

surface and E_{Formate} the energy of a single gas phase formate molecule. If $\Delta E < 0$ then the

additional oxygen aids the formate adsorption. Our results for the total energies of the different Cu-surfaces (with and without oxygen) yield the following bonding energies per

molecule: $E_{\text{binding}}^{\text{formate Cu(110) oxygen}} = -3.1035$ eV, $E_{\text{binding}}^{\text{formate Cu(110)}} = -3.4955$ eV, i.e. a small positive adsorption energy difference, $\Delta E = +0.3920$ eV per formate molecule. This means that the oxygen does

not increase the attraction interaction between the adsorbed formate molecules. But, again we would like to point out, that we have tested the equilibrium configurations of adsorbed formate with and without preadsorbed oxygen at $T = 0$. The effect of the adsorbed oxygen might be more important for reducing the barrier for adsorption of the second formate molecule in the c(2x2) Cu(110) surface cell. In fact, due to the presence of oxygen a new reaction path for the adsorption of formate from gas phase formic acid is opening up: instead of release H_2 when the molecules are adsorbed, with the additional oxygen, water can be formed. This is indeed experimentally observed [PBJ97]. A theoretical investigation of the kinetics has to be left to future investigations due to the very high computational demands.

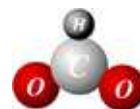
For all configurations we found that the molecule is sitting with its molecular plane perpendicular to the Cu(110)-surface. For low coverage (one formate molecule in the unit cell) we found that in the stable configuration the molecule is in a bridge position (each oxygen of the carboxylate group binds a single copper atom so that the carboxylate group forms a bridge between two nearest-neighbor copper atoms along to $[1\bar{1}0]$ direction). The Cu surface atoms that are not binding directly to oxygen atoms show inward relaxations as on the clean Cu(110) surface. In contrast, nearly no relaxation relative to the ideal unrelaxed Cu(110) surface is found for the Cu atoms that are forming the bonds with O atoms.

At high coverage (two formate molecules in the unit cell) the most stable configuration is the one with both molecules in bridge positions. The Cu-surface atoms show outward relaxations larger than in the low coverage case. The geometries of both formate molecules are quite similar to that of the molecule at low coverage. We found that an attractive interaction between the formate molecules should occur at high coverage.

In the case of oxygen-precovered Cu-surface, at high coverage of formate molecules, we find again that the stable configuration is the one with both molecules in bridge positions.

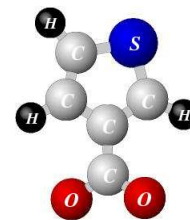
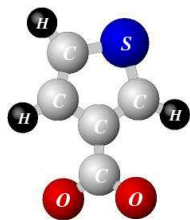


FORMATE-Cu(110) SURFACE SYSTEMS



A large outward relaxation of the Cu surface layer is found. The molecular geometry of the formate molecules does not change significantly and it is similar as in the previously discussed systems. The extra oxygen atom (the 0.25ML oxygen monolayer) is only slightly displaced from its fourfold hollow site starting position. This oxygen atom binds more strongly to the second layer Cu atom than to the first layer atoms.

The Cu-O bond length is practically the same in all configurations and does not depend on the coverage ratio. The oxygen adsorption does not influence the binding of the oxygen atoms of the carboxylate group with the first layer of the Cu-surface. The main changes due to oxygen coverage are in the first interlayer relaxations. With increasing coverage the first Cu-surface layer relaxes towards the positions corresponding to the unrelaxed (110) surface, and for the oxygen precovered surface the inward relaxation for the clean Cu(110) surface is over-compensated and turned into a large outward relaxation.



Chapter 7

3-Thiophene carboxylate on Cu(110) surface

7.1 Introduction

The family of five-membered heterocycles is of basic importance in chemistry and physics. This family includes thiophene and its derivatives, which are the main constituents of the polymeric organic conductors [BRV72, SL01, SAK01]. The discovery of conducting polymers has proven to be of great scientific and practical interest. Conducting polymers are being used in the field of material science as electromagnetic shielding, antistatic coatings on photographic films, and for windows with changeable optical properties. New promising applications include micro- and molecular-electronics, as well as quantum computing. [SK00, SAK01, Phi00, SKB00, SDB01, JB01, CDL00].

There is an increasing interest in the adhesion and growth of oriented polymeric materials on surfaces. Much work is now undertaken in molecular self-assembly experiments which lead to oriented growth of organic films. These motivate investigations to understand the properties of the polymer-precursor-substrate interfaces. With such information it should be possible to fabricate a specific polymer-surface structure whose chemistry and physics can be controlled and optimized to achieve specific desired properties.

Polythiophene and its derivatives play an important role as a conducting polymer. The self-assembling of the thiophene derivatives is expected to produce organic films with novel and interesting properties. Experiments provide information on the bonding, lateral interactions, charge distribution, orientation and the alignment of molecular adsorbates on surfaces. Ab initio calculations are a powerful method to aid the interpretation of experiments, and to provide a basic understanding and forecasting of the intra- and inter-molecular interactions present in the observed structures.

In the present chapter we focus on the study of the (2x1) structure of 3-thiophene carboxylic acid on Cu(110) surface. The structure is shown in Figure “3-thiophene carboxylate 1a”.

3-THIOPHENE CARBOXYLATE ON Cu(110) SURFACE

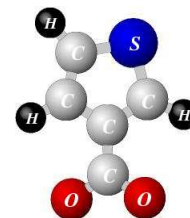
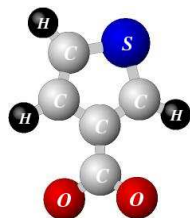
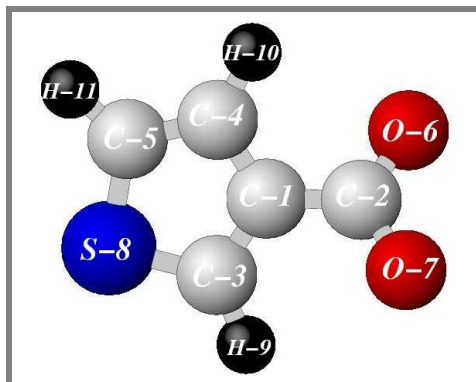


Figure 3-thiophene carboxylate (3TC) 1a: Schematic view of the 3-thiophene carboxylate molecule. The atoms are numbered as used in our structure optimization of the free radical discussion.

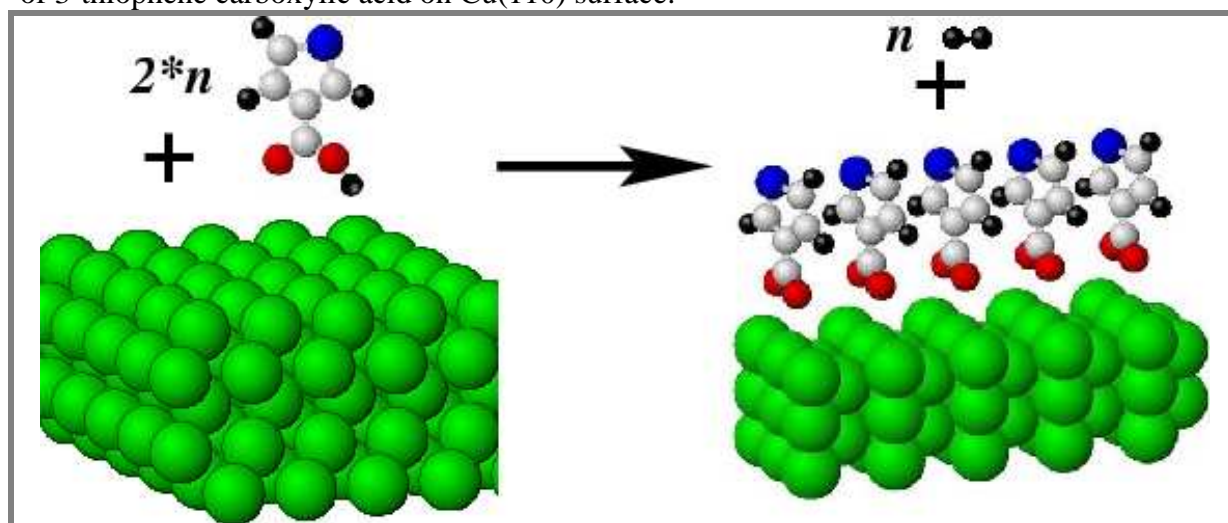


Experiments, like high-resolution electron energy loss spectroscopy (HREELS), scanning tunneling microscopy (STM) and low electron energy diffraction (LEED), have been performed on this system [FCB96].

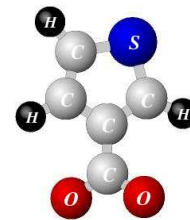
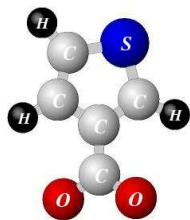
The HREELS shows that at low coverage the 3-thiophene carboxylic acid lies flat on the surface with its π orbitals interacting with the surface atoms. It has been shown that at high coverage the hydrogen atom of the carboxylate group is lost and the molecule binds to the surface as 3-thiophene carboxylate (3TC). The hydrogen leaves the surface as H_2 molecule (see Figure “3-thiophene carboxylate 1b”).

Electron scattering (HREELS) results indicate that when the coverage increases the molecules reorient perpendicular to the surface with the carboxylate group oriented in the $[1\bar{1}0]$ direction of the surface. The (2×1) super structure that is formed is confirmed also by the LEED experiments. In the gas phase the 3TC-molecules have a planar geometry. At high coverage the thiophene rings of the molecules feel a steric repulsion, which they can reduce by rotation, thus breaking the planar geometry. Experiments suggest that they rotate by $20\text{--}30^\circ$ away from the $[1\bar{1}0]$ direction [FCB96].

Figure 3-thiophene carboxylate (3TC) 1b: Schematic view of the high coverage adsorption of 3-thiophene carboxylic acid on Cu(110) surface.



In the following we first discuss our *ab initio* results for the free 3TC-molecule and then for the structure of the 3TC-molecules adsorbed on Cu(110) surface.



7.2 3-thiophene carboxylate free radical

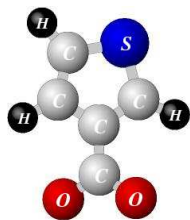
The molecule (see Figure “3-thiophene carboxylate 1a”) contains a thiophene ring that is formed by four sp^2 -hybridized carbon atoms and a sulfur atom. Formally the ring structure can be assumed to derive from a benzene molecule by replacing two of the annular CH groups with sulfur. In this five-membered ring the sulfur atom acts as an electron donating heteroatom by contributing two electrons to the aromatic sextet, and thus the thiophene ring is considered to be an electron-rich heterocycle. The fact that the lone pair on sulfur contributes to the aromaticity is seen in the lower dipole moment of the thiophene compared to its saturated analogue tetrahydrothiophene.

The atomic and electronic structure of the 3-thiophene carboxylate (3TC) radical has been optimized using the PBE-GGA functional for the exchange-correlation. The calculation has been performed in a box of $12 \times 11.5 \times 6.5 \text{ \AA}^3$ using a $3 \times 3 \times 3$ k-point set and a energy cutoff of 25 Ry. The corresponding pseudopotentials of the atoms have been generated using the same PBE-GGA scheme. Their characterization is given in the Apendix “Parameters and tests of the PAW pseudopotentials”.

Atomic structure

To optimize the structure of 3TC we have started with a configuration where the angles and bond lengths are equal to experimental values for the acid form. The atoms of the 3-thiophene carboxylate have been allowed to relax without constraint till the energy minimum is reached. In the final relaxed configuration the thiophene ring and carboxylate group of the molecule are in the same plane. The calculated bond lengths and angles and are given in the Table “3-thiophene carboxylate 1”. They can be compared with those measured for the crystalline structure of 3-thiophene carboxylic acid [HR62, VHW68] or those calculated for the molecule in the gas phase with ab initio molecular orbital calculations [TRL02]. One should mention that in the references two different C-O bond lengths are given because they correspond to the carboxylic group (COOH). The shorter one is corresponding to the double bond that is formed by one of the oxygen atoms with the carbon. The longer one corresponds to a single C-O bond. The 3-thiophene carboxylate radical does not contain the acidic hydrogen, so the two oxygen atoms are indistinguishable, and their bonds to the carboxylate carbon are equivalent. As one would expect the calculated C-O bond lengths for the radical are practically equal. Due to the differences of the C-O bonds in the carboxylic acid and in the carboxylate groups the O-C-O angles differ.

The calculated bond lengths and angles for the thiophene ring agree well with those calculated for the thiophene ring in the corresponding gas phase of the acid or with those measured for the crystalline structure formed by the acid in the solid phase (see Table “3-thiophene carboxylate 1”).



3-THIOPHENE CARBOXYLATE FREE RADICAL

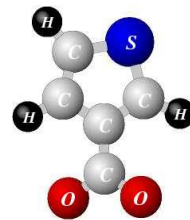


Table 3-thiophene carboxylate 1: The bond lengths (Å) and bond angles (degrees) of 3-thiophene carboxylate radical.

bond	this work	Ref. [TRJ02]	Ref. [HR62]	Ref. [VHW68]
C ² -O ⁶	1.276	1.209	1.235	1.24
C ² -O ⁷	1.277	1.347	1.332	1.32
C ² -C ¹	1.415	1.464	1.474	1.51
C ¹ -C ³	1.353	1.380	1.406	1.38
C ¹ -C ⁴	1.364	1.410	1.437	1.41
C ⁴ -C ⁵	1.348	1.371	1.508	1.44
C ⁵ -S ⁸	1.620	1.687	1.708	1.73
C ³ -S ⁸	1.630	1.697	1.699	1.70
C ³ -H ⁹	1.110	1.078		
C ⁴ -H ¹⁰	1.107	1.079		
C ⁵ -H ¹¹	1.112	1.078		
angle				
C ³ -S ⁸ -C ⁵	94.00	92.90	98.00	95.20
S ⁸ -C ⁵ -C ⁴	111.68	111.50	106.00	108.80
S ⁸ -C ³ -C ¹	111.27	111.00	110.40	109.10
C ³ -C ¹ -C ⁴	112.06	112.8	112.5	114.6
C ⁵ -C ⁴ -C ¹	111.00	111.8	113.3	112.3
O ⁶ -C ² -O ⁷	115.14	123.00	123.6	124.6

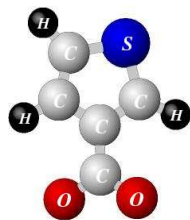
Electronic structure

In order to understand the electronic structure of the 3-thiophene carboxylate radical the partial local density of states (PLDOS) has been calculated for each of the atoms of the molecule. The atoms are identified by numbers in Figure “3-thiophene carboxylate 2 and 3”, where also the PLDOS-spectra are shown.

The PLDOS-spectra for 3-thiophene carboxylate can be understood partially in analogy to the formate spectra (see Chapter 6 Formate on Cu(110) surface). The carboxylate group is the same, but the five-atom thiophene ring replaces the hydrogen atom of the formate. Indeed, for the atoms forming the **carboxylate group** (O⁶-C²-O⁷) we find the same gross feature as for the respective atoms in formate: (i) a set of levels close to the Fermi energy (-1.5...-0.0 eV) which correspond to combinations of p_z orbitals (π-sytem perpendicular on the molecular plane) as well as anti-bonding combinations of p_x, p_y and s orbitals (in the molecular plane); (ii) a set of levels in the range (-10.0...-2.5 eV), which correspond to the σ-binding combinations of the p-orbitals; (iii) low lying levels below -12 eV which correspond to mostly s-type tightly bond electrons. However, due to the presence of the ring, there are also differences: (i) there are more levels close to the Fermi energy since there are more p_z-electrons which contribute to the π-sytem; (ii) there are additional binding states both of s and p character which involve the C² atom due to the binding with the C¹ atom of the ring.

Thiophene ring: In general the interval corresponding to the bonding of the atoms of the five-membered ring lies between -18.0...-3.0 eV. For the C and Sulfur atoms the low-lying states (<-10.0 eV) have mostly s-type characteristics. The high lying states of these

3-THIOPHENE CARBOXYLATE FREE RADICAL



atoms have p-type character. The PLDOS-spectra of the C atoms binding the S atom have similar characteristic, but different compared with PLDOS-spectra of the other C atoms.

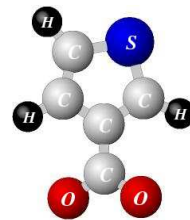
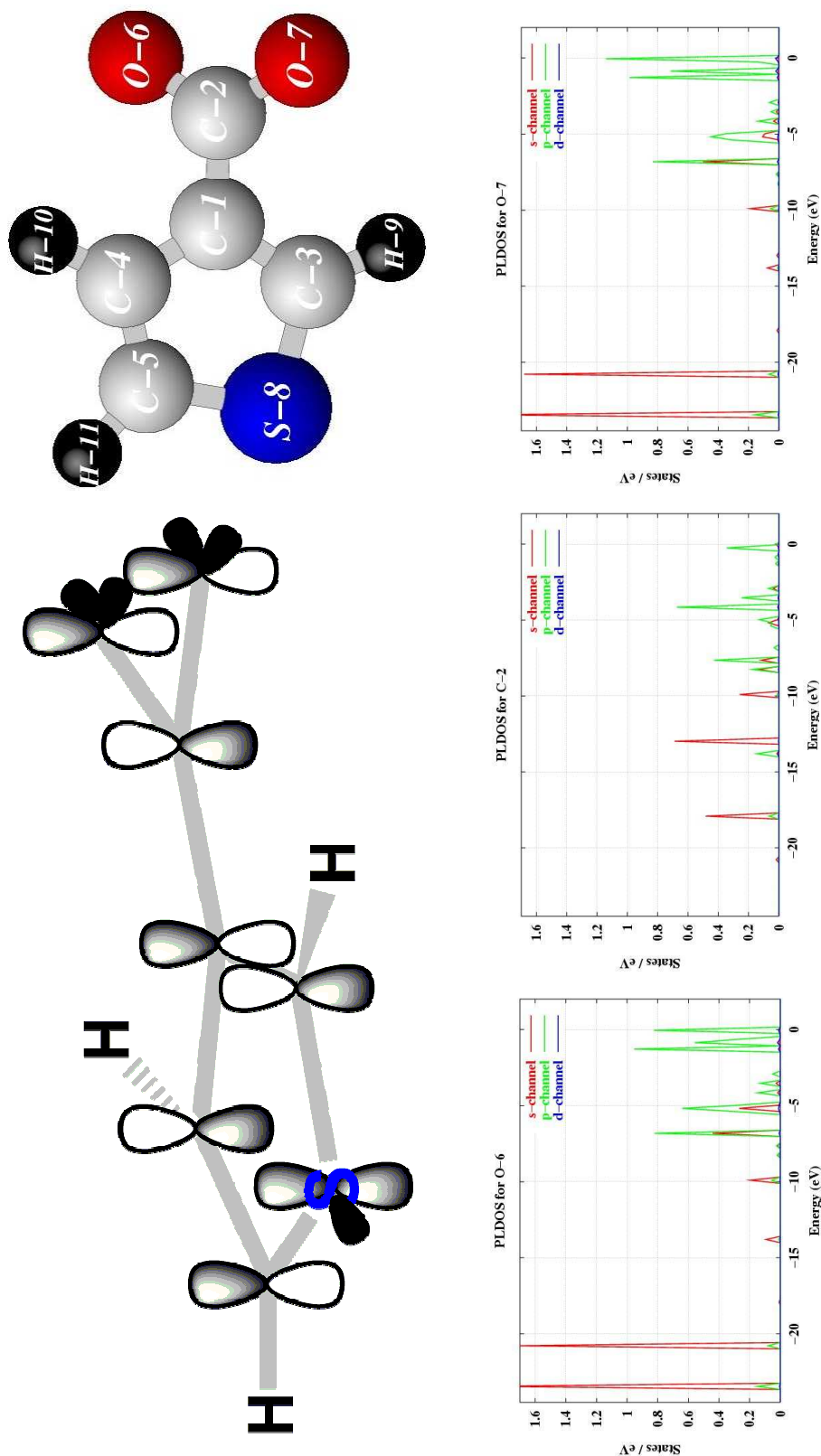
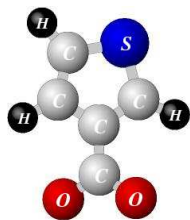


Figure 3-thiophene carboxylate 2: Structure and atom numbers of the 3-TC radical, a schematic view of the p_z -orbitals, and the PLDOS of the atoms contained in the carboxylate group, O-C-O.





3-THIOPHENE CARBOXYLATE FREE RADICAL

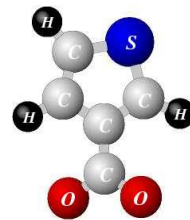
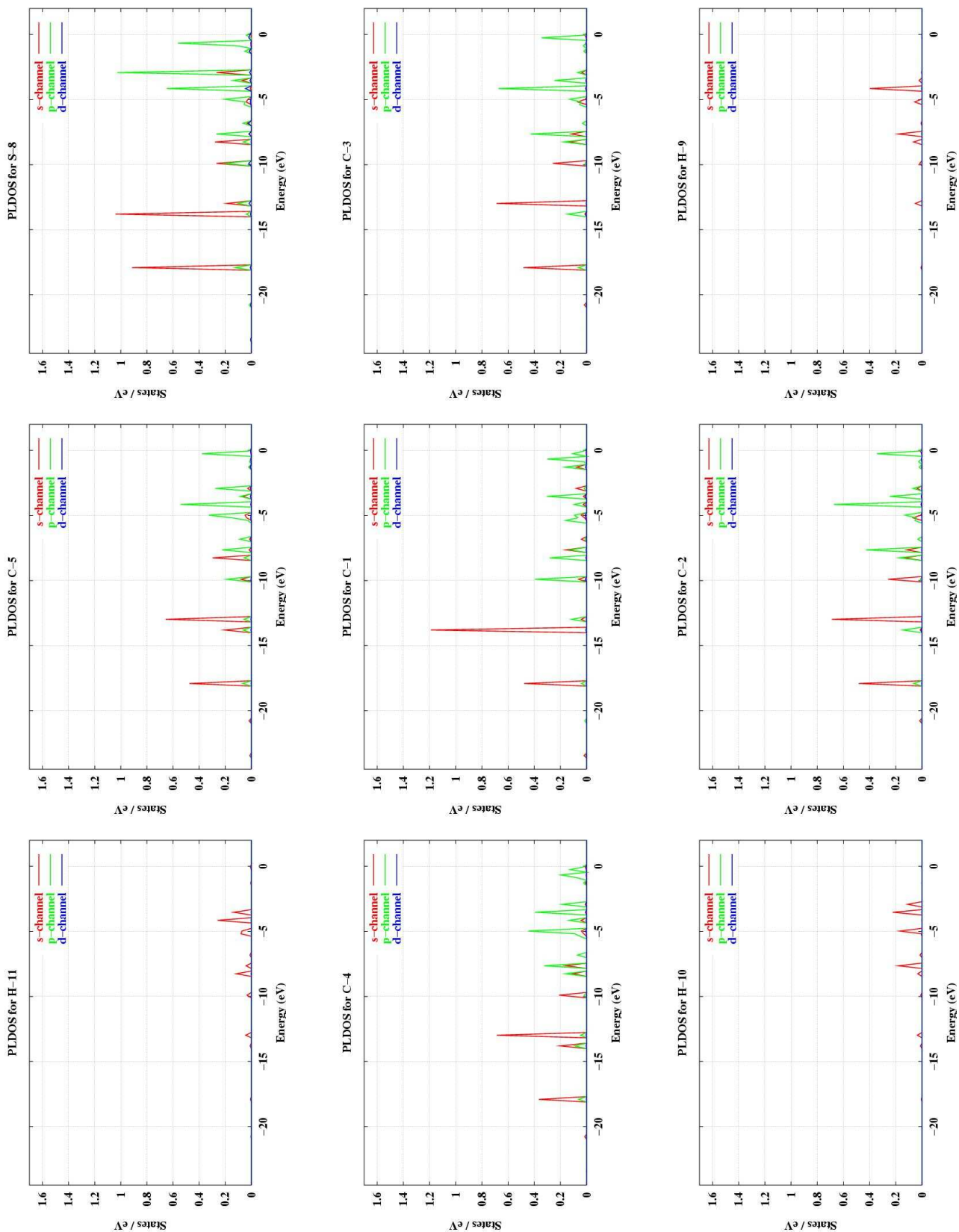
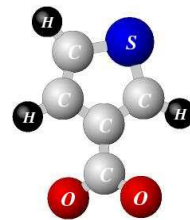
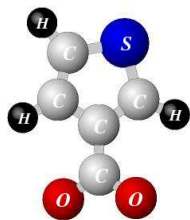


Figure 3-thiophene carboxylate 3: The PLDOS of the atoms contained in the thiophene ring of the 3-thiophene carboxylate radical.





7.3 3-thiophene carboxylate-Cu(110) system

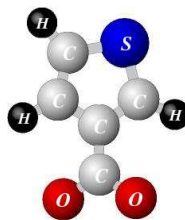
In order to understand the structure and the nature of the bonding of 3-thiophene carboxylate molecule to the Cu(110)-substrate we have performed ab initio calculations for a (2x1) supercell using PBE-GGA functional for exchange-correlation. The pseudopotentials used are generated with the same PBE-GGA functional; the generation parameters are discussed in the Appendix “Parameters and Tests of the PAW-pseudopotentials”.

The HREELS experiments [FCB96] suggest that the thiophene ring is rotated with respect to the carboxylate group by about 30° . The experiments give no indication of the possible reconstruction of the copper atoms in the surface under the molecular layer. In order to get good starting positions for a full structure optimization a series of survey calculations has been performed.

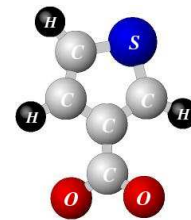
Dense packing of 3-thiophene carboxylate on Cu(110): Ring rotation

First, a calculation of the structure of the Cu(110) surface using a (1x1) lateral unit cell and a slab containing 7-layers and a 10 Å vacuum has been performed. The forces have been relaxed down to a level of 10^{-2} mRy/a.u. The relaxed positions of this slab have been used as starting positions for the copper atoms in the calculations of the geometrical optimization of 3-thiophene carboxylate Cu(110) surface system.

Secondly, a series of calculations has been done in order to get a good estimation of the rotation angle of the thiophene ring with respect to the $[1\bar{1}0]$ direction and of the bond distance of the carboxylate group to the Cu surface. A system containing the molecule and two copper atoms has been optimized in a big box. The copper atoms have been placed under the oxygen atoms of the carboxylate group, in a planar geometry. The copper atoms are kept fixed at the nearest neighbors distance along the $[1\bar{1}0]$ direction of the Cu(110) surface during the calculation, and only the molecule is allowed to relax. The relaxed positions of the planar 3-thiophene carboxylate radical have been used as starting positions for this new molecule-2-copper atoms system. The calculation has been performed in a box of $14.5 \times 11.5 \times 6.5 \text{ Å}^3$ using a $3 \times 3 \times 3$ k-point set with an energy cutoff of 25 Ry and the PBE-GGA functional for exchange-correlation. The relaxation is performed till the energetic minimum is reached (atomic forces less than 0.1 mRy/a.u.). With these optimized positions the lateral dimensions of the box are reduced to $a \cdot \sqrt{2}$, a (with $a = 3.641 \text{ Å}$ being the copper-fcc lattice constant). In this way the new box has the dimensions $14.5 \times (a \cdot \sqrt{2}) \times (a) \text{ Å}^3$ and contains the copper atoms in the same arrangement and distances as in an ideal single layer of the Cu(110) surface. This new system can be viewed as a (2x1) structure of the 3-thiophene carboxylate on Cu(110) surface with the planar molecule aligned along to $[1\bar{1}0]$ direction. With this arrangement a series of calculations have been performed to estimate the rotation angle of the thiophene ring. Without relaxing the atom distances the thiophene ring is rotated from 0° up to 90° (in steps of 5°) relative to carboxylate group. The energy of the unit cell versus rotation angle it is shown in Figure “3-thiophene-carboxylate-Cu(110)-single-layer 1”.

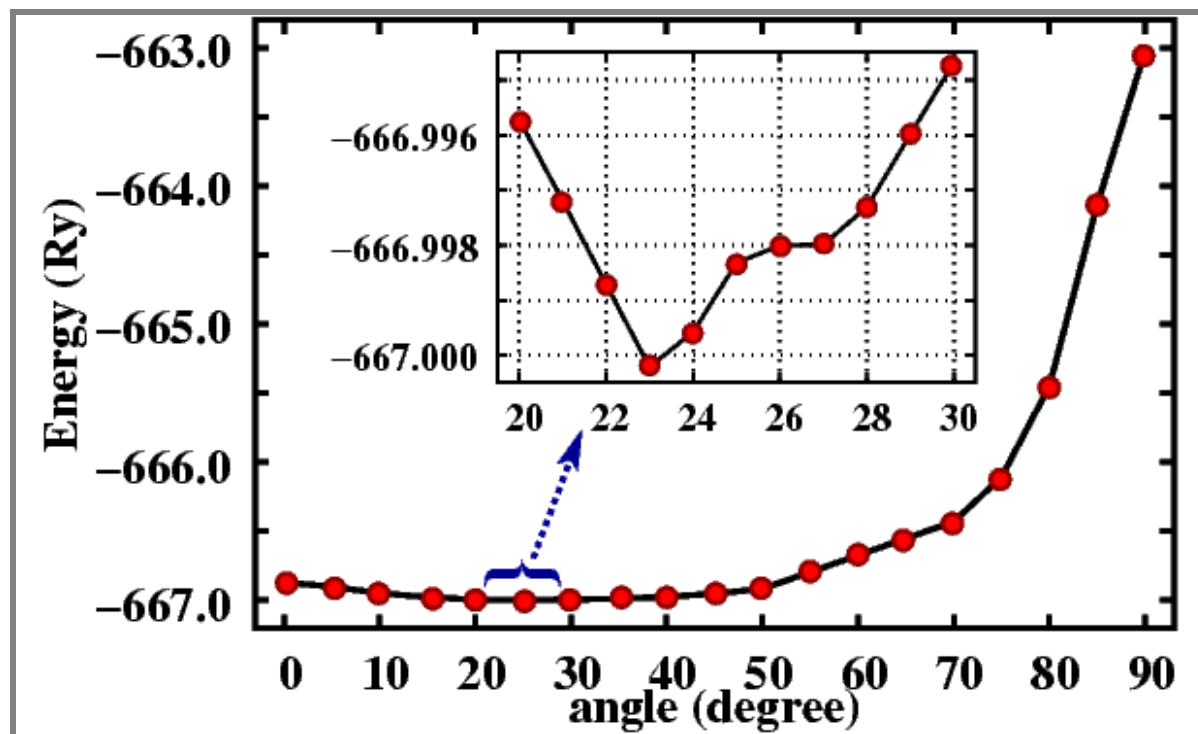


3-THIOPHENE CARBOXYLATE-Cu(110) SYSTEM



The minimum is located in the interval 20° - 30° . For this interval another series of calculations has been done using smaller steps of 1° . We found that the minimum energy is corresponding to a rotation angle of 23° of the thiophene ring with respect to the $[1\bar{1}0]$ direction.

Figure 3-thiophene-carboxylate-Cu(110)-single-layer 1: Energy versus rotation angle.



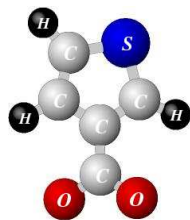
3-thiophene carboxylate on Cu(110)-surface: Full relaxation

The minimum energy configuration of 3-thiophene on Cu(110) found by these calculations (bond lengths, bond angles and rotation angle) has been used as a starting point for the full calculations using a thicker slab.

In the calculations of the (2x1) structure of 3-thiophene carboxylate on Cu(110) surface a set of $1 \times 3 \times 4$ k-points and an energy cutoff of 25 Ry has been used. The supercell contains 7 layers of copper (14 atoms) and a molecule (2×11 atoms) one each side of the copper slab. The inversion symmetry of the system has been included in the calculations. The dimension of the unit cell is $7 \cdot a \cdot \sqrt{2}$ (vertical), $a \cdot \sqrt{2}$, a (lateral). $a = 3.641 \text{ \AA}$ is the copper-fcc lattice constant fitted for bulk calculations using $12 \times 12 \times 12$ k-point set. The vacuum region above the molecules has a thickness of 7.0 \AA (vertical distance between two adjacent molecules).

Four of the most probable configurations of the molecules on top of Cu(110) surface have been optimized: the thiophene molecules are placed on so called 'bridge' or 'top' positions above the first or second Cu-layer with the thiophene ring rotated with 23° relative to the carboxylate group. 'Bridge' or 'top' positions refer to the position of the C-atom with respect to the Cu layer. For the 'bridge' position the oxygen atoms are on top of the two nearest-neighbor copper atoms so that the carboxylate group is forming a bridge between the copper atoms. In the 'top' position the carbon of the carboxylate group is on top of a copper-surface atom and the oxygen atoms in the bridge position between two copper nearest-neighbors.

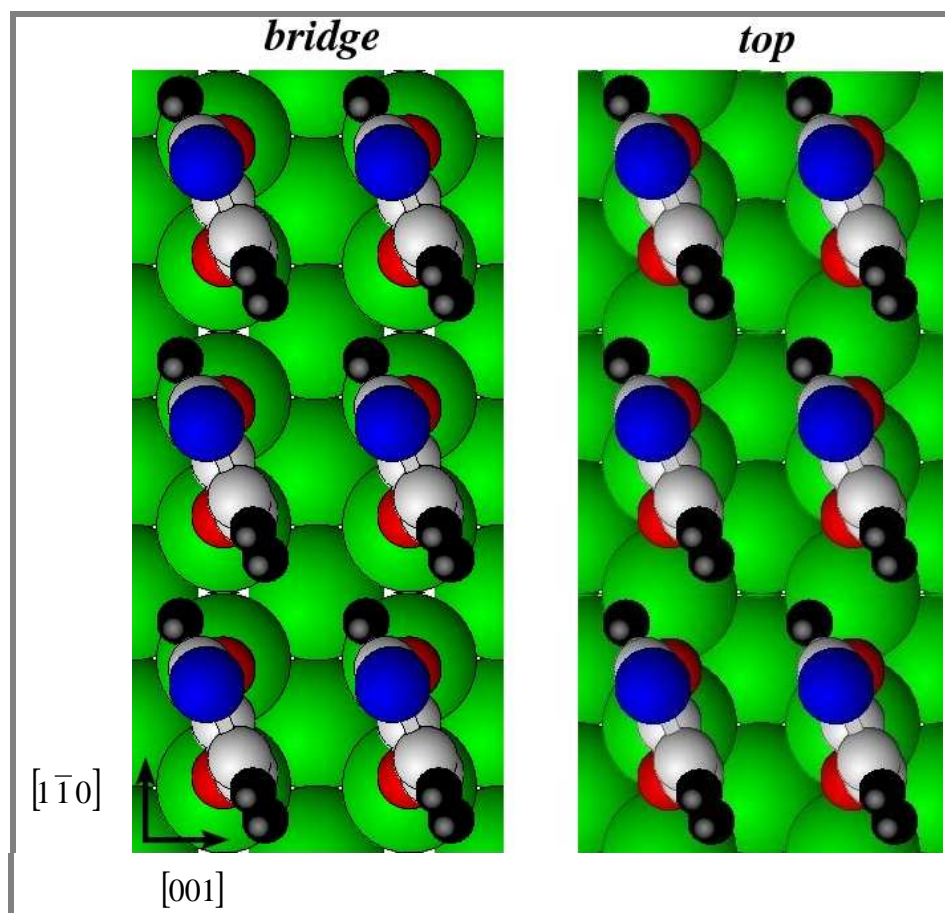
3-THIOPHENE CARBOXYLATE-Cu(110) SYSTEM



The first two layers of the Cu surface and the molecule have been allowed to relax without constraint. The optimization has been done until the energetic minimum has been reached. The relaxed structures are shown in the Figure “3-thiophene-carboxylate-Cu(110) system 1a-1c”.

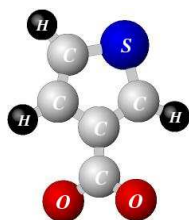
In the following we present the results of our calculations, discussing the relative energies, the bond lengths of the Cu-O bonds, the bond lengths in the thiophene ring, the bond angles of the molecules, and the relaxation of the Cu-surface atoms. Then we will discuss the electronic structure of the attached molecule in the most stable configuration and compare it to the free radical at the clean Cu surface.

Figure 3-thiophene-carboxylate-Cu(110) system 1a: The figure shows a top view of the (2x1) structure of 3-thiophene carboxylate ‘*bridge*’ and ‘*top*’ configurations above the first layer. By displacing the molecule along to [100] directions with a half of the lattice constant the other two configurations are obtained: ‘*top*’ and ‘*bridge*’ configurations above the second layer (Cu-green, O-red, C-gray, S-blue, H-dark grey).

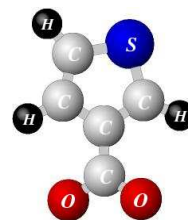


Energetics and Structure

The energetically most stable configuration is the ‘*bridge*’ configuration in which the oxygen atoms are on top of two nearest-neighbor copper atoms of the first layer. In a simple picture, the oxygen atoms are binding the Cu atoms and the thiophene molecular structure is unaffected except for the rotation. The carboxylate group is in a plane parallel to the $[1\bar{1}0]$ direction, and the thiophene ring rotated with 23.72° away from the $[1\bar{1}0]$. In Table “3-thiophene-carboxylate-Cu(110) system 1” the energy differences of the calculated structures are given. The most stable one is taken as reference (zero level), the positive energies show

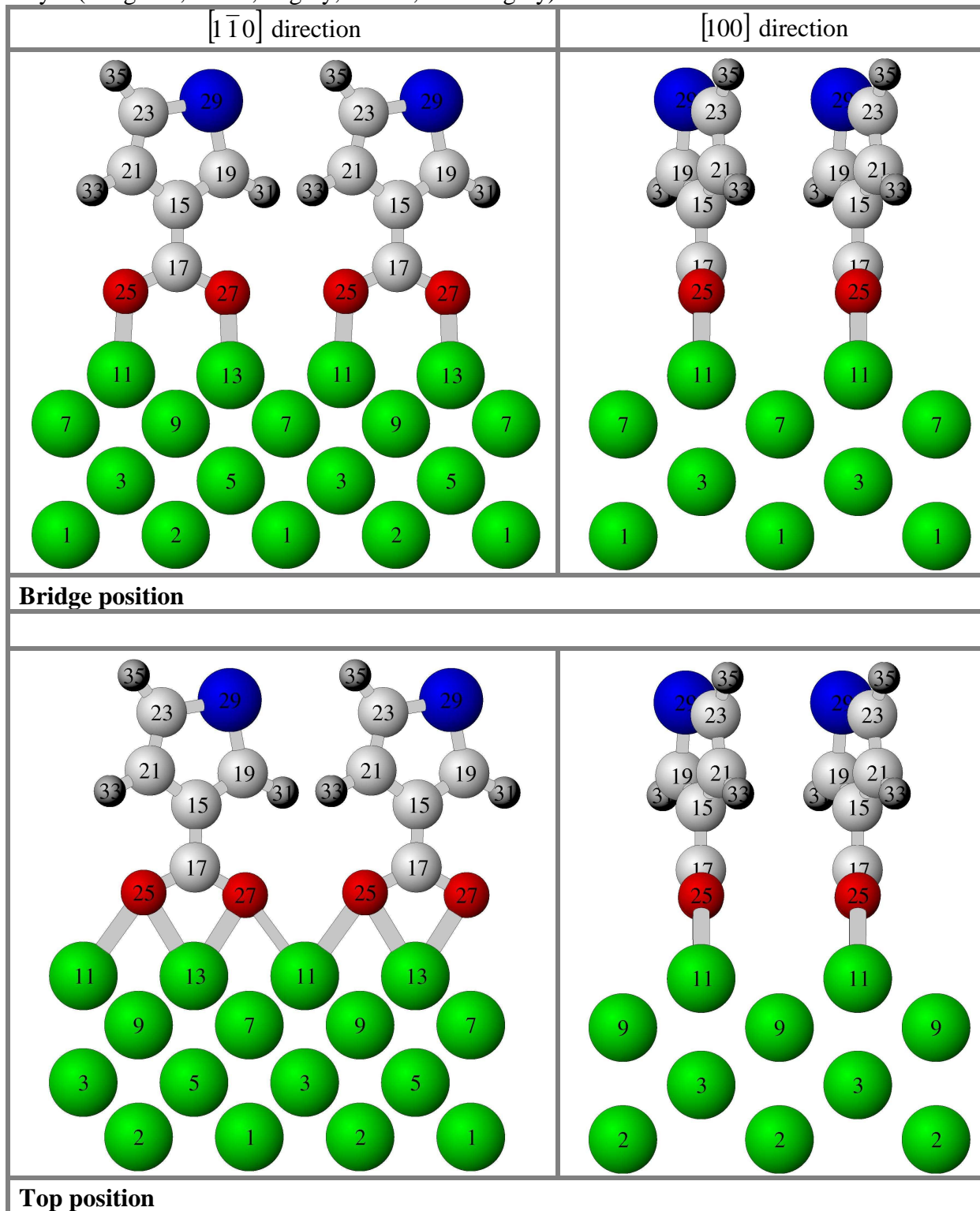


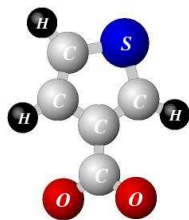
3-THIOPHENE CARBOXYLATE-Cu(110) SYSTEM



the reduction of the stability of the other structures, causing a decrease of the probability to populate the respective configuration in experiments.

Figure 3-thiophene-carboxylate-Cu(110) system 1-b: Side view of the 3-thiophene carboxylate in bridge (upper panels) and top (lower panels) positions above the first layer (Cu-green, O-red, C-gray, S-blue, H-dark grey).





3-THIOPHENE CARBOXYLATE-Cu(110) SYSTEM

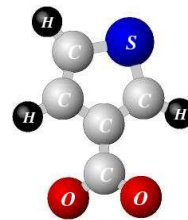
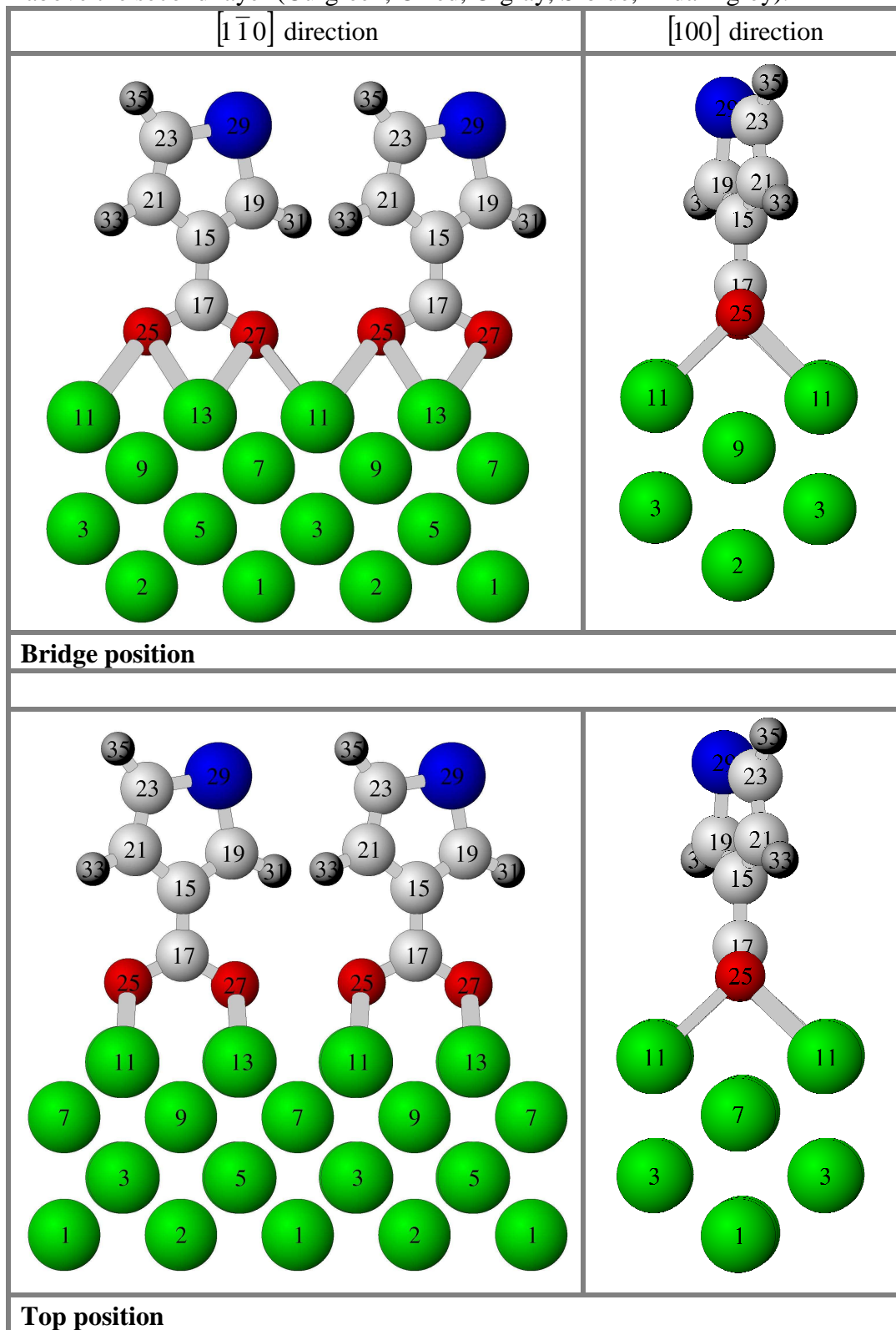
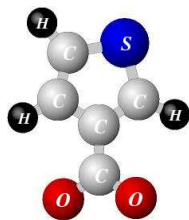


Figure 3-thiophene-carboxylate-Cu(110) system 1-c : Side view of the 3-thiophene carboxylate in bridge (upper panels) and top (lower panels) positions above the second layer (Cu-green, O-red, C-gray, S-blue, H-dark grey).





3-THIOPHENE CARBOXYLATE-Cu(110) SYSTEM

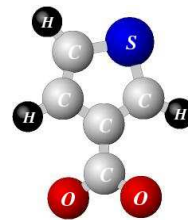


Table 3-thiophene-carboxylate-Cu(110) system 1: (the energies are expressed in eV)

configuration	Above first layer	Above second layer
bridge	0.000	+1.992
top	+0.985	+1.080

The relative stability of the different configurations can be explained in terms of chemical interaction of the oxygen atoms with the copper surface atoms. In Table “3-thiophene carboxylate 2” below the Cu-O bond lengths for the optimized configurations are given. When the 3-thiophene carboxylate is on the ‘*bridge*’ position above the first layer, the shortest Cu-O bonds are formed. In this configuration the oxygen atoms are sitting directly on top of the copper atoms, and a strong interaction between a copper atom and an oxygen atom can be achieved.

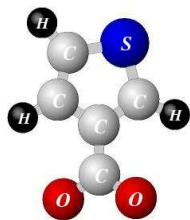
Table 3-thiophene-carboxylate-Cu(110) system 2: Cu-O bond lengths (the bond lengths are given in Å)

configuration	Bond (Å)	Above first layer	Above second layer
bridge	Cu ¹¹ -O ²⁵	1.925	2.959
	Cu ¹³ -O ²⁷	1.924	2.821
	Cu ¹¹ -O ²⁷	-	2.900
	Cu ¹³ -O ²⁵	-	2.823
top	Cu ¹¹ -O ²⁵	2.389	2.516
	Cu ¹³ -O ²⁷	2.224	2.516
	Cu ¹¹ -O ²⁷	2.334	3.660
	Cu ¹³ -O ²⁵	2.264	3.516

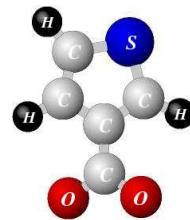
Table 3-thiophene carboxylate 3: The bond lengths (Å) in the thiophene ring for the different optimized configurations.

Bond (Å)	Above first layer		Above second layer	
	bridge	top	bridge	top
C ¹⁷ -O ²⁵	1.327	1.331	1.332	1.333
C ¹⁷ -O ²⁷	1.327	1.329	1.335	1.337
C ¹⁵ -C ¹⁷	1.459	1.455	1.484	1.492
C ¹⁵ -C ¹⁹	1.390	1.388	1.394	1.397
C ¹⁵ -C ²¹	1.424	1.422	1.434	1.437
C ²¹ -C ²³	1.384	1.382	1.386	1.387
C ¹⁹ -S ²⁹	1.731	1.730	1.735	1.736
C ²³ -S ²⁹	1.752	1.752	1.750	1.750
C ¹⁹ -H ³¹	1.114	1.113	1.113	1.114
C ²¹ -H ³³	1.116	1.118	1.115	1.115
C ²³ -H ³⁵	1.115	1.111	1.118	1.119

The conformational changes of the adsorbed molecule compared with a free 3-thiophene carboxylate radical are:



3-THIOPHENE CARBOXYLATE-Cu(110) SYSTEM



• the planarity of the molecule is broken because the thiophene ring rotates relative to the plane formed by the carboxylate group. The angle of rotation remains practically the same for all the configurations. This angle is approximately 24° and does not depend on how the molecules are bound to the Cu-surface atoms. This rotation is due to the strong lateral interactions that appear between the hydrogen atoms of the neighboring thiophene rings.

• the O-C-O angle of the carboxylate group is changed due to the bonding of the oxygen atoms to the Cu atoms. In the case of the most stable configuration the O-C-O angle is 127° , i.e. 12° larger than for the isolated radical. All the other configurations have the O-C-O angle around 124° . This is close to the experimental value for the crystal structure of 3-thiophene carboxylic acid.

The C-O bond lengths and O-C-O angle are practically identical to those for the formate-Cu(110)-system. The Cu-O bond lengths in the case of thiophene carboxylate are smaller with approximately 0.07 \AA than the corresponding ones of the formate molecule.

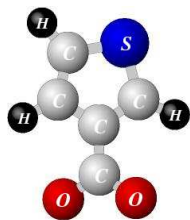
Table 3-thiophene carboxylate (3TC) 4: The angles in the thiophene ring and of the carboxylate group for the different optimized configurations. The rotation angle of the thiophene ring relative to the $[1\bar{1}0]$ is also given.

angle	Above first layer		Above second layer	
	bridge	top	bridge	top
$S^{29}-C^{19}-C^{15}$	111.05	111.06	112.14	112.56
$C^{19}-C^{15}-C^{21}$	113.60	113.99	111.83	111.08
$C^{15}-C^{21}-C^{23}$	112.08	111.44	113.20	113.77
$C^{21}-C^{23}-S^{29}$	111.48	112.06	111.23	110.98
$C^{19}-S^{29}-C^{23}$	91.77	91.43	91.59	91.59
$O^{25}-C^{17}-O^{27}$	127.65	124.99	124.05	124.00
Roration angle of the thiophene ring	23.72°	23.80°	23.83	23.77

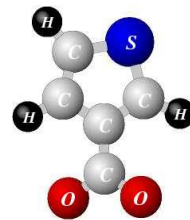
The bond lengths and angles in the thiophene ring are just slightly changed from one configuration to another. The only obvious changes appear at the interface carboxylate-group/Cu-surface, more precisely for the Cu-O bond lengths and the first interlayer distances of the copper substrate. The Table “3-thiophene carboxylate 5” gives the contractions of these first interlayer distances.

Table 3-thiophene carboxylate 5: The changes of the first interlayer distances of Cu(110)-surface (in percent) are given in percentage for different configurations of adsorbed 3TC.

Bond (\AA)	Above first layer		Above second layer	
	bridge	top	bridge	top
$Cu^{11}-Cu^9$	-10.05	-11.20	-12.86	-5.56
$Cu^{11}-Cu^7$	-10.05	-11.20	-12.86	-5.56
$Cu^{13}-Cu^7$	-11.92	-11.47	-9.14	-4.95
$Cu^{13}-Cu^9$	-11.92	-11.47	-9.14	-4.95
Clean Cu(110) surface	-11.00			



3-THIOPHENE CARBOXYLATE-Cu(110) SYSTEM



For each configuration the carboxylate group binds only to Cu atoms of the first layer. For a given configuration each of the oxygen atoms will form one or two bonds with neighboring Cu atoms. In the relaxed configurations there are some small lateral displacement of the outermost copper surface atoms towards the oxygen atoms (from 0.07 up to 0.12 Å). This has as an effect on the bonding of the first-layer copper surface atoms relative to the second-layer copper surface atoms. From the interlayer distances given in the table above, one can see that for the ‘*top*’-type configurations the displacements of the first-layer atoms relative to the second layer atoms are symmetrical. This is not the case in the ‘*bridge*’-type configurations where the first interlayer relaxations of copper atoms that bound the oxygen atoms differ by almost 2%. In all configurations the C¹⁵-C¹⁷ bond (connecting the carboxyl group to the thiophene ring) remains perpendicular to the (110) surface.

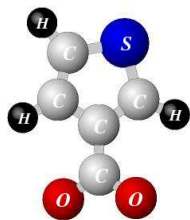
Electronic structure

The electronic structure is analyzed with the help of the Partial local density of states (PLDOS). The PLDOS has been calculated for all the atoms of the unit cell in all configurations. We discuss the results for the most stable 3-thiophene-carboxylate adsorption configuration. The corresponding plots are found in the following figures. We start at the inner Cu layer and end with the thiophene ring.

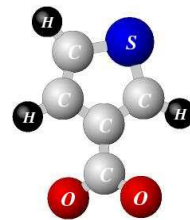
Cu-atoms: The Cu¹ and Cu² bulk-type atoms have the bulk characteristics with p- and d-type states in the energy interval of -4.8 up to -2 eV (see also Appendix “PLDOS for clean Cu(110) surface”). For the Cu³, Cu⁵, Cu⁷ and Cu⁹ the s- and p-states keep their main characteristics as the Cu¹ and Cu², but the d-band is narrowing. The copper-surface atoms (Cu¹¹, Cu¹³) have a characteristic d-band higher peak at -1.0eV. This peak does not appear at the other Cu-slab atoms. O²³ and O²⁷ have a large p-type band in the energy range of d-band of copper-surface atoms. These states are attributed to the Cu-O bonding.

3-thiophene carboxylate molecule: Compared to the spectra of the free radical, we generally observe a shift of all picks to lower energy. The low-lying s-type peaks (<< -12 eV) are shifted almost rigidly due to the change of the average potential when the molecules are bound to the Cu-surface. In addition, the states close to the Fermi energy and in the range of the d-band to the copper are individually shifted due to hybridization when the respective orbitals are participating in the bonding to the Cu-atoms. This is particularly true for the highest levels that belong to a large extend to the oxygen atoms of **carboxylate group**. We expect that all p-electrons residing on the oxygen atoms to participate in the binding to the Cu surface. The most pronounce binding effect can be observed for the peak at -1.0 eV, which can be identified on the oxygen atoms and Cu-atoms of the first layer.

Thiophene ring: The PLDOS of the atoms forming the thiophene ring have quite similar characteristics for all the configurations. Moreover, from the analysis of the bond lengths and angles of the thiophene ring one concludes that the type of bonding of the carboxylate group to the Cu surface does not have a significant influence on the properties of the thiophene ring. In general the energy interval corresponding to the bonding of the atoms of the five-membered ring lies between -18.0...-4.5 eV. Also the low-lying s-type states at -14.0 and/or -15.0 and -18.0eV are characteristic for the atoms of the thiophene ring but they are not present at the carboxylic carbon (C¹⁷). The atoms S²⁹, C²³, C²¹ and C¹⁹ have a characteristic p-type state at -2.0eV, but C¹⁵ and the carboxylic carbon (C¹⁷) do not have this p-type state. Since there is no direct interaction of the thiophene ring with the Cu-surface we can conclude that the p-type states at -2.0eV corresponds to part of the π -conjugated electron system of the thiophene ring localized at the S²⁹, C²³, C²¹ and C¹⁹ atoms. The rotation of the thiophene ring relative to the plane of the carboxylate group must have an influence on the

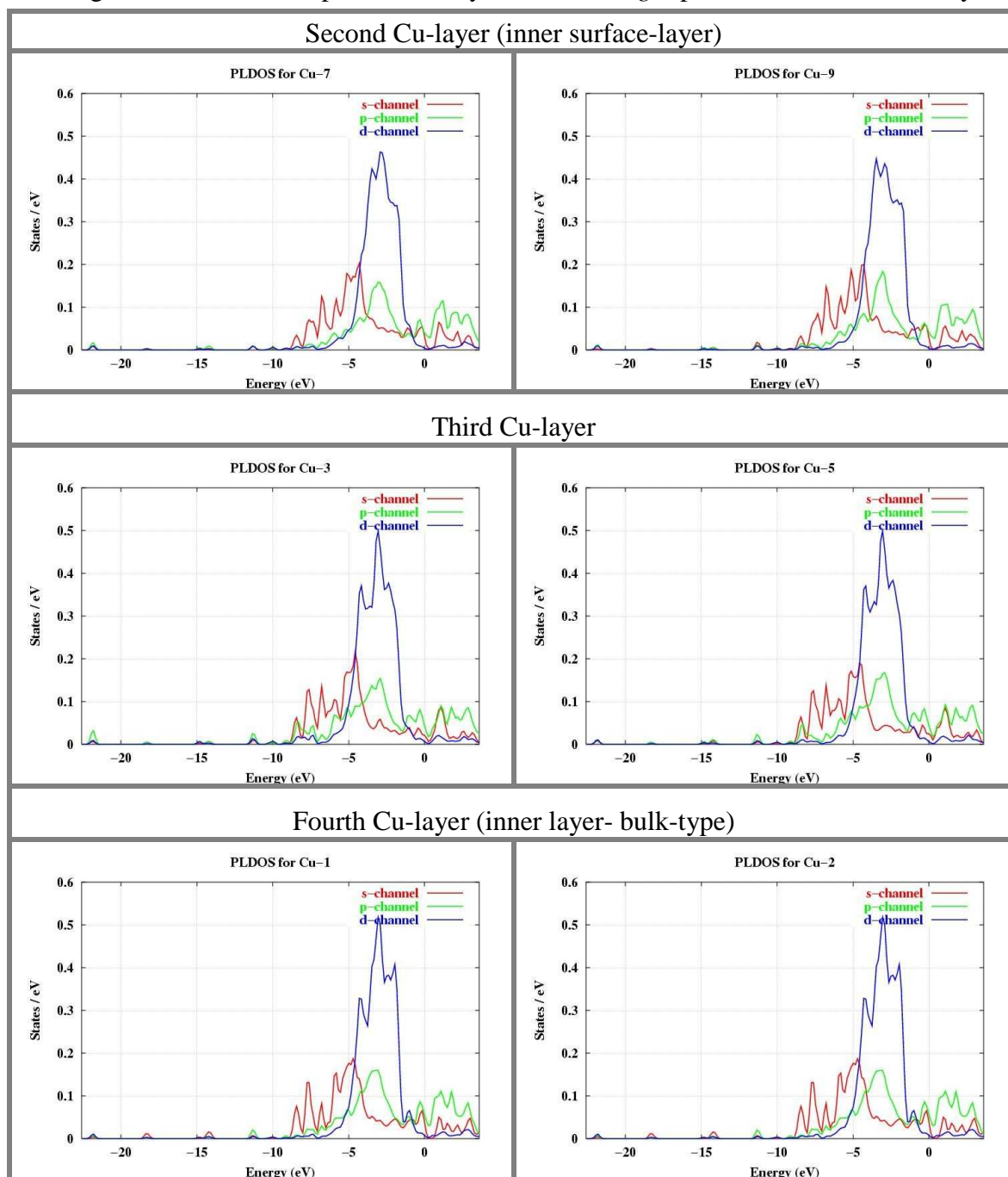


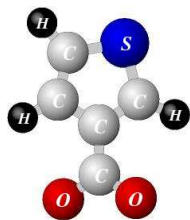
3-THIOPHENE CARBOXYLATE-Cu(110) SYSTEM



coherence of the π -electrons. We speculate that the existence of the peak at -2.0 eV at all ring atoms which falls directly into the gap of the split p-band of the carboxylate-oxygen atoms could be a sign of decomposition of the π -conjugated electron system caused by the rotation of the thiophene ring. Apparently, the binding to the copper surface of the carboxylic group localizes the conjugated p-type states mostly to the ring region. They do not extend as much to the carboxylate group, as is the case for the free 3TC radical. A detailed analysis of this point is planned.

Figure 3-thiophene-carboxylate-Cu(110) system 2-a: The PLDOS of the Cu-bulk type atoms for the configuration when 3-thiophene carboxylate is in 'bridge' position above the first layer.





3-THIOPHENE CARBOXYLATE-Cu(110) SYSTEM

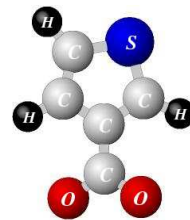
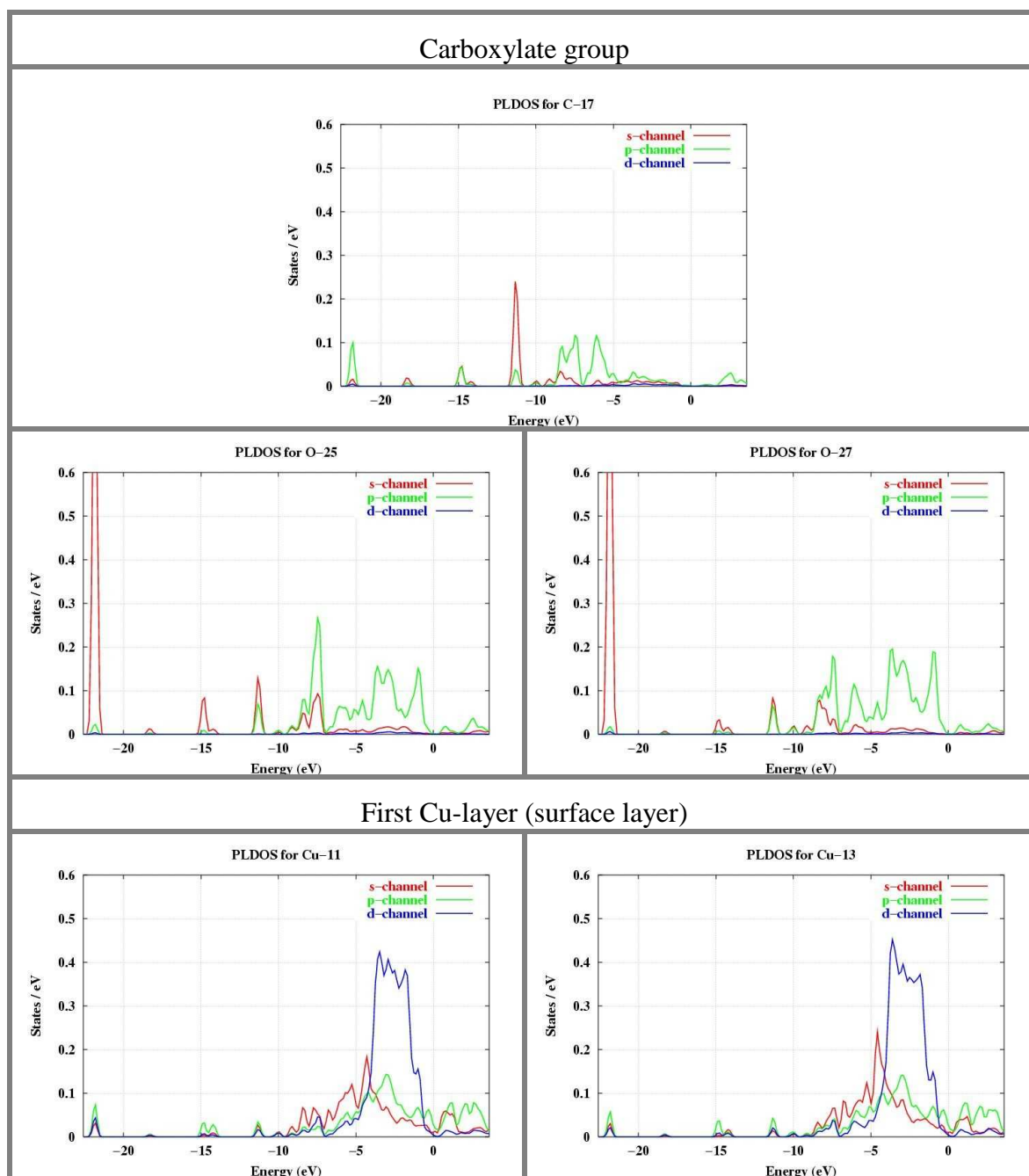
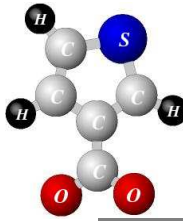


Figure 3-thiophene-carboxylate-Cu(110) system 2-c: The PLDOS of the copper outermost surface atoms and carboxylate group for the configuration when 3-thiophene carboxylate is in ‘bridge’ position above the first layer. The most pronounced binding effect can be observed for the peak at -1.0 eV, which can be identified on the oxygen atoms and Cu-atoms of the first layer. This peak is specific for the carboxylate group of the 3-thiophene carboxylate molecule. It does not appear in the case of formate adsorption on Cu(110) surface (see Figure “Formate-Cu(110) system 4b”) (for O atoms the s-type level below -24 eV is not shown).





3-THIOPHENE CARBOXYLATE-Cu(110) SYSTEM

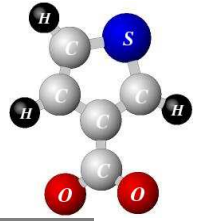
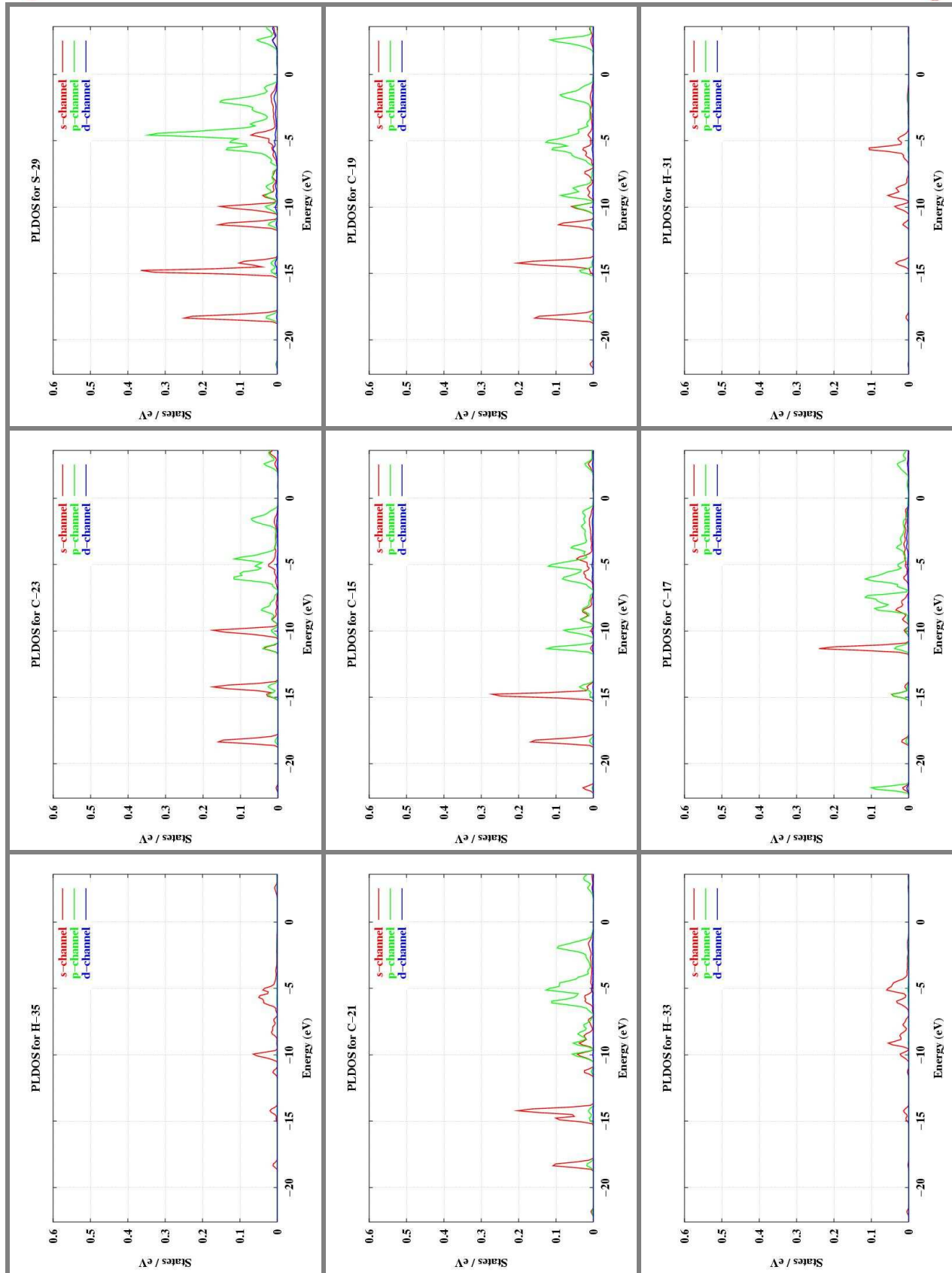
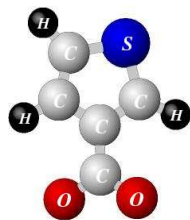


Figure 3-thiophene-carboxylate-Cu(110) system 2-b: The PLDOS of the thiophene ring atoms for the configuration when 3-thiophene carboxylate is in ‘bridge’ position above the first layer



3-THIOPHENE CARBOXYLATE-Cu(110) SYSTEM



In the stable configuration the molecule sits perpendicular in bridge position above the first Cu-surface layer with the carboxylate group oriented along to the $[1\bar{1}0]$ direction (see Figure “3-thiophene carboxylate-Cu(110) system”). The

most important change due to adsorption is the geometry of the molecule. In the gas phase the single molecule has a planar geometry with an extended π -system over the thiophene ring and carboxylate group. The adsorption of the molecule breaks this planarity. There are strong lateral interactions that appear between the hydrogen atoms of neighboring thiophene rings. As a consequence, in the adsorbed molecules the thiophene rings are rotated by 24° relative to the carboxylate group.

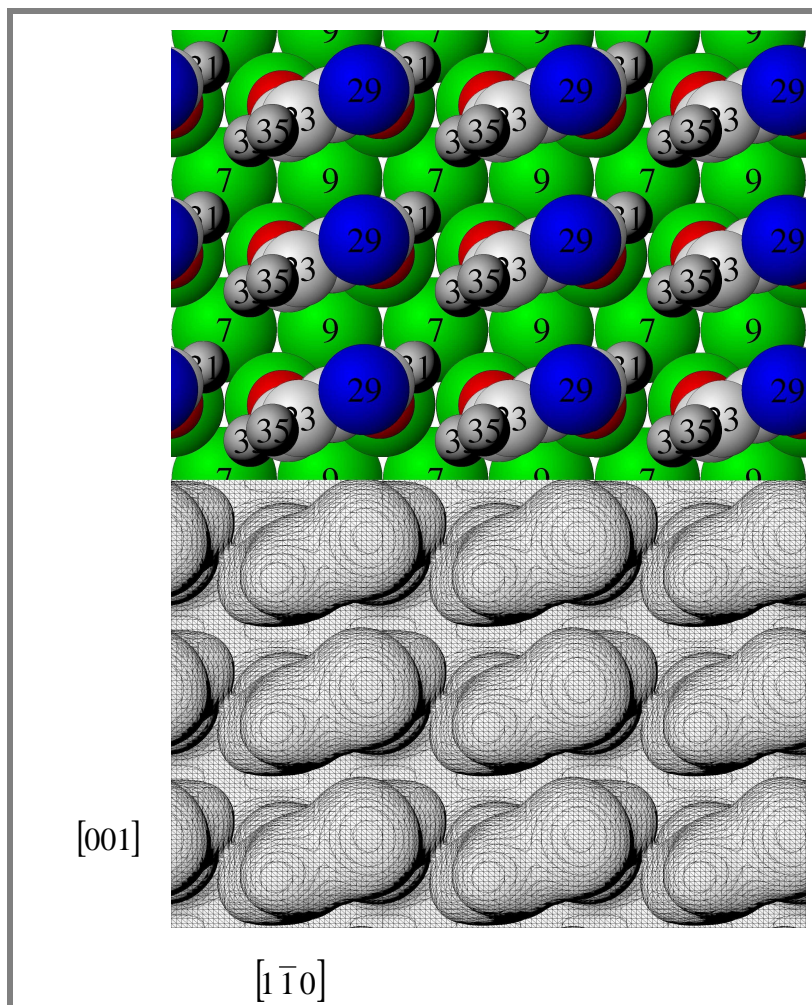
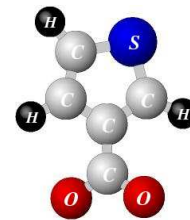
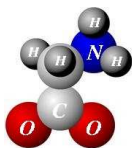


Figure 3-thiophene carboxylate-Cu(110) system: A top view of the bridge configuration and a surface of constant electron charge (lower part). The thiophene rings are rotated by 24° relative to the carboxylate group due to the strong lateral interactions that appear between the hydrogen atoms of neighboring thiophene rings. (Cu-green, O-red, C-gray, S-blue, H-dark grey)

This is nicely demonstrated in Figure “3-thiophene carboxylate-Cu(110) system” which shows the top view of the adsorbed molecules together with a surface of constant electron charge. The big cap on the right side of each molecule belongs to the S atom. As can be seen, the rotation of the thiophene ring increases the distance between the H atoms of the neighboring molecules in the row and decreases the distance of the S atom (negative charge) to the CH group (positive charge) of the next row of molecules.

The relaxations of the Cu-surface layer are almost the same as those of the clean Cu(110) surface. There are small lateral displacements of the Cu-atoms towards the oxygen atoms. We speculate that the π -system is affected by the rotation of the thiophene ring. This remains to be analyzed in detail. If it turns out to be an important effect, adsorption of 3TC on different fcc-metals (Pt, Ag, Au, Pd) should be considered. They have larger lattice constants and thus the ring rotation is expected to be less pronounced.



Chapter 8

Glycinate on Cu(110)-surface

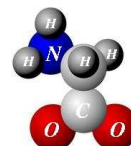
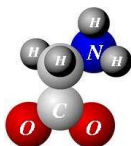
8.1 Introduction

It is crucial to understand the interaction of biologically active molecules, such as proteins and peptides, with metal surfaces, because they are key elements of many advanced and emerging technologies ([CV02],[BR03], [RSY03], [Rav03]) such as: (i) preparation of biomaterials and ensuring the biocompatibility by coating inorganic surfaces; (ii) fabrication of biosensors; (iii) (bio)molecular electronics.

Important for all applications are the structures of adsorbed molecules: (i) the type of binding to the surface (which functional group is involved, e.g. S-bonding, N-bonding, O-bonding or carboxylate(OCO)-bonding); (ii) the interaction between molecules and (iii) availability of the other specific functional groups of the molecular structure where specific biomolecules can be attached.

The study of model species such as the simple amino acids can be very helpful for the understanding of more complex systems. Especially the adsorption of glycine on surfaces represents a model system for chemisorption of biofunctional molecules and can be seen as a first step towards understanding the interaction of peptides and proteins with metallic surfaces. The interaction of amino acids and peptides with metal ions in the solution has been extensively studied and there is a large amount of data in the literature related to such organometallic complexes. However, the interactions of these molecules with metal surfaces are much less understood ([TKW03], [NON03], [NHP00]).

The α -amino acids represent the building blocks of many peptides and proteins. Hydrolysis of most proteins and peptides produces about twenty different amino acids of which glycine is the simplest one. Glycine ($\text{H}_2\text{N}-\text{CH}_2-\text{COOH}$) has an important function in the of neurotransmitter system. The two functional groups of glycine (amino group NH_2 and carboxyl COOH) have a complex chemical behavior: in the gase phase glycine exists in a nonionic form, in the solid phase it exists in a “zwitterionic” form, where the acidic hydrogen is transferred to the basic aminogroup. In solution, the form of glycine is determined by the pH : in acidic solutions it exists in the cationic form, in neutral solutions it is in a “zwitterionic” form and in basic solutions it exists in an anionic form.



8.2 Chirality and the Biological Importance

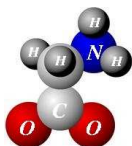
The importance of understanding the structure of α -amino acids is connected to their biological significance. The α -C denoted with * represents an asymmetric center in all amino acids, $\text{H}_2\text{NC}^*\text{RHCO}_2\text{H}$, when R (radical) is not a hydrogen atom. This induces the optical activity and chirality of the natural aminoacids and so the specificity and selectivity in all biological processes. The chirality expresses the fact that an object and its mirror image are not superimposable by any translation or rotation of the entire object, or by rotating part of the molecule around a simple sp^3 -bond. In essence, this means that a compound is chiral if the center carbon C^* binds 4 different molecular groups. A chiral object can exist in two distinguishable mirror forms, which are referred to as enantiomeric forms of the molecule. Glycine is the only amino acid, which doesn't have this asymmetric center. Thus it is not a chiral molecule, although it can be considered as a prochiral molecule, because the substitution of one hydrogen atom with another radical will establish the asymmetry at the α -C in the molecule and induce the chirality. Also, when the glycine molecules are adsorbed at a surface, one can distinguish left and right enantiomers, and so the chirality is induced in the molecule-substrate ensemble (see Figure Glycinate 1).

Since chirality has profound effects especially in biology – all forms of life on Earth use exclusively one mirror form of amino acids – much attention has been paid to this property for adsorbed molecules. Different forms of surface induced chirality have been defined. For recent reviews of experimental work on adsorption of complex organic molecules with special emphasis on chirality we refer to the work of Barlow and Raval [BR03]. We have chosen to study the adsorption of glycinate on Cu(110) by ab initio calculation because it offers the opportunity to study the aspects of bonding of different functional groups (carboxylate OCO and amino NH_2) to the surface and the surface induced chirality with a relatively small molecule [CHR02].

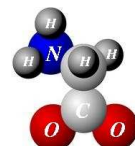
8.3 Experimental Structure Determination

The adsorption of the glycine molecule on the non-chiral Cu(110)-surface induces an organization of the adsorbates in ordered arrays with both different types of enantiomers present. There is no geometric or energetic reason for the preferential adsorption of one enantiomer for isolated molecules. The question is whether an interaction between adsorbed molecules exists which leads to a preferential adsorption of only one form.

Experiments have been performed on the copper-surface-glycinate system using scanning energy-selective photoelectron spectroscopy. The technique exploits the interference between the directly emitted photoelectron wavefield from an adsorbate core level with the components of the same wavefield elastically scattered by the surrounding atoms thus providing information on the location of the near-neighbors to the emitter. The N 1s and O 1s photoelectron diffraction was used to determine the structure of glycine adsorbed on Cu(110).



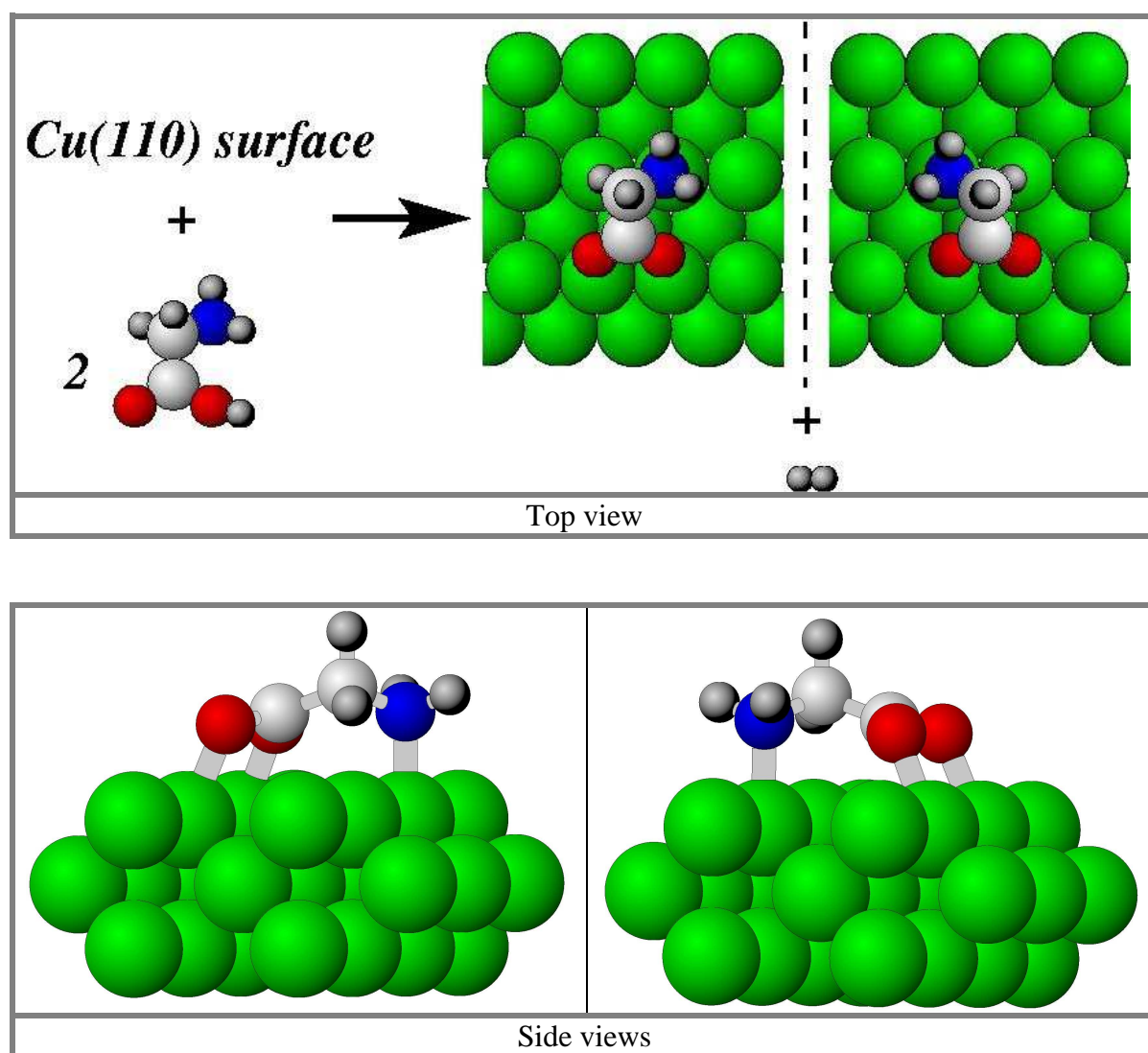
GLYCINATE ON Cu(110) SURFACE



LEED observations show that a (3x2) structure is formed. In Figure Glycinate 1 the adsorption structure is shown in *top* view for both, and two side views for one of the enantiomers. The molecule is bound to the surface across a pair of $[1\bar{1}0]$ rows by the two oxygen atoms of the carboxylate group and the nitrogen of the amino group. The C-C axis lies approximately parallel to the surface in the $[001]$ direction. The N-atom is displaced by 0.24 ± 0.1 Å along the $[1\bar{1}0]$ direction off an on-top Cu site, the Cu-N bond length being approx 2.04 Å. The oxygen atoms are displaced from the on-top site by 0.8 Å in the $[001]$ direction towards to amino group, with the Cu-O bond of 2.03 Å, the tilting of the bond with respect to the surface normal is $23 \pm 2^\circ$ [BWS98].

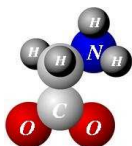
Figure Glycinate 1: Glycinate binds to the Cu(110) in a flat-lying configuration via both functional groups: carboxylate (-OCO-) and amino (-NH₂).

- (a) upper panel: The two possible enantiomer configurations of glycinate adsorbed on the Cu(110) surface.
 (b) lower panel: Two sides views of one of the enantiomers bonded at the surface.

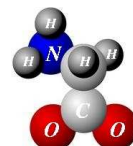


Reflection absorption infrared spectroscopy confirms the structure described above and suggests the existence of hydrogen bonds: CH...O and NH...O [BKH98].

A detailed study of the ordered monolayer of glycinate adsorbed on Cu(110) is presented in [HKW98]. The experimentalists have analyzed the molecular orientation using



GLYCINATE ON Cu(110) SURFACE

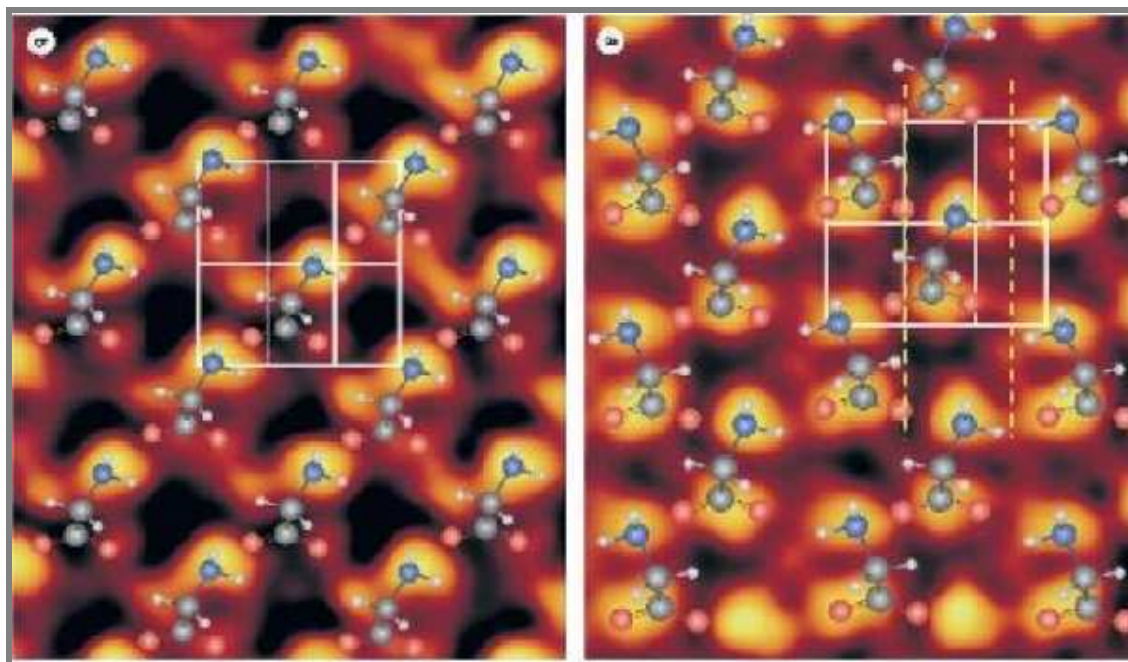


several techniques: XPS X-ray Photoelectron Spectroscopy, NEXFAS Near Edge X-ray Adsorption Fine Structure, XPD X-ray Photoelectron Diffraction, and LEED Low Electron Energy Diffraction.

The first attempt to calculate the structure of the adsorbed glycinate was done using a cluster model with 15 Cu atoms and one glycinate molecule [NHP00]. This model is only a crude representation of the real system.

Using the STM, Chen [CFR02] suggested that the adsorption of glycinate on Cu(110) induces chirality on the surface. The high-resolution STM images show two different molecular arrangements in the unit cell: the homochiral with a pseudo-centered structure and the heterochiral with clear glide plane symmetry (see Figure Glycinate 2).

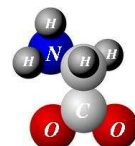
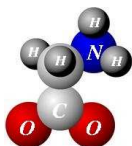
Figure Glycinate 2: The experimental STM images propose two possible configurations: homochiral domain (left panel) and heterochiral domain (right panel) [CFR02].



Other experiments [HKW98, TKW03] suggest that only the heterochiral domain exists and the two different STM images are obtained because an asymmetric object is scanned with an asymmetric tip.

Atom		N atom	O atom
bond length with Cu atom		2.04 ± 0.02	2.02/2.00
displacement from on-top site	$[1\bar{1}0]$ direction	0.24 ± 0.10	0.08/0.22
	$[001]$ direction	0.00 ± 0.15	0.68/0.97

Based on the above experimental data one can imagine four possible adsorption configurations: a heterochiral and a homochiral domain where the two molecules in the unit cell can be rotated relative to each other by 0° or 180° . We have performed ab initio calculations for all four configurations. In the following chapters we first present our results for the free glycinate radical, and then the atomic and electronic structure of these configurations will be discussed.



8.4 Glycinate Free Radical

The atomic and electronic structure of the glycinate radical molecule has been analyzed using LDA and PBE-GGA functionals for exchange-correlation. The calculation has been performed in a box of 17.5x13.5x11.5 Å using one k-point at (000) and a cutoff energy 25 Ry. Using a larger k-point set does not change the results. The exact parameters of the pseudopotentials (for C, N, O) used are given in the Appendix “Parameters and Tests of the PAW-pseudopotentials” (the LDA pseudopotentials include the large partial core-correction, and for the GGA case pseudopotentials with small partial core-correction have been used).

Molecular structure

The geometries obtained using both approximations for the exchange-correlation functional are quite similar. The structure of the glycine radical shown in Figure Glycinate 3 (next page) and the angles and the bond lengths are given in Table Glycinate 1.

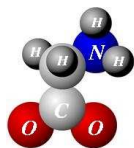
Table Glycinate 1: The calculated bond length and angle for glycinate molecule. The experimental values are from ref. [McG99] and correspond to glycine molecule.

Bond length (Å)				Angles (degree)			
	LDA	GGA	Exp.	Atoms no.	LDA	GGA	Exp.
C ¹ -C ²	1.487	1.456	1.520	H ⁸ -N ⁵ -H ⁹	109.24	111.63	112.5
C ¹ -N ⁵	1.428	1.495	1.463	H ⁸ -N ⁵ -C ¹	111.81	114.94	113.8
C ² -O ³	1.315	1.256	1.223	N ⁵ -C ¹ -H ⁷	110.93	111.50	111.7
C ² -O ⁴	1.310	1.252	-	N ⁵ -C ¹ -C ²	109.65	111.13	110.6
C ¹ -H ⁶	1.148	1.139	1.098	H ⁶ -C ¹ -H ⁷	94.49	104.79	107.4
C ¹ -H ⁷	1.138	1.129	-	O ³ -C ² -O ⁴	117.48	118.26	-
N ⁵ -H ⁸	1.067	1.067	1.000				
N ⁵ -H ⁹	1.065	1.062	-				

The calculated bond lengths are comparable with experimental data obtained for the glycine molecule from microwave spectroscopic results and with other literature data based on theoretical studies of different glycine conformers ([McG99], [HBS99]).

Electronic structure

To understand the electronic bonds in the glycinate radical molecule in a simple approach, one can consider the C² atom as sp² hybridized, having three simple σ bonds with the C¹, O³, O⁴ and a p_z orbital perpendicular on the O³-C²-O⁴ plane. Each of the oxygen atoms has a p_z orbital perpendicular to a plane spanned by the simple σ bond to the carbon C², and two pairs of electrons. Each p_z orbital is occupied with one electron; the p_z orbital of the C² is formally forming two half π -bonds with the oxygen atoms, which are occupied by two electrons, and so one p_z electron will be shared by the two oxygen atoms. As a result the oxygen atoms acquire additional electrons. The weakly bound electrons residing at the N and N atoms are available for the bonding to the Cu(110) surface. The C¹ and N⁵ atoms can be viewed as having sp³ hybridization.



GLYCINATE FREE RADICAL

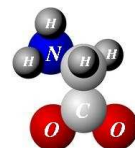
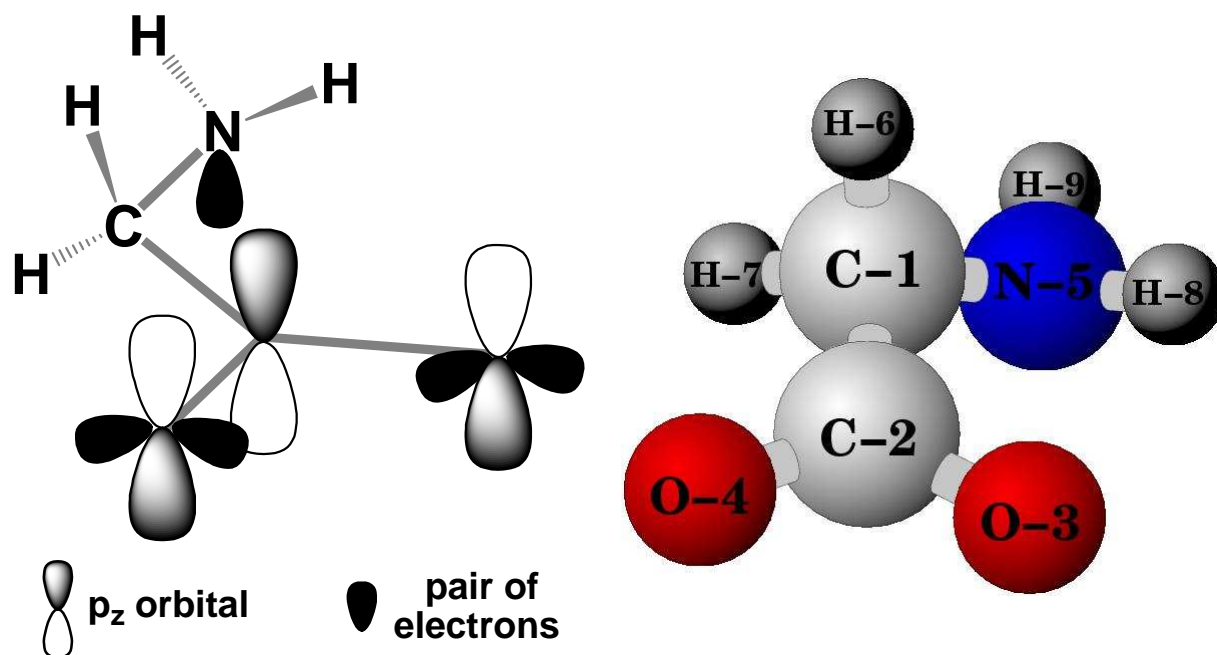


Figure Glycinate 3: Structure of the glycinate radical molecule (right panel) and a schematic view of valence electrons (left).

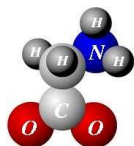


In order to understand the bonds and the electron distribution in the glycinate molecule a calculation of the Partial Local Density of States (PLDOS) in a sphere around each atom has been performed Figure Glycinate 5.

The C¹-H⁶ is simple σ covalent bond. For the H⁶ the bonding states are lying in the interval -12.5 to 0 eV. The distances from H⁶ to the oxygen atoms are large (2.81, 3.16 for LDA and 2.76, 2.83 for GGA respectively), and since there is also a carbon atom in between, an H-O interaction is excluded. The H⁷ has different PLDOS characteristics than H⁶. The H⁷-O⁴ distance is smaller (2.59 for LDA, 2.46 for GGA), and a small interaction exists. It is known that the nitrogen atom is more electronegative than the hydrogen atom. The N-H bond is slightly ionic, so that the PLDOS characteristics are different than for the previous hydrogen atoms.

The carboxylate group shows similar features as for the formate molecule (see Formate 2, 3). The weakly bound electrons are located in the energy range -1.5...0.0 eV. These electrons correspond to combinations of p_z-orbitals (π -system perpendicular on the OCO plane) as well as anti-bonding combinations of p_x, p_y and s orbitals (in the OCO plane). The nitrogen atom has no π -electrons. The peak at -0.5 eV located at the oxygen atoms corresponds to a π -state (see also Figure Formate 2 and 3). It has negligible intensity at the nitrogen atom. The N⁵-atom spectrum shows two peaks at -1.5 and 0.0 eV corresponding to weakly bound electrons that can possibly participate in the binding of the glycine to a metal ion or a metal surface. The bonding states of the N⁵-C¹ are located in the energy range -18.0...-3.5 eV (two low lying s-type states at -15.0 and -13.0 eV and more p-type states in the energy range -8.5...-3.5 eV).

The C²-PLDOS shows predominantly p-type states in the interval -21.0...-3.5 eV which participate in the molecular bonding.



GLYCINATE FREE RADICAL

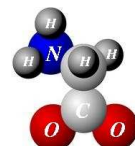
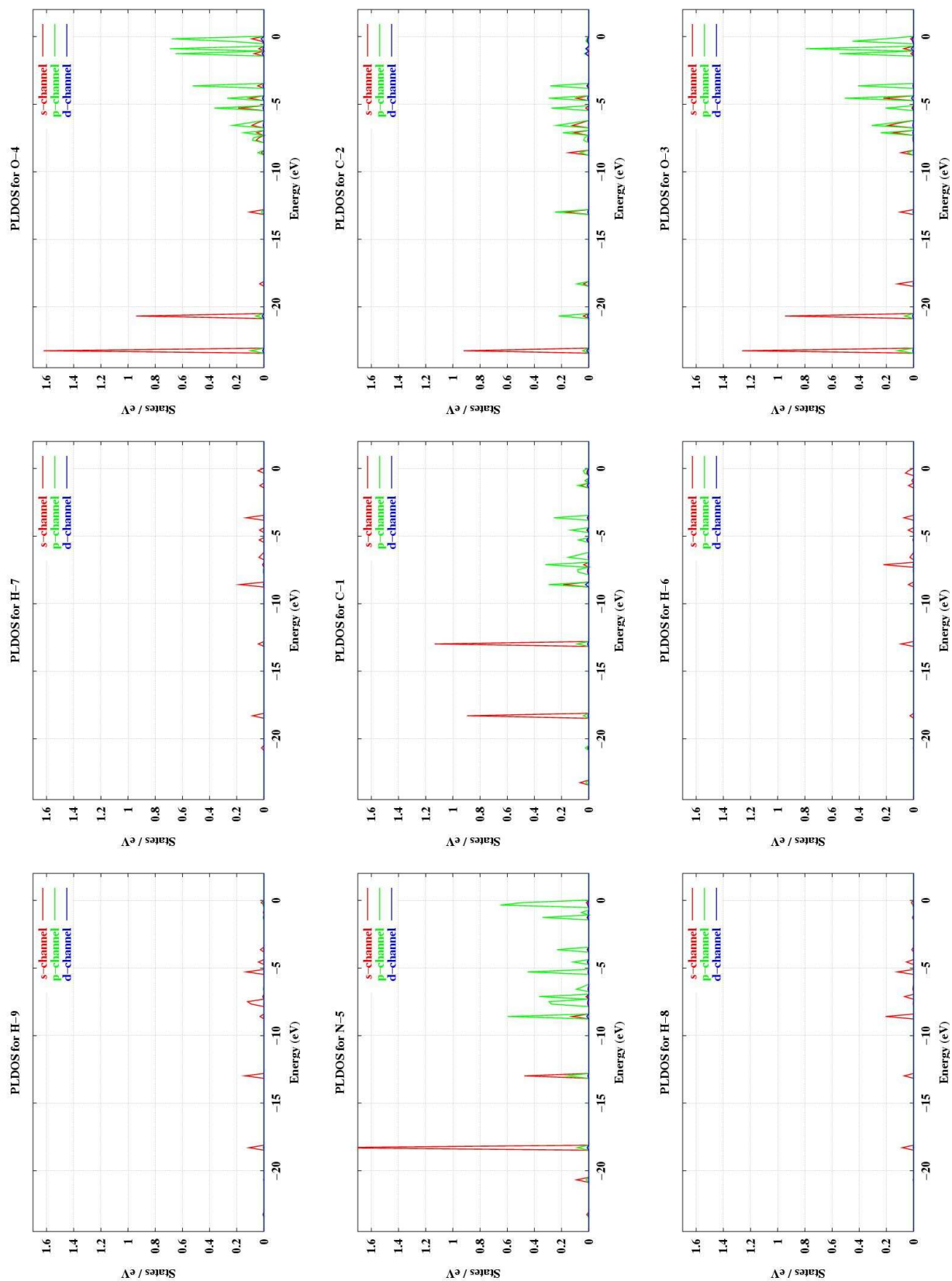
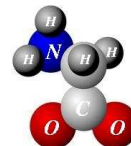
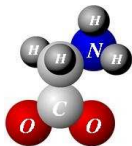


Figure Glycinate 5: GGA Partial local density of states of the glycinate (radical) molecule.





8.5 Glycinate-Cu(110) system

The discussion is arranged in the following way: we first present the energetics of the different configurations and the reason for the order of stability in terms of bond strengths. Then, we present details about the atomic structure and general characteristics of PLDOS-spectra of the adsorbed molecules for the most stable configuration “Heterochiral domain 1”. We discuss the differences with the other configurations, which characterize the different bond geometries and strengths, as well.

The optimized configurations are shown in four figures (Cu-green, O-red, C-gray, N-blue, H-dark grey.):

- Figure “Heterochiral domain 1” where the unit cell contains both enantiomers (“left” and “right”) and direction from the carboxylate group to the amino group of both molecules oriented in $[100]$ direction;
- Figure “Heterochiral domain 2” with the orientation of one molecule turned with 180° to the $[100]$ direction;
- Figure “Homochiral domain 1” with two enantiomers of the same type and both molecules oriented in the $[100]$ direction;
- Figure “Homochiral domain 2” with the orientation of one molecule turned by 180° to the $[100]$ direction.

Computational details

The LDA and GGA calculations of the glycinate on Cu(110) have been performed using an inversion-symmetric slab containing 5 layers of Cu and two glycinate molecules on the each sides of the slab. The unit cell has the dimension $4 \cdot a \cdot \sqrt{2}$ (vertical), $3 \cdot a \cdot \sqrt{2} / 2$, $2 \cdot a$ (lateral) with a being the theoretical bulk lattice constant of the copper-fcc 3.559 Å for LDA and 3.641 for GGA for a **12x12x12** k-point set.

For the LDA calculations a **1x2x2** k-point set has been used and a **1x3x3** in the case of GGA. The vacuum is larger than 7.50 Å for the LDA, and 7.70 Å for the GGA. For both cases (LDA and GGA) an energy-cutoff of 25 Ry was used.

In the starting configurations we have used the previously relaxed positions of the Cu(110) surface, the molecules have been placed such that the N and O atoms are on top of Cu-surface atoms. For all structures the first two layers of the surface and the molecules were allowed to relax without any constraint.

The geometries that have been obtained using the GGA and LDA functional for the exchange-correlation potential are quite similar.

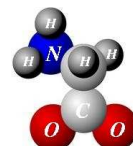
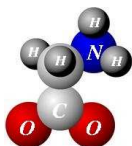
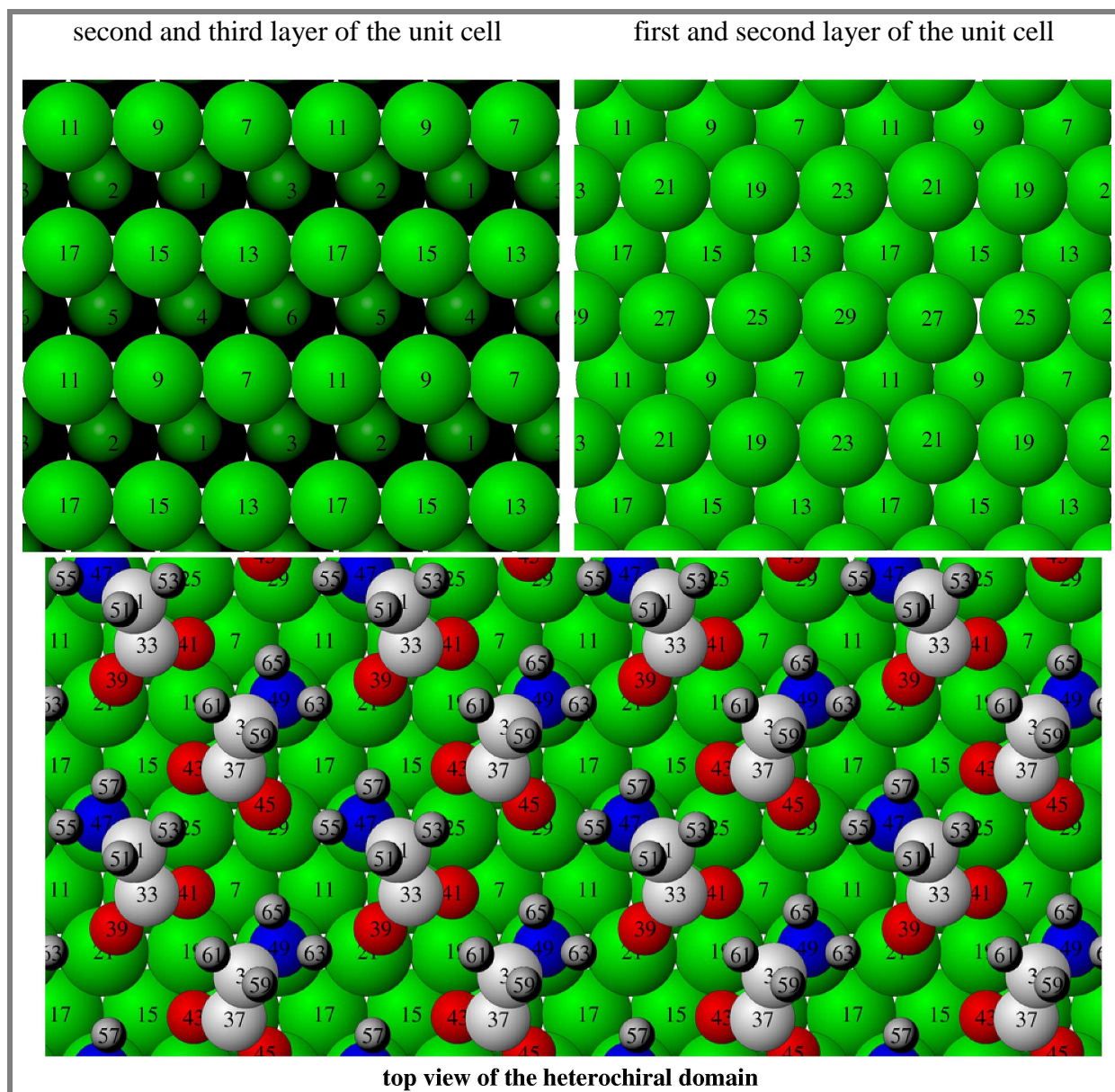


Figure Heterochiral domain 1: The top view of the final relaxed configuration of the “Heterochiral domain 1”. Two different enantiomers are present in the unit cell with the C-C-axis oriented similarly relative to the Cu-surface. The Cu²¹, C¹⁹, C²³ are aligned along to the $[1\bar{1}0]$ direction and Cu²¹ and Cu²⁷ define the $[100]$ direction. Both molecules bind the copper surface strongly via the nitrogen atoms (N⁴⁷, N⁴⁹) that are on top of copper atoms (for each nitrogen atom a single bond with a copper atom is formed). For each molecule one of the oxygen atoms (O³⁹, O⁴⁵) is sitting on top of a copper atom forming a strong bond. The other oxygen atom (O⁴¹, O⁴³) of each molecule is situated in “bridge”-position between two copper atoms along to the $[100]$ direction. Each of the O⁴¹ and O⁴³ forms two bonds with two Cu atoms. The analysis of the distances between the different hydrogen and oxygen atoms of the adsorbed molecules suggests that hydrogen bonds are formed (the shorter ones are between O⁴⁵...H⁵⁵ and O³⁹...H⁶³). The calculated bond lengths between the atoms in the molecules and with the surface are given in Table “Heterochiral domain 1”.



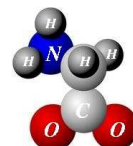
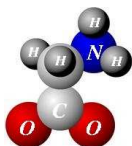
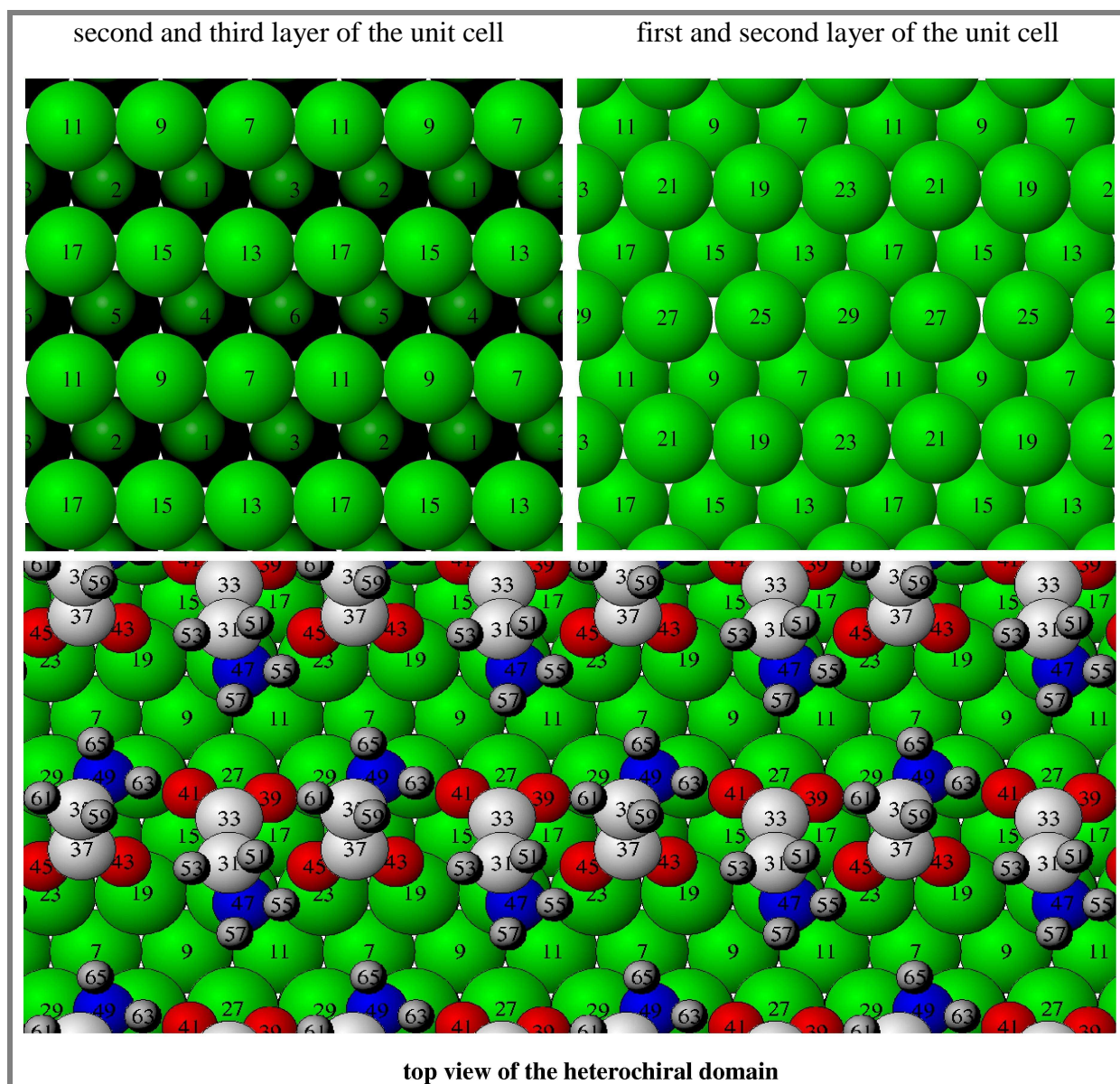


Figure Heterochiral domain 2: Both enantiomers are present in the unit cell but rotated with 180° relative to each other. The minimum energy configuration corresponds to the geometry for which the carboxylic oxygen atoms and nitrogen atom are alternatively aligned along $[1\bar{1}0]$. One of the molecules binds the copper surface strongly via the N⁴⁷ atom that is on top of a copper atom (a single bond with a copper atom is formed) and less with the oxygen atoms because each of them binds two copper atoms. The other molecule binds to the copper surface strongly via the two oxygen atoms that are on top of two neighboring copper atoms and weaker via the nitrogen atom that forms two bonds with two copper atoms of the surface. From the analysis of the H...O distances one can see that hydrogen bonds are formed, which seem to be stronger (because they are shorter) than in the case when the molecules are not rotated (see Table “Heterochiral domain 2”).



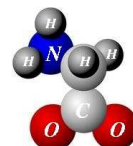
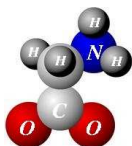
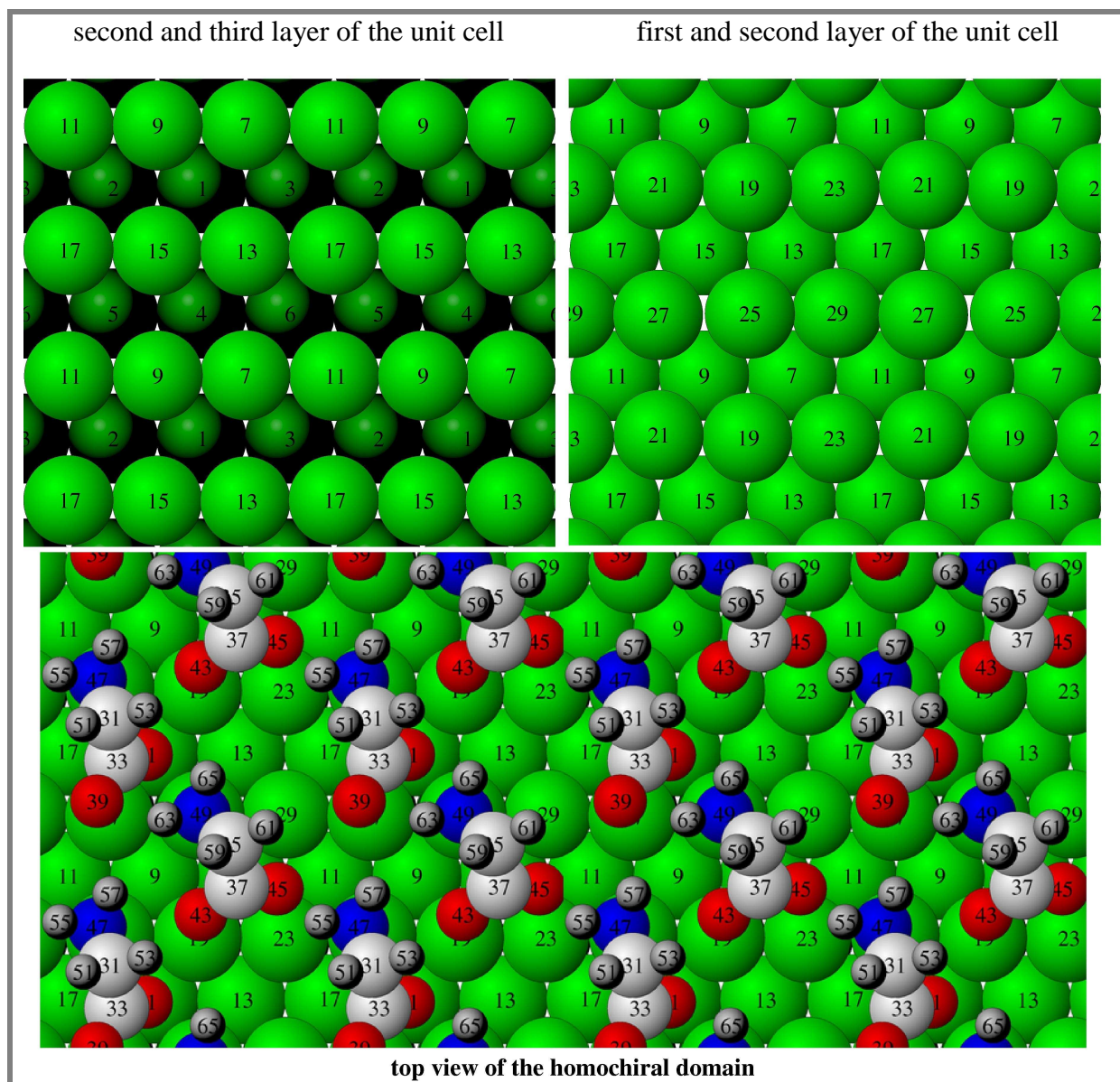


Figure-1 Homochiral domain 1: Two enantiomers of the same type are in the unit cell. For this configuration each of the molecules binds differently to the copper surface. One of the molecules binds to the surface such that each of the nitrogen and oxygen atoms is forming short bonds with a copper atom (around 2 Å). The other molecule binds to the copper surface strongly via the nitrogen atom and less with the oxygen atoms. The analysis of the O...H distances shows that hydrogen bonds are formed (see Table “Homochiral domain 1”).



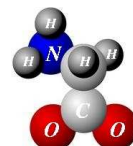
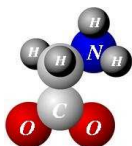
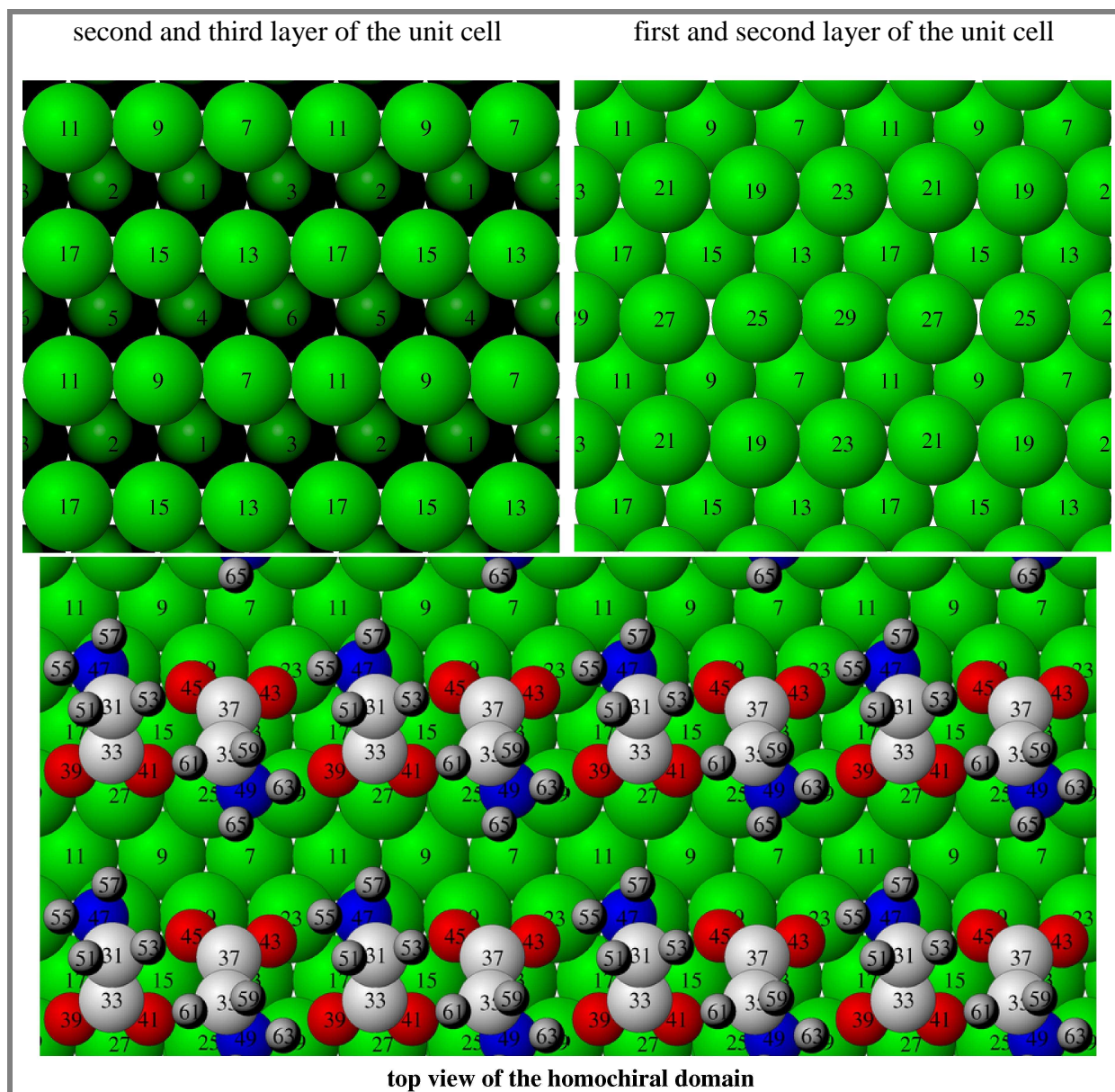


Figure Homochiral domain 2: Two enantiomers of the same type in the unit cell but rotated with 180° relative to each other. In this configuration one of the molecules binds to the copper surface via a strong nitrogen-copper bond and weaker oxygen-copper bonds, since the oxygen atoms are binding two neighboring copper atoms. The other molecule binds to the surface via two strong oxygen-copper bonds and weaker bond with the nitrogen atom. The analysis of the O...H distances shows that between the molecules strong hydrogen bonds are formed (see Table “Homochiral domain 2”).



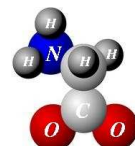
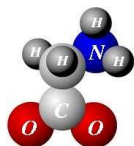
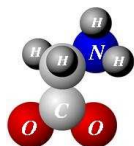


Table Heterochiral domain 1: The important bond lengths for the “Heterochiral domain 1” (for the numbering of the atoms see Figure “Heterochiral domain 1”).

Bond length in the molecules (Å)			Bond length of the Cu-surface atoms with N and O atoms (Å)			O...H distances (Å)		
	LDA	GGA		LDA	GGA		LDA	GGA
C ³¹ -C ³³	1.491	1.517	N ⁴⁷ -Cu ²⁷	2.036	2.109	O ⁴⁵ ...H ⁵⁵	1.980	2.082
C ³⁵ -C ³⁷	1.489	1.513						
C ³¹ -H ⁵¹	1.115	1.114	N ⁴⁹ -Cu ²³	2.028	2.099	O ³⁹ ...H ⁶³	2.024	2.062
C ³⁵ -H ⁵⁹	1.139	1.139						
C ³¹ -H ⁵³	1.136	1.134	O ³⁹ -Cu ²¹	2.191	2.213	O ⁴¹ ...H ⁶¹	2.345	2.234
C ³⁵ -H ⁶¹	1.136	1.133						
C ³¹ -N ⁴⁷	1.467	1.487	O ⁴¹ -Cu ¹⁹	2.308	2.229	O ⁴³ ...H ⁵³	2.452	2.456
C ³⁵ -N ⁴⁹	1.465	1.489						
N ⁴⁷ -H ⁵⁵	1.080	1.080	O ⁴¹ -Cu ²⁵	2.464	2.543	O ⁴¹ ...H ⁶⁵	2.542	2.436
N ⁴⁹ -H ⁶³	1.082	1.079						
N ⁴⁷ -H ⁵⁷	1.080	1.076	O ⁴⁵ -Cu ²⁹	2.191	2.223	O ⁴³ ...H ⁵⁷	2.615	2.543
N ⁴⁹ -H ⁶⁵	1.080	1.075						
C ³³ -O ³⁹	1.319	1.329	O ⁴³ -Cu ²⁵	2.229	2.281	O ³⁹ ...H ⁶¹	2.985	2.879
C ³⁷ -O ⁴³	1.320	1.335						
C ³³ -O ⁴¹	1.320	1.333	O ⁴³ -Cu ²⁹	2.396	2.481			
C ³⁷ -O ⁴⁵	1.322	1.327						

Table Heterochiral domain 2: The important bond lengths for the “Heterochiral domain 2” (for the numbering of the atoms see Figure “Heterochiral domain 2”).

Bond length in the molecules (Å)			Bond length of the Cu-surface atoms with N and O atoms (Å)			O...H distances (Å)		
	LDA	GGA		LDA	GGA		LDA	GGA
C ³¹ -C ³³	1.550	1.575	N ⁴⁷ -Cu ²¹	2.196	2.208	O ⁴⁵ ...H ⁵⁵	2.633	2.682
C ³⁵ -C ³⁷	1.490	1.496						
C ³¹ -H ⁵¹	1.134	1.101	N ⁴⁹ -Cu ²⁵	2.391	2.429	O ³⁹ ...H ⁶¹	1.860	1.961
C ³⁵ -H ⁵⁹	1.146	1.137	N ⁴⁹ -Cu ²⁹	2.615	2.754			
C ³¹ -H ⁵³	1.128	1.128	O ³⁹ -Cu ²⁷	2.269	2.285	O ⁴¹ ...H ⁶³	1.390	1.329
C ³⁵ -H ⁶¹	1.130	1.124						
C ³¹ -N ⁴⁷	1.479	1.497	O ³⁹ -Cu ²⁹	2.468	2.512	O ⁴³ ...H ⁵³	3.290	3.218
C ³⁵ -N ⁴⁹	1.464	1.464						
N ⁴⁷ -H ⁵⁵	1.085	1.067	O ⁴¹ -Cu ²⁷	2.440	2.507	O ⁴⁵ ...H ⁵¹	2.653	2.685
N ⁴⁹ -H ⁶³	1.110	1.072						
N ⁴⁷ -H ⁵⁷	1.088	1.089	O ⁴¹ -Cu ²⁵	2.476	2.563			
N ⁴⁹ -H ⁶⁵	1.067	1.060						
C ³³ -O ³⁹	1.317	1.338	O ⁴⁵ -Cu ²³	1.962	2.030			
C ³⁷ -O ⁴³	1.300	1.342						
C ³³ -O ⁴¹	1.329	1.353	O ⁴³ -Cu ¹⁹	2.015	2.078			
C ³⁷ -O ⁴⁵	1.308	1.336						



GLYCINATE-Cu(110) SYSTEM

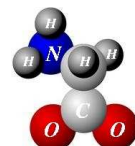
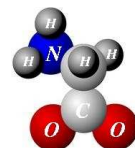
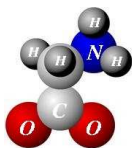


Table Homochiral domain 1: The important bond lengths for the “Homochiral domain 1” (for the numbering of the atoms see Figure “Homochiral domain 1”).

Bond length in the molecules (Å)			Bond length of the Cu-surface atoms with N and O atoms (Å)			O...H distances (Å)		
	LDA	GGA		LDA	GGA		LDA	GGA
C ³¹ -C ³³ C ³⁵ -C ³⁷	1.491 1.481	1.510 1.504	N ⁴⁷ -Cu ²¹	2.061	2.127	O ⁴⁵ ...H ⁵⁵	1.737	1.601
C ³¹ -H ⁵¹ C ³⁵ -H ⁵⁹	1.122 1.139	1.117 1.134	N ⁴⁹ -Cu ²³	2.034	2.111	O ³⁹ ...H ⁶³	2.021	2.089
C ³¹ -H ⁵³ C ³⁵ -H ⁶¹	1.140 1.137	1.136 1.131	O ³⁹ -Cu ²⁷	2.465	2.534	O ⁴¹ ...H ⁶⁵	2.223	2.301
C ³¹ -N ⁴⁷ C ³⁵ -N ⁴⁹	1.454 1.460	1.468 1.467	O ⁴¹ -Cu ²⁷	2.359	2.413	O ⁴³ ...H ⁵³	2.222	2.284
N ⁴⁷ -H ⁵⁵ N ⁴⁹ -H ⁶³	1.083 1.086	1.080 1.180	O ⁴¹ -Cu ²⁵	2.565	2.792	O ⁴¹ ...H ⁶³	2.271	2.338
N ⁴⁷ -H ⁵⁷ N ⁴⁹ -H ⁶⁵	1.080 1.072	1.074 1.071	O ⁴⁵ -Cu ²³	2.0564	2.003	O ³⁹ ...H ⁶³	2.021	2.089
C ³³ -O ³⁹ C ³⁷ -O ⁴³	1.315 1.316	1.322 1.323	O ⁴³ -Cu ¹⁹	2.0291	2.056			
C ³³ -O ⁴¹ C ³⁷ -O ⁴⁵	1.331 1.334	1.342 1.336						

Table Homochiral domain 2: The important bond lengths for the “Homochiral domain 2” (for the numbering of the atoms see Figure “Homochiral domain 2”).

Bond length in the molecules(Å)			Bond length of the Cu-surface atoms with N and O atoms (Å)			O...H distances (Å)		
	LDA	GGA		LDA	GGA		LDA	GGA
C ³¹ -C ³³ C ³⁵ -C ³⁷	1.489 1.490	1.523 1.527	N ⁴⁷ -Cu ²¹	2.070	2.136	O ⁴⁵ ...H ⁵³	2.000	1.991
C ³¹ -H ⁵¹ C ³⁵ -H ⁵⁹	1.137 1.142	1.131 1.137	N ⁴⁹ -Cu ²⁵ N ⁴⁹ -Cu ²⁹	2.400	2.376	O ³⁹ ...H ⁶³	1.553	1.643
C ³¹ -H ⁵³ C ³⁵ -H ⁶¹	1.127 1.128	1.124 1.123	O ³⁹ -Cu ²⁷	2.589	2.660	O ⁴¹ ...H ⁶¹	2.002	1.989
C ³¹ -N ⁴⁷ C ³⁵ -N ⁴⁹	1.473 1.465	1.492 1.485	O ³⁹ -Cu ²⁹	2.434	2.508	O ⁴³ ...H ⁵⁵	1.710	1.758
N ⁴⁷ -H ⁵⁵ N ⁴⁹ -H ⁶³	1.087 1.092	1.077 1.084	O ⁴¹ -Cu ²⁷	2.064	2.103			
N ⁴⁷ -H ⁵⁷ N ⁴⁹ -H ⁶⁵	1.079 1.073	1.073 1.072	O ⁴¹ -Cu ²⁵	2.505	2.598			
C ³³ -O ³⁹ C ³⁷ -O ⁴³	1.305 1.301	1.313 1.326	O ⁴⁵ -Cu ²³	2.006	2.072			
C ³³ -O ⁴¹ C ³⁷ -O ⁴⁵	1.311 1.305	1.332 1.318	O ⁴³ -Cu ¹⁹	2.242	2.293			



Energetics and Bond Strength

For the final relaxed configurations the bond lengths between the atoms of the molecule are very little changed from the C-C, C-N, C-O, N-H and C-H bonds in the free radical, that means that the molecules bind the surface as an entity and no elongation or strong intramolecular deformation occurs. The Cu atoms do not show a specific reconstruction of the copper surface under the molecular layer, they remain close to the positions of the clean Cu(110) surface.

The most stable configuration is found to be the “Heterochiral domain 1”. The Table Glycinate on Cu (110) system contains the energy differences of the calculated structures. The most stable one is taken as reference (zero level). The positive energies indicate the decreasing of stability of the given configuration. The Figures “Heterochiral domain 1”, “Heterochiral domain 2”, “Homochiral domain 1”, “Homochiral domain 2” show the top views of the final relaxed configurations.

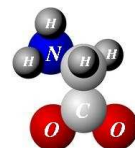
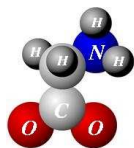
Table Glycinate on Cu (110) system: (The energies are expressed in eV)

Domain	Heterochiral (0 rotated)	Homochiral (0 rotated)	Homochiral (180 rotated)	Heterochiral (180 rotated)
LDA	0.000	0.823	2.129	3.128
GGA	0.000	0.770	1.235	2.482

The stability can be explained in terms of the chemical interaction of the molecules with the atoms of the copper surface (When quoting numbers we refer to the GGA-results). In the most stable configuration, “Heterochiral domain 1”, six strong bonds are formed: two N-Cu bonds of 2.10 Å and four O-Cu bonds of 2.21 up to 2.28 Å. Also, between the molecules two hydrogen bonds are formed (see Figure “Heterochiral domain 1” and Table “Heterochiral domain 1”).

In the “Homochiral domain 1” four strong bonds are formed: two N-Cu bonds and another two Cu-O bonds of one molecule. The other two Cu-O bonds of the second molecule are longer by 0.3 to 0.4 Å, and are thus much weaker. In this configuration three strong hydrogen bonds are formed, one more than in the previous configuration. It is known that a hydrogen bond reduces the energy by some tenths eV, but this is not enough to compensate the weaker Cu-O bonds (see Figure “Homochiral domain 1” and Table “Homochiral domain 1”). Thus the “Heterochiral domain 1” has the lower energy due to the strong Cu-O and Cu-N bonds.

In the “Homochiral domain 2”, where the molecules are 180° rotated relative to each other in the unit cell, only three strong bonds are formed: one Cu-N of one molecule and two Cu-O bonds of the other molecule. The other Cu-N and Cu-O are weaker since they are elongated by 0.37 to 0.45 Å compared to the other ones. The molecules interact strongly along the $[1\bar{1}0]$ direction and not at all in the $[100]$ direction (see “Figure Homochiral domain 2” and “Homochiral domain 2”). This can be nicely seen in Figure “Glycinate-Cu(110) system” (left panel) which shows a top view of the absorbed molecules together with a surface of constant electron charge.



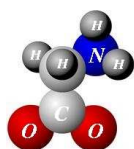
For the last configuration, “Heterochiral domain 2”, the arrangement of the molecules in the unit cell weakens the interaction of the molecules with the surface even more. Only two strong Cu-O bonds are formed. The presence of both enantiomers in the unit cell and the rotation relative to each other places one nitrogen atom on top of a copper atom. This interacts with an oxygen atom of the other molecule, as well. So, the Cu-N bond length is longer by 0.07 Å than in the “Homochiral domain 2”. The other Cu-N and Cu-O bond lengths are quite large; also from the analysis of the H...O distances one sees that only two strong H...O interactions exist (see Figure “Heterochiral domain 2” and Table “Heterochiral domain 2” and also Figure “Glycinate-Cu(110) system”: right panel).

Our conclusion is that the chemical bonds of the nitrogen and oxygen atoms of the molecules with the copper-surface atoms make the difference in the stability of the different structures. The arrangement where stronger bonds with the surface atoms are formed is more stable. For the “Heterochiral domain 1” the molecules adsorbed at the surface are arranging themselves in a more homogeneous structure compared with the other structures (see Figure “Glycinate-Cu(110) system” where a top view of the absorbed molecules together with a surface of constant electron charge for relaxed configuration is presented). Although for some structures more or stronger hydrogen bonds are formed they do not have a big influence on the relative stability of the configurations.

Our results for the most stable configuration (Heterochiral domain 1) are in good agreement with the LEED patterns [BWS98] that show the presence of glide plane symmetry in the surface unit cell. One should mention that this glide plane symmetry couldn’t formally occur in the Homochiral domains. Also, the N-Cu bond 2.10 (2.03) Å for GGA (LDA) are in good agreement with the 2.04 determined experimentally by XPD [HKW98].

The two nitrogen atoms in the “Heterochiral domain 1” are practically equivalently displaced along the $[1\bar{1}0]$ direction (N^{47} 0.03 Ås and N^{47} 0.04 Å) and only two distinct oxygen positions are present in the system, as well. Contrary, for the “Homochiral domain 1” the two nitrogen atoms occupy non-equivalent positions. Also, there are four different copper-oxygen bonds, which is inconsistent with XPD data [TKW03].

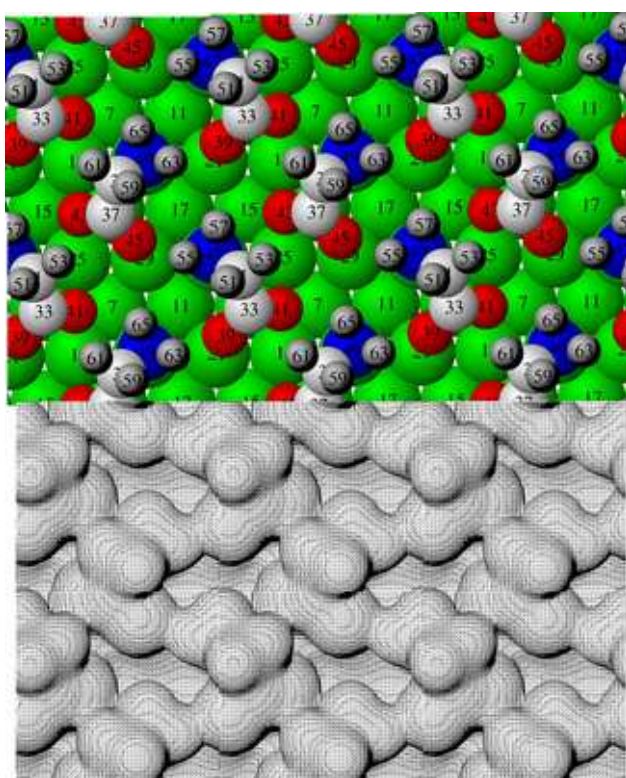
Another important observation is that for the “Heterochiral domain 1” the hydrogen atoms bonded to the carbon atom are nonequivalent and distinct relative to the surface: one hydrogen bond is almost parallel, and the other one is perpendicular to the surface. This makes the carbon atom a *chiral* center in the molecule. For the “Homochiral domain 1”, where the molecules are binding differently to the copper surface, just one molecule in the unit cell has a chiral carbon, for the other molecule the C-H bonds angles relative to the surface are 57° and 28°, and are thus less distinct.



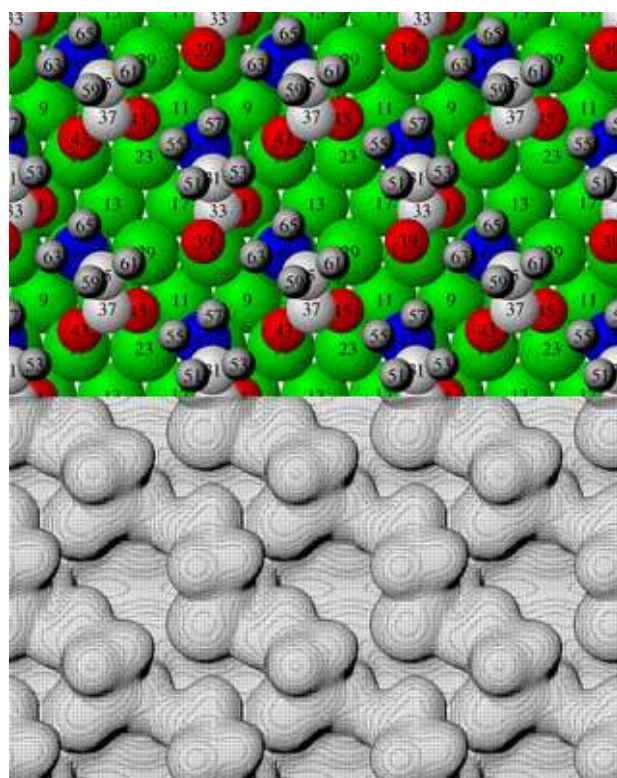
GLYCINATE-Cu(110) SYSTEM



Figure Glycinate-Cu(110) system: Top views of the absorbed molecules together with a surface of constant electron charge for relaxed configuration.



(Molecules are with 0° rotated relative to each other)
Heterochiral domain 1

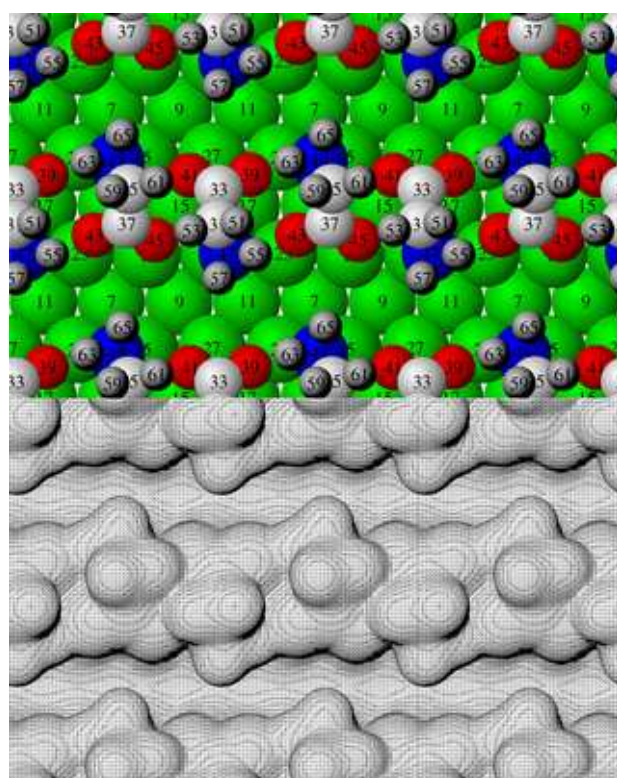
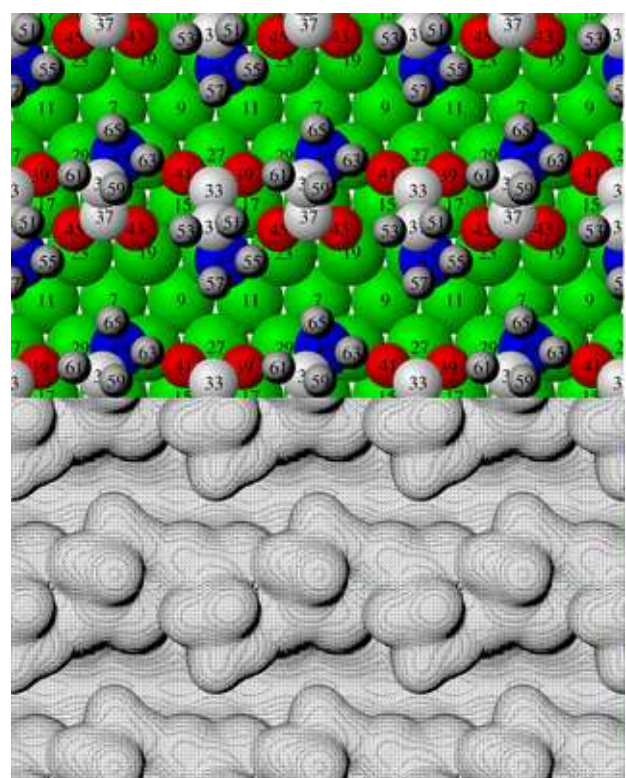


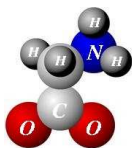
Homochiral domain 1

Heterochiral domain 2

(Molecules are with 180° rotated relative to each other)

Homochiral domain 2





Atomic and Electronic Structure

In the following will present some details of the atomic structure and some general characteristics of PLDOS-spectra for the molecules' atoms of the relaxed configurations. At first, we will discuss the characteristics of the most stable configuration, "Heterochiral domain 1", and then some specifics of the other ones.

Heterochiral domain 1: both enantiomers are present in the unit cell

The molecules, oriented with their main axis N-C-C along to the $[100]$ direction, are forming alternatively bridges between Cu atoms of the surface. The $C^{31}-H^{51}$ and $C^{35}-H^{59}$ bonds are almost parallel to the normal at the surface. The $C^{31}-H^{53}$ and $C^{35}-H^{61}$ bonds are almost parallel to the surface. The bonds formed by the N and O atoms with the Cu(110)-surface are: $Cu^{21}-O^{39}$, $Cu^{29}-O^{45}$, $Cu^{19}-O^{41}-Cu^{25}-O^{43}-Cu^{19}$, $Cu^{27}-N^{47}$, $Cu^{23}-N^{49}$ (see Figure "Heterochiral domain 1" and Table "Heterochiral domain 1").

The O^{39} and O^{45} are displaced from on top position of the Cu atoms along to $[001]$ direction. The O^{41} and O^{43} are binding alternatively both Cu^{19} and Cu^{25} . They are situated in a bridge position between these copper atoms along to $[100]$ direction. The positions of O^{39} and O^{45} atoms can be practically considered equivalent. The other atoms O^{41} , O^{43} are in equivalent positions, as well. The N atoms are situated in equivalent positions relative to the on top Cu atoms. They are displaced from the ideal top site positions of the Cu(110) surface in opposite directions (with 0.03 and 0.05 Å) along $[1\bar{1}0]$. The Cu atoms that are binding these nitrogen atoms are slightly following the nitrogen displacement (0.01 and 0.02 Å).

The electronic structure of the molecules' atoms is analyzed with the help of Partial Local Density of States (PLDOS). Compared with the spectra of isolated radical, we generally observe a shift of all peaks to lower energy (Figure-1, 2 PLDOS "Heterochiral domain 1"). The low-lying s-type peaks ($\ll -13.0$ eV) are shifted almost rigidly due to the change of average potential when the molecules bind the Cu surface. In addition, the states close to the Fermi energy down to -5.0 eV are individually shifted due to the hybridization when the respective orbitals are participating in bonding to Cu atoms. This is characteristic for the N atom of the amino group and O atoms of the carboxylate group. We expect that all p-electrons residing on the N and O atoms corresponding to these states participate in binding to the Cu surface.

The analysis of the distances between the different hydrogen and oxygen atoms of the adsorbed molecules suggest that hydrogen bonds are formed. All hydrogen atoms have different PLDOS-spectra. We conclude that oxygen-hydrogen interaction cannot be excluded.

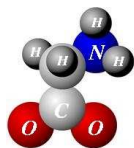
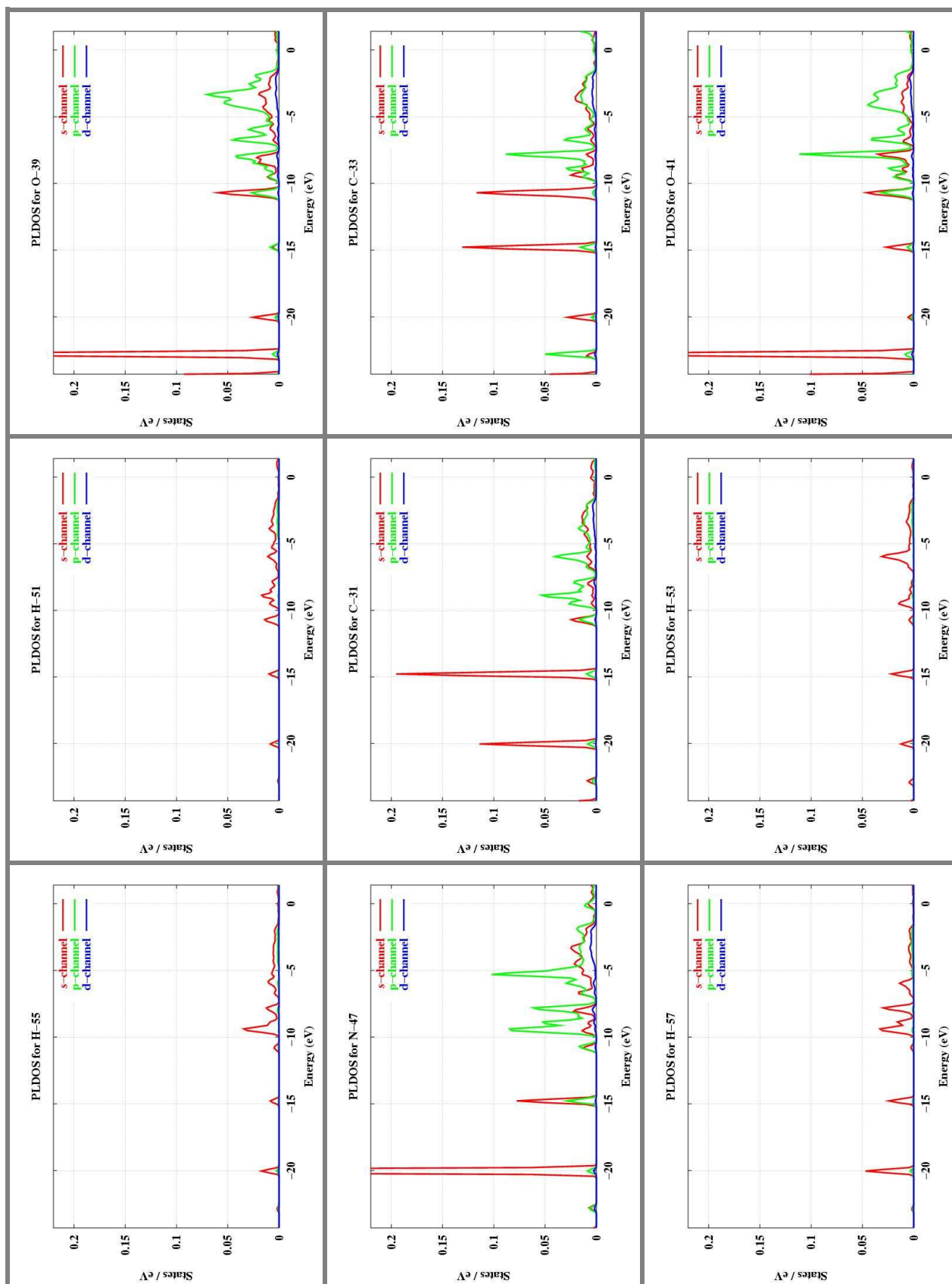


Figure-1 PLDOS Heterochiral domain 1: GGA-PLDOS of the first molecule's atoms: N⁴⁷, C³¹, C³³, O³⁹, O⁴¹, H⁵¹, H⁵³, H⁵⁵, H⁵⁷. (The deeper s-type state at -23.53 eV is not shown)



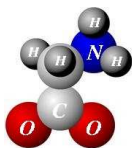
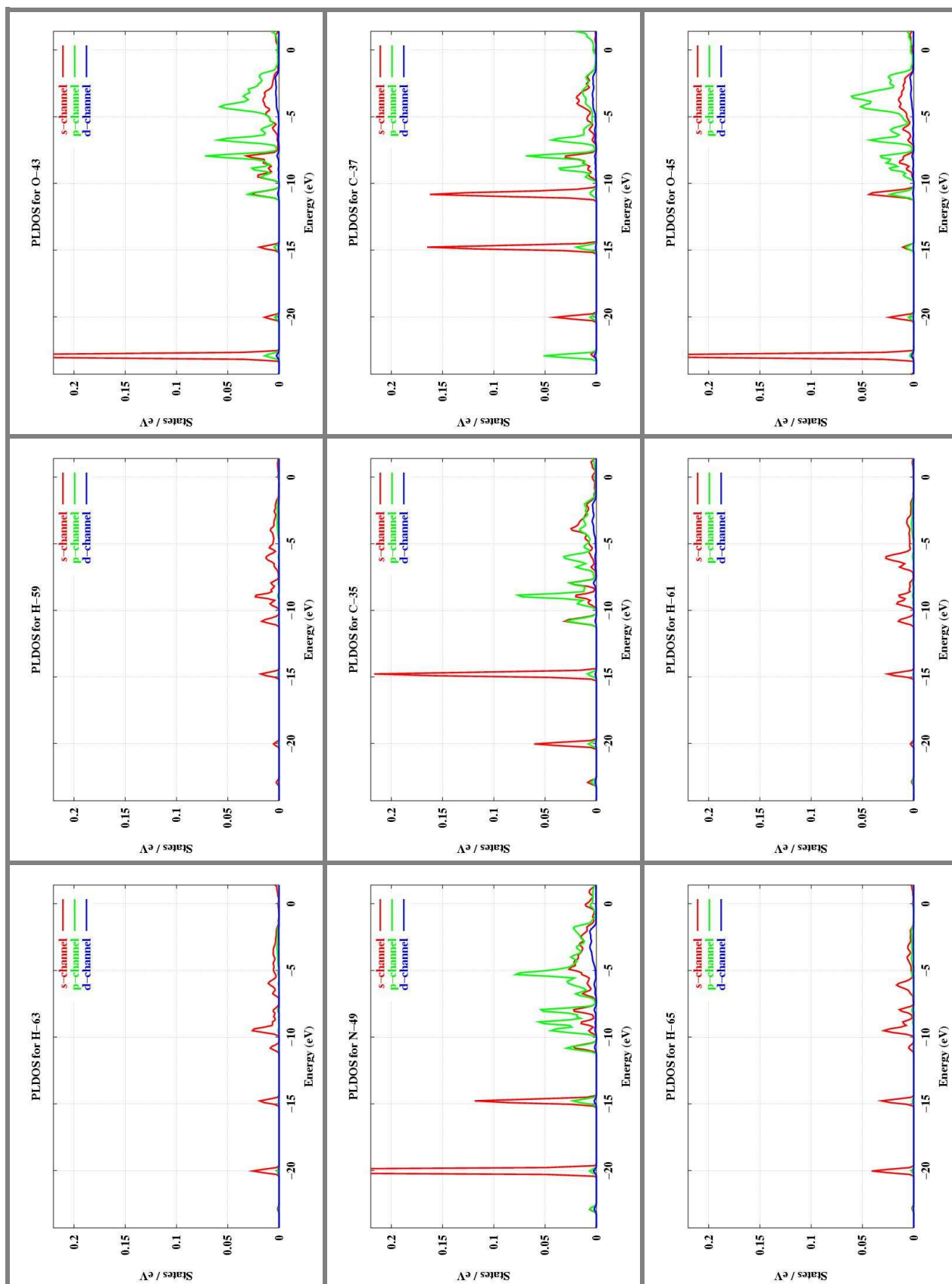
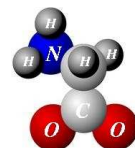
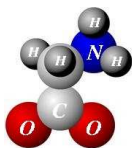


Figure-2 PLDOS Heterochiral domain 1: GGA-PLDOS of the second molecule's atoms: N⁴⁹, C³⁵, C³⁷, O⁴³, O⁴⁵, H⁵⁹, H⁶¹, H⁶³, H⁶⁵. (The deeper s-type state at -23.53 eV is not shown).



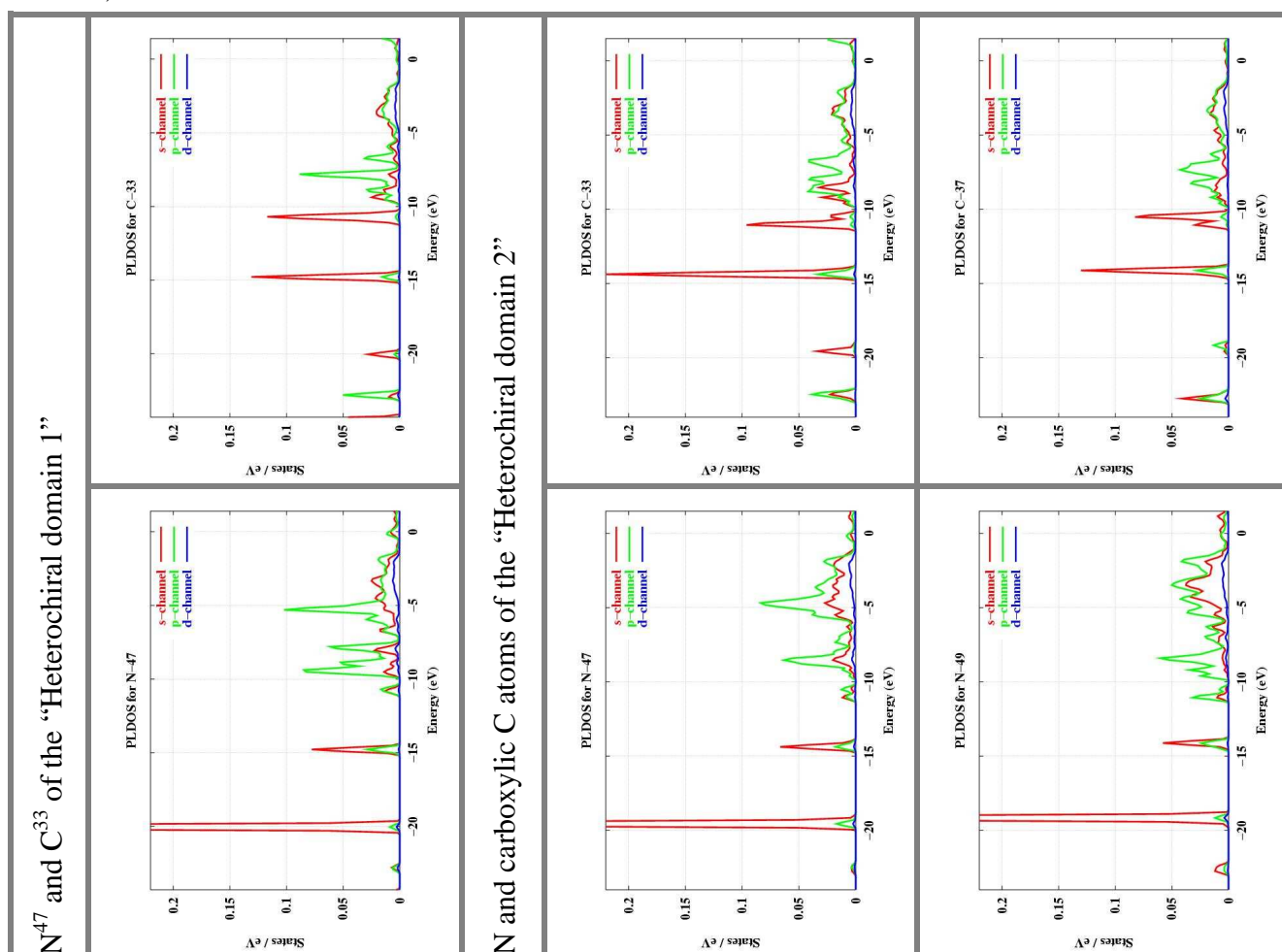


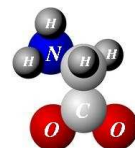
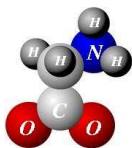
Heterochiral domain 2: both enantiomers are present in the unit cell but rotated with 180° relative to each other.

The starting configuration has been chosen with the nitrogen and oxygen atoms on top of copper atoms. Due to the interaction between molecules, the final configuration has one molecule with the nitrogen atom in a bridge position between neighboring copper atoms along to $[1\bar{1}0]$ direction and the oxygen atoms in top of copper atoms. The other molecule has the nitrogen on a top position and the oxygen atoms in bridge ones. The analysis of both geometrical and electronic configurations shows that each of the molecules is binds different the copper surface (see Figure “Heterochiral domain 2” and Table “Heterochiral domain 2”).

Compared to previous configuration, “Heterochiral domain 1”, no interaction between the molecules along to the $[100]$ direction is observed (see Figure “Heterochiral domain 2” and Figure “Glycinate-Cu(110) system” left panel).

Figure-1 PLDOS Heterochiral domain 2: The different characteristics of N and carboxylic C atoms for the Heterochiral domain 2 compared with N and C atoms of the most stable configuration “Heterochiral domain 1”. (i) For the N atoms of the “Heterochiral domain 1” these high p-type peaks are below -5.0 eV, but for the N atoms of the “Heterochiral domain 2” these peaks are above -5.0 eV; (ii) The carboxylic carbon (C^{33}) of the “Heterochiral domain 1” has a nearly degenerate peak around -11.0 eV. This is clearly split in two peaks for the carboxylic carbon atoms (C^{33} , C^{37}). Moreover, relative intensity of these two is different and depends if the oxygen atoms are occupying on-top positions (for C^{37}) or bridge position (for C^{33}).





The O^{43} and O^{45} are forming a single bond with the Cu^{19} and Cu^{23} atoms.

Relative to the copper surface their position can be considered equivalent. Each of the O^{39} and O^{41} are forming two bonds with copper nearest neighbors. These oxygen atoms are situated in bridge positions along to the $[1\bar{1}0]$ direction and practically their position is equivalent relative to the copper surface (see Figure “Heterochiral domain 2”). We conclude that the carboxylate groups bind different the Cu surface compared with the “Heterochiral domain 1”. The PLDOS of all oxygen atoms shows similar characteristics, but differences can be seen in the PLDOS-spectra of the carboxylic carbons (see Figure-1 PLDOS “Heterochiral domain 2”).

There are two different N-Cu bond lengths (with N^{47} slightly displaced from on-top position and N^{49} in bridge position). The PLDOS-spectra of the two nitrogen atoms has different p-type characteristics in the binding energy range -10.0 up to -2.0 eV. For the “Heterochiral domain 1” N^{47} has the p-type peak at slightly below -5.0 eV. This peak is slightly above -5.0 eV for the “Heterochiral domain 2” (see Figure-1 PLDOS “Heterochiral domain 2”).

Homochiral domain 1: two enantiomers of the same type in the unit cell.

The carboxylate group of one molecule binds the surface via the O^{43} and O^{45} atoms. The bond lengths have similar length although O^{43} is with 0.73 Å and O^{45} with 1.44 Å displaced from on-top positions along to $[100]$ direction. For the other carboxylate group, O^{41} is situated in a hollow site between four copper atoms of the first layer and on top of a copper atom from the second layer. It forms weaker bonds with all of them. The O^{39} is displaced along to $[1\bar{1}0]$ direction with 0.70 Ås from on top of a copper atom from the first layer. The bond length is much larger compared with the ones formed by the other oxygen atoms of the other molecule. There are four different positions of the oxygen atoms. Each of the molecules binds different the copper surface. The corresponding PLDOS shows slightly different characteristics.

The N^{49} is sitting on top of a copper atom and the N^{47} is displaced along to the $[1\bar{1}0]$ direction with 0.4 Å. The bond lengths are almost equal and their corresponding PLDOS-spectra show similar characteristics.

Homochiral domain 2: two enantiomers of the same type in the unit cell but rotated with 180° relative to each other.

The starting configuration has been chosen with the oxygen and nitrogen atoms situated on top of the copper atoms. Due to the interaction between molecules, including hydrogen bonds, the final relaxed configuration has two of the oxygen and one nitrogen atoms in the bridge positions along to $[1\bar{1}0]$ direction. There are no interactions between the molecules along to $[001]$ direction (see Figure “Glycinate-Cu(110) system”).

Relative to the copper surface can be considered that two by two the oxygen positions are equivalent. The PLDOS-spectra of the O and N atoms shows similar characteristics. The carboxylic carbon atoms show different characteristics in PLDOS-spectra (see Figure-1 “Homochiral domain 2”). The trend is the same as in for the “Heterochiral domain 2”.

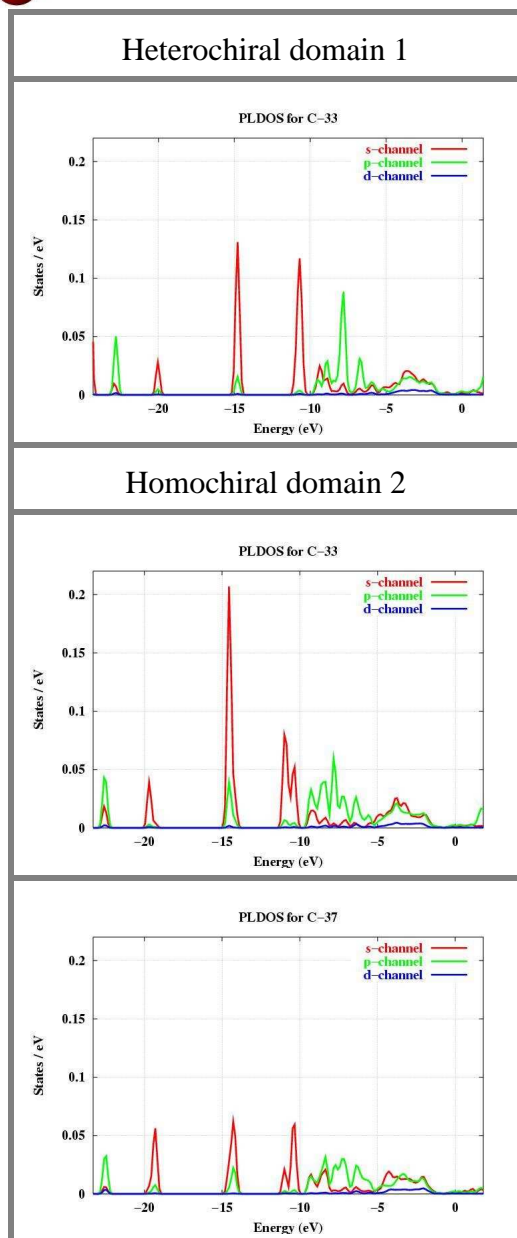
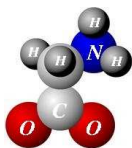


Figure-1 PLDOS Homochiral domain 2: The different characteristics of carboxylic C atoms for the “Homochiral domain 2” compared with carboxylic C atom of the most stable configuration “Heterochiral domain 1”.

The carboxylic C of the “Heterochiral domain 1” has a nearly degenerate s-type peak around -11.0 eV. For the “Homochiral domain 2”, the interactions between the molecules, and with the Cu-surface atoms, as well, have as main effect the clear splitting of this s-type peak. The splitting can be seen also in the “Heterochiral domain 2” where the molecules are with 180° rotated relative to each other.

We conclude that the most stable configuration is the “Heterochiral domain 1”, where both enantiomers are present in the unit cell with 0° rotated relative to each other. The molecules are lying flat and bind to the surface via both functional groups (carboxylate -COO- and amino H₂N-). In this configuration short and strong Cu-N and Cu-O bonds are formed. For one molecule the N and one O atom are slightly displaced from on-top Cu-sites. The other O atom is forming a bridge between two Cu-surface atoms along to [100] direction. The N atoms of the molecules have equivalent positions and the four O atoms occupy two distinct positions relative to the Cu surface. The hydrogen atoms that bind the carbon atom are nonequivalent and distinct relative to the surface: one bond direction is almost parallel and the other is almost perpendicular to the surface. This shows that the carbon atom is a *chiral* center in the molecule. There are interactions between the adsorbed glycinate molecules via hydrogen bonds. We assume that two stronger hydrogen bonds are formed.

Summary and Outlook

In the following, we summarize the main contributions of the present work for the understanding of the interaction between organic molecules with the Cu(110) surface by performing *ab initio* calculations. We have used the program package **EStCoMPP** (Electronic Structure Code for Material Properties and Processes) that is based on density functional theory, pseudopotential and supercell approaches.

In order to describe accurately the molecule-metal surface interaction we have implemented the generalized gradient approximation (GGA) ([PW92], [PBE96-98]) for the exchange-correlation functional in the **EStCoMPP**-package. This includes two atomic generation programs (one used to generate norm-conserving type pseudopotentials of the Kleinman-Bylander form (**KB**) [BHS82, KB82], and the other used to generate non-norm-conserving type pseudopotentials using the projector-augmented plane wave method (**PAW**) [Blö94, Kro01]) and the main program used in the solid-state calculations. In the main program the gradient-corrected exchange-correlation functional can be evaluated using two schemes: a traditional scheme¹ [PBE92, PBE96-97] and a new scheme proposed by White and Bird² [WB94]. In addition, a new scheme to calculate the partial core-correction charge³ (PCC) in real space has been implemented.

A series of pseudopotentials have been generated: Si, Cd, S, Ti, O, Cu, N, C, Pt, Ga (PAW-type) and Sr (KB-type). Several calculations including various bulk crystals (Si-cubic, Cd-hex, CdO-cubic, CdS-cubic, CdS-hex, SrO, TiO-cubic, SrTiO₃-sc, SiO₂-hex, TiN-cubic, Pt-cubic, PtGa₂-cubic, Cu-cubic) and molecules (SiH₃, NO, CO, CN, O₂, NH₃, CH₄, formate, 3-thiophene carboxylate and glycinate) have been performed in order to verify the accuracy of our generated pseudopotentials, and the approximations to the exchange-correlation functional. All tests show that our results are in good agreement with experimental and theoretical data in the literature.

¹ The traditional scheme uses the second order derivatives whose calculation requires the use of a high-quality representation of the density on the FFT-grid.

² In this formulation the total exchange-correlation potential and energy are exactly calculated on the minimum FFT-grid by using a product of first order gradients instead of second order derivatives.

³ This approach takes into account the tail of the core-electrons in the calculation of the exchange-correlation potential and energy. The real space implementation avoids the oscillations, and negative values of the real space charge, when the FFT is performed on a finite plane-wave basis set.

Cadmium Complexes in Si and Ge

Using the local density approximation (LDA) we have performed calculations in order to search for the correct local geometry of the Cd-vacancy and Cd-interstitial complexes in Si and Ge. We found that for both Si and Ge the substitutional Cd-vacancy complex is unstable and relaxes to a split vacancy complex with the Cd on the bond center site. Also, for the Cd-interstitial complex we obtained a highly symmetrical split configuration. For these geometries a collaboration group [HH03] has calculated the electric field gradients (EFG's) of these complexes and found that they are in good agreement with experiments.

The main part of this thesis is the investigation of the bonding of the carboxylate group of several molecules to the Cu(110) surface: formate, 3-thiophene carboxylate (planar molecules) and glycinate (3-dimensional structure).

This is prerequisite for the study of possible applications of organic molecules in catalysis, sensors, adhesion, corrosion inhibition, molecular recognition, optoelectronics lithography and molecular (bio)electronic devices.

Formate molecule

Several geometries corresponding to low and high coverages of formate molecules in a (2x2) unit cell on clean and oxygen-precovered Cu surface have been optimized. For all configurations we found that the molecule is sitting with its molecular plane perpendicular to the Cu(110)-surface. For low coverage (one formate molecule in the unit cell) we found that in the stable configuration the molecule is in a bridge position (each oxygen of the carboxylate group binds a single copper atom so that the carboxylate group forms a bridge between two nearest-neighbor copper atoms along to $[1\bar{1}0]$ direction). The Cu surface atoms that are not binding directly to oxygen atoms show inward relaxations as on the clean Cu(110) surface. In contrast, nearly no relaxation relative to the ideal unrelaxed Cu(110) surface is found for the Cu atoms that are forming the bonds with O atoms.

At high coverage (two formate molecules in the unit cell) the most stable configuration is the one with both molecules in bridge positions. The Cu-surface atoms show outward relaxations larger than in the low coverage case. The geometries of both formate molecules are quite similar to that of the molecule at low coverage.

In the case of oxygen-precovered Cu-surface, at high coverage of formate molecules, we find again that the stable configuration is the one with both molecules in bridge positions. A large outward relaxation of the Cu surface layer is found. The molecular geometry of the formate molecules does not change significantly and it is similar as in the previously discussed systems. The extra oxygen atom (the 0.25ML oxygen monolayer) is only slightly displaced from its fourfold hollow site starting position. This oxygen atom binds more strongly to the second layer Cu atom than to the first layer atoms.

The Cu-O bond length is practically the same in all configurations and does not depend on the coverage ratio. The oxygen adsorption does not influence the binding of the oxygen atoms of the carboxylate group with the first layer of the Cu-surface. The main changes due to oxygen coverage are in the first interlayer

relaxations. With increasing coverage the first Cu-surface layer relaxes towards the positions corresponding to the unrelaxed (110) surface, and for the oxygen precovered surface the inward relaxation for the clean Cu(110) surface is over-compensated and turned into a large outward relaxation.

3-thiophene carboxylate molecule

Four different geometries corresponding to a (2x1) unit cell (high coverage) of 3-thiophene carboxylate molecules on Cu(110) surface have been optimized. In the final stable configuration the molecule sits perpendicular to the surface in bridge position above the first Cu-surface layer with the carboxylate group oriented along to the $[1\bar{1}0]$ direction. The most important change due to adsorption is in the geometry of the molecule. In the gas phase the single molecule has a planar geometry with an extended π -system over the thiophene ring and carboxylate group. The adsorption of the molecule breaks this planarity. There are strong lateral interactions that appear between neighboring thiophene rings. As a consequence, in the adsorbed molecules the thiophene rings are rotated by 24° relative to the carboxylate group.

The relaxations of the Cu-surface layer are almost the same as those of the clean Cu(110) surface. Compared with the case of formate adsorption on Cu(110) surface (high and low coverage) the Cu-O bonds and the O-C-O angles are slightly shorter (0.07 Å and 3° respectively). Also, the first interlayer distance differs. While in the case of the formate-Cu(110) system the Cu-surface layer relaxes outward relative to the clean Cu(110) surface, for the 3-thiophene-carboxylate-Cu(110) system the Cu-surface layer is practically unchanged. There are small lateral displacements of the Cu-atoms towards the oxygen atoms. Although the planarity of the molecule is broken, and the π -system is affected accordingly (decomposed to carboxylate group and thiophene ring), we believe that a small interaction of the π -system of the thiophene ring via carboxylate group with the Cu-surface exist.

Glycinate molecule

In the case of the glycinate molecules adsorbed on the Cu(110) surface (two molecules in a (3x2) unit cell) several geometries have been optimized. The most stable one was found to be the Heterochiral domain 1, where both enantiomers are present in the unit cell with zero degree rotated relative to each other. The molecules are lying flat and bind to the surface via both functional groups (carboxylate -OCO- and amino H_2N -). In this configuration short and strong Cu-N and Cu-O bonds are formed. The hydrogen atoms that are binding the carbon atom are non-equivalent and distinct relative to the surface: one bond direction is almost parallel and the other is perpendicular to the surface. This makes the carbon atom a chiral center in the molecule. The N and one O atom of each molecule are slightly displaced from on-top Cu-sites. The other O atom is forming a bridge between two Cu-surface atoms along to $[100]$ direction. The carboxylate group is no longer perpendicular to the surface as in the case of formate or 3-thiophene carboxylate molecules. For the glycinate-Cu(110) system, the Cu-O bonds are 0.22-0.29 Å larger than in the case of the formate- or 3-thiophene carboxylate-Cu(110) systems. There are interactions between the adsorbed glycinate molecules via more hydrogen bonds. From the H-O distances we deduce

that two stronger hydrogen bonds are formed. The Heterochiral domain 1 shows a glide plane symmetry that is also observed in the experiments.

Outlook

Our results for the optimized geometries open the possibility to thoroughly investigate the electronic structure of adsorbed molecules, in particular of the interaction of the conjugated π -system with the metal surfaces.

(a-1) We plan to study further other adsorption of the carboxylic acids containing conjugated aromatic π -systems. Several studies should be performed on the adsorption of the carboxylic acids with similar structures as the 3-thiophene carboxylic acid where one replaces the heteroatom (S) of the thiophene ring with Se and/or Te atoms (yielding selenophene and tellurophene rings). A very interesting question is the influence of the heteroatom (S, Se, Te) on the π -system and on the bonding of the molecule to the surface (rotation angle, bond lengths and electronic structure). One can also replace the carbon of the carboxylic group with a boron or nitrogen atom (see Table “Proposed Molecules”). The influence of the B or N atoms⁴ on the bonding properties and most importantly on the interaction of the π -system with metal-surface should be investigated.

Table Proposed Molecules:

	where X: S 3-thiophene-carboxylic acid Se 3-selenophene-carboxylic acid Te 3-tellurophene-carboxylic acid
	S 3-thiophene- boronic acid Se 3-selenophene- boronic acid Te 3-tellurophene- boronic acid
	S 3-nitrothiophene Se 3-nitroselenophene Te 3-nitrotellurophene

(a-2) We will investigate the rotation of the five-membered ring of the π -system and its influence on the distribution of π -electrons over the molecules. The rotation angle and the interaction of the π -electrons with the metal surface (see molecules on Table “Proposed Molecules”) can possibly be changed when the molecules are adsorbed on (110)-surfaces of other noble metals, e.g. Pt, Pd, Au or Ag which have larger lattice constants than Cu, and thus the ring rotation is expected to be smaller.

⁴ No π -bond with the oxygen atom is formed because the B atom has fewer valence electrons than the C atom. The N atom forms π -bond with the oxygen atom, and it has more valence electrons than the C atom as well.

(b) the glycinate can be regarded as an anchoring group for a series of more complicated molecules which bind to the surface via both functional groups, amino (-NH_2) and carboxylate (-OCO-). In principle, the hydrogen atom of the glycinate molecule, that is almost perpendicular on the (110)-surface, can be replaced by a functional group able to interact specifically with other incoming species. Another possibility is the replacement of the hydrogen by a π -system rings to get closer to molecules considered for molecular electronics.

Appendix A.1.

Functional (variational) derivative¹

Functional derivatives play the same role for functionals as the concept of the partial derivatives play for function of n variables. We consider the functional:

$$J(y) = \int_a^b F(x, y, y') dx \quad (\text{A.1.-1})$$

where $y(a) = A$ and $y(b) = B$.

The approach here is first to reformulate the functional by discretization as a function of n -variables and then pass to the limit $n \rightarrow \infty$. Now we will divide the interval $[a, b]$ into $n + 1$ equal subintervals by introducing the points:

$$x_0 = a, x_1, x_2, \dots, x_n, x_{n+1} = b, \quad x_{i+1} - x_i = \Delta x \quad (\text{A.1.-2})$$

In this way the smooth function $y(x)$ is replaced by polygonal lines $(x_0, y_0), (x_1, y_1), \dots, (x_n, y_n), (x_{n+1}, y_{n+1})$, where $y(x_i) = y_i$. So (A.1.-1) can be approximated by the sum:

$$J(y_1, y_2, y_3, \dots, y_n) = \sum_{i=1}^n F\left(x_i, y_i, \frac{y_{i+1} - y_i}{\Delta x}\right) \Delta x \quad (\text{A.1.-3})$$

which is a function of n variables.

In the next step we will calculate the partial derivatives $\frac{\partial J(y_1, y_2, y_3, \dots, y_n)}{\partial y_k}$. Since in equation (A.1.-3) the variable y_k appears just in two terms, i.e. for $i = k$ and $i = k - 1$, we have:

$$\frac{\partial J}{\partial y_k} = \frac{\partial}{\partial y_k} \left(F\left(x_k, y_k, \frac{y_{k+1} - y_k}{\Delta x}\right) + F\left(x_{k-1}, y_{k-1}, \frac{y_k - y_{k-1}}{\Delta x}\right) \right) \cdot \Delta x \quad (\text{A.1.-4})$$

¹ For more details about functional and functional derivatives see "Calculus of variations", I.M. Gelfand and S.V. Fomin (Moscow State University) 1963, Prentice-Hall Inc.

APPENDIX A.1.

The derivative of the term $F\left(\mathbf{x}_k, \mathbf{y}_k, \frac{\mathbf{y}_{k+1} - \mathbf{y}_k}{\Delta \mathbf{x}}\right)$ will give two terms because F depends of \mathbf{y}_k and² $\mathbf{y}'_k = f(\mathbf{y}_k)$:

$$\begin{aligned} \frac{\partial \mathbf{J}}{\partial \mathbf{y}_k} = & \left\{ \frac{\partial}{\partial \mathbf{y}_k} F\left(\mathbf{x}_k, \mathbf{y}_k, \left(\frac{\mathbf{y}_{k+1} - \mathbf{y}_k}{\Delta \mathbf{x}}\right)_{\text{cons tan } t}\right) + \frac{\partial}{\partial \mathbf{y}_k} F\left(\mathbf{x}_k, (\mathbf{y}_k)_{\text{cons tan } t}, \frac{\mathbf{y}_{k+1} - \mathbf{y}_k}{\Delta \mathbf{x}}\right) \right. \\ & \left. + \frac{\partial}{\partial \mathbf{y}_k} F\left(\mathbf{x}_{k-1}, \mathbf{y}_{k-1}, \frac{\mathbf{y}_k - \mathbf{y}_{k-1}}{\Delta \mathbf{x}}\right) \right\} \Delta \mathbf{x} \end{aligned} \quad (\text{A.1.-5})$$

The second and third term on the right-hand side can be written as derivatives with respect to \mathbf{y}'_k , because only the \mathbf{y}'_k -term in F is differentiated with respect to \mathbf{y}_k :

$$\begin{aligned} \frac{\partial \mathbf{J}}{\partial \mathbf{y}_k} = & \frac{\partial}{\partial \mathbf{y}_k} F(\mathbf{x}_k, \mathbf{y}_k, \mathbf{y}'_k) \cdot \Delta \mathbf{x} + \frac{\partial}{\partial \mathbf{y}'_k} F(\mathbf{x}_k, \mathbf{y}_k, \mathbf{y}'_k) \underbrace{\frac{\partial \mathbf{y}'_k}{\partial \mathbf{y}_k}}_{-1} \cdot \Delta \mathbf{x} \\ & + \frac{\partial}{\partial \mathbf{y}'_{k-1}} F(\mathbf{x}_{k-1}, \mathbf{y}_{k-1}, \mathbf{y}'_{k-1}) \underbrace{\frac{\partial \mathbf{y}'_{k-1}}{\partial \mathbf{y}_{k-1}}}_{+1} \cdot \Delta \mathbf{x} \end{aligned} \quad (\text{A.1.-6})$$

$$\frac{1}{\Delta \mathbf{x}} \cdot \frac{\partial \mathbf{J}}{\partial \mathbf{y}_k} = \frac{\partial F(\mathbf{x}_k, \mathbf{y}_k, \mathbf{y}'_k)}{\partial \mathbf{y}_k} - \frac{1}{\Delta \mathbf{x}} \cdot \left\{ \frac{\partial F(\mathbf{x}_k, \mathbf{y}_k, \mathbf{y}'_k)}{\partial \mathbf{y}'_k} - \frac{\partial F(\mathbf{x}_{k-1}, \mathbf{y}_{k-1}, \mathbf{y}'_{k-1})}{\partial \mathbf{y}'_{k-1}} \right\} \quad (\text{A.1.-7})$$

For the case when $n \rightarrow \infty$ and $\Delta \mathbf{x} = 0$, the relation (A.1.-7) converges to the limit:

$$\frac{\delta \mathbf{J}}{\delta \mathbf{y}} = \frac{\partial F(\mathbf{x}, \mathbf{y}, \mathbf{y}')}{\partial \mathbf{y}} - \frac{d}{d \mathbf{x}} \left(\frac{\partial F(\mathbf{x}, \mathbf{y}, \mathbf{y}')}{\partial \mathbf{y}'} \right) \quad (\text{A.1.-8})$$

In the case of the exchange correlation potential, $\mathbf{x} = \vec{\mathbf{r}}$ and³ $\frac{d}{d \vec{\mathbf{r}}} = \nabla$ so that one can write⁴:

$$v_{xc}(\mathbf{r}) = \frac{\delta E_{xc}}{\delta n(\vec{\mathbf{r}})} = \frac{\partial f_{xc}}{\partial n(\vec{\mathbf{r}})} - \nabla \cdot \frac{\partial f_{xc}}{\partial \nabla n(\vec{\mathbf{r}})} \quad (\text{A.1.-9})$$

² One should keep in mind that $n \rightarrow \infty$ and $\Delta \mathbf{x} \rightarrow 0$ so we can write $\mathbf{y}'_k \approx \frac{\mathbf{y}_{k+1} - \mathbf{y}_k}{\Delta \mathbf{x}}$

³ $\nabla = \left(\frac{\partial}{\partial x} \vec{\mathbf{i}} + \frac{\partial}{\partial y} \vec{\mathbf{j}} + \frac{\partial}{\partial z} \vec{\mathbf{k}} \right)$

⁴ Another way to arrive to this equation is using the Taylor theorem. For details see Appendix A, pag.250 in “Density-Functional Theory of Atoms and Molecules”, R.G. Parr and W. Yang, Oxford Univ. Press 1989

Appendix A.2.

Exchange-correlation terms in DFT

The gradient corrected exchange-correlation energy can be written as:

$$E_{xc}[\mathbf{n}(\vec{r})] = \int f_{xc}(\mathbf{n}(\vec{r}), |\nabla \mathbf{n}(\vec{r})|) d\vec{r} \quad (\text{A.2.-1})$$

and the exchange-correlation potential is defined as a functional or variational derivative of E_{xc} with respect to the density $\mathbf{n}(\vec{r})$:

$$v_{xc}(\vec{r}) = \frac{\delta E_{xc}[\mathbf{n}(\vec{r})]}{\delta \mathbf{n}(\vec{r})} = \frac{\partial f_{xc}(\mathbf{n}(\vec{r}), |\nabla \mathbf{n}(\vec{r})|)}{\partial \mathbf{n}(\vec{r})} - \nabla \frac{\partial f_{xc}(\mathbf{n}(\vec{r}), |\nabla \mathbf{n}(\vec{r})|)}{\partial \nabla \mathbf{n}(\vec{r})} \quad (\text{A.2.-2})$$

(see Appendix A.1 how one can show the validity of relation A.2.-2).

Normally, the exchange dependent part and correlation dependent part of the potential and energy are additive:

$$\begin{cases} E_{xc} = E_x + E_c \\ v_{xc} = v_x + v_c \end{cases} \quad (\text{A.2.-3})$$

This allows us to write the contributions in the exchange-correlation energy density as a sum of two contributions:

$$f_{xc}(\mathbf{n}(\vec{r}), |\nabla \mathbf{n}(\vec{r})|) = f_x(\mathbf{n}(\vec{r}), |\nabla \mathbf{n}(\vec{r})|) + f_c(\mathbf{n}(\vec{r}), |\nabla \mathbf{n}(\vec{r})|) \quad (\text{A.2.-4})$$

as a sum of the f_x -exchange function and f_c -correlation function.

In the case of a spin polarized system the corresponding relations are:

$$\begin{aligned} E_{xc}[\mathbf{n}^\uparrow(\vec{r}), \mathbf{n}^\downarrow(\vec{r})] &= E_x[\mathbf{n}^\uparrow(\vec{r}), \mathbf{n}^\downarrow(\vec{r})] + E_c[\mathbf{n}^\uparrow(\vec{r}), \mathbf{n}^\downarrow(\vec{r})] \\ E_x[\mathbf{n}^\uparrow(\vec{r}), \mathbf{n}^\downarrow(\vec{r})] &= \frac{1}{2} \{ E_x[2\mathbf{n}^\uparrow(\vec{r})] + E_x[2\mathbf{n}^\downarrow(\vec{r})] \} \\ E_x[\mathbf{n}(\vec{r})] &= \int \mathbf{n}(\vec{r}) \mathcal{E}_x^{\text{hom}}(\mathbf{n}(\vec{r})) F_x(s) d\vec{r}^3 \\ E_c[\mathbf{n}^\uparrow(\vec{r}), \mathbf{n}^\downarrow(\vec{r})] &= \int (\mathbf{n}^\uparrow(\vec{r}) + \mathbf{n}^\downarrow(\vec{r})) \{ \mathcal{E}_c^{\text{hom}}(\mathbf{r}_s, \zeta) + H(\mathbf{r}_s, \zeta, t) \} \end{aligned} \quad (\text{A.2.-5})$$

APPENDIX A.2

$$\begin{aligned} v_{xc}^\sigma[n^\uparrow(\vec{r}), n^\downarrow(\vec{r}), \vec{r}] = & \frac{\partial f_{xc}(n^\uparrow(\vec{r}), |\nabla n^\uparrow(\vec{r})| n^\downarrow(\vec{r}), |\nabla n^\downarrow(\vec{r})|)}{\partial n^\sigma(\vec{r})} \\ & - \nabla \frac{\partial f_{xc}(n^\uparrow(\vec{r}), |\nabla n^\uparrow(\vec{r})| n^\downarrow(\vec{r}), |\nabla n^\downarrow(\vec{r})|)}{\partial \nabla n^\sigma(\vec{r})} \end{aligned} \quad (\text{A.2.-6})$$

where $\sigma = \uparrow$ (up), $\sigma = \downarrow$ (down) and $n(\vec{r}) = n^\uparrow(\vec{r}) + n^\downarrow(\vec{r})$. We wrote these formulae here because the functionals that we are going to use are formulated with spin polarization [PW92, PBE96-98].

The traditional generalized gradient approximation yields potential functions, which are rapidly varying near the ion core, and in order to approximate these using the plane wave basis set, one needs a very large number of plane waves (high energy cut-off). In the LDA, the charge density has Fourier components only for reciprocal lattice vectors $\mathbf{G} \leq 2\mathbf{G}_{\max}$. For an accurate calculation of energy and potential the corresponding real space grid associated with the FFT grid in reciprocal space must go beyond $2\mathbf{G}_{\max}$. The energy depends on $|\nabla n(\vec{r})|$ only, but the potential requires also terms proportional to $\nabla^2 n(\vec{r})$ and $\nabla n(\vec{r}) \cdot \nabla |\nabla n(\vec{r})|$. The last terms cause the problem in the Fourier coefficients. In practice one has to take a FFT grid with $\mathbf{G} \leq 4\mathbf{G}_{\max}$ to obtain $\nabla n(\vec{r}) \cdot \nabla |\nabla n(\vec{r})|$ with satisfactory accuracy.

White and Bird [WB94] have suggested a more efficient scheme in which one can rewrite the gradient terms of exchange-correlation energy using functions that can be calculated precisely on the minimal FFT grid. In practice, the exchange-correlation energy and the exchange-correlation potential are discrete sums over \mathbf{N} real-space grid points of the minimum FFT grid ($2\mathbf{G}_{\max}$):

$$\left\{ \begin{aligned} E_{xc}(\vec{R}) &= \frac{\Omega_{cell}}{N} \sum_{\vec{R}} f_{xc}(n(\vec{R}), |\nabla n(\vec{R})|) \\ v_{xc}(\vec{R}) &= \frac{N}{\Omega_{cell}} \frac{dE_{xc}}{dn(\vec{R})} = \frac{\partial f_{xc}(n(\vec{R}), |\nabla n(\vec{R})|)}{\partial n(\vec{R})} + \sum_{\vec{R}'} \frac{\partial f_{xc}(n(\vec{R}'), |\nabla n(\vec{R}')|)}{\partial \nabla n(\vec{R}')} \cdot \frac{d \nabla n(\vec{R}')}{dn(\vec{R})} \end{aligned} \right. \quad (\text{A.2.-7})$$

Since we are working with the charge in the reciprocal space one can calculate the derivatives as:

$$\begin{aligned} n(\vec{r}) &= \sum_{\vec{G}} n(\vec{G}) e^{-i\vec{G} \cdot \vec{r}} \quad \text{and} \quad n(\vec{G}) = \frac{1}{N} \sum_{\vec{R}} n(\vec{R}) e^{i\vec{G} \cdot \vec{R}} \\ \nabla n(\vec{r}) &= - \sum_{\vec{G}} i\vec{G} n(\vec{G}) e^{-i\vec{G} \cdot \vec{r}} = - \frac{1}{N} \sum_{\vec{G}, \vec{R}} i\vec{G} n(\vec{R}) e^{-i\vec{G} \cdot (\vec{r} - \vec{R})} \end{aligned} \quad (\text{A.2.-8})$$

where \mathbf{N} is the number of the reciprocal-lattice vectors \vec{G} of the minimum FFT grid ($2\mathbf{G}_{\max}$).

The reformulation of the exchange correlation potential is:

$$v_{xc}(\vec{R}) = \frac{\partial f_{xc}(n(\vec{R}), |\nabla n(\vec{R})|)}{\partial n(\vec{R})} - \frac{1}{N} \sum_{\vec{G}, \vec{R}'} i\vec{G} \frac{\nabla n(\vec{R}')}{|\nabla n(\vec{R}')|} \frac{\partial f_{xc}(n(\vec{R}), |\nabla n(\vec{R})|)}{\partial |\nabla n(\vec{R}')|} \times e^{i\vec{G} \cdot (\vec{R} - \vec{R}')} \quad (\text{A.2.-9})$$

in which one can see that the exchange correlation potential can be calculated exactly using the FFT minimum grid and no higher-quality representation of the charge density is required.

Appendix A.3.

Explicit formula of the terms used in calculation of exchange-correlation energy and potential

The terms of relation (A.2.-2), the derivative of the exchange-correlation function with respect to the $\mathbf{n}(\vec{r})$ and the derivatives with respect to the $\nabla \mathbf{n}(\vec{r})$ can be written as sum over derivatives of exchange function and correlation function:

$$\begin{aligned} \frac{\partial f_{xc}(\mathbf{n}^\uparrow(\vec{r}), \mathbf{n}^\downarrow(\vec{r}), \nabla \mathbf{n}^\uparrow(\vec{r}), \nabla \mathbf{n}^\downarrow(\vec{r}))}{\partial \mathbf{n}(\vec{r})} &= \frac{\partial f_x}{\partial \mathbf{n}(\vec{r})} + \frac{\partial f_c}{\partial \mathbf{n}(\vec{r})} \\ \frac{\partial f_{xc}(\mathbf{n}^\uparrow(\vec{r}), \mathbf{n}^\downarrow(\vec{r}), \nabla \mathbf{n}^\uparrow(\vec{r}), \nabla \mathbf{n}^\downarrow(\vec{r}))}{\partial \nabla \mathbf{n}(\vec{r})} &= \frac{\partial f_x}{\partial \nabla \mathbf{n}(\vec{r})} + \frac{\partial f_c}{\partial \nabla \mathbf{n}(\vec{r})} \end{aligned} \quad (\text{A.3.-1})$$

The exchange function is defined as:

$$f_x(\mathbf{n}^\uparrow(\vec{r}), \mathbf{n}^\downarrow(\vec{r}), \nabla \mathbf{n}^\uparrow(\vec{r}), \nabla \mathbf{n}^\downarrow(\vec{r})) = (\mathbf{n}^\uparrow(\vec{r}) + \mathbf{n}^\downarrow(\vec{r})) \cdot \varepsilon_x^{\text{hom}}(\mathbf{n}(\vec{r})) \cdot F_x(s) \quad (\text{A.3.-2})$$

where $\mathbf{n}(\vec{r}) = \mathbf{n}^\uparrow(\vec{r}) + \mathbf{n}^\downarrow(\vec{r})$ is the total charge (spin-up and spin-down) and $s(\vec{r})$ is the normalized density gradient (see equation 1.3-10, Chapter 1.3).

The derivatives of the exchange function are:

$$\begin{aligned} \frac{\partial f_x}{\partial \mathbf{n}^\sigma(\vec{r})} &= (\mathbf{n}^\uparrow(\vec{r}) + \mathbf{n}^\downarrow(\vec{r})) \cdot F_x(s) \frac{\partial \varepsilon_x^{\text{hom}}(\mathbf{n}(\vec{r}))}{\partial \mathbf{n}^\sigma(\vec{r})} + \varepsilon_x^{\text{hom}}(\mathbf{n}(\vec{r})) \cdot \left\{ F_x(s) - \frac{4s}{3} \frac{\partial F_x(s)}{\partial s} \right\} \\ \frac{\partial f_x}{\partial \nabla \mathbf{n}^\sigma(\vec{r})} &= \frac{\varepsilon_x^{\text{hom}}(\mathbf{n}(\vec{r}))}{2k_F} \cdot \frac{\partial F_x(s)}{\partial s} \end{aligned} \quad (\text{A.3.-3})$$

Finally, the expression for the exchange potential for spin-up or spin down is:

$$\begin{aligned} v_x^\sigma(\mathbf{n}^\uparrow(\vec{r}), \mathbf{n}^\downarrow(\vec{r}), \vec{r}) &= \frac{\partial f_x}{\partial \mathbf{n}^\sigma(\vec{r})} - \nabla \frac{\partial f_x}{\partial \nabla \mathbf{n}^\sigma(\vec{r})} = (\mathbf{n}^\uparrow(\vec{r}) + \mathbf{n}^\downarrow(\vec{r})) \cdot F_x(s) \frac{\partial \varepsilon_x^{\text{hom}}(\mathbf{n}(\vec{r}))}{\partial \mathbf{n}^\sigma(\vec{r})} \\ &+ \varepsilon_x^{\text{hom}}(\mathbf{n}(\vec{r})) \cdot \left\{ F_x(s) - \frac{4s}{3} \frac{\partial F_x(s)}{\partial s} \right\} - \nabla \left(\frac{\varepsilon_x^{\text{hom}}(\mathbf{n}(\vec{r}))}{2k_F} \cdot \frac{\partial F_x(s)}{\partial s} \right) \end{aligned} \quad (\text{A.3.-4})$$

APPENDIX A.3.

The correlation function is defined as:

$$f_C(\mathbf{n}^\uparrow(\vec{r}), \mathbf{n}^\downarrow(\vec{r}), \nabla \mathbf{n}^\uparrow(\vec{r}), \nabla \mathbf{n}^\downarrow(\vec{r})) = (\mathbf{n}^\uparrow(\vec{r}) + \mathbf{n}^\downarrow(\vec{r})) \cdot \{ \varepsilon_C^{\text{hom}}(\mathbf{r}_s, \xi) + \mathbf{H}(\mathbf{r}_s, \xi, t) \} \quad (\text{A.3.-5})$$

Correspondingly, the derivatives of the correlation function are:

$$\begin{aligned} \frac{\partial f_C}{\partial \mathbf{n}^\sigma} &= \varepsilon_C^{\text{hom}}(\mathbf{r}_s, \xi) + \mathbf{H}(\mathbf{r}_s, \xi, t) + \left(-\frac{1}{3} \mathbf{r}_s \right) \cdot \left(\frac{\partial \varepsilon_C^{\text{hom}}(\mathbf{r}_s, \xi)}{\partial \mathbf{r}_s} + \frac{\partial \mathbf{H}(\mathbf{r}_s, \xi, t)}{\partial \mathbf{r}_s} \right) + (\text{sign}(\sigma) - \xi) \cdot \\ &\left(\frac{\partial \varepsilon_C^{\text{hom}}(\mathbf{r}_s, \xi)}{\partial \xi} + \frac{\partial \mathbf{H}(\mathbf{r}_s, \xi, t)}{\partial \xi} \right) + (-t) \left(\frac{\partial \mathbf{H}(\mathbf{r}_s, \xi, t)}{\partial t} \right) \cdot \left\{ \frac{(\text{sign}(\sigma) - \xi)}{3\Phi} \left((1 - \xi)^{\frac{1}{3}} - (1 + \xi)^{\frac{1}{3}} \right) + \frac{7}{6} \right\} \\ \frac{\partial f_C}{\partial \nabla \mathbf{n}^\sigma} &= \frac{\nabla \mathbf{n}(\mathbf{r})}{|\nabla \mathbf{n}(\mathbf{r})|} \cdot \frac{1}{2\Phi \mathbf{k}_s} \frac{\partial \mathbf{H}(\mathbf{r}_s, \xi, t)}{\partial t} \end{aligned} \quad (\text{A.3.-6})$$

The relation which is used to calculate the correlation is:

$$\begin{aligned} \mathbf{v}_C^\sigma(\mathbf{n}^\uparrow(\vec{r}), \mathbf{n}^\downarrow(\vec{r}), \vec{r}) &= \\ &\varepsilon_C^{\text{hom}}(\mathbf{r}_s, \xi) + \mathbf{H}(\mathbf{r}_s, \xi, t) + \left(-\frac{\mathbf{r}_s}{3} \right) \cdot \left(\frac{\partial \varepsilon_C^{\text{hom}}(\mathbf{r}_s, \xi)}{\partial \mathbf{r}_s} + \frac{\partial \mathbf{H}(\mathbf{r}_s, \xi, t)}{\partial \mathbf{r}_s} \right) + (\text{sign}(\sigma) - \xi) \cdot \\ &\left(\frac{\partial \varepsilon_C^{\text{hom}}(\mathbf{r}_s, \xi)}{\partial \xi} + \frac{\partial \mathbf{H}(\mathbf{r}_s, \xi, t)}{\partial \xi} \right) + (-t) \left(\frac{\partial \mathbf{H}(\mathbf{r}_s, \xi, t)}{\partial t} \right) \cdot \left\{ \frac{(\text{sign}(\sigma) - \xi)}{3\Phi} \cdot \right. \\ &\left. \left((1 - \xi)^{\frac{1}{3}} - (1 + \xi)^{\frac{1}{3}} \right) + \frac{7}{6} \right\} - \nabla \left(\frac{1}{2\Phi \mathbf{k}_s} \frac{\partial \mathbf{H}(\mathbf{r}_s, \xi, t)}{\partial t} \right) \cdot \frac{\nabla \mathbf{n}(\vec{r})}{|\nabla \mathbf{n}(\vec{r})|}. \end{aligned} \quad (\text{A.3.-7})$$

where $\mathbf{k}_s = \left(\frac{4\mathbf{k}_F}{\pi} \right)^{\frac{1}{2}}$ and the significance of the other terms is given in Chapter 1.3.

Appendix A.4.

Formulae

The Legendre Polynomial $P_l^m(x)$ satisfies the differential equation:

$$\left[(1-x^2) \left(\frac{d}{dx} \right)^2 - 2x \left(\frac{d}{dx} \right) + l(l+1) - \frac{m^2}{1-x^2} \right] P_l^m(x) = 0 \quad (\text{A.4.-1})$$

The formula for $P_l^m(x)$ given by Rodrigues:

$$P_l^m(x) = \frac{(1-x^2)^{\frac{m}{2}}}{2^l l!} \left(\frac{d}{dx} \right)^{l+m} (x^2-1)^l \quad (\text{A.4.-2})$$

with the condition of orthogonality:

$$\begin{aligned} \int_{-1}^{+1} P_l^m(x) P_{l'}^m(x) dx &= \frac{2\delta_{ll'} (l+m)!}{(2l+1)(l-m)!} \\ \int_{-1}^{+1} P_l^m(x) P_{l'}^{m'}(x) \frac{dx}{1-x^2} &= \frac{\delta_{mm'} (l+m)!}{m(l-m)!} \end{aligned} \quad (\text{A.4.-3})$$

The complex spherical harmonics $Y_n^m(\theta, \varphi)$ are defined as:

$$Y_{lm}(\theta, \varphi) = (-1)^m \sqrt{\frac{2l+1}{4\pi} \frac{(l-m)!}{(l+m)!}} P_l^m(\cos(\theta)) e^{im\varphi} \quad (\text{A.4.-4})$$

with the complete orthogonality integral:

$$\int_{\varphi=0}^{2\pi} \int_{\theta=0}^{\pi} Y_{lm}^*(\theta, \varphi) Y_{l'm'}(\theta, \varphi) \sin(\theta) d\theta d\varphi = \delta_{ll'} \delta_{mm'} \quad (\text{A.4.-5})$$

The real spherical harmonics $y_{lm}(\theta, \varphi)$ are defined as:

$$\begin{aligned} y_{lm} &= \frac{(-1)^m}{\sqrt{2}} (Y_{lm}^*(\theta, \varphi) + Y_{lm}(\theta, \varphi)) = \sqrt{2} (-1)^m \text{Re}(Y_{lm}), \quad (m > 0) \\ y_{lm} &= Y_{l0}, \quad (m = 0) \\ y_{l-m} &= \frac{1}{\sqrt{2}i} (Y_{lm}(\theta, \varphi) - Y_{lm}^*(\theta, \varphi)) = \sqrt{2} \text{Im}(Y_{lm}), \quad (m < 0) \end{aligned} \quad (\text{A.4.-6})$$

with the complete orthogonality integral:

$$\int_{\varphi=0}^{2\pi} d\varphi \int_{\theta=0}^{\pi} y_{lm}(\theta, \varphi) y_{l'm'}(\theta, \varphi) \sin(\theta) d\theta = \delta_{ll'} \delta_{mm'} \quad (\text{A.4.-7})$$

APPENDIX A.4.

Table of real spherical harmonics for $l \leq 2$:

l	m	y_{lm}	$\frac{\partial y_{lm}}{\partial \theta}$	$\frac{\partial^2 y_{lm}}{\partial \theta^2}$
1	-1	$\frac{1}{2} \frac{\sqrt{3} \sin(\theta) \sin(\varphi)}{\sqrt{\pi}}$	$\frac{1}{2} \frac{\sqrt{3} \cos(\theta) \sin(\varphi)}{\sqrt{\pi}}$	$-\frac{1}{2} \frac{\sqrt{3} \sin(\theta) \sin(\varphi)}{\sqrt{\pi}}$
1	0	$\frac{1}{2} \frac{\sqrt{3} \cos(\theta)}{\sqrt{\pi}}$	$-\frac{1}{2} \frac{\sqrt{3} \sin(\theta)}{\sqrt{\pi}}$	$-\frac{1}{2} \frac{\sqrt{3} \cos(\theta)}{\sqrt{\pi}}$
1	+1	$\frac{1}{2} \frac{\sqrt{3} \cos(\theta) \sin(\varphi)}{\sqrt{\pi}}$	$\frac{1}{2} \frac{\sqrt{3} \cos(\theta) \cos(\varphi)}{\sqrt{\pi}}$	$-\frac{1}{2} \frac{\sqrt{3} \sin(\theta) \cos(\varphi)}{\sqrt{\pi}}$
2	-2	$\frac{1}{4} \frac{\sqrt{15} \sin^2(\theta) \sin(2\varphi)}{\sqrt{\pi}}$	$\frac{1}{2} \frac{\sqrt{15} \sin(\theta) \cos(\theta) \sin(2\varphi)}{\sqrt{\pi}}$	$\frac{1}{2} \frac{\sqrt{15} (2 \cos^2(\theta) - 1) \sin(2\varphi)}{\sqrt{\pi}}$
2	-1	$\frac{1}{2} \frac{\sqrt{15} \sin(\theta) \cos(\theta) \sin(\varphi)}{\sqrt{\pi}}$	$\frac{1}{2} \frac{\sqrt{15} (2 \cos^2(\theta) - 1) \sin(\varphi)}{\sqrt{\pi}}$	$-\frac{2}{\sqrt{\pi}} \frac{\sqrt{15} \sin(\theta) \cos(\theta) \sin(\varphi)}{\sqrt{\pi}}$
2	0	$\frac{1}{4} \frac{\sqrt{5} (3 \cos^2(\theta) - 1)}{\sqrt{\pi}}$	$-\frac{3}{2} \frac{\sqrt{5} \cos(\theta) \sin(\theta)}{\sqrt{\pi}}$	$-\frac{3}{2} \frac{\sqrt{5} (3 \cos^2(\theta) - 1)}{\sqrt{\pi}}$
2	+1	$\frac{1}{2} \frac{\sqrt{15} \sin(\theta) \cos(\theta) \cos(\varphi)}{\sqrt{\pi}}$	$\frac{1}{2} \frac{\sqrt{15} (2 \cos^2(\theta) - 1) \cos(\varphi)}{\sqrt{\pi}}$	$-\frac{2}{\sqrt{\pi}} \frac{\sqrt{15} \sin(\theta) \cos(\theta) \cos(\varphi)}{\sqrt{\pi}}$
2	+2	$\frac{1}{4} \frac{\sqrt{15} \sin^2(\theta) \cos(2\varphi)}{\sqrt{\pi}}$	$\frac{1}{2} \frac{\sqrt{15} \sin(\theta) \cos(\theta) \cos(2\varphi)}{\sqrt{\pi}}$	$\frac{1}{2} \frac{\sqrt{15} (2 \cos^2(\theta) - 1) \cos(2\varphi)}{\sqrt{\pi}}$

l	m	$\frac{\partial y_{lm}}{\partial \varphi}$	$\frac{\partial^2 y_{lm}}{\partial \varphi^2}$	$\frac{\partial^2 y_{lm}}{\partial \theta \partial \varphi}$
1	-1	$\frac{1}{2} \frac{\sqrt{3} \sin(\theta) \cos(\varphi)}{\sqrt{\pi}}$	$-\frac{1}{2} \frac{\sqrt{3} \sin(\theta) \sin(\varphi)}{\sqrt{\pi}}$	$\frac{1}{2} \frac{\sqrt{3} \cos(\theta) \cos(\varphi)}{\sqrt{\pi}}$
1	0	0	0	0
1	+1	$-\frac{1}{2} \frac{\sqrt{3} \sin(\theta) \sin(\varphi)}{\sqrt{\pi}}$	$-\frac{1}{2} \frac{\sqrt{3} \sin(\theta) \cos(\varphi)}{\sqrt{\pi}}$	$-\frac{1}{2} \frac{\sqrt{3} \cos(\theta) \sin(\varphi)}{\sqrt{\pi}}$
2	-2	$\frac{1}{2} \frac{\sqrt{15} \sin^2(\theta) \cos(2\varphi)}{\sqrt{\pi}}$	$-\frac{\sqrt{15} \sin^2(\theta) \sin(2\varphi)}{\sqrt{\pi}}$	$\frac{\sqrt{15} \sin(\theta) \cos(\theta) \cos(2\varphi)}{\sqrt{\pi}}$
2	-1	$\frac{1}{2} \frac{\sqrt{15} \sin(\theta) \cos(\theta) \cos(\varphi)}{\sqrt{\pi}}$	$-\frac{1}{2} \frac{\sqrt{15} \sin(\theta) \cos(\theta) \sin(\varphi)}{\sqrt{\pi}}$	$\frac{1}{2} \frac{\sqrt{15} (2 \cos^2(\theta) - 1) \cos(\varphi)}{\sqrt{\pi}}$
2	0	0	0	0
2	+1	$-\frac{1}{2} \frac{\sqrt{15} \sin(\theta) \cos(\theta) \sin(\varphi)}{\sqrt{\pi}}$	$-\frac{1}{2} \frac{\sqrt{15} \sin(\theta) \cos(\theta) \cos(\varphi)}{\sqrt{\pi}}$	$-\frac{1}{2} \frac{\sqrt{15} (2 \cos^2(\theta) - 1) \sin(\varphi)}{\sqrt{\pi}}$
2	+2	$-\frac{1}{2} \frac{\sqrt{15} \sin^2(\theta) \sin(2\varphi)}{\sqrt{\pi}}$	$-\frac{\sqrt{15} \sin^2(\theta) \cos(2\varphi)}{\sqrt{\pi}}$	$-\frac{\sqrt{15} \sin(\theta) \cos(\theta) \sin(2\varphi)}{\sqrt{\pi}}$

APPENDIX A.4.

Table of real spherical harmonics for $l = 3$ (part 1):

l	m	y_{lm}	$\frac{\partial y_{lm}}{\partial \theta}$	$\frac{\partial^2 y_{lm}}{\partial \theta^2}$
3	-3	$\frac{1}{8} \frac{\sqrt{70} \sin^3(\theta) \sin(3\varphi)}{\sqrt{\pi}}$	$\frac{3}{8} \frac{\sqrt{70} \sin^2(\theta) \cos(\theta) \sin(3\varphi)}{\sqrt{\pi}}$	$\frac{3}{8} \frac{\sqrt{70} \sin(\theta) (3 \cos^2(\theta) - 1) \sin(3\varphi)}{\sqrt{\pi}}$
3	-2	$\frac{1}{4} \frac{\sqrt{105} \sin^2(\theta) \cos(\theta) \sin(2\varphi)}{\sqrt{\pi}}$	$\frac{1}{4} \frac{\sqrt{105} \sin(\theta) (3 \cos^2(\theta) - 1) \sin(2\varphi)}{\sqrt{\pi}}$	$\frac{1}{4} \frac{\sqrt{105} \cos(\theta) (9 \cos^2(\theta) - 7) \sin(2\varphi)}{\sqrt{\pi}}$
3	-1	$\frac{1}{8} \frac{\sqrt{42} (4 \sin(\theta) - 5 \sin^3(\theta)) \sin(\varphi)}{\sqrt{\pi}}$	$\frac{1}{8} \frac{\sqrt{42} \cos(\theta) (-11 + 15 \cos^2(\theta)) \sin(\varphi)}{\sqrt{\pi}}$	$-\frac{1}{8} \frac{\sqrt{42} \sin(\theta) (-11 + 45 \cos^2(\theta)) \sin(\varphi)}{\sqrt{\pi}}$
3	0	$\frac{1}{4} \frac{\sqrt{7} (5 \cos^3(\theta) - 3 \cos(\theta))}{\sqrt{\pi}}$	$-\frac{3}{4} \frac{\sqrt{7} \sin(\theta) (5 \cos^2(\theta) - 1)}{\sqrt{\pi}}$	$-\frac{3}{4} \frac{\sqrt{7} \cos(\theta) (15 \cos^2(\theta) - 11)}{\sqrt{\pi}}$
3	+1	$\frac{1}{8} \frac{\sqrt{42} \sin(\theta) (5 \cos^2(\theta) - 1) \cos(\varphi)}{\sqrt{\pi}}$	$\frac{1}{8} \frac{\sqrt{42} \cos(\theta) (-11 + 15 \cos^2(\theta)) \cos(\varphi)}{\sqrt{\pi}}$	$-\frac{1}{8} \frac{\sqrt{42} \sin(\theta) (-11 + 45 \cos^2(\theta)) \cos(\varphi)}{\sqrt{\pi}}$
3	+2	$\frac{1}{4} \frac{\sqrt{105} \sin^2(\theta) \cos(\theta) \cos(2\varphi)}{\sqrt{\pi}}$	$\frac{1}{4} \frac{\sqrt{105} \sin(\theta) (3 \cos^2(\theta) - 1) \cos(2\varphi)}{\sqrt{\pi}}$	$\frac{1}{4} \frac{\sqrt{105} \cos(\theta) (9 \cos^2(\theta) - 7) \cos(2\varphi)}{\sqrt{\pi}}$
3	+3	$\frac{1}{8} \frac{\sqrt{70} \sin^3(\theta) \cos(3\varphi)}{\sqrt{\pi}}$	$\frac{3}{8} \frac{\sqrt{70} \sin^2(\theta) \cos(\theta) \cos(3\varphi)}{\sqrt{\pi}}$	$\frac{3}{8} \frac{\sqrt{70} \sin(\theta) (3 \cos^2(\theta) - 1) \cos(3\varphi)}{\sqrt{\pi}}$

APPENDIX A.4.

Table of real spherical harmonics for $l = 3$ (part 2):

l	m	$\frac{\partial y_{lm}}{\partial \varphi}$	$\frac{\partial^2 y_{lm}}{\partial \varphi^2}$	$\frac{\partial^2 y_{lm}}{\partial \theta \partial \varphi}$
3	-3	$\frac{3 \sqrt{70} \sin^3(\theta) \cos(3\varphi)}{8 \sqrt{\pi}}$	$-\frac{9 \sqrt{70} \sin^3(\theta) \sin(3\varphi)}{8 \sqrt{\pi}}$	$\frac{9 \sqrt{70} \cos(\theta) \sin^2(\theta) \sin(3\varphi)}{8 \sqrt{\pi}}$
3	-2	$\frac{1 \sqrt{105} \sin^2(\theta) \cos(\theta) \cos(2\varphi)}{2 \sqrt{\pi}}$	$-\frac{\sqrt{105} \sin^2(\theta) \cos(\theta) \sin(2\varphi)}{\sqrt{\pi}}$	$\frac{1 \sqrt{105} \sin(\theta) (3 \cos^2(\theta) - 1) \cos(2\varphi)}{2 \sqrt{\pi}}$
3	-1	$\frac{1 \sqrt{42} (4 \sin(\theta) - 5 \sin^3(\theta)) \cos(\varphi)}{8 \sqrt{\pi}}$	$-\frac{1 \sqrt{42} (4 \sin(\theta) - 5 \sin^3(\theta)) \sin(\varphi)}{8 \sqrt{\pi}}$	$\frac{1 \sqrt{42} \cos(\theta) (-11 + 15 \cos^2(\theta)) \cos(\varphi)}{8 \sqrt{\pi}}$
3	0	0	0	0
3	+1	$-\frac{1 \sqrt{42} \sin(\theta) (5 \cos^2(\theta) - 1) \sin(\varphi)}{8 \sqrt{\pi}}$	$-\frac{1 \sqrt{42} \sin(\theta) (5 \cos^2(\theta) - 1) \cos(\varphi)}{8 \sqrt{\pi}}$	$-\frac{1 \sqrt{42} \cos(\theta) (-11 + 15 \cos^2(\theta)) \sin(\varphi)}{8 \sqrt{\pi}}$
3	+2	$-\frac{1 \sqrt{105} \sin^2(\theta) \cos(\theta) \sin(2\varphi)}{2 \sqrt{\pi}}$	$-\frac{\sqrt{105} \sin^2(\theta) \cos(\theta) \cos(2\varphi)}{\sqrt{\pi}}$	$-\frac{1 \sqrt{105} \sin(\theta) (3 \cos^2(\theta) - 1) \sin(2\varphi)}{2 \sqrt{\pi}}$
3	+3	$\frac{3 \sqrt{70} \sin^3(\theta) \sin(3\varphi)}{8 \sqrt{\pi}}$	$-\frac{9 \sqrt{70} \sin^3(\theta) \cos(3\varphi)}{8 \sqrt{\pi}}$	$-\frac{9 \sqrt{70} \cos(\theta) \sin^2(\theta) \sin(3\varphi)}{8 \sqrt{\pi}}$

APPENDIX A.4.

Table of real spherical harmonics for $l = 4$ (part 1):

l	m	y_{lm}	$\frac{\partial y_{lm}}{\partial \theta}$	$\frac{\partial^2 y_{lm}}{\partial \theta^2}$
4	-4	$\frac{3}{16} \frac{\sqrt{35} \sin^4(\theta) \sin(4\varphi)}{\sqrt{\pi}}$	$\frac{3}{4} \frac{\sqrt{35} \sin^3(\theta) \cos(\theta) \sin(4\varphi)}{\sqrt{\pi}}$	$\frac{3}{4} \frac{\sqrt{35} \sin^2(\theta) (4 \cos^2(\theta) - 1) \sin(4\varphi)}{\sqrt{\pi}}$
4	-3	$\frac{3}{8} \frac{\sqrt{70} \sin^3(\theta) \cos(\theta) \sin(3\varphi)}{\sqrt{\pi}}$	$\frac{3}{8} \frac{\sqrt{70} \sin^3(\theta) (4 \cos^2(\theta) - 1) \sin(3\varphi)}{\sqrt{\pi}}$	$\frac{3}{8} \frac{\sqrt{70} \sin(\theta) \cos(\theta) (8 \cos^2(\theta) - 5) \sin(3\varphi)}{\sqrt{\pi}}$
4	-2	$\frac{3}{8} \frac{\sqrt{5} \sin^2(\theta) (7 \cos^2(\theta) - 1) \sin(2\varphi)}{\sqrt{\pi}}$	$\frac{3}{2} \frac{\sqrt{5} \sin(\theta) \cos(\theta) (7 \cos^2(\theta) - 4) \sin(2\varphi)}{\sqrt{\pi}}$	$\frac{3}{2} \frac{\sqrt{5} (28 \cos^4(\theta) - 29 \cos^2(\theta) + 4) \sin(2\varphi)}{\sqrt{\pi}}$
4	-1	$\frac{3}{8} \frac{\sqrt{10} \sin(\theta) \cos(\theta) (7 \cos^2(\theta) - 3) \sin(\varphi)}{\sqrt{\pi}}$	$\frac{3}{8} \frac{\sqrt{10} (28 \cos^4(\theta) - 27 \cos^2(\theta) + 3) \sin(\varphi)}{\sqrt{\pi}}$	$-\frac{3}{4} \frac{\sqrt{10} \sin(\theta) \cos(\theta) (56 \cos^2(\theta) - 27) \sin(\varphi)}{\sqrt{\pi}}$
4	0	$\frac{3}{16} \frac{35 \cos^4(\theta) - 30 \cos^2(\theta) + 3}{\sqrt{\pi}}$	$-\frac{15}{4} \frac{\sin(\theta) \cos(\theta) (7 \cos^2(\theta) - 3)}{\sqrt{\pi}}$	$-\frac{15}{4} \frac{28 \cos^4(\theta) - 27 \cos^2(\theta) + 3}{\sqrt{\pi}}$
4	+1	$\frac{3}{8} \frac{\sqrt{10} \sin(\theta) \cos(\theta) (7 \cos^2(\theta) - 3) \cos(\varphi)}{\sqrt{\pi}}$	$\frac{3}{8} \frac{\sqrt{10} (28 \cos^4(\theta) - 27 \cos^2(\theta) + 3) \cos(\varphi)}{\sqrt{\pi}}$	$-\frac{3}{4} \frac{\sqrt{10} \sin(\theta) \cos(\theta) (56 \cos^2(\theta) - 27) \cos(\varphi)}{\sqrt{\pi}}$
4	+2	$\frac{3}{8} \frac{\sqrt{5} \sin^2(\theta) (7 \cos^2(\theta) - 1) \cos(2\varphi)}{\sqrt{\pi}}$	$\frac{3}{2} \frac{\sqrt{5} \sin(\theta) \cos(\theta) (7 \cos^2(\theta) - 4) \cos(2\varphi)}{\sqrt{\pi}}$	$\frac{3}{2} \frac{\sqrt{5} (28 \cos^4(\theta) - 29 \cos^2(\theta) + 4) \cos(2\varphi)}{\sqrt{\pi}}$
4	+3	$\frac{3}{8} \frac{\sqrt{70} \sin^3(\theta) \cos(\theta) \cos(3\varphi)}{\sqrt{\pi}}$	$\frac{3}{8} \frac{\sqrt{70} \sin^2(\theta) (4 \cos^2(\theta) - 1) \cos(3\varphi)}{\sqrt{\pi}}$	$\frac{3}{4} \frac{\sqrt{70} \sin(\theta) \cos(\theta) (8 \cos^2(\theta) - 5) \cos(3\varphi)}{\sqrt{\pi}}$
4	+4	$\frac{3}{16} \frac{\sqrt{35} \sin^4(\theta) \cos(4\varphi)}{\sqrt{\pi}}$	$\frac{3}{4} \frac{\sqrt{35} \sin^3(\theta) \cos(\theta) \cos(4\varphi)}{\sqrt{\pi}}$	$\frac{3}{4} \frac{\sqrt{35} \sin^2(\theta) (4 \cos^2(\theta) - 1) \cos(4\varphi)}{\sqrt{\pi}}$

APPENDIX A.4.

Table of real spherical harmonics for $l = 4$ (part 1):

l	m	$\frac{\partial y_{lm}}{\partial \varphi}$	$\frac{\partial^2 y_{lm}}{\partial \varphi^2}$	$\frac{\partial^2 y_{lm}}{\partial \theta \partial \varphi}$
4	-4	$\frac{3}{16} \frac{\sqrt{35} \sin^4(\theta) \cos(4\varphi)}{\sqrt{\pi}}$	$-3 \frac{\sqrt{35} \sin^4(\theta) \sin(4\varphi)}{\sqrt{\pi}}$	$-3 \frac{\sqrt{35} \sin^3(\theta) \cos(\theta) \cos(4\varphi)}{\sqrt{\pi}}$
4	-3	$\frac{9}{8} \frac{\sqrt{70} \sin^3(\theta) \cos(\theta) \cos(3\varphi)}{\sqrt{\pi}}$	$-\frac{27}{8} \frac{\sqrt{70} \sin^3(\theta) \cos(\theta) \sin(3\varphi)}{\sqrt{\pi}}$	$\frac{9}{8} \frac{\sqrt{70} \sin^2(\theta) (4 \cos^2(\theta) - 1) \cos(3\varphi)}{\sqrt{\pi}}$
4	-2	$\frac{3}{4} \frac{\sqrt{5} \sin^2(\theta) (7 \cos^2(\theta) - 1) \cos(2\varphi)}{\sqrt{\pi}}$	$-\frac{3}{2} \frac{\sqrt{5} \sin^2(\theta) (7 \cos^2(\theta) - 1) \sin(2\varphi)}{\sqrt{\pi}}$	$3 \frac{\sqrt{5} \sin(\theta) \cos(\theta) (7 \cos^2(\theta) - 4) \cos(2\varphi)}{\sqrt{\pi}}$
4	-1	$\frac{3}{8} \frac{\sqrt{10} \sin(\theta) \cos(\theta) (7 \cos^2(\theta) - 3) \cos(\varphi)}{\sqrt{\pi}}$	$-\frac{3}{8} \frac{\sqrt{10} \sin(\theta) \cos(\theta) (7 \cos^2(\theta) - 3) \sin(\varphi)}{\sqrt{\pi}}$	$\frac{3}{8} \frac{\sqrt{10} (28 \cos^4(\theta) - 27 \cos^2(\theta) + 3) \cos(\varphi)}{\sqrt{\pi}}$
4	0	0	0	0
4	+1	$-\frac{3}{8} \frac{\sqrt{10} \sin(\theta) \cos(\theta) (7 \cos^2(\theta) - 3) \sin(\varphi)}{\sqrt{\pi}}$	$-\frac{3}{8} \frac{\sqrt{10} \sin(\theta) \cos(\theta) (7 \cos^2(\theta) - 3) \cos(\varphi)}{\sqrt{\pi}}$	$-\frac{3}{8} \frac{\sqrt{10} (28 \cos^4(\theta) - 27 \cos^2(\theta) + 3) \sin(\varphi)}{\sqrt{\pi}}$
4	+2	$-\frac{3}{4} \frac{\sqrt{5} \sin^2(\theta) (7 \cos^2(\theta) - 1) \sin(2\varphi)}{\sqrt{\pi}}$	$-\frac{3}{2} \frac{\sqrt{5} \sin^2(\theta) (7 \cos^2(\theta) - 1) \cos(2\varphi)}{\sqrt{\pi}}$	$-3 \frac{\sqrt{5} \sin(\theta) \cos(\theta) (7 \cos^2(\theta) - 4) \sin(2\varphi)}{\sqrt{\pi}}$
4	+3	$-\frac{9}{8} \frac{\sqrt{70} \sin^3(\theta) \cos(\theta) \cos(3\varphi)}{\sqrt{\pi}}$	$-\frac{27}{8} \frac{\sqrt{70} \sin^3(\theta) \cos(\theta) \sin(3\varphi)}{\sqrt{\pi}}$	$-\frac{9}{8} \frac{\sqrt{70} \sin^2(\theta) (4 \cos^2(\theta) - 1) \sin(3\varphi)}{\sqrt{\pi}}$
4	+4	$-\frac{3}{4} \frac{\sqrt{35} \sin^4(\theta) \sin(4\varphi)}{\sqrt{\pi}}$	$-3 \frac{\sqrt{35} \sin^4(\theta) \cos(4\varphi)}{\sqrt{\pi}}$	$-3 \frac{\sqrt{35} \sin^3(\theta) \cos(\theta) \sin(4\varphi)}{\sqrt{\pi}}$

APPENDIX A.4.

The plane-wave can be written in terms of Bessel- and complex spherical-harmonics according to the formula:

$$\mathbf{e}^{i\vec{k}\cdot\vec{r}} = 4\pi \sum_{l,m} i^l Y_{lm}^*(\Omega_{\vec{k}}) Y_{lm}(\Omega_{\vec{r}}) \mathbf{j}_l(\vec{k}\vec{r}) = 4\pi \sum_{l,m} i^l Y_{lm}(\Omega_{\vec{k}}) Y_{lm}^*(\Omega_{\vec{r}}) \mathbf{j}_l(\vec{k}\vec{r}) \quad (\text{A.4.-8})$$

where the spherical Bessel functions are (up to $l = 4$):

$$\mathbf{j}_0(\vec{k}\vec{r}) = \frac{\sin(\vec{k}\vec{r})}{\vec{k}\vec{r}} \quad (\text{A.4.-9})$$

$$\mathbf{j}_1(\vec{k}\vec{r}) = \frac{\sin(\vec{k}\vec{r})}{(\vec{k}\vec{r})^2} - \frac{\cos(\vec{k}\vec{r})}{\vec{k}\vec{r}} \quad (\text{A.4.-10})$$

$$\mathbf{j}_2(\vec{k}\vec{r}) = \left[\frac{3}{(\vec{k}\vec{r})^3} - \frac{1}{\vec{k}\vec{r}} \right] \sin(\vec{k}\vec{r}) - \frac{3}{(\vec{k}\vec{r})^2} \cos(\vec{k}\vec{r}) \quad (\text{A.4.-11})$$

$$\mathbf{j}_3(\vec{k}\vec{r}) = \left[\frac{15}{(\vec{k}\vec{r})^4} - \frac{6}{(\vec{k}\vec{r})^2} \right] \sin(\vec{k}\vec{r}) + \left[-\frac{15}{(\vec{k}\vec{r})^3} + \frac{1}{\vec{k}\vec{r}} \right] \cos(\vec{k}\vec{r}) \quad (\text{A.4.-12})$$

$$\mathbf{j}_4(\vec{k}\vec{r}) = \left[\frac{105}{(\vec{k}\vec{r})^5} - \frac{45}{(\vec{k}\vec{r})^3} + \frac{1}{\vec{k}\vec{r}} \right] \sin(\vec{k}\vec{r}) + \left[-\frac{105}{(\vec{k}\vec{r})^4} + \frac{10}{(\vec{k}\vec{r})^2} \right] \cos(\vec{k}\vec{r}) \quad (\text{A.4.-13})$$

Appendix A.5.

Details about the GGA implementation in the subroutines of EStCoMPP-program

In the pseudopotential generation programs the values for the key (k_{xc} : governs the choice of the exchange-correlation functional) used to perform calculation with GGA functional are: 63-66 for PW91, 73-76 for PBE, 83-86 for PBE-review [PW92, PBE96-98], the last digit the choice of the 3-to-6 point formula for calculating the derivatives.

Since in the atomic program the calculations are done for a single atom the charge is spherical and a simple radial mesh is used:

$$r(i) = (e^{a(i-1)} - 1) \cdot b \quad (\text{A.5-1})$$

In the subroutine `grdchlh_new2.f` the first and second derivatives are calculated on the radial mesh in a "semi-analytical" form (the help array dr/di is calculated in the subroutine `rmesh.f`) accordingly to the expressions:

$$\frac{dn(r_{[i]})}{dr_{[i]}} = \frac{dn(r_{[i]})}{di} \frac{1}{dr_{[i]}/di} \quad (\text{A.5-2})$$

$$\frac{d^2n(r_{[i]})}{dr_{[i]}^2} = \left(\frac{d^2n(r_{[i]})}{di^2} - a \frac{dn(r_{[i]})}{di} \right) \frac{1}{(dr_{[i]}/di)^2} \quad (\text{A.5-3})$$

The parts $\frac{dn(r_{[i]})}{di}$ and $\frac{d^2n(r_{[i]})}{di^2}$ are evaluated numerically using a 3- up to 6-point

formula. Then using the derivatives all the gradients and different product of gradients are calculated in the subroutine `mkg10_new.f`. All these are used in the subroutine `ve_xcallg_new.f` to calculate the exchange-correlation potential and energy (v_{xc} , E_{xc}) due to the given electron density. The subroutines are implemented such that one can deal also with spin-polarized calculations, although we do not use this feature at the moment.

In the atomic-generation programs the radial grid is dense (at least 750 points on a radius of 1.1 a.u) so that the calculation of the first and second derivatives is very accurately done. In the solid-state calculation program the supercell real-space grid is generated by the FFT using a plane-wave cutoff of $g_{maxqp} \times G_{max}$ where g_{maxqp} is equal 2. This is usually dense enough for getting a good description of the electron density in the LDA approximation. But for the GGA case it turns out that for the calculation of second derivatives a grid at least four times denser is required. If a coarse grid is used, the second derivatives are not accurate enough, and as a result the exchange correlation potential is not well described. This will introduce oscillations in the charge from a self-consistent step to the other so that in many cases, where the charge is strongly varying in the space (i.e. single molecules,

APPENDIX A.5.

molecules at the surfaces or simple surfaces), the number of sc-iterations required to achieve convergence can be much larger than the number of sc-iterations required when using the “Bird and White”-scheme.

The values for the keys, k_{xc} -governing the choice of the exchange-correlation functional, used to perform calculations with GGA functionals are: 33-PW91, 34-PBE, 35-PBE-review in the case of traditional scheme ($gmaxqp \times G_{max}$), and 76-PBE, 86- PBE-review for using the Bird and White-scheme.

For the KB-potentials (norm-conserving) the only contribution to the charge density charge density is the plane-wave part. This can be expressed as:

$$n(\vec{r}) = \sum_{\vec{G}} n(\vec{G}) e^{-i\vec{G} \cdot \vec{r}} \quad (A.5-4)$$

Thus, the derivatives of the charge density are analytically calculated in the reciprocal space, and via FFT's transformed to real space. All the gradients and their products are then available on the real space FFT-grid.

In the subroutine potgen.F the first and second derivatives of the charge density in the reciprocal space are calculated accordingly to the formulas:

$$\frac{dn(\vec{r})}{dx_j} = \sum_{\vec{G}} (-iG_j) n(\vec{G}) e^{-i\vec{G} \cdot \vec{r}} \quad (A.5-5)$$

$$\frac{d^2 n(\vec{r})}{dx_k dx_j} = \sum_{\vec{G}} (-i)^2 G_k G_j n(\vec{G}) e^{-i\vec{G} \cdot \vec{r}} \quad (A.5-6)$$

with $k, j = X, Y, Z$. Then, FFT's are performed to find out the first- and second- order and mixed derivatives in real space. The subroutine mkgxyz3_GGA.F creates the gradients in the real space, and the subroutine ve_xcallg_new.f is used to calculate the exchange-correlation potential and energy (v_{xc} , E_{xc}).

If the Bird and White-scheme is used instead of evaluating second order derivatives the subroutine fxc_pbe_wb.f calculates the quantities accordingly to formula (A.2-9), and then the exchange-correlation potential and energy the exchange-correlation potential is computed.

In the case of the PAW-pseudopotentials, because they are non-norm-conserving, two types of charge densities exist inside of the augmentation spheres: “true” and “smooth”. The plane waves are over all space in the supercell. The “smooth” charge density represents the contribution of the pseudo wave function (plane-waves) inside of the PAW augmentation spheres. This has to be replaced by the “true” charge density corresponding to the true wave functions inside of augmentation region in order to recover the total charge of the atoms (see Chapter 3.4, formula 3.4-9). Since the projectors used for transformation are given on a radial mesh, the two charge contributions are expressed on the same radial mesh inside of the spheres, and the exchange-correlation potential is calculated on this mesh. The two charges, their derivatives and gradients are conveniently evaluated in spherical polar coordinates. In the subroutine vxcvd.F E_{xc} and v_{xc} are calculated for the both charges using the y_{lm} components up to $l = 4$.

In order to accurately treat non-spherical charges an angular grid corresponding to 128 radial directions is constructed on each sphere. Along each of these directions an exponential radial grid is used on which the projectors are given. There are at least 750 radial points. The number of points is determined in the pseudopotential generation program, and it depends on

APPENDIX A.5.

the radius of the pseudopotential. The subroutine `pol_angle.F` calculates the angles θ and φ for all grid-points in the sphere, which are then used as an input in the gradients calculation.

The y_{lm} and all angular derivatives like: $\frac{\partial y_{lm}}{\partial \theta}$, $\frac{\partial^2 y_{lm}}{\partial \theta^2}$, $\frac{\partial y_{lm}}{\partial \varphi}$, $\frac{\partial^2 y_{lm}}{\partial \varphi^2}$, $\frac{\partial^2 y_{lm}}{\partial \theta \partial \varphi}$, up to $l = 4$, expressed in the real space, are programmed in the subroutine `lgndr2_new.F` (A detailed table with all formula is given in Appendix A.4). All the other derivatives like radial and mixed (radial-angular) derivatives as $\frac{\partial}{\partial r}$, $\frac{\partial^2}{\partial r^2}$, $\frac{\partial^2}{\partial r \partial \theta}$, $\frac{\partial^2}{\partial r \partial \varphi}$ are calculated in `grdchlh_new3.F` subroutine using a 6 point-formula.

The necessary y_{lm} -dependent gradients are calculated in `mkgyml.F`. The terms are collected and the exchange-correlation potential and energy are determined in the subroutine `ve_xcallg_new.F`. More detailed explanations can be found in the comments of the subroutines.

Appendix B

Partial core-correction in real space

The calculation the partial core-correction charge density in real space is done in several steps in the subroutines: `prprhoc_new.F`, `grdchlh_new2.F`, `prprhoc_real_space.F` and `splint.f`. First, the subroutine `prprhoc_new.F` reads the core charge for each type of atom and defines a sphere of a given radius for each atom. This radius is chosen at the point where the outer tail of the core charge is smaller than 10^{-6} . Then, in the subroutine `grdchlh_new2.F` are calculated first and second derivatives (the partial core-correction charge density is always a spherical charge given on a radial mesh an so only radial derivatives are calculated).

Knowing the position of the atoms in the unit cell the next step consists in identifying the points of the real space grid of the unit cell (associated with the FFT), which are inside of each defined atom sphere. For all this points the distances from the atom-position to the grid points inside of each sphere are calculated. By using a cubic-spline interpolation function (subroutine `splint.f`) the values of the partial core-correction charge densities are calculated and properly assigned to each of the real space grid points of the unit cell.

Observation: The sphere around an atom, which contains the partial core-correction, is not always entirely confined in the same unit cell, or in other words, depending on the position of the atom, part of the defined partial core-correction sphere extends to neighboring unit cells. This corresponds to the case that different parts of the partial core-correction sphere are situated in different places of the unit cell. One can identify the proper real space grid points and calculate the values of the partial core-correction charge density by displacing the atom in all the equivalent positions in the neighboring unit cells (for details please see the comments in `prprhoc_real_space.F`).

Appendix C

Parameters and Tests of the PAW-pseudopotentials

C 1: Detailed information of the generated pseudopotentials

Carbon

The pseudopotential was generated using the keys **LDA** (kxc=2, [VWN80]) and **GGA** (kxc=76, [PBE96-98]). In order to construct the projectors (two per each *l*-channel) two configurations have been chosen: one is the ground-state (with the occupancy of the *l*-channels $2s^2 2p^2$); the ground state eigenvalues yielding the bound states were used to generate the projectors. As second configuration the same occupancy for s- and p- channels has been chosen, but it contains in addition the **d**-channel (with 0 occupancy), which is taken as local potential. For this second atom one has the freedom to choose different reference eigenvalues in such a way that they are positioned in the range of the valence eigenvalues of a given compound. These eigenvalues in general yield as solutions non-bound states. The exact parameters used in generation of the pseudopotential are listed in the table below:

Carbon pseudopotential table 1:

Atom number	s-channel		p-channel		d-channel	
	radius	energy	radius	energy	radius	energy
1 ($2s^2 2p^2$)	1.10	-1.009802	1.10	-0.388706	---	---
2 ($2s^2 2p^2 3d^0$)	1.10	-0.700000	1.10	-0.700000	1.10	-0.300000

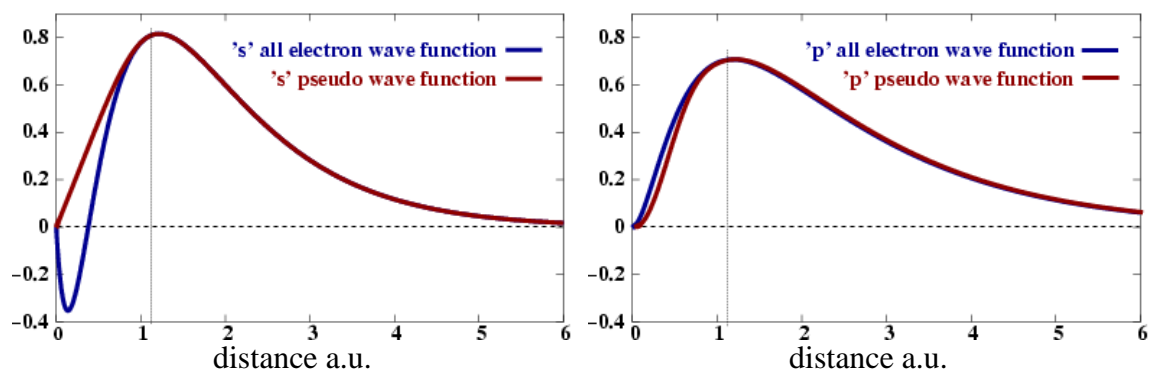
Before the reliability of the constructed pseudopotential is proven many tests have to be made. In the atomic generation program for two additional excited configurations of the carbon atom ($2s^1 2p^3$ and $2s^{1.5} 2p^{2.5}$) all-electron and pseudopotential calculations are performed and the valence eigenvalues are compared (see Carbon pseudopotential table 2).

Carbon pseudopotential table 2:

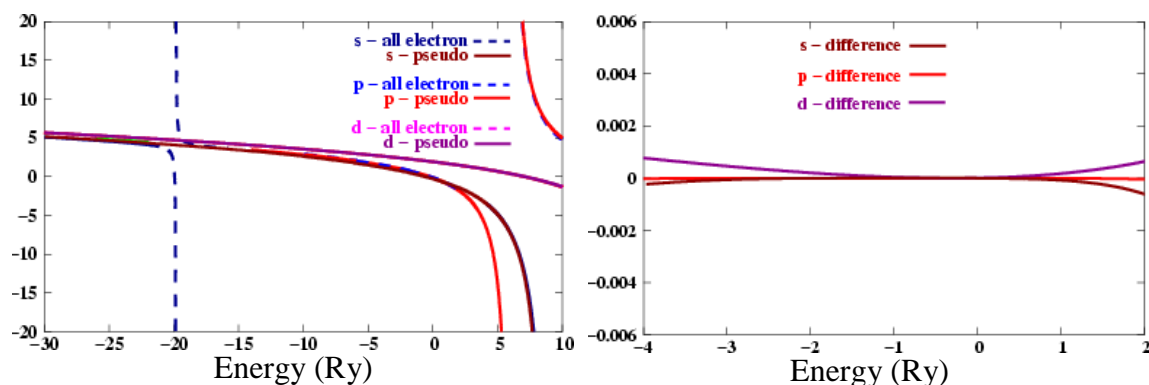
Atom number	s-channel		p-channel		excited energies	
	All-electron	Pseudo	All-electron	Pseudo	All-electron	Pseudo
1 ($2s^2 2p^2$)	-1.009802	-1.009858	-0.388706	-0.388749	0.000000	0.000000
3 ($2s^1 2p^3$)	-1.042740	-1.042851	-0.419940	-0.419979	0.622003	0.622047
4 ($2s^{1.5} 2p^{2.5}$)	-1.026852	-1.026936	-0.404822	-0.404861	0.310789	0.310804

PARAMETERS OF THE PSEUDOPOTENTIALS

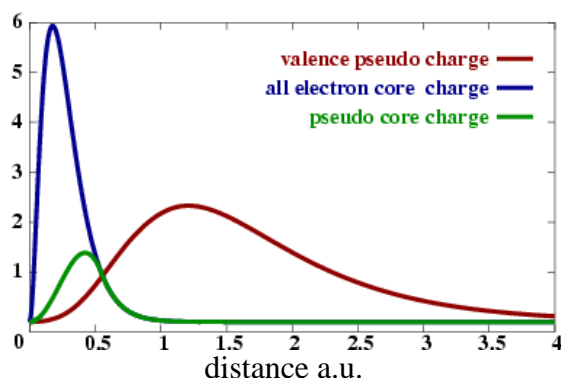
Carbon figure 1: the ‘2s’ and ‘2p’ pseudo and all electron bound state wave functions in the ground state configuration of C are identical starting from 1.1 a.u. (represented by dotted line).



Carbon figure 2: Logarithmic derivatives and their differences in the range of valence electrons: the dotted blue resonance that appears near -20 Ry is due to the $1s^2$ core level, since the pseudopotential describes only the properties of the valence electrons this resonance is smoothed out by the logarithmic derivative of the ‘s’ pseudo-wave-function.



Carbon figure 3: Charge densities of the C.



The first analysis (in the atomic generation program) shows that a good carbon pseudopotential has been generated.

The partial core-correction (pseudo core charge) is taken from the atom with the ground-state configuration (no. 1) and is fitted at r_{PCC} 0.544 a.u. This corresponds to a large partial core-correction (due to the small radius).

Using the same values for cutoff radii and reference energies another pseudopotential has been generated where the partial core-correction is fitted at 1.1 a.u. (radius of the pseudopotential). This corresponds to a small partial core-correction (due to the large radius).

PARAMETERS OF THE PSEUDOPOTENTIALS

Rappe criterion ([RRKJ90]) suggest a cut-off energy of 36 Ry for the convergence of the total energy.

Nitrogen

The pseudopotential for Nitrogen atom was generated using **LDA** (kxc=2) and **GGA** (kxc=76) schemes for the exchange correlation potential. For the construction of the two projectors two configurations were used: (1) the ground state with the occupancy of the *l*-channels **2s² 2p³** where the projectors are taken to be the bound state eigenfunctions and (2) the same occupancy of the **s**- and **p**-channels has been chosen with different reference energies. In addition the **3d**-channel (with 0 occupancy) potential is taken as local potential. The exact parameters used for generating the Nitrogen pseudopotential are listed below:

Nitrogen table 1:

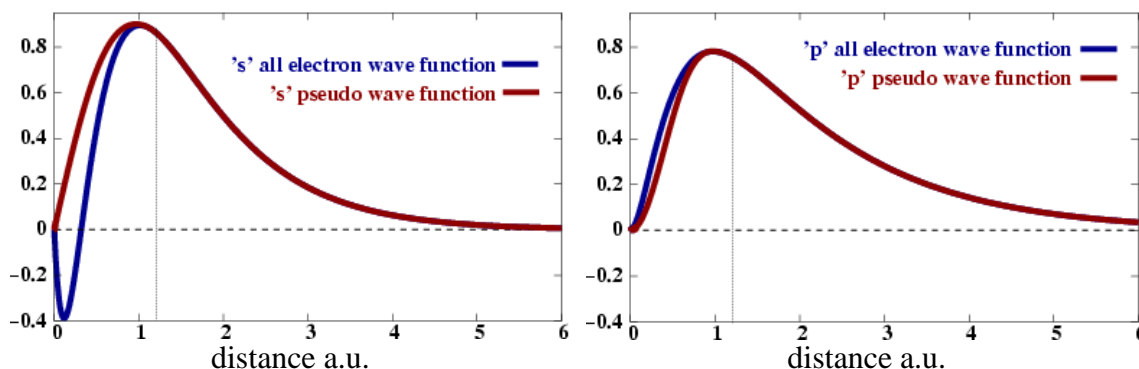
Atom number	s-channel		p-channel		d-channel	
	radius	energy	radius	energy	radius	energy
1 (2s ² 2p ³)	1.2	-1.363963	1.2	-0.521450	---	---
2 (2s ² 2p ³ 3d ⁰)	1.2	-0.950000	1.2	-0.950000	1.2	-0.400000

As tests all-electron and pseudopotential calculations were done for two excited configurations of the atom with the occupancy: **2s^{1.5} 2p^{3.5}** and **2s¹ 2p⁴** (see table below).

Nitrogen table 2:

Atom number	s-channel		p-channel		excited energies	
	All-electron	Pseudo	All-electron	Pseudo	All-electron	Pseudo
1 (2s ² 2p ²)	-1.363963	-1.363964	-0.521450	-0.521450	0.000000	0.000000
3 (2s ^{1.5} 2p ^{3.5})	-1.380694	-1.380719	-0.537110	-0.537110	0.421529	0.421537
4 (2s ¹ 2p ⁴)	-1.396614	-1.396658	-0.552054	-0.552054	0.843568	0.843596

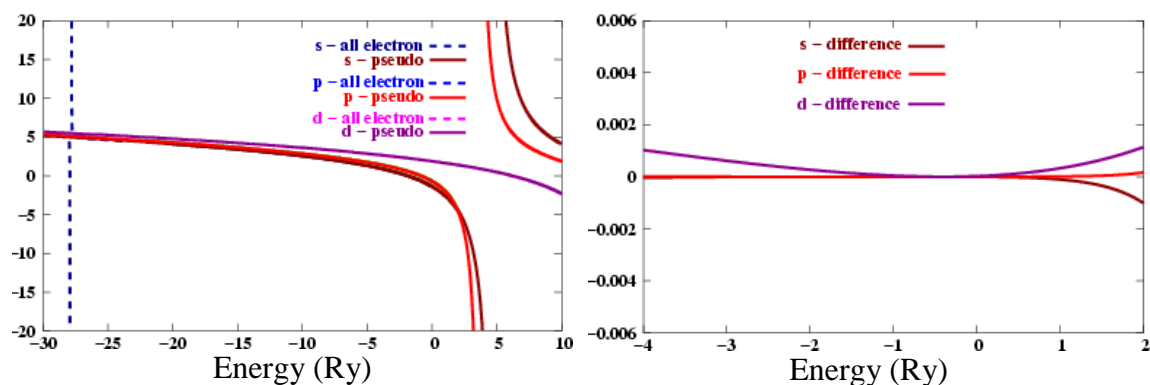
Nitrogen figure 1: ‘2s’ and ‘2p’ all-electron and pseudo-wave functions: for the case of nitrogen there is one valence electron more than in the case of carbon, so that the **s** and **p** all-electron wave functions are more localized. The cut-off radius 1.2 a.u. of the pseudopotential is larger than the position of the maximum of the wave functions.



PARAMETERS OF THE PSEUDOPOTENTIALS

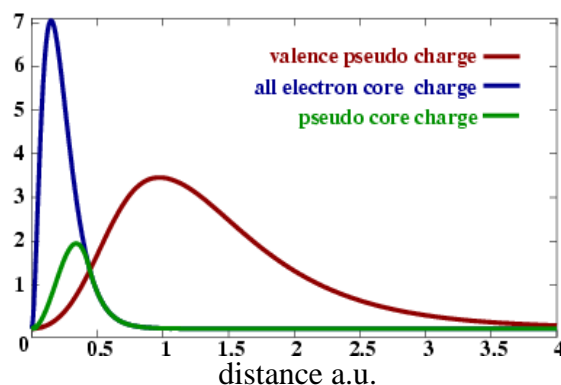
A pseudopotential is easier to construct when the wave function has its maximum localized (close to the nucleus) and the radius of the pseudopotential is larger than this maximum. But another factor that makes it difficult to generate a pseudopotential is the height of the maximum. The 1.2 a.u. cut-off radii (for all the l -channels) of the nitrogen pseudopotential is larger than the position of the maximum of the wave functions, but its height is large and the radius is too close to this maximum. This makes it difficult to construct the nitrogen pseudopotential.

Nitrogen figure 2: Logarithmic derivatives and their differences in the range of the valence electrons.



The logarithmic derivatives of the pseudo-wave functions do not show any resonances because the pseudo-wave functions are without nodes.

Nitrogen figure 3: Charge densities of the N.



The larger partial core-correction (pseudo core charge) was fitted at r_{PCC} 0.438 a.u. using the ground state configuration of atom no. 1. The radius is smaller than in the case of the carbon pseudopotential. The intersection point where the pseudo core-charge becomes smaller than the valence pseudo-charge is determined on one hand by the localization of the wave functions (stronger in the case of the nitrogen than for the carbon) and on the other hand by the cut-off radius of the pseudopotential. For a larger cut-off radius the intersection point is shifted to higher values, then the all-electron core charge becomes smaller there, and automatically the partial core-correction taken into account is smaller. Also for the nitrogen a pseudopotential that takes into account the small pseudo core-charge fitted at a larger radius (1.2 a.u.) has been generated.

Since we use the pseudopotential in the calculations for molecules, where the bond lengths are quite small, we need to construct the pseudopotential with a small cut-off radius.

PARAMETERS OF THE PSEUDOPOTENTIALS

This small radius can introduce ghost states and in order to eliminate them, deep reference energies have to be used for the construction of the second projector. Rappe criterion suggest a cut-off energy of 36 Ry for the convergence of the total energy.

Oxygen

The ground states with the occupancy $2s^2 2p^4$ and the bound state energies have been used to generate the first series of projectors. For the second series of projectors reference energies yielding unbound states are used. The **d**-channel pseudopotential (with 0 occupancy) was taken as local potential. The exact parameters used in generation of the pseudopotential are listed in the Oxygen table 1:

Oxygen table 1:

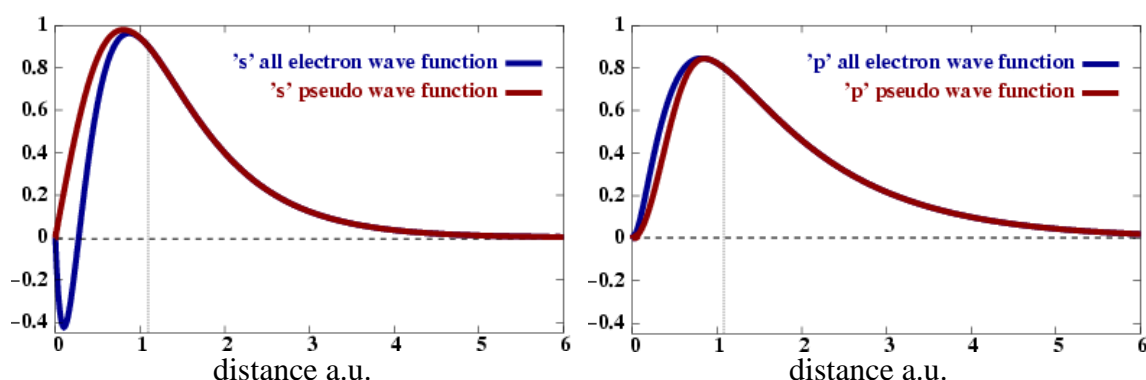
Atom number	s-channel		p-channel		d-channel	
	radius	energy	radius	energy	radius	energy
1 ($2s^2 2p^4$)	1.10	-1.757696	1.10	-0.664255	---	---
2 ($2s^2 2p^4 3d^0$)	1.10	-0.400000	1.10	-0.090000	1.10	-0.400000

In the oxygen case three configurations have been used to test the pseudopotential in the atomic generation program: $2s^{1.9} 2p^{4.1}$, $2s^{1.7} 2p^{4.3}$ and $2s^2 2p^3$ (positive ion).

Oxygen table 2:

Atom number	s-channel		p-channel		excited energies	
	All-electron	Pseudo	All-electron	Pseudo	All-electron	Pseudo
1 ($2s^2 2p^2$)	-1.757696	-1.757696	-0.664255	-0.664256	0.000000	0.000000
3 ($2s^{1.9} 2p^{4.1}$)	-1.761145	-1.761149	-0.667419	-0.667419	0.109358	0.109358
4 ($2s^{1.7} 2p^{4.3}$)	-1.767966	-1.767980	-0.673676	-0.673676	0.328160	0.328161
5 ($2s^2 2p^3$)	-2.911417	-2.911444	-1.797568	-1.797581	1.208230	1.208233

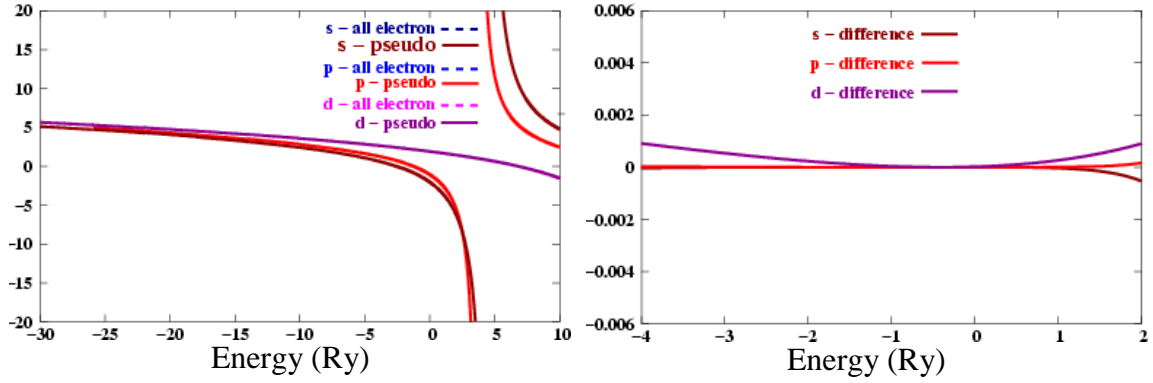
Oxygen figure 1: '2s' and '2p' all-electron and pseudo-wave functions for O.



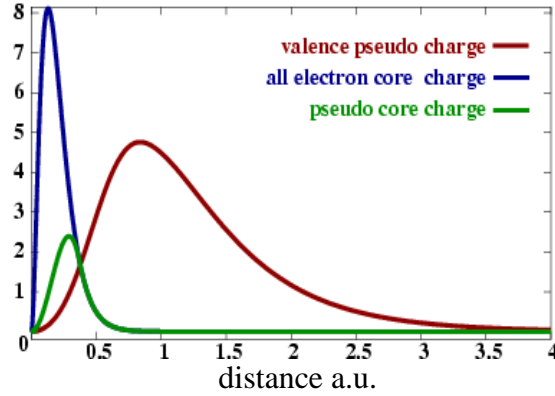
PARAMETERS OF THE PSEUDOPOTENTIALS

Also in the case of oxygen the cut-off radii of the pseudopotentials (1.1 a.u.) are larger than the maximum position of the wave functions but since the electronic charge is larger than in the case of carbon and nitrogen the wave functions are strongly localized close to the nucleus. The cut-off radii of the pseudopotential are close to the value of the maximum of the wave functions. This makes it difficult to generate the pseudopotential. In the case of carbon and nitrogen low reference energies for the second projector have been used to eliminate the ghost state. In the case of oxygen these reference energies are higher (especially for the **p**-channel).

Oxygen figure 2: Logarithmic derivatives and their differences in the range of valence electrons. The **1s** resonance is lower than -30 Ry.



Oxygen figure 3: Charge densities.



Due to the strong localization of the wave functions the all-electron core-charge is even more localized for the oxygen atom than for nitrogen and carbon. Thus the partial core-correction is fitted at even smaller r_{PCC} 0.373 a.u. Also, a pseudopotential with the same cutoff radii but with small partial core-correction has been generated. Rappe criterion suggest a cut-off energy of 36 Ry for the convergence of the total energy.

Using the same reference energies in the constructions of the second series of projectors but larger cutoff radius of 1.4 a.u. another pseudopotential has been generated which can successfully be used for oxide bulk calculations (please see the next part of the bulk tests). For this one the Rappe criterion suggest a cut-off energy of 30 Ry for the convergence of the total energy.

Sulfur

Sulfur has the same number of valence electrons like the oxygen atom but they are on the next higher shell. As it is expected, the cut-off radius will be larger than in the oxygen case but, since there is no fix rule how to construct a good pseudopotential, the parameters which have been used to get good oxygen pseudopotential, cannot be used in sulfur case. The only thing, which one needs to do, is to try different radii and reference energies. The ground state with the occupancy of the *l*-channels $3s^2 3p^4$ has been used to generate the first series of projectors, the second series of projectors have been generated with reference energies yielding unbound states. The *d*-channel (with 0 occupancy) was taken as local potential. The exact parameters used in the generation of the pseudopotential are listed in the Sulfur table 1:

Sulfur table 1:

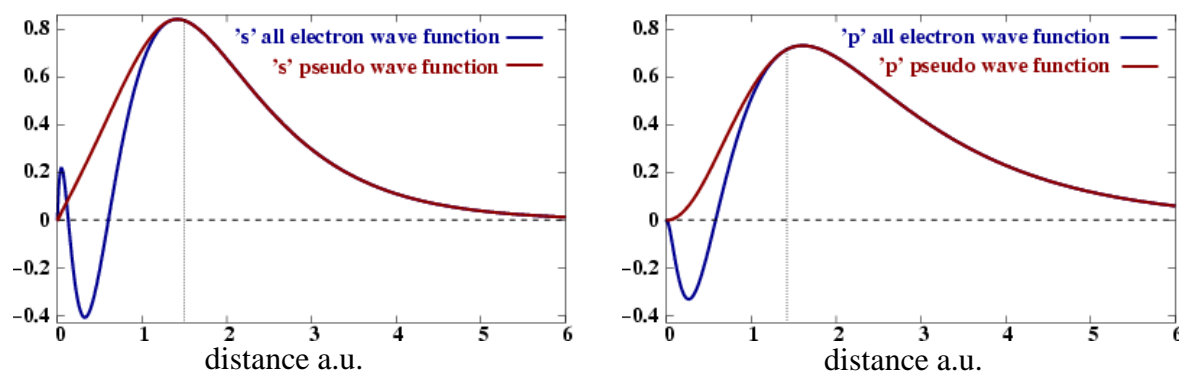
Atom number	s-channel		p-channel		d-channel	
	radius	energy	radius	energy	radius	energy
1 ($3s^2 3p^4$)	1.40	-1.260020	1.40	-0.516051	---	---
2 ($3s^2 3p^4 3d^0$)	1.40	-0.100000	1.40	-0.800000	1.10	-3.7

Tests were done in the atomic generation program for this pseudopotential for three excited configurations (see table below): $3s^2 3p^3$ (positive ion), $3s^2 3p^5$ (negative ion) and $3s^{1.8} 3p^{4.2}$ (excited configuration).

Sulfur table 2:

Atom number	s-channel		p-channel		excited energies	
	All-electron	Pseudo	All-electron	Pseudo	All-electron	Pseudo
1 ($3s^2 3p^4$)	-1.260020	-1.260020	-0.516051	-0.516114	0.000000	0.000000
3 ($3s^2 3p^3$)	-2.021729	-2.022004	-1.235380	-1.235663	0.865992	0.866232
4 ($3s^2 3p^5$)	-0.653452	-0.653411	0.053520	0.053495	-0.214414	-0.214419
5 ($3s^{1.8} 3p^{4.2}$)	-1.270080	-1.270092	-0.524275	-0.524343	0.148978	0.148966

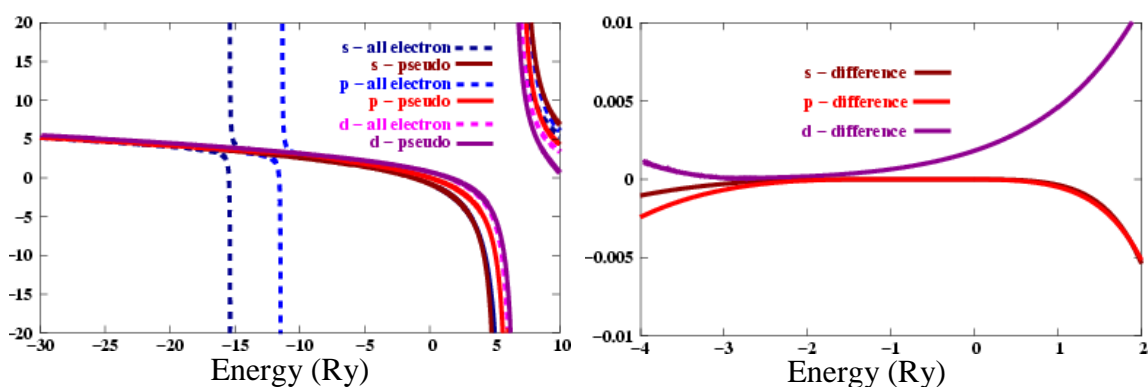
Sulfur figure 1: '3s' and '3p' all-electron and pseudo-wave functions for S.



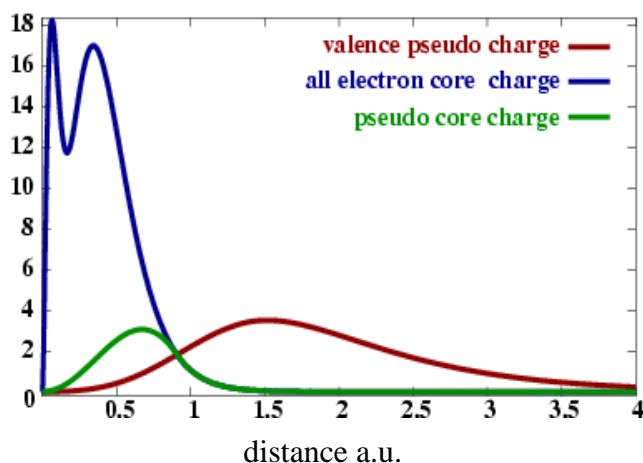
PARAMETERS OF THE PSEUDOPOTENTIALS

The sulfur valence wave functions are not as localized as for the **2p**-atoms and they have a large maximum. For the calculation of the molecules we need a small cutoff radius that is close to the maximum of the wave functions. Moreover, for the **3p** wave-function the cutoff radius is smaller than the maximum of the wave function and thus the construction of the corresponding pseudo-wave-function becomes difficult. In contrast to the oxygen case, the ghost states that appear in the **p**-channel are shifted to higher energies (above 15 Ry) when a low reference energy is used in the construction of the second projector. For the **s**-channel the ghost states are eliminated by using a smaller cutoff radius (1.1 a.u.) for the local (**d**) potential and a corresponding low reference energy.

Sulfur figure 2: Logarithmic derivatives and their differences in the range of valence electrons.



Sulfur figure 3: Charge densities.



Since for the sulfur there are more core electrons, the intersection point where the all-electron core charge becomes comparable to the pseudo valence charge is at $r_{PCC} = 0.91$ a.u. For one of the generated pseudopotentials we use the large partial core-correction that is fitted at this intersection point, and for the other one a small pseudo core-charge is fitted at 1.4 a.u. Rappe criterion suggest a cut-off energy of 20.25 Ry for the convergence of the total energy.

Silicon

The silicon pseudopotential can be easily constructed within a norm-conserving scheme using one projector per each channel. For comparison (to check the implementation of **GGA** and of partial core-correction) a **PAW**-pseudopotential with 2 projectors per l -channel was generated. The bound state configuration is $3s^2 3p^2$ and the occupancy of the channels for the second atom is $3s^2 3p^2 3d^0$, the **d**-channel was taken as local potential. The exact parameters used in generation of the pseudopotential using are listed in the Silicon table 1:

Silicon table 1:

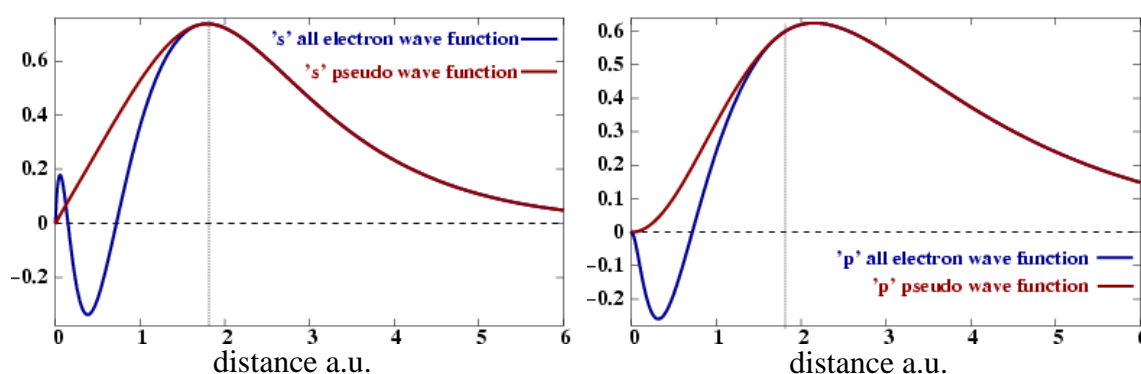
Atom number	s-channel		p-channel		d-channel	
	radius	energy	radius	energy	radius	energy
1 ($3s^2 3p^2$)	1.80	-0.791461	1.80	-0.300634	---	---
2 ($3s^2 3p^2 3d^0$)	1.80	-0.100000	1.80	-0.400000	1.40	-1.900000

The test done in the atomic generation program for this pseudopotential was by using three excited configurations: $3s^2 3p^1$ (positive ion), $3s^{1.8} 3p^{2.2}$ and $3s^1 3p^3$ (see table below).

Silicon table 2:

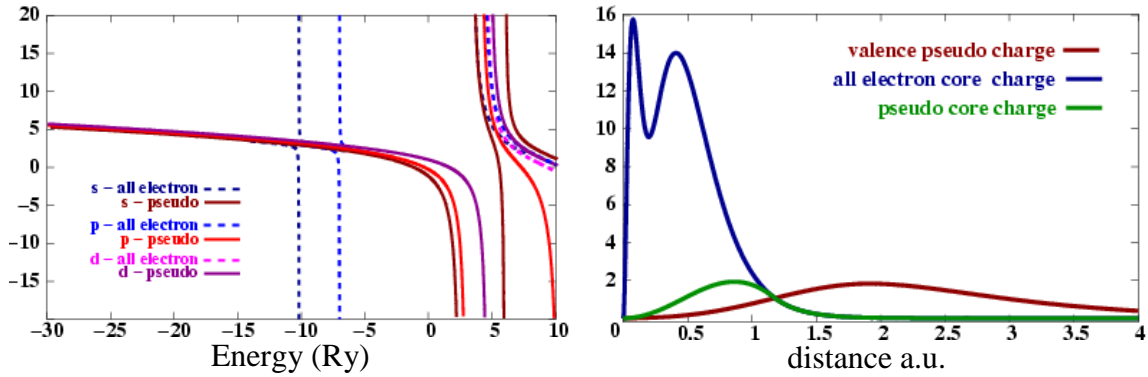
Atom number	s-channel		p-channel		excited energies	
	All-electron	Pseudo	All-electron	Pseudo	All-electron	Pseudo
1 ($3s^2 3p^2$)	-0.791461	-0.791461	-0.300634	-0.300664	0.000000	0.000000
3 ($3s^2 3p^1$)	-1.395371	-1.395668	-0.857537	-0.857770	0.569682	0.569787
4 ($3s^{1.8} 3p^{2.2}$)	-0.802879	-0.802909	-0.309583	-0.309621	0.098414	0.098410
5 ($3s^1 3p^3$)	-0.845810	-0.845960	-0.343417	-0.343489	0.496766	0.496792

Silicon figure 1: '3s' and '3p' all-electron and pseudo-wave functions for the Silicon **PAW**-pseudopotential.



PARAMETERS OF THE PSEUDOPOTENTIALS

Silicon figure 2: Logarithmic derivatives and charge densities of the Silicon **PAW**-pseudopotential



The large partial core-correction for silicon **PAW**-pseudopotential is fitted at a radius of 1.16 a.u. Rappe criterion suggest a cut-off energy of 16 Ry for the convergence of the total energy.

Silicon is a simple case for which one can construct norm-conserving and also non-norm-conserving pseudopotentials using a relative small plane wave basis set (G_{\max} from 3.5 to 4.0) in the both cases. The parameters used are given in the next tables:

Tabel Silicon 1: Si norm-conserving (Kleimman-Bylander) pseudopotential:

Atom number	Cutoff radii (a.u)		
	s-channel	p-channel	d-channel
1 ($3s^2 3p^2$) neutral atom	1.15	1.25	-
2 ($3s^2 3p^{0.25} 3d^{0.75}$) positive ion	1.15	1.25	1.25

The local potential has been chosen for $l = 0$, s-channel, from the atom number 1.

Copper

For the copper atom six projectors have been generated (using **LDA**-[VWN80] and **GGA**-[PBE96-98]): two for each **s**-, **p**- and **d**-channels. The ground state with the occupancy $4s^1 4p^0 3d^{10}$ has been used for generating the projectors corresponding to the bound states. The **p**-level has no electrons, and the **p**-bound state is very extended. This makes difficult to obtain a good transferable pseudopotential with a small cutoff radius. The second series of projectors have been generated with reference energies yielding unbound states. The **4f**-channel (with 0 occupancy) is used as local potential. The exact parameters used in generation of the pseudopotential are listed in the Copper table 1:

Copper table 1:

Atom number	s-channel		p-channel		d-channel		f-channel	
	radius	Energy	radius	energy	radius	energy	radius	energy
1 ($4s^1 4p^0 3d^{10}$)	2.00	-0.32622	2.40	-0.05184	2.10	-0.05184	---	---
2 ($4s^1 4p^0 3d^{10} 4f^0$)	2.00	0.70000	2.40	0.90000	2.10	-0.17000	1.60	0.60000

PARAMETERS OF THE PSEUDOPOTENTIALS

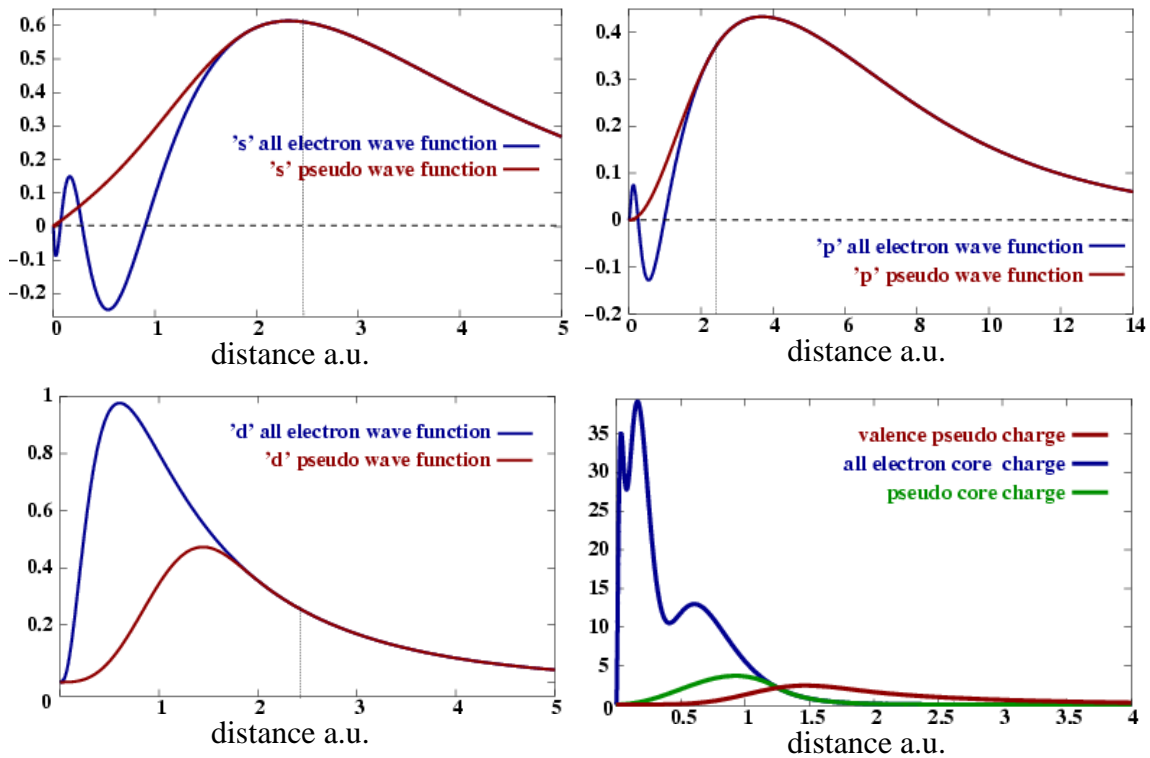
The **d**-all-electron wave function is quite localized and the cutoff radius of 2.1 a.u. is far away from the maximum of wave function. Using higher reference energies for the local potential the ghost states in the other *l*-channels are easily shifted to non-harming high energies. The radius of the pseudopotential is determined by the **p**-channel, the construction of the corresponding pseudo-wave-function being difficult due to the large radius of the maximum of the all-electron **p**-wave function. In order to shift the ghost states and to get a pseudopotential with good convergence in solid state calculations for the **s**- and **p**- channels high reference energies are used when the second projectors are generated.

In the atomic generation program three excited configurations with different occupancy of the **s**-, **p**- and **d**-channels have been used to test the pseudopotential, atom 3 with $4s^1 4p^{0.2} 3d^{9.8}$, atom 4 with $4s^{0.7} 4p^{0.3} 3d^{10}$ and atom 5 with $4s^2 4p^0 3d^9$ (see Copper table 2).

Copper table 2:

Atom number	s-channel		p-channel		d-channel		excited energies	
	All-electron	Pseudo	All-electron	Pseudo	All-electron	Pseudo	All-electron	Pseudo
1	-0.32622	-0.32624	-0.05184	-0.05185	-0.38318	-0.383187	0.00000	0.00000
3	-0.36703	-0.36663	-0.07701	-0.07688	-0.47807	-0.479728	0.07304	0.07304
4	-0.36225	-0.36247	-0.07874	-0.07880	-0.43439	-0.433967	0.08345	0.08348
5	-0.41720	-0.41546	-0.08895	-0.08837	-0.72777	-0.747650	0.17637	0.18509

Copper figure 1: '4s', '4p' and '3d' all-electron and pseudo-wave functions for the Cu PAW-pseudopotential.

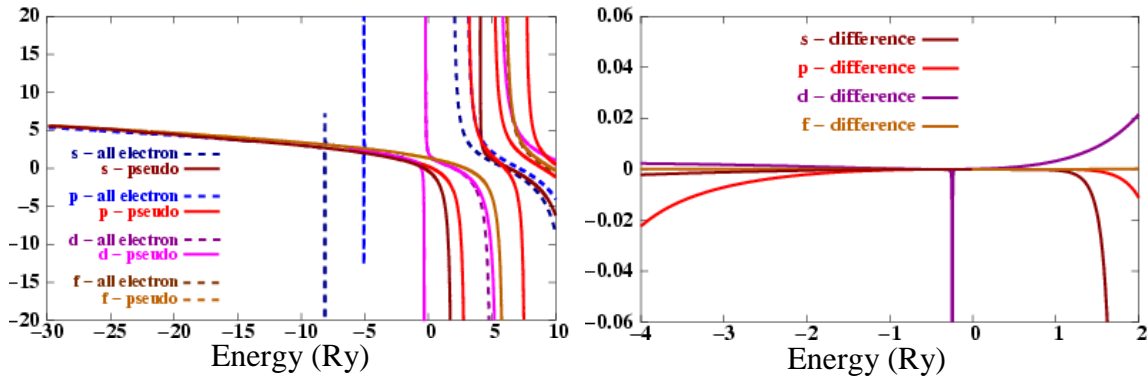


Due to the relatively small cutoff radii of the pseudopotential, the intersection radius of the all-electron core-charge with the valence pseudo charge is quite large, close to the maximum of the valence pseudo-charge. Thus, the overlap of the tail of the all-electron core-

PARAMETERS OF THE PSEUDOPOTENTIALS

charge and valence pseudo charge is much larger than in the other generated pseudopotentials. The partial core-charge is fitted at 1.24 a.u. The pseudo core-charge has a higher maximum than the valence pseudo charge, while in the case of carbon, nitrogen and oxygen is the other way around. Rappe criterion suggest a cut-off energy of 23 Ry for the convergence of the total energy.

Copper figure 2: Logarithmic derivatives and their differences of the copper pseudopotential. The peak which appear in the differences of logarithmic derivatives is the 3d resonance of the all electron and pseudo-wave function.



Cadmium

For the cadmium atom six projectors have been generated: two for each **s**-, **p**- and **d**-channels using the **LDA** scheme for the exchange-correlation potential. The ground state has the occupancy $5s^2 5p^0 4d^{10}$. We used the bound states to construct the first series of projectors, although the $5p$ -level has no electrons. This is quite extended and the **p**-channel determines the augmentation radius of the pseudopotential. The second series of projectors have been generated with reference energies yielding unbound states. The $4f$ -channel (with 0 occupancy) is used as local potential. The partial core-correction is taken from the second atom at a radius of 2.3 a.u. The exact parameters used in generation of the pseudopotential are listed in the table below:

Cadmium table 1:

Atom number	s-channel		p-channel		d-channel		f-channel	
	radius	energy	radius	energy	radius	energy	radius	energy
1 ($5s^2 5p^0 4d^{10}$)	2.33	-0.40845	2.60	-0.10524	2.60	-0.10525	---	---
2 ($5s^2 5p^0 4d^{10} 4f^0$)	2.33	-0.10000	2.60	-0.40000	2.60	-0.60000	2.60	-0.40000

Compared with the copper pseudopotential negative reference energies are used to generate the second projector in order to eliminate the ghost states.

In the atomic generation program three other excited configurations with different occupancy of the **s**-, **p**- and **d**-channels have been used to test the pseudopotential, atom 3 with $5s^2 5p^{0.6} 3d^{9.4}$, atom 4 with $5s^{1.5} 5p^{0.5} 4d^{10}$ and atom 5 with $5s^{1.5} 5p^{0.8} 4d^{9.7}$.

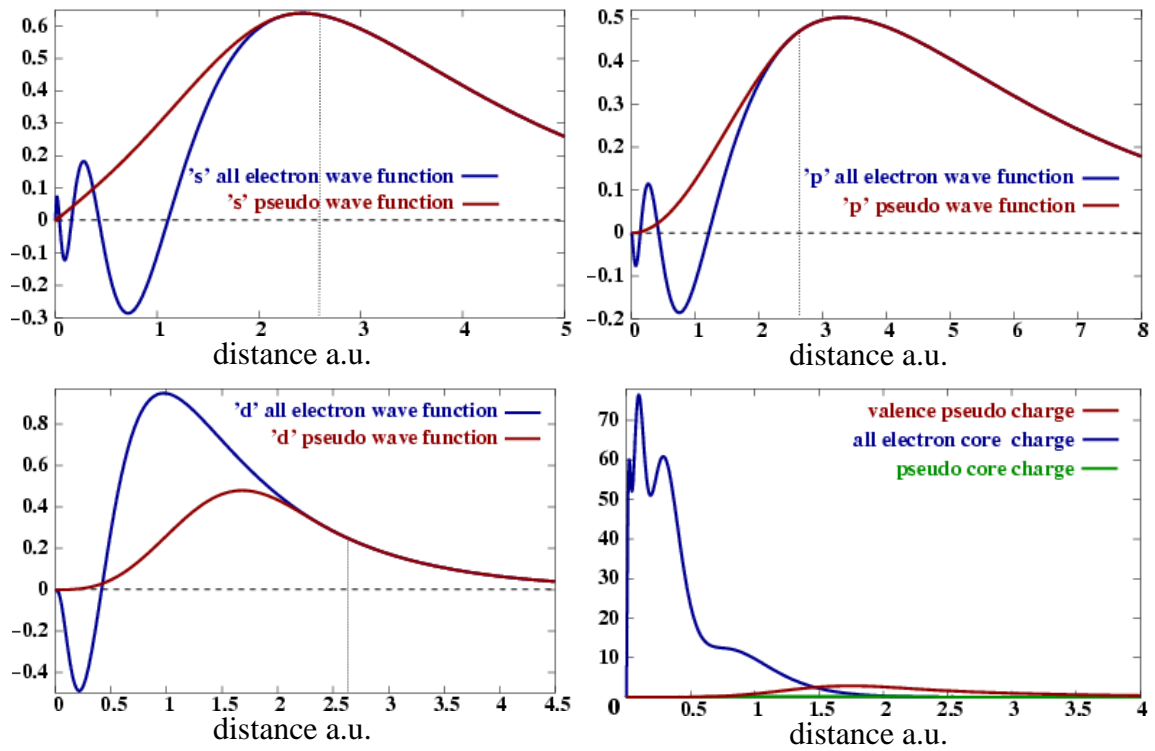
Rappe criterion suggest a cut-off energy of 20.25 Ry for the convergence of the total energy.

PARAMETERS OF THE PSEUDOPOTENTIALS

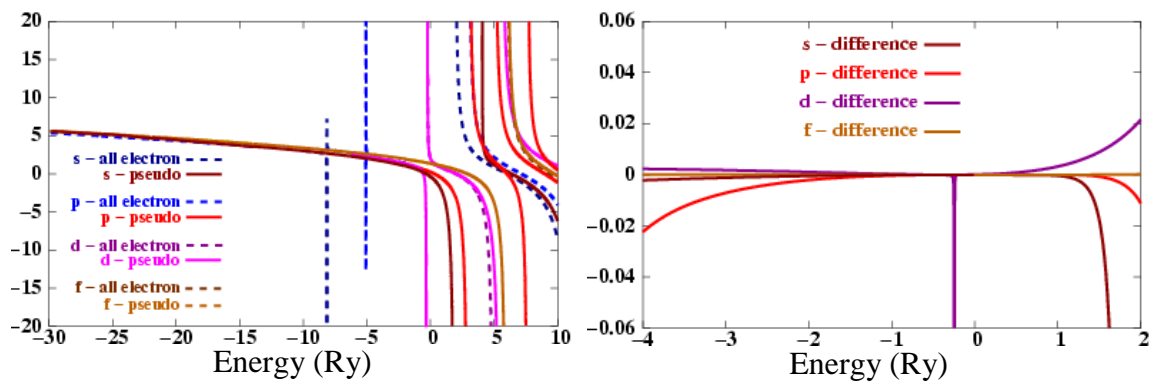
Cadmium table 2:

Atom number	s-channel		p-channel		d-channel		excited energies	
	All-electron	Pseudo	All-electron	Pseudo	All-electron	Pseudo	All-electron	Pseudo
1	-0.40845	-0.40848	-0.10524	-0.10525	-0.94105	-0.94105	---	---
3	-0.50827	-0.50880	-0.16745	-0.16729	-1.19207	-1.19757	0.55791	0.55978
4	-0.45137	-0.45141	-0.13881	-0.13882	-1.00670	-1.00679	0.15381	0.15381
5	-0.49867	-0.49880	-0.16692	-0.16687	-1.12829	-1.13198	0.42819	0.42877

Cadmium figure 1: '5s', '5p' and '4d' all-electron and pseudo-wave functions for the Cd PAW-pseudopotential.



Cadmium figure 2: Logarithmic derivatives and their differences for the cadmium pseudopotential.



Gallium

For the gallium atom six projectors have been generated: two for each **s**-, **p**- and **d**-channels. The ground state has the occupancy $4s^2 4p^1 3d^{10}$ that is used to construct the projectors corresponding to the bound states. The **4p**-level has one electron and thus the extended **p**-bound state has the largest cutoff radius. The second series of projectors has been generated using reference energies, which yield unbound states. The **4f**-channel (with 0 occupancy) is used as local potential. The small partial core-correction is taken from atom no. 2 at a radius of 1.97 a.u. The exact parameters used in generation of the pseudopotential are listed in the table below:

Gallium table 1:

Atom number	s-channel		p-channel		d-channel		f-channel	
	radius	energy	radius	energy	radius	energy	radius	energy
1 ($4s^2 4p^1 3d^{10}$)	1.95	-0.65603	2.00	-0.20326	2.20	-1.47240	---	---
2 ($4s^2 4p^1 3d^{10} 4f^0$)	1.95	-0.20000	2.10	-0.60000	2.00	0.60000	2.20	-0.99000

Due to the large radius of the maximum of the **p**-all-electron wave-function and the fact that the radius of the pseudopotential is smaller than this maximum the ghost states in the **p**-channel are shifted when different cutoff radii in the construction of the two projectors are used. The low reference energy of the local potential eliminates the ghost states that appear in the **s**-channel.

An observation here is that sometimes the ghost states that appear in one **l**-channel are not due to the specific parameters used in the construction of the projector of that **l**-channel. The ghost states are eliminated when the cutoff radii or/and reference energies of other **l**-channels are changed, although the **l**-channels themselves are well described for the those parameters.

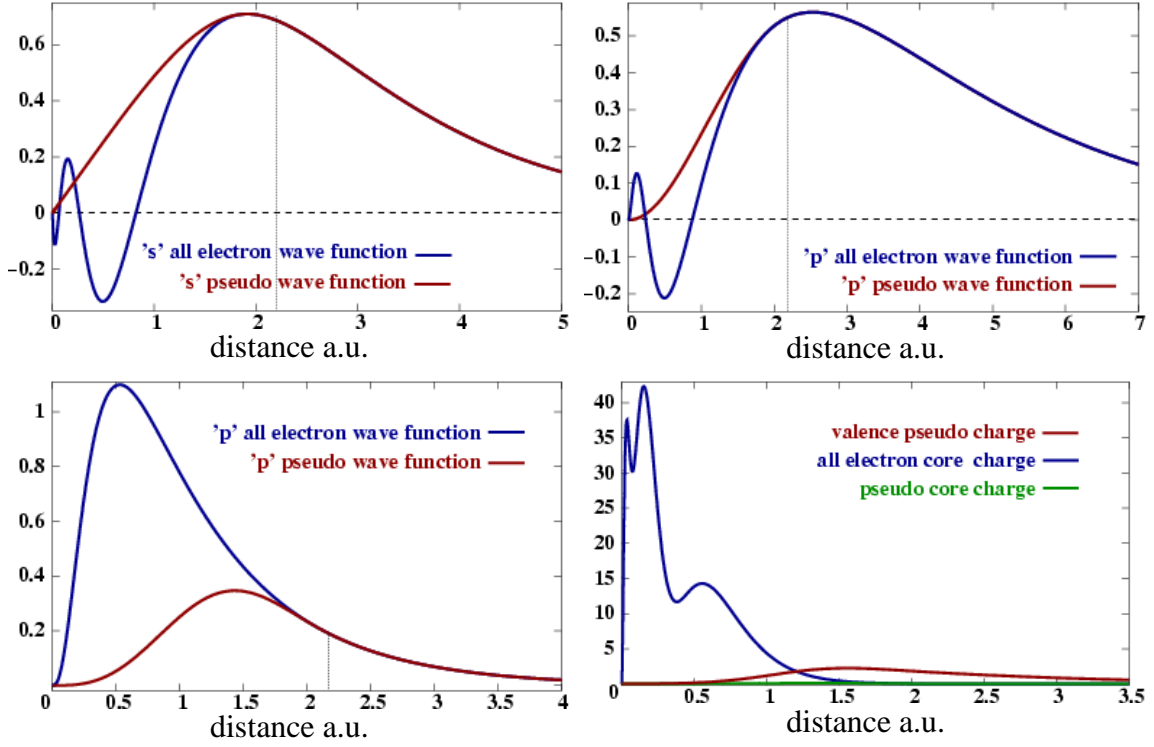
In the atomic generation program three other excited configurations with different occupancy of the **s**-, **p**- and **d**-channels have been used to test the pseudopotential, atom 3 with $4s^2 4p^{1.1} 3d^{9.9}$, atom 4 with $4s^{1.9} 4p^{1.1} 3d^{10}$ and atom 5 with $4s^{1.7} 4p^{1.3} 3d^{10}$ occupancy of the **l**-channels.

Gallium table 2:

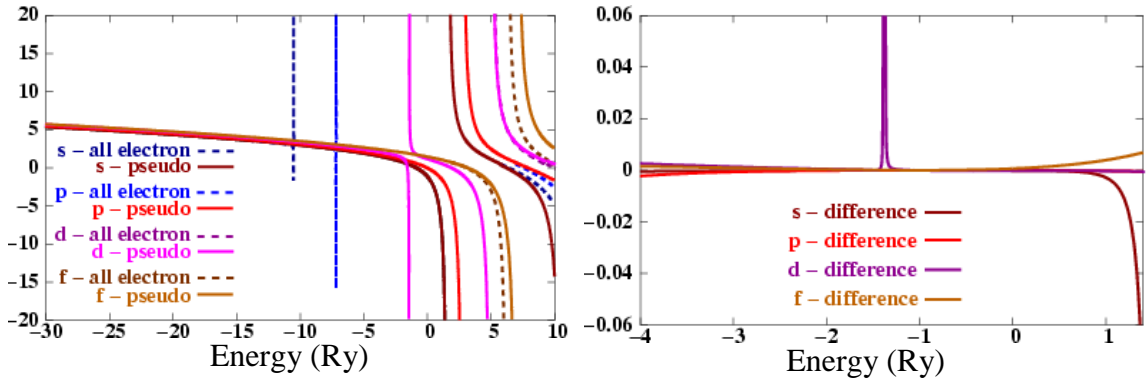
Atom number	s-channel		p-channel		d-channel		excited energies	
	All-electron	Pseudo	All-electron	Pseudo	All-electron	Pseudo	All-electron	Pseudo
1	-0.65603	-0.65607	-0.20326	-0.20329	-1.47240	-1.47240	---	---
3	-0.67399	-0.67395	-0.21317	-0.21316	-1.53696	-1.54116	0.12964	0.12985
4	-0.66437	-0.66441	-0.20914	-0.20916	-1.48635	-1.48629	0.04540	0.04540
5	-0.68054	-0.68059	-0.68059	-0.22054	-1.51364	-1.51345	0.13692	0.13693

PARAMETERS OF THE PSEUDOPOTENTIALS

Gallium figure 1: ‘4s’, ‘4p’ and ‘3d’ all-electron and pseudo-wave functions and charge densities for the Ga PAW-pseudopotential.



Gallium figure 2: Logarithmic derivatives and their differences.



Rappe criterion suggest a cut-off energy of 18.5 Ry for the convergence of the total energy.

Titanium 1(generated using neutral configuration)

In the case of the titanium pseudopotential two projectors for each **s**-, **p**- and **d**-channels have been generated. The neutral ground state that has been chosen in the construction of this pseudopotential has the occupancy $3s^2 3p^6 3d^4$. This is used to construct the projectors corresponding to the bound states. The second series of projectors has been generated from the same configuration with reference energies yielding unbound states. The **4f**-channel (with 0 occupancy) is used as local potential. A small partial core-correction is taken into account fitted at 1.19 a.u. (atom no 2). The exact parameters used in generation of the pseudopotential are listed in Titanium table 1.

PARAMETERS OF THE PSEUDOPOTENTIALS

Titanium table 1:

Atom number	s-channel		p-channel		d-channel		f-channel	
	radius	energy	radius	energy	radius	energy	radius	energy
1 (3s ² 3p ⁶ 3d ⁴)	1.70	-4.14392	1.70	-2.48986	2.00	-0.08393	---	---
2 (3s ² 3p ⁶ 3d ⁴ 4f ⁰)	1.20	-0.30000	1.30	-0.40000	2.00	-0.30000	2.00	-0.60000

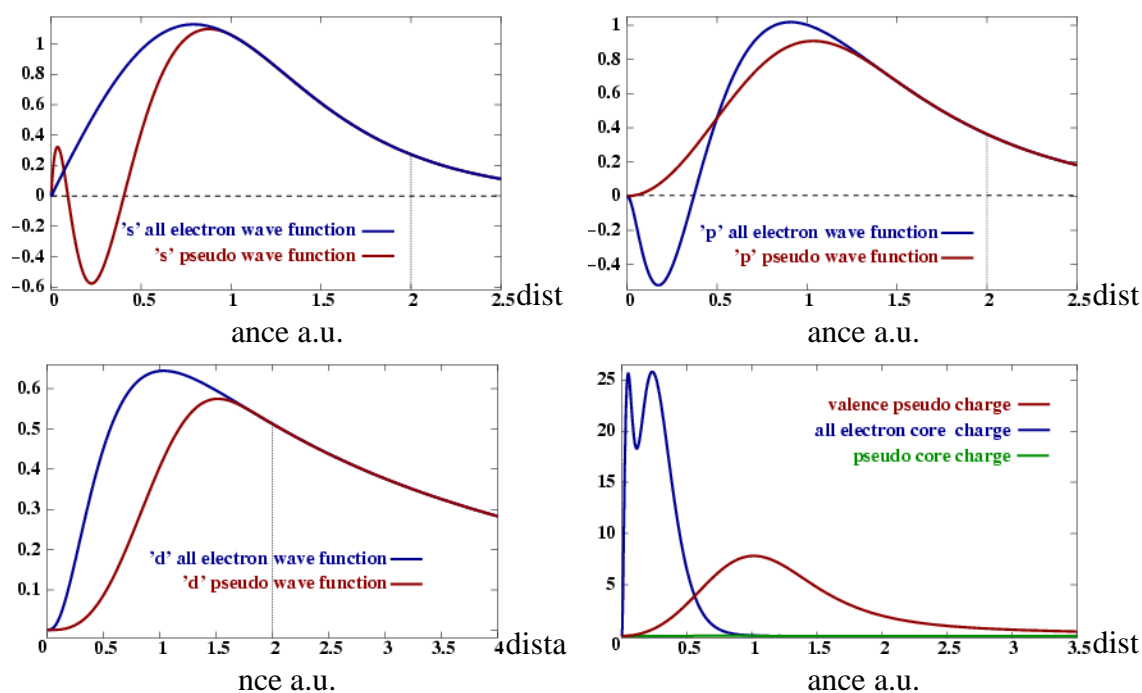
The construction of the projectors for the **d**-channel is difficult due to the small cutoff radius required for the pseudopotential. The **d**-electrons are not localized but rather spread over a large distance in space. Even if in the construction of the '**d**' pseudo-wave-function ghost states do not appear the projectors generated for the **d**-channel will introduce ghost states in **s**- and **p**-channels. These are eliminated or shifted to higher energies only when in the construction of the second projector for **s**- and **p**-channels a small cutoff radius is taken into account.

In the atomic generation program three other excited configurations with different occupancy of the **s**-, **p**- and **d**-channels have been used to test the pseudopotential, atom 3 with 3s² 3p^{5.9} 3d^{4.1}, atom 4 with 3s² 3p^{5.8} 3d^{4.2} and atom 5 with 3s² 3p⁶ 3d³ (positive ion) occupancy of the *l*-channels.

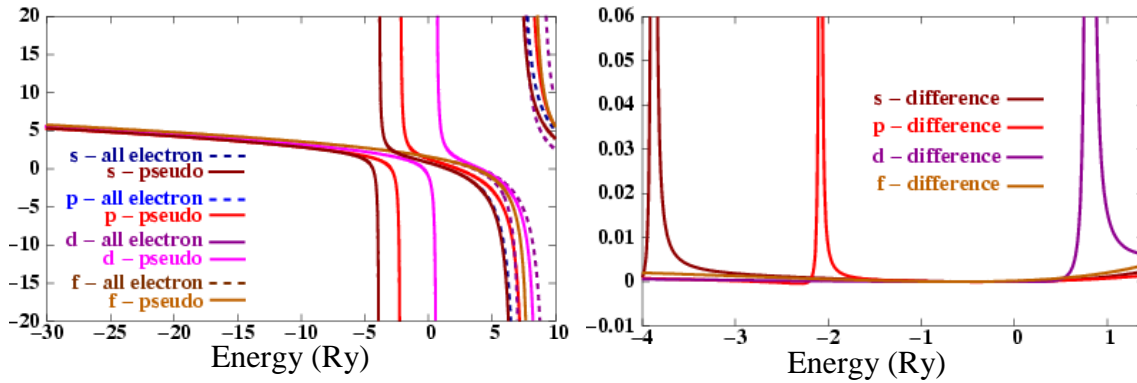
Titanium table 2:

Atom number	s-channel		p-channel		d-channel		excited energies	
	All-electron	Pseudo	All-electron	Pseudo	All-electron	Pseudo	All-electron	Pseudo
1	-4.14392	-4.14394	-2.48986	-2.48989	-0.08393	-0.083936	—	—
3	-4.15052	-4.15086	-2.49588	-2.49621	-0.08587	-0.085873	0.24079	0.24081
4	-4.15705	-4.15771	-2.50184	-2.50248	-0.08784	-0.087851	0.48200	0.48206
5	-4.72609	-4.72597	-3.06881	-3.06871	-0.61186	-0.611892	0.31647	0.31648

Titanium figure 1: '3s', '3p' and '3d' all-electron and pseudo-wave functions and charge densities for the Ti PAW-pseudopotential.



Titanium figure 2: Logarithmic derivatives and their differences.



Rappe criterion suggest a cut-off energy of 21 Ry for the convergence of the total energy.

Titanium 2 (generated using ionic configuration)

Another titanium pseudopotential has been generated considering the ground state as being a partial ionic configuration with the occupancy $4s^2 3p^6 3d^{0.5}$. For this pseudopotential six projectors have been constructed, two projectors for the s-, p- and d-channels, but compared with the previous ones the s-projectors are constructed considering as valence states the 4s levels. The second series of projectors has been generated from the same configuration with reference energies yielding unbound states. The 4f-channel (with 0 occupancy) is used as local potential. A small partial core-correction is taken into account fitted at 2.31 a.u. (atom no 2). The exact parameters used in generation of the pseudopotential are listed in the Titanium table 3.

The cutoff radius for the s-channel is smaller than the maximum of the wave function and ghost states appear. These can be shifted only when high reference energy for the second s-projector and a low reference energy for the local f-potential are used.

In the atomic generation program three other excited configurations with different occupancy of the s-, p- and d-channels have been used to test the pseudopotential, atom 3 with $4s^2 3p^6 3d^2$, atom 4 with $4s^2 3p^6 3d^1$ and atom 5 with $4s^2 3p^{5.5} 3d^2$ occupancy of the l-channels.

Titanium table 3:

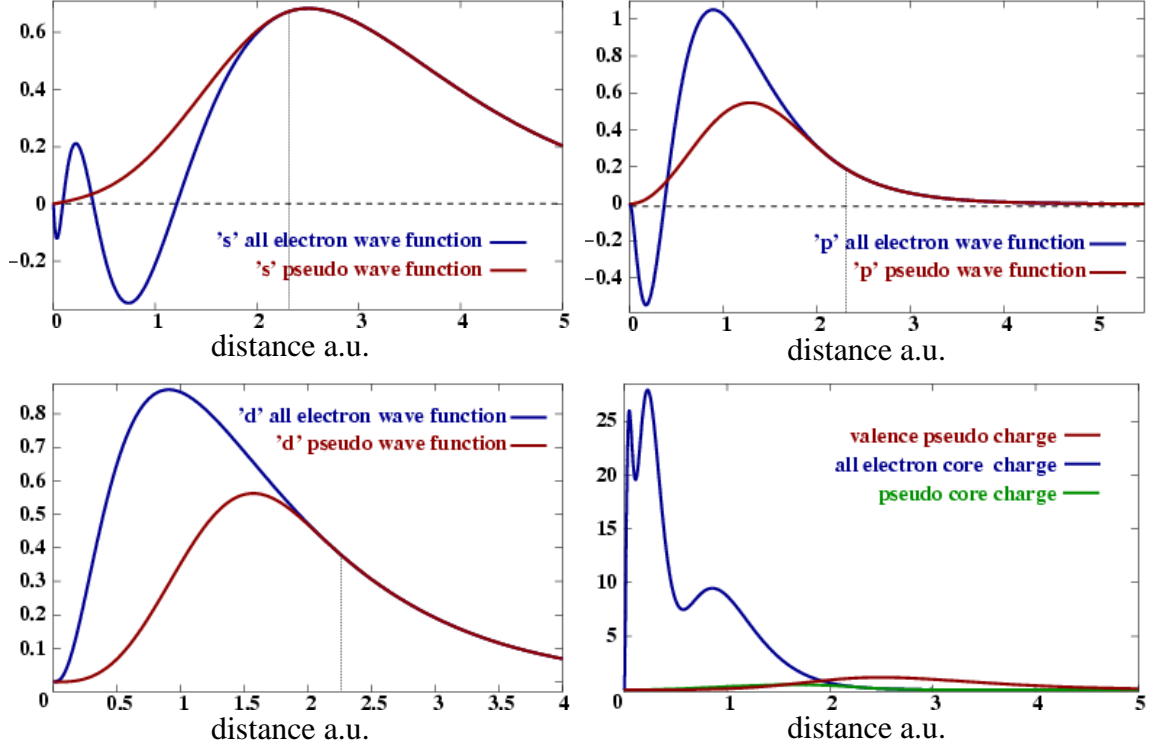
Atom number	s-channel		p-channel		d-channel		f-channel	
	radius	energy	radius	energy	radius	energy	radius	energy
1 ($4s^2 3p^6 3d^{0.5}$)	2.30	-1.20865	2.30	-4.34719	2.30	-1.72812	---	---
2 ($4s^2 3p^6 3d^{0.5} 4f^0$)	2.30	1.90000	2.30	-1.20000	1.80	-1.00000	2.30	-2.60

Titanium table 2:

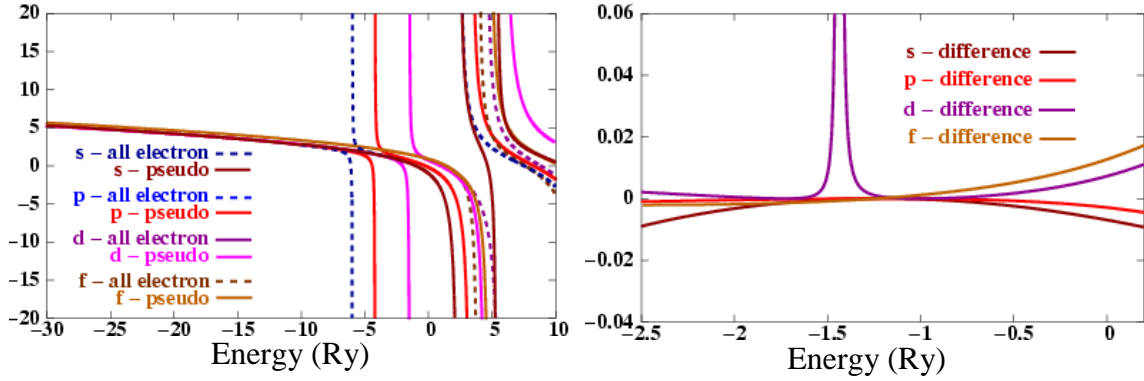
Atom number	s-channel		p-channel		d-channel		excited energies	
	All-electron	Pseudo	All-electron	Pseudo	All-electron	Pseudo	All-electron	Pseudo
1	-1.20865	-1.20870	-4.34719	-4.34719	-1.72812	-1.728125	—	—
3	-0.33421	-0.33624	-2.84589	-2.83492	-0.34002	-0.333330	-1.47964	-1.47227
4	-0.88503	-0.88545	-3.78690	-3.78117	-1.20380	-1.199500	-0.73074	-0.72958
5	-0.59787	-0.59897	-3.33239	-3.32554	-0.77511	-0.769900	0.06204	0.06487

PARAMETERS OF THE PSEUDOPOTENTIALS

Titanium figure 3: ‘4s’, ‘3p’ and ‘3d’ all-electron and pseudo-wave functions and charge densities for the Ti PAW-pseudopotential.



Titanium figure 4: Logarithmic derivatives and their differences.



Platinum

For the platinum atom six projectors have been generated: two for each **s**-, **p**- and **d**-channels. The ground state has the occupancy $5s^2 5p^6 5d^{10}$ that is used to construct the projectors corresponding to the bound states. The second series of projectors has been generated from the same configuration with reference energies yielding unbound states. The **5f**-channel (with 0 occupancy) is used as local potential. The small partial core-correction is taken from atom no. 2 at a radius of 1.99 a.u. The exact parameters used in generation of the pseudopotential are listed in the Platinum table 1.

The **d**-channel is that one which determines the augmentation radius of the pseudopotential due to the extended **d** all-electron wave-function. Although the all-electron wave functions that characterize the **s**- and **p**-channels are quite localized, in the construction of the projector corresponding to the unbound states small cutoff radii have to be used in order to eliminate the ghost states.

PARAMETERS OF THE PSEUDOPOTENTIALS

Platinum table 1:

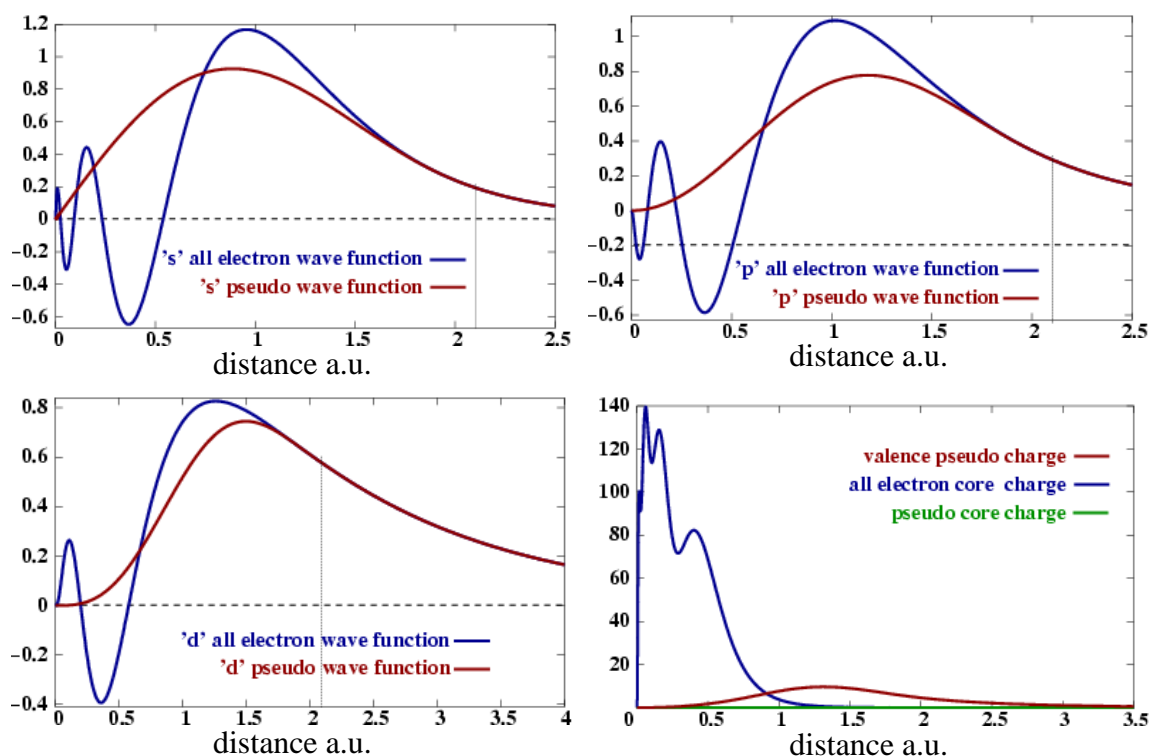
Atom number	s-channel		p-channel		d-channel		f-channel	
	radius	energy	radius	energy	radius	energy	radius	energy
1 (5s ² 5p ⁶ 5d ¹⁰)	2.10	-5.66213	2.10	-3.53681	2.10	-0.36012	---	---
2 (5s ² 5p ⁶ 5d ¹⁰ 5f ⁰)	1.25	-1.20000	1.40	-1.20000	2.10	-1.20000	2.10	-1.10000

In the atomic generation program three other excited configurations with different occupancy of the s-, p- and d-channels have been used to test the pseudopotential, atom 3 with 5s² 5p⁶ 5d⁹, atom 4 with 5s² 5p⁶ 5d⁸ and atom 5 with 5s² 5p^{5.8} 5d^{8.7} occupancy of the *l*-channels.

Platinum table 2:

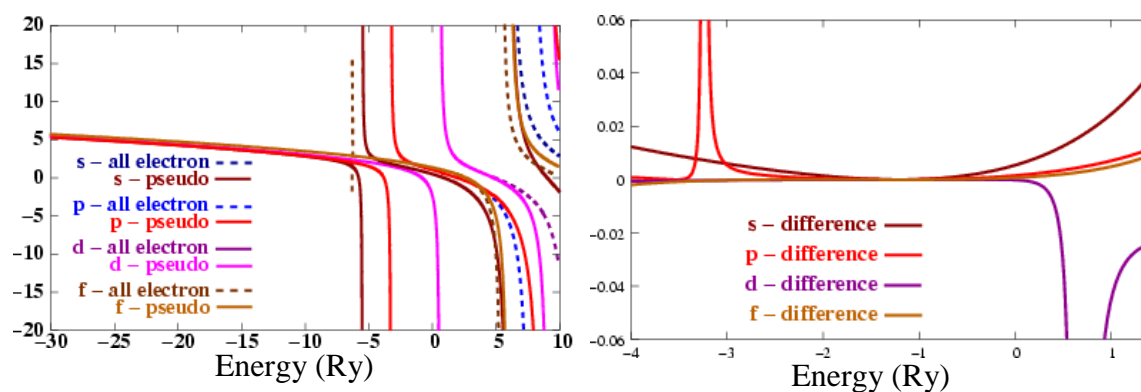
Atom number	s-channel		p-channel		d-channel		excited energies	
	All-electron	Pseudo	All-electron	Pseudo	All-electron	Pseudo	All-electron	Pseudo
1	-5.66213	-5.66214	-3.53681	-3.53681	-0.36061	-0.360614	---	---
3	-6.46544	-6.46554	-4.33435	-4.33449	-1.10704	-1.107095	0.72147	0.72149
4	-7.41120	-7.41216	-5.26964	-5.27047	-1.97782	-1.978180	2.25512	2.25531
5	-6.94617	-6.94708	-4.80802	-4.80874	-1.54217	-1.542400	2.03179	2.03193

Platinum figure 1: '5s', '5p' and '5d' all-electron and pseudo-wave functions and charge densities for the Pt PAW-pseudopotential.



PARAMETERS OF THE PSEUDOPOTENTIALS

Platinum figure 2: Logarithmic derivatives and their differences.



Rappe criterion suggest a cut-off energy of 25 Ry for the convergence of the total energy.

Tests of the PAW-pseudopotentials

C 2.1: Bulks¹

Silicon bulk

Silicon is a simple case for which one can construct norm-conserving and also non-norm-conserving pseudopotentials using a relative small plane wave basis set (G_{\max} from 3.5 to 4.0) in both cases.

The results for the Si norm-conserving pseudopotential obtained for different sets of **k**-points and different energy cutoff (expressed as G_{\max}) are:

Table Silicon 3: The calculated **LDA** Si bulk lattice constant (Å) for different sets of **k**-points and different cutoff energies. (The experimental lattice constant is $a_{\text{exp}} = 5.43$ Å)

k-point	G_{\max}		
	3.0	3.5	4.0
5x5x5	5.425	5.411	5.397
6x6x6	5.424	5.407	5.394
9x9x9	5.413	5.406	5.393
12x12x12	5.423	5.406	5.393

k-point	G_{\max}	
	3.7	4.0
4x4x4	5.411	5.401

One can see that the lattice constant is well described at $G_{\max} = 4$ with a set of **4x4x4** **k**-point. These calculations have been done for the case when no partial core-correction is taken into account.

In the case of **GGA** pseudopotential the results for the fitted lattice constant using the upper parameters ($G_{\max} = 4$, **4x4x4** **k**-point) and three different functionals for the exchange-correlation are:

Table Silicon 4: The calculated **GGA** Si bulk lattice constant (Å) for different exchange-correlation functionals (**4x4x4** **k**-point).

Exchange-correlation functional	Type of fitting	
	UEBR ²	MURN ³
PW91	5.411	5.410
PBE	5.414	5.413
PBE_review	5.420	5.419

As expected for the **GGA**, the lattice constant is slightly larger than the LDA result. Using the same parameters for the energy cutoff and set of **k**-points, **PBE-GGA** functional, but in addition a partial core-correction taken at a radius of 1.19 a.u. (the intersection point of valence charge density and true all-electron core charge density), the lattice constant is 5.400 (UEBR fit), 5.410 (MURN fit).

¹ The experimental lattice constants of the following bulks are taken from “Crystal structures” (University of Arizona, Tucson) by Ralph W. G. Wyckoff, Printed and Published by Robert E. Krieger Publishing Company, INC (1992). For all bulks they are expressed in (Å).

² For UEBR-fit see [BS88]

³ For MURN-fit see [Mur44]

TESTS OF THE PAW-PSEUDOPOTENTIALS

In principle for the Si atom no partial core-correction (**PCC**) needs to be taken into account, but an important observation is that when using **GGA** functional one always should include a small partial core-correction. If the energy of a single Si atom in a big box is computed within the **GGA** and no **PCC** is considered, then the energy of the atom in the big box is higher than the energy of the single atom obtained from the atomic program; to overcome this problem the **PCC** needs to be included in the calculation.

Cd-metal bulk -hexagonal

In the case of cadmium the pseudopotential was generated and used with a large radius from where the partial core correction has been fitted: 2.60 a.u. (which is the radius of the pseudopotential).

The experimental lattice constants for cadmium metal are: $a = 2.98$ and $c = 5.62$ Å with the $c/a = 1.8859$. The **k**-point set used to perform the calculation for fitting the lattice constant was **15x15x15** with a cutoff energy corresponding to $G_{\max} = 4.5 \text{ Ry}^{1/2}$. The **LDA** fitted parameters are $a_{\text{theoretic}} = 2.974$ for UEBR fit (2.976 for MURN fit) and $c_{\text{theoretic}} = 5.573$ (5.570 MURN fit) with the $(c/a)_{\text{theoretic}} = 1.8739$ (1.8716 MURN fit).

CdO bulk -fcc

Two different oxygen pseudopotentials with small and large cutoff radius, respectively have been used. For these pseudopotentials the cutoff radius was also used to fit the partial core correction and this means that a small **PCC** was taken into account. The fitted lattice constant using the UEBR and MURN function for different energy cutoffs are presented in the table below. In this case the proper energy cutoff at which the lattice constant can be considered converged corresponds to the $G_{\max} = 5.0 \text{ Ry}^{1/2}$. The experimental lattice constant is $a = 4.695$ (Å).

Table CdO 1: Cd with $r_{\text{cut}} = 2.6$ and O with $r_{\text{cut}} = 1.4$, **9x9x9 k-point set, LDA**

G_{\max}	UEBR	error %	MURN	error %
4.0	4.629	-1.40	4.643	-1.10
4.5	4.637	-1.23	4.629	-1.40
5.0	4.672	-0.48	4.671	-0.51
5.5	4.662	-0.70	4.660	-0.74
6.0	4.660	-0.74	4.580	-2.44

Table CdO 2: Cd with $r_{\text{cut}} = 2.6$ and O with $r_{\text{cut}} = 1.1$, **6x6x6 k-point set, LDA**

G_{\max}	UEBR	error %	MURN	error %
4.0	4.705	+ 0.20	4.673	- 0.45
4.5	4.653	- 0.89	4.639	- 1.11
5.5	4.665	- 0.64	4.645	- 1.05

The GGA result using **6x6x6 k-point set** and an energy cutoff of **30.25 Ry** ($G_{\max} = 5.5 \text{ Ry}^{1/2}$) gives a lattice constant of 4.817 for UEBR and MURN fit (larger with 2.59 % than experimental).

CdS bulk -fcc

The experimental lattice constant is $a_{\text{exp}} = 5.818$. The sulfur pseudopotential used to perform the calculation uses a small partial core-correction fitted at a radius of 1.4 a.u.; a **3x3x3** k-point set has been chosen in the calculation.

Table CdS-fcc: Cd with $r_{\text{cut}} = 2.6$ and S with $r_{\text{cut}} = 1.4$, **3x3x3** k-point set, **LDA**

G_{max}	UEBR	error %	MURN	error %
4.0	5.844	0.44	5.837	0.32
4.5	5.771	-0.80	5.763	-0.94
5.5	5.740	-1.34	5.743	-1.28

CdS bulk -hexagonal

The experimental lattice constants are $a_{\text{exp}} = 4.1348$ and $c_{\text{exp}} = 6.749$. The same pseudopotentials like above have been used in the calculations. A **3x3x2** k-point set has been considered to describe well the lattice parameters.

Table CdS-hexagonal: Cd with $r_{\text{cut}} = 2.6$ and S with $r_{\text{cut}} = 1.4$, **3x3x2** k-point set, **LDA**

G_{max}		a (Å)	error %	c (Å)	error %	c/a	error %
4.2	UEBR	4.099	-0.86	6.698	-1.20	1.6340	0.10
	MURN	4.104	-0.74	6.680	-1.60	1.6276	-0.28
4.5	UEBR	4.041	-2.26	6.551	-3.07	1.6211	-0.68
	MURN	4.009	-3.04	6.539	-3.25	1.6310	-0.07

SrO bulk -fcc

A **9x9x9** k-point set was used in the calculations with two different cutoff energies. The pseudopotential for the oxygen is that one with a small cutoff radius and a small partial core-correction. The experimental lattice constant is $a_{\text{exp}} = 5.1602$, the fitted parameters are given below.

Table SrO-fcc 1: Sr with $r_{\text{cut}} =$ and O with $r_{\text{cut}} = 1.1$, **9x9x9** k-point set, **LDA**

G_{max}	UEBR	error %	MURN	error %
5.0	5.078	- 1.58	5.071	- 1.71
5.5	5.070	- 1.73	5.063	-1.86

TiO bulk -fcc

Two different pseudopotentials (**PSP**) have been used to perform calculation in order to fit the lattice constant of the TiO-fcc. One is obtained from a neutral configuration and the other one from an ionic configuration (the parameters are given in the previous section), and for the oxygen atom both pseudopotentials with small and large cutoff radius were used, as well. The experimental lattice constant is $a_{\text{exp}} = 4.1766$ Å.

Table TiO-fcc 1: Ti neutral PSP and O with $r_{\text{cut}} = 1.4$, **4x4x4** k-point set, **LDA**

G_{max}	UEBR	error %	MURN	error %
5.0	4.235	1.39	4.234	1.37
5.5	4.203	0.63	4.201	0.58

TESTS OF THE PAW-PSEUDOPOTENTIALS

Table TiO-fcc 2: Ti neutral PSP and O $r_{cut} = 1.4$ with, **9x9x9** k-point set, **LDA**

G_{max}	UEBR	error %	MURN	error %
5.0	4.222	1.08	4.223	1.11
5.5	4.199	0.53	4.195	0.44
6.0	4.189	0.29	4.185	0.20
6.5	4.186	0.22	4.182	0.13

Table TiO-fcc 3: Ti ion PSP and O with $r_{cut} = 1.4$, **9x9x9** k-point set, **LDA**

G_{max}	UEBR	error %	MURN	error %
5.0	4.185	0.20	4.185	0.20
5.5	4.181	0.10	4.174	-0.06

Table TiO-fcc 4: O with $r_{cut} = 1.1$, **9x9x9** k-point set, **LDA**, $G_{max} = 5.5 \text{ Ry}^{1/2}$

Ti-PSP	UEBR	error %	MURN	error %
neutral configuration $r_{cut} = 2.0 \text{ a.u.}$	4.187	0.24	4.181	0.10
ionic configuration $r_{cut} = 2.3 \text{ a.u.}$	4.185	0.20	4.185	0.20

SrTiO₃ bulk-sc

The experimental lattice constant is $a_{exp} = 3.905 \text{ \AA}$.

Table SrTiO₃-fcc: Ti neutral PSP and O with $r_{cut} = 1.4$, **5x5x5** k-point set, **LDA**

G_{max}	UEBR	error %	MURN	error %
5.3	3.848	-1.45	3.798	-2.74
5.5	3.850	-1.40	3.805	-2.56
6.0	3.863	-1.07	3.812	-2.38

SiO₂ bulk -hexagonal

In the case of SiO₂ a **9x9x8** k-point set has been used; the pseudopotential used for oxygen was that one with the large cutoff radius and for the silicon the simple norm-conserving pseudopotential (KB-type) without partial core-correction. The experimental lattice parameters are: $a_{exp} = 4.913$ and $c_{exp} = 5.404 \text{ \AA}$ with the $c/a = 1.0999$.

Table SiO₂-hexagonal 1: Si with $r_{cut} = 1.25$ and O with $r_{cut} = 1.1$, **LDA**

G_{max}		a (Å)	error %	c (Å)	error %	c/a	error %
4.5	UEBR	4.864	-0.99	5.377	-0.54	1.1055	-0.50
	MURN	4.860	-1.07	5.375	-0.59	1.1070	-0.63
5.0	UEBR	4.863	-1.01	5.366	-0.77	1.1035	-0.31
	MURN	4.859	-1.01	5.363	-0.89	1.1037	-0.34
5.5	UEBR	4.872	-0.83	5.374	-0.61	1.1035	-0.28
	MURN	4.870	-0.87	5.375	-0.59	1.1037	-0.34

TiN bulk -fcc

The experimental lattice parameter is $a_{\text{exp}} = 4.235 \text{ \AA}$. The **9x9x9** k-point set has been used. For the nitrogen pseudopotential a small partial core-correction was taken into account, it was fitted on a radius of 1.2 a.u.

Table TiN-fcc 1: Ti neutral PSP and N with $r_{\text{cut}} = 1.2$, LDA

G_{max}	UEBR	error %	MURN	error %
4.7	4.141	- 2.21	1.141	- 2.20
5.0	4.140	- 2.24	4.140	- 2.24
5.5	4.128	- 2.128	4.125	- 2.59

Table TiN-fcc 1: Ti ion PSP with $r_{\text{cut}} = 1.4$ and N with $r_{\text{cut}} = 1.2$, LDA

G_{max}	UEBR	error %	MURN	error %
4.8	4.216	- 0.43	4.211	- 0.54
5.2	4.174	- 1.40	4.170	- 1.42

Pt-metal fcc

We used the platinum pseudopotential from where the partial core correction has been fitted at large radius: 2.00 a.u (the radius of the pseudopotential is 2.1 a.u.). The experimental lattice constants for platinum metal is $a_{\text{exp}} = 3.923 \text{ \AA}$.

Table Pt-fcc 1: LDA results for a **9x9x9** k-point set

G_{max}	UEBR	error %	MURN	error %
5.0	3.933	+ 0.26	3.933	+ 0.26
5.5	3.921	- 0.02	3.921	- 0.02
6.0	3.919	- 0.10	3.918	- 0.12

PtGa₂ fcc

For this bulk a **9x9x9** k-point set was used, too. The gallium pseudopotential has been constructed using a radius of 2.2 a.u and the partial core-correction is fitted at a radius of 2.1 a.u. The experimental lattice constant is $a_{\text{exp}} = 5.911 \text{ \AA}$.

Table PtGa₂-fcc: LDA results for a **9x9x9** k-point set

G_{max}	UEBR	error %	MURN	error %
4.5	5.889	- 0.36	5.889	- 0.37
5.0	5.867	- 0.73	5.857	- 0.90
5.5	5.861	- 0.83	5.856	- 0.92

GaAs and GaP fcc

The pseudopotentials for As and P that have been used are the norm-conserving pseudopotentials (KB-type) and they have been generated and tested by the previous PhD students. The **4x4x4 k**-point set has been used to perform the calculations.

Table GaAs-fcc: LDA results, $a_{\text{exp}} = 5.653 \text{ \AA}$.

G_{max}	UEBR	error %	MURN	error %
4.0	5.600	-0.93	5.618	-0.61
4.5	5.622	-0.54	5.591	-1.09
5.0	5.613	-0.70	5.506	-2.06

Table GaP-fcc: LDA results, $a_{\text{exp}} = 5.450 \text{ \AA}$.

G_{max}	UEBR	error %	MURN	error %
4.0	5.289	-2.95	5.269	-3.32
4.5	5.397	-0.97	5.392	-1.06
5.0	5.389	-1.11	5.387	-1.15

Cu-metal fcc

Two different copper pseudopotentials for two cutoff radii: 2.6 and 2.4 a.u. have been generated. The results for the one with the large cutoff radius (the partial core-correction is taken for a large radius of 2.6 a.u.) for different **k**-point sets are given in the tables below.

Table Cu-fcc 1: 6x6x6 k-point set, PCC on a radius of 2.6 a.u.

G_{max}	UEBR	error %	MURN	error %
4.0 -LDA	3.566	-1.21	3.559	-1.41
5.0 -LDA	3.557	-1.46	3.556	-1.49
5.0 -GGA	3.679	-1.91	3.672	-1.71

Table Cu-fcc 2: LDA results, 9x9x9 k-point set, PCC at a radius of 2.6 a.u.

G_{max}	UEBR	error %	MURN	error %
4.0	3.540	-1.91	3.537	-2.02
4.5	3.533	-2.13	3.531	-2.18
5.0	3.531	-2.18	3.530	-2.21
5.3	3.531	-2.18	3.530	-2.21
5.5	3.531	-2.18	3.530	-2.21

Table Cu-fcc 3: LDA results, 15x15x15 k-point set, PCC at a radius of 2.6 a.u.

G_{max}	UEBR	error %	MURN	error %
4.0	3.534	-2.10	3.531	-2.18
4.5	3.531	-2.18	3.529	-2.24
5.0	3.530	-2.21	3.528	-2.27
5.3	3.530	-2.21	3.528	-2.27
5.5	3.530	-2.21	3.528	-2.27
5.7	3.530	-2.21	3.528	-2.27

TESTS OF THE PAW-PSEUDOPOTENTIALS

One can conclude that for the energy cutoff of 25 **Ry** the lattice parameter is converged. Anyway, the error in the estimation of the lattice constant can be considered satisfactory. Using a **16x16x16 k**-point set and repeating the calculation for this energy cutoff yield to $a_{\text{theoretical}} = 3.549$ for UEBR fit (3.545 for MURN fit). In all the previous calculation a small partial core-correction has been used. Taking into account a bigger partial core-correction and (fitted at the intersection point of the valence charge with core charge: 1.33 a.u.) and using the same k-point set and energy cutoff and PBE-GGA formalism for the exchange-correlation energy and potential the results for the lattice constant are: $a_{\text{theoretical}} = 3.672$ for UEBR fit (3.658 for MURN fit). For all these calculations we find a small overlap of the pseudopotentials spheres at the minimum lattice constant.

A new pseudopotential with the small cutoff radius of 2.4 a.u. has been generated to avoid this overlap. In this case the partial core-correction used was fitted at a radius of 1.23 a.u.

Table Cu-fcc 4: 16x16x16 k-point set, $r_{\text{cut}} = 2.4$, PCC at a radius of 1.23 a.u.

G_{max}	UEBR	error %	MURN	error %
4.5 -LDA	3.510	- 2.70	3.496	- 3.10
5.0 -LDA	3.560	- 1.39	3.553	-1.50
5.0 -GGA	3.658	+ 1.34	3.657	+ 1.30

The conclusion is that the last pseudopotential describes well the properties of the Cu atom. In order to test further the new Cu-pseudopotential some more calculations of the relaxation of Cu(110) surface have been performed. The parameters used where: **3x12x17 k**-point set and an energy cutoff of 25 **Ry**, with 7 and 13 Cu layers, and 9.51 and 19.02 a.u. vacuum above Cu surface. The symmetry group that has been used was D_{2h}^1 . The results of the interlayer relaxation for this surface are in good agreement with experimental data end with other calculated relaxations that have been reported in the literature. In the Table “Cu(110) surface 1” the results are summarized (see references on the next page).

TESTS OF THE PAW-PSEUDOPOTENTIALS

Table Cu(110) surface 1: Interlayer relaxation (Δ %) of Cu(110) surface

	Present calculations					LDA-PP Rodach ¹	FLAPW-GGA Da Silva ²	PAW-GGA VASP, Liem ³	Experimental Adams ⁴
	LDA				GGA				
	7 layers		13 layers		7 layers	-	13 layers	6 layers	-
vacuum a.u	9.51	19.02	9.51	-	9.51	-	-	14.59	-
E_{surf} (eV atom)	1.301	1.078	1.422	-	-	-	0.907	0.893	-
Δ_{12}	- 11.00	- 11.46	- 11.07	-11.42	- 11.01	- 9.30	- 9.73	- 10.08	- 3.0 to - 10.0
Δ_{23}	+ 3.59	+ 3.38	+ 3.72	+ 3.39	+ 3.60	+ 2.08	+ 3.63	+ 5.30	0.0 to 8.0
Δ_{34}	-1.69	- 1.99	- 2.14	- 2.32	-1.45	+ 1.10	- 1.16	+ 0.10	-
Δ_{45}	-	-	- 0.39	- 0.95	-	-	+ 0.39	-	-
Δ_{56}	-	-	- 0.98	- 1.02	-	-	- 0.08	-	-
Δ_{67}	-	-	- 0.87	- 1.12	-	-	+ 0.14	-	-

¹-Th. Rodach, K.P. Bohnen, K.M. Ho, Surf. Sci. 286(1993) 66;

²- J.L. Da Silva PRB submitted (2004);

³- S.Y. Liem, G. Kresse, J.H.R. Clarke, Surf. Sci. 415(1998) 194;

⁴- D.L. Adams, H.B. Nielsen, J.N. Andersen, Surf. Sci. 128(1983) 294.

C 2.2: Molecules⁴

SiH₃ molecule

A series of calculations using **LDA** and **GGA** have been done for the SiH₃ molecule in order to compare the results obtained with Si norm-conserving pseudopotential (**KB**) and non-norm-conserving pseudopotential (**PAW**). In all these cases partial core-correction has been used but with different ways of fitting. To our experience, asymmetric molecules like SiH₃ are very sensitive to the correct application of partial core correction. In both cases the real space implementation of **PCC** is used, in the case of the **KB**-type pseudopotential the partial core-charge is simply added to the charge due to the plane-waves that is calculated on the real space grid. In the case of **PAW**-type the **PCC** is added to the smooth and true charge densities inside of the augmentation sphere. For the **PAW**-type of the Si pseudopotential the **PCC** is taken into account on a radial mesh inside the augmentation sphere and on the normal **FFT** real space grid outside the sphere. For H a purely local pseudopotential is used. The results presented have been obtained by relaxing all hydrogen atoms without any constraint (i.e. no symmetry has been used).

Table 1 SiH₃ molecule: bond lengths and angles for **LDA** and **GGA** exchange-correlation functionals.

	Si-H bond length (a.u)	α : H-Si-H angle (degree)	H-H distance (a.u)
KB-LDA	1.4970	111.64	2.4769
PAW-LDA	1.5036	111.72	2.4891
KB-GGA	1.4523	113.30	2.4265
PAW-GGA	1.4587	114.79	2.4577

In both cases, **LDA** and **GGA**, the Si-H bond length and H-Si-H angle are in very good agreement for the **KB**- and **PAW**-type pseudopotentials. The radius from where the partial core-correction was fitted is 1.19 for the **KB**-pseudopotential and 1.16 for the **PAW**-pseudopotential. The calculation has been done in a cubic box of 8.5^3 \AA^3 using the gamma point and an energy cutoff of 25 **Ry** ($G_{\max} = 5 \text{ Ry}^{1/2}$).

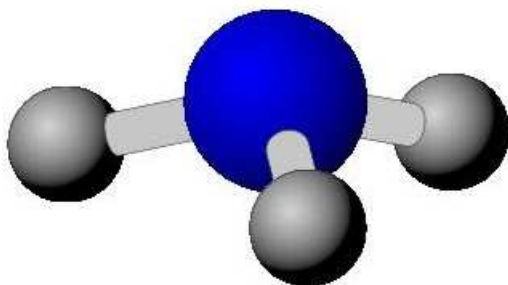


Figure SiH₃ molecule:

blue – Si atom
grey – H atom

The next tables present LDA and GGA bond length for different molecules, for the GGA two values for the bond length have been calculated: one is corresponding to the case when the second derivatives have been evaluated on a grid corresponding to $2 \cdot G_{\max}$ and the

⁴ All the bond length are in a.u.

TESTS OF THE PAW-PSEUDOPOTENTIALS

second one is corresponding to the case when using the Bird and White scheme for which the evaluation of the second derivatives is very accurate.

NO molecule

A series of calculations has been carried out for the NO molecule. In the tables below we present the results in the case of using a small partial core-correction for both atoms (the radii used to fit the **PCC** are equal to the radii of the pseudopotentials).

Table NO: gamma point, small **PCC**, experimental bond length = 2.175 a.u., cubic box of $a = 10 \text{ \AA}$.

G_{\max}	LDA	Error %	GGA 2 G_{\max}	Error %	GGA Bird-White	Error %
4.0	2.806	+ 29.0	2.827	+ 30.00	2.803	+ 28.9
4.5	2.542	+ 16.8	2.560	+ 17.7	2.435	+ 11.9
5.0	2.359	+ 8.4	2.367	+ 9.2	2.364	+ 8.68
5.5	2.239	+ 2.9	2.256	+ 3.7	2.235	+ 2.75
6.0	2.181	+ 0.3	2.199	+ 1.1	2.191	+ 0.72
6.5	2.165	- 0.5	2.184	+ 0.4	2.178	+ 0.1
7.0	2.165	- 0.5	2.185	+ 0.5	2.175	0.0
7.5	2.166	- 0.4	2.186	+ 0.5	-	-

The results obtained by other groups are: 2.169^{ref-1} using LDA (- 0.27%), 2.189 (+ 0.64%) [PBE96-98], 2.181 (+ 0.27%) [ES99], 2.192 (+ 0.78%) [AB99] using **GGA**.

When taking into account a larger partial core-correction and using an energy cutoff of 25 Ry ($G_{\max} = 5.0 \text{ Ry}^{1/2}$) the **LDA** bond length is 2.357 a.u. with 8.5% larger than experimental, but when using **GGA** within the Bird and White scheme the bond length is 2.320 a.u with 6.7% larger than experimental, so the larger partial core-correction helps to get bond length shorter with 2% at the same energy cutoff.

CO molecule

In the case of the CO molecule it was very difficult to reach a reasonable level of selfconsistency for the **GGA** calculation on a grid corresponding to $2 \cdot G_{\max}$. This is because of the large oscillations that occur in the evaluation of the gradients (second derivatives) from one selfconsistent step to the next. In the case of using the Bird and White scheme for the calculation of second derivatives the oscillations are not present anymore and the calculation of the bond length can be performed. The radii where the partial core-correction is fitted are equal to the augmentation radii of the pseudopotentials; this means that a small **PCC** is being taken into account.

Table CO 1: gamma point, small **PCC**, experimental bond length = 2.131 a.u., cubic box of $a = 10 \text{ \AA}$

G_{\max}	LDA	Error %	GGA Bird-White	Error %
4.0	2.469	+ 15.9	2.490	+ 16.9
4.5	2.404	+ 12.8	2.418	+ 13.4
5.0	2.284	+ 7.2	2.277	+ 6.9
5.5	2.197	+ 3.1	2.189	+ 2.7
6.0	2.148	+ 0.8	2.146	+ 0.7
6.5	2.131	0.0	2.138	+ 0.3
7.0	2.129	- 0.1	2.134	+ 0.2

TESTS OF THE PAW-PSEUDOPOTENTIALS

The calculated bond lengths for a larger partial core-correction (see details of the pseudopotentials) are presented in the table below.

Table CO 2: gamma point, large **PCC**, experimental bond length 2.131 a.u., cubic box of $a = 10 \text{ \AA}$.

G_{\max}	LDA	Error %	GGA Bird-White	Error %
5.0	2.283	+ 7.1	2.266	+ 6.3
8.0	2.126	- 0.2	2.104	- 1.25

The results reported in the literature for the bond lengths are: 2.150^r(+0.9%) [ES99] and 2.146 (+0.7%) [AB99] for the case of using the **GGA** formalism for the exchange correlation potential.

In the case of the CO molecule using a larger partial core-correction for both pseudopotentials at the same energy cutoff ($G_{\max} = 5.0 \text{ Ry}^{1/2}$) the bond length is just with 0.6% smaller than in the case of using the smaller partial core-correction, so the influence of the **PCC** is much smaller than in the case of the NO molecule.

CN molecule

Again the first results are for the case of considering a small partial core-correction for both pseudopotentials. The structure of the molecule can easily be converged using a grid of $2 \cdot G_{\max}$ in the calculation of the second derivatives. The same accuracy of the bond length is obtained with the Bird and White scheme, the only difference is that for the latter the number of iterations required for reaching the selfconsistency is less than half of the number of iterations needed when using a real space grid corresponding to $2 \cdot G_{\max}$.

Table CN: gamma point, small **PCC**, experimental bond length = 2.214 a.u., cubic box of $a = 10 \text{ \AA}$.

G_{\max}	LDA	Error %	GGA $2 G_{\max}$	Error %	GGA Bird-White	Error %
4.0	2.419	+ 9.2	2.436	+ 10.0	2.376	+ 9.8
4.5	2.351	+ 6.2	2.367	+ 6.9	2.362	+ 6.7
5.0	2.286	+ 3.3	2.301	+ 3.9	2.287	+ 3.3
5.5	2.235	+ 0.9	2.250	+ 1.6	2.235	+ 0.9
6.0	2.210	- 0.2	2.227	+ 0.6	2.214	0.0
6.5	2.204	- 0.4	2.221	+ 0.3	2.210	- 0.2
7.0	2.203	- 0.5	2.221	+ 0.3	2.210	-0.2

Using the larger partial core-correction and the energy cutoff of 25 **Ry** the bond length is 2.280 (+ 3.1%) with **LDA** and 2.230 with **GGA** (+ 0.8%). In the ref-2 the **LDA** bond length is 2.203 (- 0.5%) and **GGA** is 2.218 (+ 0.2) ([PBE96-98], [ES99], [AB99], [DB93]).

O₂ molecule

The bond length of the oxygen molecule has been calculated taking into account a small partial core-correction. The calculation of the second derivatives on the real space grid corresponding to $2 \cdot G_{\max}$ introduces oscillations from one self-consistent step to the next one so that it becomes difficult to converge the system. Increasing the temperature and changing the mixing parameter can improve the convergence but the oscillations are still present and a big number of iterations are needed to achieve the required self-consistency.

Table O₂: gamma point, small PCC, experimental bond length = 2.283 a.u., cubic box of a = 10 Å.

G_{\max}	LDA	Error %	GGA 2 G_{\max}	Error %	GGA Bird-White	Error %
4.0	2.957	+ 29.6	2.972	+ 30.2	2.813	+ 23.2
4.5	2.684	+ 17.7	2.699	+ 18.2	2.578	+ 12.9
5.0	2.482	+ 8.8	2.498	+ 9.4	2.382	+ 4.34
5.5	2.344	+ 2.8	2.362	+ 3.4	2.333	+ .2.2
6.0	2.272	- 0.4	2.294	+ 0.5	2.277	- 0.2
6.5	2.265	- 0.7	2.293	+ 0.4	2.288	+ 0.2
7.0	2.277	- 0.2	2.308	+ 1.1	2.295	+ 0.5

When an energy cutoff of 30.25 Ry is used the calculated bond lengths agree well with the experimental ones and other GGA data from literature: 2.306 (+ 1.1%) [PBE96-98], 2.299 (+ 0.8%) [ES99] and 2.307(+ 1.2%) [AB99].

NH₃ molecule

The experimental bond length N-H is 1.192 a.u. and the angle HNH is 106.68°. The nitrogen pseudopotential has been generated by taking into account a small partial core-correction fitted at the augmentation radius of the pseudopotential. The calculations have been performed in a cubic box with a = 14 Å.

Table NH₃ 1: LDA results, gamma point, nitrogen pseudopotential with small PCC

G_{\max}	Bond length	Error %	Angle (degree)	Error %
4.0	2.197	+ 14.9	94.71	- 11.2
4.5	2.118	+ 10.8	98.14	- 8.0
5.0	2.036	+ 6.5	101.71	- 4.6
5.5	1.973	+ 3.2	105.09	- 1.5
6.0	1.945	+ 1.7	106.46	- 0.2
6.5	1.933	+ 1.1	107.20	+ 0.5
7.0	1.932	+ 1.0	107.3	+ 0.6

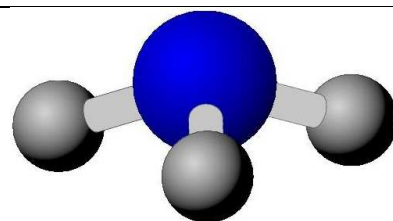


Figure NH₃ molecule:
blue – N atom
grey – H atom

TESTS OF THE PAW-PSEUDOPOTENTIALS

Table NH₃ 2: GGA results, gamma point, nitrogen pseudopotential with small PCC, real space grid corresponding to $2 \cdot G_{\max}$

G_{\max}	Bond length	Error %	Angle (degree)	Error %
4.0	2.110	+ 10.4	98.52	- 7.6
4.5	2.109	+ 10.3	97.52	- 8.6
5.0	2.020	+ 5.7	102.45	- 3.9
5.5	1.960	+ 2.5	106.13	- 0.5
6.0	1.926	+ 0.8	111.14	+ 4.18
6.5	1.913	+ 0.1	112.70	+ 5.64
7.0	1.912	0.0	109.20	+ 2.36

Table NH₃ 3: GGA results, gamma point, N pseudopotential with small PCC, Bird and White scheme.

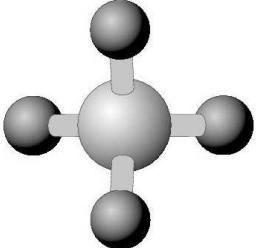
G_{\max}	Bond length	Error %	Angle (degree)	Error %
4.0	2.201	+ 15.11	94.61	- 11.3
4.5	2.122	+ 10.9	97.69	- 8.4
5.0	2.038	+ 6.6	100.97	- 5.3
5.5	1.974	+ 3.24	104.15	- 2.4
6.0	1.946	+ 1.77	105.45	- 1.2
6.5	1.933	+ 1.09	106.15	- 0.5
7.0	1.922	+ 1.04	106.24	- 0.4

The calculated N-H bond length and H-N-H angle reported in the literature are 1.930 a.u. (+0.94%) and 107.3^0 (+0.58) for **LDA** and 1.9331 a.u. (+1.10%) and 105.6^0 (-1.01%) for **GGA** ([PBE96-98], [ES99], [AB99], [DB93]).

CH₄ molecule

The experimental C-H bond length is 2.052 a.u. The **LDA** bond lengths reported in the literature are: 2.074 a.u. [PBE96-98], 2.081 a.u. [DB93] and for the **GGA** functional 2.071 a.u. (+0.92) [PBE96-98], 2.073 a.u. (+1.02) [AB99]. In the calculation of the C-H bond length for the carbon atom a partial core correction fitted on a large radius has been used. The results for different energy cutoff are listed in the Table “CH₄ 1”.

Table CH₄ 1: gamma point, small PCC, cubic box with $a = 14 \text{ \AA}$.

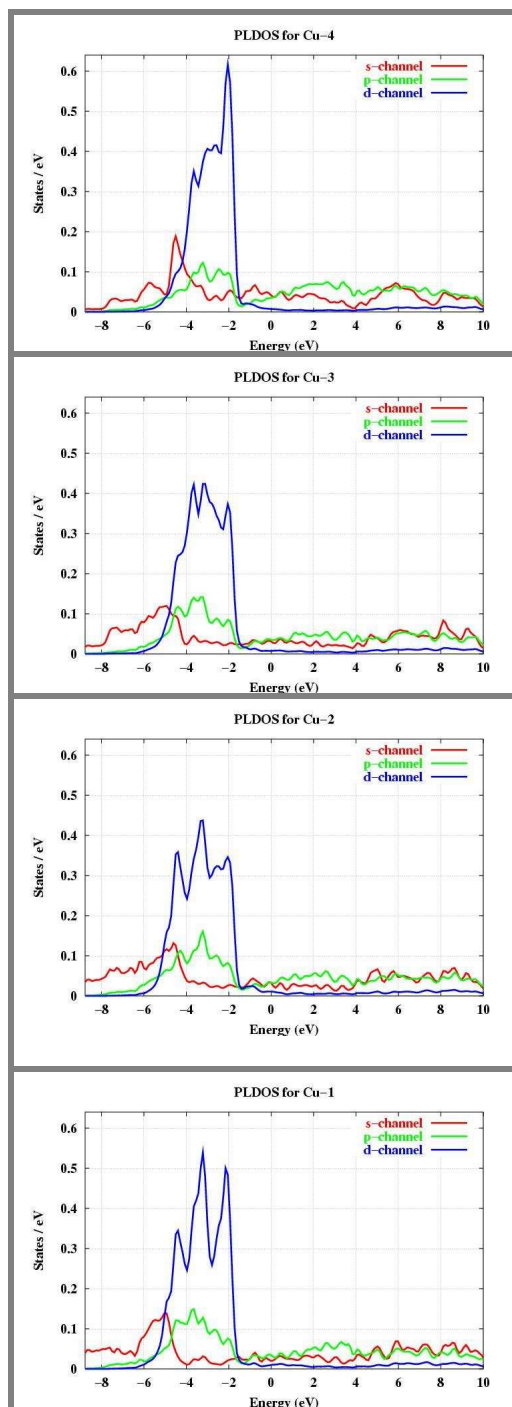
G_{\max}	LDA	Error %	GGA $2 \cdot G_{\max}$	Error %	GGA Bird-White	Error %	 <p>Fig. CH₄ molecule: light grey – C atom dark grey – H atom</p>
4.0	2.223	+ 8.33	2.216	+ 7.99	2.178	+ 6.13	
4.5	2.189	+ 6.67	2.185	+ 6.48	2.1487	+ 4.71	
5.0	2.137	+ 4.14	2.134	+ 3.99	2.100	+ 2.32	
5.5	2.092	+ 1.94	2.089	+ 1.80	2.060	+ 0.38	
6.0	2.076	+ 1.94	2.073	+ 1.02	2.039	- 0.64	
6.5	2.073	+ 1.02	2.071	+ 0.92	2.034	- 0.88	
7.0	2.074	+ 1.07	2.072	+ 0.97	2.034	- 0.86	
7.5	2.074	+ 1.07	2.072	+ 0.97	-	-	

Taking into account a large partial core correction for the carbon pseudopotential and using an energy cutoff of 25 Ry the calculated bond length is 2.112 a.u., i.e. 2.92% larger than the experimental value.

Appendix D

PLDOS for clean Cu(110) surface

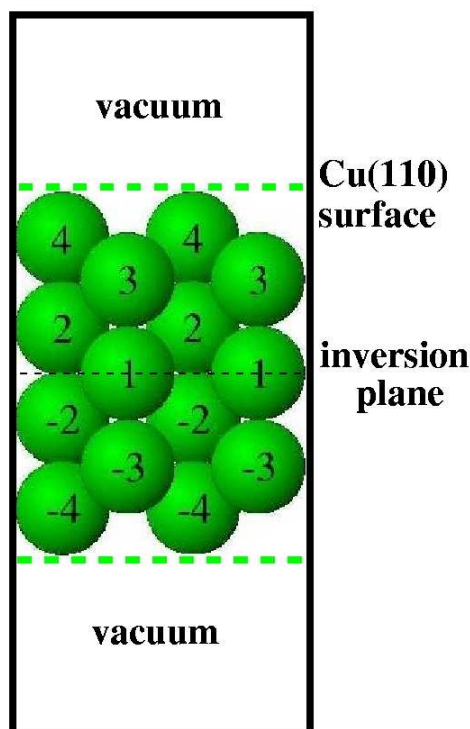
Figure PLDOS of clean Cu(110) surface:



• (right panel) side view of the supercell used in calculations of the clean Cu(110) surface (7 layers of copper).

• (left panel) the PLDOS characteristics of the Cu atoms of the supercell:

- the inner Cu¹, Cu² atoms have bulk characteristics with the d-band (and some p-type states) in the energy interval of -5.0...-2.0 eV. Most s-type states appear at lower energy interval: -8.5...-4.5 eV.
- for the Cu³ and Cu⁴ the d-band is narrowing (energy range of -4.5...-2.0 eV and -4.0...-1.9 eV, respectively). This behavior is due to the smaller coordination number of the surface atoms.



It is often helpful to understand which atomic states (characterized by angular-momentum) of a given atom are contributing to the eigenfunctions of the total system. Thus one calculates the partial local density of states (PLDOS) of the atom by projecting the eigenfunction to states of certain angular-momentum symmetry l in a sphere surrounding the atom μ . The angular momentum is not a conserved quantity in a solid, but formally, an expansion into different symmetry contributions can be done by decomposing plane waves into Bessel's functions j_l times spherical harmonics Y_L , where the site of atom μ is taken as the origin (see Anhang D in [Kro01]). Integration yields the quantity:

$$q_{\bar{k}\nu}^{\mu l}(\mathbf{R}) = \langle \Psi_{\bar{k}\nu} | \mathbf{P}_l^\mu | \Psi_{\bar{k}\nu} \rangle = \int_{S_\mu} d\mathbf{r}^3 \left| \langle \bar{\mathbf{r}}_\mu | \mathbf{P}_l^\mu | \Psi_{\bar{k}\nu} \rangle \right|^2 \quad (\text{D-1})$$

where the matrix elements are (see equation A.4.8):

$$\langle \bar{\mathbf{r}}_\mu | \mathbf{P}_l^\mu | \Psi_{\bar{k}\nu} \rangle = \frac{e^{i\bar{\mathbf{k}}\bar{\mathbf{r}}_\mu}}{\sqrt{\Omega}} \sum_{\bar{\mathbf{G}}} c_{\bar{k}\nu}^{\bar{\mathbf{G}}} e^{-i\bar{\mathbf{G}}\bar{\mathbf{r}}_\mu} 4\pi \sum_m i^{-l} j_l(\bar{\mathbf{k}} + \bar{\mathbf{G}} | \bar{\mathbf{r}}_\mu) Y_L(\bar{\mathbf{k}} + \bar{\mathbf{G}}) Y_L(\bar{\mathbf{r}}_\mu) \quad (\text{D-2})$$

and the integration is performed in a sphere S_μ around the atom μ . A suitable choice of the radius of the sphere is apparently half of the nearest-neighbor distance.

The partial local density of states is defined as:

$$\text{PLDOS} : D_L^\mu(\varepsilon) = \int_{1.\text{BZ}} d\mathbf{k}^3 \sum_\nu q_{\bar{k}\nu}^{\mu l} \delta(\varepsilon - \varepsilon_{\bar{k}\nu}) \quad (\text{D-3})$$

The pseudopotential approach guarantees that using pseudo-wave functions (expanded in plane waves) the PLDOS-spectra describe exactly the distribution of the energy levels. For the norm-conserving pseudopotentials (Kleinman-Bylander form where the wave-functions are norm-conserving) the relative heights of **s**-, **p**- and **d**-levels are correctly reproduced as well. This is not true for non-norm-conserving pseudopotentials (PAW form). Since the pseudo-wave functions are non-norm-conserving, for a correct description of the relative heights of the l -channels, the augmentation charge should be added.

All PLDOS-spectra in this thesis have been calculated using only the pseudo-wave functions. This means that the relative heights of **s**-, **p**- and **d**-levels are not exactly described. This is specially the case of the pseudopotentials for which d-pseudo-wave functions have been constructed (see the plots of all electron and pseudo-wave functions of the pseudopotentials in Appendix “Parameters and Tests of the PAW-pseudopotentials”).

Bibliography

- [AA02]. A. Antons, *First Principles investigations of the Initial Stages of Surfactant Mediated Growth on the Si(111) Substrate*, PhD thesis, RWTH Aachen, **2002**
- [AB99]. C. Adamo, V. Barone, *J. Chem. Phys.*, 110(13):6161, **1999**
- [AW93]. N. Achziger, W. Witthuhn, *Phys. Rev. B*, 47:6990, **1993**
- [BS88]. A. Banerja, J. R. Smith, *Phys. Rev. B*, 37(12):6632, **1988**
- [Bar61]. J. Bardeen, *Phys. Rev. Lett.*, 6:57, **1961**
- [Bec93]. A. D. Becke, *J. Chem. Phys.*, 98:5648, **1993**
- [Ber02]. Ralf Berger, *Berechnung von Stufenkanten auf der As-bedeckten Si(111)-Oberfläche mit einem parallelisierten ab initio Programm*, PhD-thesis, RWTH-Aachen, **2002**
- [BG80]. U. von Barth and C. D. Gelatt., *Phys. Rev. B*, 21(6):2222, **1980**
- [BH54]. M. Born, K. Huang, *Dynamical Theory of Crystal Lattices*, Oxford Univ. Press, **1954**
- [BH72]. U. von Barth and L. Hedin. *J. Phys. Chem.*, 5:1629, **1972**
- [BHS82]. G. B. Bachelet, D. R. Hamann, M. Schlüter, *Phys. Rev. B*, 26(8):4199, **1982**
- [BKH98]. S. M. Barlow, K. J. Kitching, S. Haq, N. V. Richardson, *Surf. Scie.*, 401:322, **1998**
- [BR03]. S. M. Barlow, R. Raval, *Surf. Scie. Rep.*, 50:201, **2003**
- [BPO86]. M. Bader, A. Puschmann, C. Ocal, J. Haase, *Phys. Rev. Lett.*, 57:3273, **1986**
- [Blö90]. P. E. Blöchel, *Phys. Rev. B.*, 41(8):4514, **1990**
- [Blö94]. P. E. Blöchel, *Phys. Rev. B.*, 50:17953, **1994**
- [Blü88] S. Blügel, *First Principles calculations of the Electronic Structure of Magnetic Overlayers on Transition Metal Surfaces*. PhD thesis, RWTH Aachen, **1988**
- [BS88] A. Banerjea, J. R. Smith, *Phys. Rev. B*, 37:6632, **1988**
- [BD87]. D. W. Bullett, W. G. Dawson, *Progr. Surf. Scie.*, 25(1-4):275, **1987**
- [BD88]. D. W. Bullett, W. G. Dawson, *Vacuum*, 38(4-5):389, **1988**
- [BRV72]. T. J. Barton, R. W. Roth, J. G. Verkade, *J. Am. Chem. Soc.*, 94:8854, **1972**
- [BWS98]. N. A. Booth, D. P. Woodruff, O. Schaff, T. Gießel, R. Lindsay, P. Baumgärtel, A. M. Bradshaw, *Surf. Scie.*, 397:258, **1998**
- [CA80]. D. M. Ceperley, B. J. Alder, *Phys. Rev. Lett.*, 45:566, **1980**
- [CC73]. D. J. Chadi, M. L. Cohen, *Phys. Rev. B*, 8:5747, **1973**
- [CDL00]. B. Crone, A. Dodabalapur, Y. Y. Lin, R. W. Filas, Z. Bao, A. Laduca, R. Sarpeshkar, H. E. Katz, W. Li, *Nature*, 403:521, **2000**
- [CFR02]. Q. Chen, D.J. Frankel, N. V. Richardson, *Surf. Scie.*, 497:37, **2002**
- [CP85]. R. Car, M. Parrinello, *Phys. Rev. Lett.*, 55:2471, **1985**
- [CV02]. N.K. Chaki, K. Vijayamohan, *Biosensor & Bioelectrocics*, 17:1, **2002**
- [Dav75]. W. E. Davidson. *J. Comput. Phys.*, 17:87, **1975**.
- [DB93]. R. M. Dickson, A. D. Becke, *J.Chem.Phys.*, 99(5):3902, **1993**
- [DGR87]. M. Deicher, G. Grübel, E. Recknagel, H. Scudlik, T. Wichert, *Hyperfine Interactions*, 35:719, **1987**

- [DFS91]. H. Dürr, Th. Fauster, R. Schneider, *Surf. Sci.*, 244, 237, **1991**
- [Eng95a]. B. Engels, *Ab initio Berechnung der (110) Oberfläche von II-V Halbleitern: Simulation von Rastertunnelmikroskopie-Aufnahmen*, PhD thesis, RWTH Aachen, **1995**
- [Eng92b]. B. Engels, *Konstruktion von glatten, normerhaltenden Pseudopotentialen*, Master's thesis, RWTH Aachen, **1992**
- [Ewa21]. P. P. Ewald, *Ann. Phys.*, 64:253, **1921**
- [ES99]. M. Ernzerhof, G. E. Scuseria, *J.Chem. Phys.*, 110(11):5035, **1999**
- [FCB96]. B. G. Frederick, Q. Chen, S.M. Barlow, N. G. Condon, F. M. Leibsle, N. V. Richardson, *Surf. Sci.*, 238:352, 1996
- [FGJ90]. R. Feidenhans'l, F. Grey, R. L. Johnson, S. G. J. Mochrei, J. Bohr, M. Nielsen, *Phys. Rev. B*, 41:5240, 1990
- [FHB83]. D. Feller, E. S. Huyser, W. T. Borden, E. R. Davison, *J. Am. Chem. Soc.*, 105:1559, **1983**
- [Fle87]. R. Fletcher, *Practical Methods of optimization*, John Wiley and Sons, New York, **1987**
- [FMV87]. D. Forkel, F. Meyer, W. Witthuhn, H. Wolf, M. Deicher, M. Uhrmacher, *Hyperfine Interactions*, 35:715, **1987**
- [Ful95]. P. Fulde, *Electronic Correlations in Molecules and Solids*, 3rd enl. ed., Berlin: Springer, **1995**
- [FVP90]. U. Feuser, R. Vianden, A. F. Pasquevich, *Hyperfine Interactions*, 60:829, **1990**
- [GKS90]. X.Gonze, P. Käckell, M. Scheffler, *Phys. Rev. B.*, 41(17):12264, **1990**
- [GG99]. J. R. B. Gomes, J. A. N. F. Gomes, *Surf. Sci.*, 432:279, **1999**
- [GSS91]. X.Gonze, R.Stumpf, and M. Scheffler, *Phys. Rev. B*. 1991, 44(16), 8503
- [Har28]. D. R. Hartree, *Proceedings of the Cambridge Philosophical Society*, 24:89, **1928**
- [HAS04]. H. Höhler, N. Atodiresei, K. Schroeder, R. Zeller, P. H. Dederichs, Submitted
- [HBS99]. R. A. J. O'Hair, S. Blanksby, M. Styles, J. H. Bowie, *Inter. J. Mass. Spectr.*, 182-183:203, **1999**
- [HH03]. H. Hölger, *StörstellenKomplexe in Halbleitern: Elektronenstruktur und Hyperfeineigenschaften*, PhD thesis, RWTH Aachen, **2003**
- [HKW98]. J. Hasselström, O.Karis, M. Weinelt, N. Wassdahl, A. Nilsson, M. Nyberg, L. G. M. Peterson, M. G. Samant, J. Stöhr, *Surf. Scie.*, 407:221, **1998**
- [HR62]. P. Hudson, J. H. Robertson, *Acta Crystallogr.*, 15:737, **1962**
- [HRS86]. W. J. Hehre; L.Radom; P. v. R. Schleyer, J. Pople, *Ab Initio Molecular Orbital Theory*; John Wiley & Sons, Inc., New York, **1986**
- [HO97]. S. Hoyau, G. Ohanessian, *Chem. Phys. Lett.*, 280:266, **1997**
- [HSZ98]. H. Haesslein, R. Sielemann, C. Zistl, *Phys. Rev. Lett.* 80:2626, 1998
- [IFF03]. S. Blügel, M. Luysberg, K. Urban, R. Waser (Eds.), *Fundamentals of nanoelectronics, Lecture manuscripts of the 34th Spring School of the Department of Solid State Research* (ISSN 1433-5506), Forschungszentrum Jülich GmbH, Institut für Festkörperforschung, **2003**
- [JB01]. D. Jerome, K. Bechgaard, *Nature*, 410:162, **2001**
- [JC73]. J. D. Joannopoulos, M. L. Cohen, *J. Phys.*, C 6:1572, **1973**
- [JG89]. R. O. Jones and O. Gunnarson. *Rev. Mod. Phys.*, 61(3):689, **1989**
- [JGA00]. C. Joachim, J. K. Gimzewski, A. Aviram, *Nature*, 408:41, **2000**
- [IO00]. T. Ito, S. Okazaki, *Nature*, 406:1027, **2000**
- [IZC79]. J. Ihm, A. Zunger, M. L. Cohen, *J. Phys. Chem.: Solid State Physics*, 12:4409, **1979**

- [KB82]. L. Kleinman, D. M. Bylander, *Phys. Rev. Lett.*, 48(20):1425, **1982**
- [KFL65]. W. H. Kirchhoff, J. Farren, J. W. Linnett, *J. Chem. Phys.*, 42(4):1410, **1965**
- [Kro01]. W. Kromen, *Die Projector Augmented Wave-Methode: Ein schnelles Allelektronenverfahren für die ab-initio-Moleculardynamik*, PhD thesis, RWTH Aachen, **2001**
- [Kos84]. N. Kosugi, *J. Comp. Phys.*, 55:426, **1984**
- [KR54]. W. Kohn, N. Rostoker, *Phys. Rev.*, 94:1111, **1954**
- [KS65]. W. Kohn, L. J. Sham., *Phys. Rev. A*, 140(4):1133-1138, **1965**
- [LCF82]. S. L. Louie, S. Froyen, M. L. Cohen, *Phys. Rev. B*, 26 (4):1738, **1982**
- [Lei94]. F. M. Leibsle, *Surf. Sci.*, 311:45, **1994**
- [Lev79]. M. Levy, *Universal variational functionals of electron densities, first-order density matrices, and natural spin-orbitals and solutions of the v-representability problem. Proc. Natl. Acad. Sci.*, 76:6062, **1979**
- [LKC98]. S. Y. Liem, G. Kresse, J. H. R. Clarke, *Surf. Sci.*, 415:194, **1998**
- [Liu78] B. Liu, *Numerical Algorithms in Chemistry: Algebraic methods. Report on Workshop*, **1978**
- [JD01]. M. H. Jamroz, J. Cz. Dobrowolski, *J. Molec. Struc.*, 565-566:475, **2001**
- [McG99]. S. J. McGlone, P.S. Elmes, R. D. Brown, P. D. Godfrey, *J. Mol. Struc.*, 485-486:225, **1999**
- [MJW80]. V. L. Moruzzi, J. F. Janak, A. R. Williams, *Calculated Electronic Properties of Metals*, Pergamon, New York, **1980**
- [Mur44]. F. D. Murnagham, *Proc. Nat. Acad. Sci. U.S.A.*, 30:244, **1944**
- [PM77]. J. D. Pack, H. J. Monkhorst, *Phys. Rev. B*, 16:1748, **1977**
- [NHP00]. M. Nyberg, J. Hasselström, O. Karis, N. Wassdahl, M. Weinelt, A. Nilson, L. G. M. Petterson, *J. Chem. Phys.*, 112(12):5420, **2000**
- [NON03]. M. Nyberg, M. Odelius, A. Nilson, L. G. M. Petterson, *J. Chem. Phys.*, 119(23):12577, **2003**
- [PBE96-98]. J. P. Perdew, K. Burke, M. Ernzerhof, *Phys. Rev. Lett.*, 77:3865, **1996**; 78:1396(E), **1997**, 80:891, **1998**
- [PBJ97]. S. Poulston, R. A. Bennett, A. H. Jones, M. Bowker, *Phys. Rev. B.*, 55(19):12888, **1997**
- [Per85]. J. P. Perdew, *Phys. Rev. Lett.*, 55:1665, **1985**
- [Per86]. J. P. Perdew, *Phys. Rev. B.*, 33:8822, **1986**
- [Phi00]. P. Philips, *Nature*, 406:687, **2000**
- [PHC85]. A. Puschmann, J. Haase, M. D. Crapper, C. E. Riley, D. P. Woodruff, *Phys. Rev. Lett.*, 54(20):2250, **1985**
- [PHZ90]. S. L. Parkin, H.C. Heng, M. Y. Zhou, K. A. R. Mitchell, *Phys. Rev. B*, 41:5420, **1990**
- [PLH04]. J. Phillips, F.M. Leibsle, A. J. Holder, Todd Keith, *Surf. Sci.*, 545:1, **2004**
- [PJB97]. S. Poulston, A. Jones, R. A. Bennet, M. Bowker, *Surf. Sci.*, 377-379:66, **1997**
- [PTV92]. W. H. Press, S. A. Teukolsky, W. T. Vetterling, B. P. Flannery, *Numerical recipes in FORTRAN*, Cambridge Univ. Press, **1992**
- [PW86]. J. P. Perdew, Y. Wang, *Phys. Rev. B.*, 33:8800, **1986**
- [PW92]. J. P. Perdew, Y. Wang, *Phys. Rev. B.*, 45:13244, **1992**
- [Rav03]. R. Raval, *Current Opinion in Solid State and Materials Science*, 7:67, **2003**
- [RC87]. A. Rodriguez, C. T. Campbell, *Surf. Sci.*, 183:449, **1987**
- [Ric96]. P. Richard, *Banddiskontinuitäten an Halbleitergrenzflächen: Verspannungsabhängigkeit und Einfluß von Zwischenschichten*, PhD thesis, RWTH Aachen, **1996**

- [RSY03]. F. Rosei, M. Schunack, Y. Naitoh, P. Jiang, A. Gourdon, E. Laegsgaard, I. Stensgaard, C. Joachim, F. Besenbacher, *Progr. Surf. Scie.*, 71:95, **2003**
- [RRKJ90]. A. M. Rappe, K. M. Rabe, E. Kaxiras, and J.D. Joannopoulos, *Phys. Rev. B*, 41(2):1227, **1990**
- [RT00]. M. A. Reed, J. M. Tour, in: *Computing with molecules*, Sci. Am. 6 (June) **2000**
- [RYB94]. A. Rauk, D. Yu, P. Borowski, B. Roos, *Chem. Phys.*, 197:73, **1995**
- [TRL02]. M. Temprado, M. V. Roux, P. Jimenez, J. Z. Davalos, I. Notario, *J. Phys. Chem. A*106:11173, **2002**
- [TM90-91]. N. Troulier, J. L. Martins, *Solid State Commun.*, 74(7):613, **1990**; *Phys. Rev. B.*, 43(3):1993, **1991**
- [TKW03]. R. L. Toomes, J. -H. Kang, D. P. Woodruff, M. Polcik, M. Kittel, J. T. Hoeft, *Surf. Scie.*, 522:L9-L14, **2003**
- [ST93]. T. Schimizu, M. Tsukada, *Surf. Sci.*, 295:1017, **1993**
- [Sie98]. R. Sielemann, *Nucl. Instr. And Meth. in Phys. Res. B*, 146:329, **1998**
- [SL01]. S. W. Slayden, J. F. Liebman, *Chem. Rev.*, 101:1541, 2001
- [SAK01]. A. A. Samarkandy, A. O. Al-Youbi, R. M. Khalil, A. A. Fattah, *Bull. Electrochem.*, 17:111, **2001**
- [SK00]. J. H. Schon, Ch. Kloc, B. Batlogg, *Nature*, 406:702, **2000**
- [SPB98]. P. Stone, S. Poulston, R. A. Bennet, Nicola J. Price, M. Bowker, *Surf. Sci.*, 418:71, **1998**
- [SO82]. A. Szabo, N. S. Ostlund, *Modern Quantum Chemistry* 1st ed.; McGraw-Hill: New York, **1982**
- [SPP99]. S. L. Silva, A. A. Patel, T. M. Pham, F. M. Leibsle, *Surf. Sci.*, 441:351, **1999**
- [Van85]. D. Vanderbilt, *Phys. Rev. B.*, 32(12):8412, **1985**
- [Van90]. D. Vanderbilt, *Phys. Rev. B.*, 41(11):7892, **1990**
- [VHW68]. G. J. Visser, J. G. Heeres, J. Wolters, A. Vos, *Acta Crystallogr.*, B24:467, **1968**
- [VWN80]. S. H. Vosko, L. Wilk, and N. Nussair, *Can. J. Phys.*, 58:1200, **1980**
- [Wau92]. K. C. Waugh, *Catal. Today*, 15:51, **1992**
- [WB94]. J. A. White, D.M. Bird, *Phys. Rev. B*, 50:4954, **1994**
- [WCK88]. D.P. Woodruff, C.F. McConville, A.L.D. Kilcoyne, Th. Linder, J. Somers, M. Surman, G. Paolucci, A.M. Brandshaw, *Surf. Sci.*, 201:228, **1988**
- [Wei81]. M. Weinert, *J. Math. Phys.*, 22:2433, **1981**
- [Wig34]. E. Wigner, *Phys. Rev. B*, 46:1002, **1934**
- [WS89]. T. Wichert, M. L. Swanson, *J. Appl. Phys.*, 66:3026, **1989**
- [WGK89]. T. Wichert, M. Grübel, G. Keller, N. Schulz, H. Skudlic, *Appl. Phys. A*, 648:59, **1989**
- [UMU01]. Y. Uehara, T. Matsumoto, S. Ushioda, *Solid State Communication*, 119:671, **2001**
- [ZSH97]. C. Zistl, R. Sielemann, H. Haesslein, S. Gall, D. Bräunig, J. Bollmann, *Material Science Forum*, 258-263:53, **1997**
- [ZSP98]. P. Ziesche, S. Kurth, J. P. Perdew, *Comp. Mat. Sci.*, 11:122, **1998**
- [Y82]. M. T. Yin, *Phys. Rev. B*, 25(12):7403, **1982**

Acknowledgments

There are many people to whom I am thankful for their great support and sincere encouragement during my PhD work:

First I would like to express my gratitude to my supervisor, Prof. Dr. Kurt Schroeder, for his guidance, his invaluable help and understanding shown during many fruitful and creative discussions and the friendly co-operative atmosphere all along this time.

Then I would like to specially thank Prof. Dr. Stefan Blügel for his continuous and trustful support, his many important suggestions and constructive ideas during our discussions, particularly concerning several implementations made in our program.

My warm thanks to Prof. Dr. P.H. Dederichs for his help and friendly discussions.

I would also like to thank Prof. Dr. H. Müller-Krumbhaar for giving me the possibility to carry out this work at the Institute Theorie-III.

Warm thanks Dr. A. Antons, Dr. R. Berger, Dr. G. Bihlmayer, Dr. Vasile Caciuc, Markus Heide, Dr. Hölger Hohler, Dr. W. Kromen and Dr. Juarez L. F. da Silva for their friendly help and useful assistance.

And last but not least my sincere thanks to all those who have helped me to get here and are not named on this page but will always be remembered with affection.

Personal data

Name: Nicolae Atodiresei
Date of birth: 2. December 1975
Place of birth: Pascani (Romania)
Nationality: romanian
Marital status: married, one child
Email: n.atodiresei@fz-juelich.de

Education

1982-1986 Primary school, Pascani
1986-1990 Secondary school, Pascani
1990-1994 High-school, Pascani
Baccalaureate-1994

Academic qualifications

1994-1998 Degree of Bachelor of Science in the field of Chemistry and Physics,
Field of specialization Physical Chemistry, Faculty of Chemistry,
"Al. I. Cuza" University, Iasi (Romania)
1996/1997 1st and 2nd years of study in field of Chemistry, Field of specialization
1997/1998 Technological Biochemistry, Faculty of Chemistry,
"Al. I. Cuza" University, Iasi (Romania)
1998-2000 Diploma of Master, "Dynamics and Analysis of Chemical Systems"
Faculty of Chemistry, "Al. I. Cuza" University, Iasi (Romania)
Feb. 2001 Begin PhD-studies in the group of Prof. Dr. Kurt Schroeder
(IFF-Jülich, Germany)